Title

A STUDY OF THE_REACTIONS IT p u>pK|n- K-p ->pK-| n|n-, AND K- p--> nK| n+ n- FROM 2.1 TO 2.7 GeV/c.

Author

Friedman, Jerome H.

Publication Date

1969-04-01

UCRL-18860

cy 2

A STUDY OF THE REACTIONS $K^-p \to p\bar{K}^0\pi^-$, $K^-p \to p\bar{K}^0\pi^0\pi^-$, AND $K^-p \to n\bar{K}^0\pi^+\pi^-$ FROM 2.1 TO 2.7 GeV/c

Jerome H. Friedman
(Ph.D. Thesis)

April 1969

AEC Contract No. W-7405-eng-48

LAWRENCE RADIATION LABORATORY
UNIVERSITY of CALIFORNIA BERKELEY

UCRL-18860

cy 2

DISCLAIMER

A Study of the Reactions $K^-p \to p\bar{K}^0\pi^-$, $K^-p \to p\bar{K}^0\pi^0\pi^-$, and $K^-p \to n\bar{K}^0\pi^+\pi^-$ from 2.1 to 2.7 GeV/c.

Contents

Abstract v

I. Introduction. 1

II. The Beam 4

III. Data Reduction. 5

IV. Biases

A. The Beam 10

B. Scanning 10

C. Measurement and Spatial Reconstruction 14

D. Kinematic Fitting and Ambiguities 15

V. Total Cross Sections

A. Pathlength 20

B. Numerator 22

VI. The Maximum Likelihood Analysis. 26

VII. The Reaction $K^-p \to p\bar{K}^0\pi^-$ 33

VIII. The Reaction $K^-p \to K^{*-}_{1/2}(892)\ p$ 38

IX. The Reaction $K^-p \to p\bar{K}^0\pi^0\pi^-$ 43

X. The Reaction $K^-p \to n\bar{K}^0\pi^+\pi^-$ 47

XI. The Reaction $K^-p \to \bar{K}^*_{1/2}(892)\ N^*_{3/2}(1238)$. 50

XII. Theoretical Models

A. The Absorptive Peripheral Model. 62

B. The Regge Pole Model 72

C. The Quark Model. 78

Acknowledgements 80

Appendix 81

Footnotes and References 86

A Study of the Reactions $K^- p \to p\bar{K}^0 \pi^-$, $K^- p \to p\bar{K}^0 \pi^0 \pi^-$, and $K^- p \to n\bar{K}^0 \pi^+ \pi^-$ from 2.1 to 2.7 GeV/c.

Jerome H. Friedman

Lawrence Radiation Laboratory
University of California
Berkeley, California

ABSTRACT

The reactions $K^- p \to p\bar{K}^0 \pi^-$, $K^- p \to p\bar{K}^0 \pi^0 \pi^-$, and $K^- p \to n\bar{K}^0 \pi^+ \pi^-$ are studied in detail in the LRL 72-in. hydrogen bubble chamber in the center of mass energy range 2.27 to 2.51 GeV. Total cross sections for these reactions as a function of center of mass energy are presented. Copious resonance production is observed in all of these final states. This resonance production is studied with the aid of a maximum likelihood technique and the relative rates of the well known resonances are presented as a function of center of mass energy. The differential cross section and decay correlation parameters are measured as a function of production angle and center of mass energy for the reaction $K^- p \to K^{*-}_{1/2}(892)\, p$ using the likelihood method. The differential cross section and parameters of the joint decay angular distributions for the double resonance production reaction $K^- p \to \bar{K}^{*}_{1/2}(892)\, N^{*}_{3/2}(1238)$ are also measured as a function of production angle and center of mass energy. The results of the analyses on the reactions $K^- p \to K^{*-}_{1/2}(892)\, p$ and $K^- p \to \bar{K}^{*}_{1/2}(892)\, N^{*}_{3/2}(1238)$ are compared to the predictions of the absorptive peripheral model, The Regge pole model, and the quark model. Finally, the $K\pi\pi$ mass spectra are studied and the structure therein discussed.

I Introduction

It is the purpose of this report to study the reactions $K^- p \to p \bar{K}^o \pi^-$, $K^- p \to p \bar{K}^o \pi^o \pi^-$, and $K^- p \to n \bar{K}^o \pi^+ \pi^-$ in the center of mass energy range 2.27 to 2.51 GeV. Besides the possibility of discovering new phenomena, these reactions are interesting because of the copious production of well known resonant intermediate states leading to these final states. A study of the production and decay properties of these resonant states gives considerable information about the production mechanisms. There have been several theories for these production mechanisms proposed in recent months,[1-7] and this experiment can test the predictions of these theories as well as provide data for the testing of future theories.

The interactions were photographed in the L.R.L. 72-inch liquid hydrogen bubble chamber. K^- mesons from a separated beam at the Bevatron were introduced into the chamber with nominal laboratory momenta of 2.1, 2.45, 2.58, 2.61 and 2.7 GeV/c for a period of about two years and approximately 1.7×10^6 photographs were recorded.

The discussion of this experiment falls into two parts. First is a discussion of the general procedures that have been developed for producing, observing, and recording interactions in the hydrogen bubble chamber and then reducing the data to a form convenient for calculations.[8] This includes a description of the beam used to obtain the K^- mesons of the desired momenta and direct them into the bubble chamber. Also there is a description of the procedures for scanning the film, measuring and cataloging the events, spatial reconstruction of the bubble tracks, fitting the events to reaction hypotheses, and the separation of these

hypotheses to obtain the events representing examples of the reactions studied here.

The second part will deal with the analysis of these reactions and a detailed study of their properties. This will include, first of all, a discussion of the possible biases to the data introduced by the data reduction system, detection of these biases and the procedures introduced to account for those detected. Next the total cross sections for these reactions as a function of center of mass energy are presented along with a discussion of the procedures used to calculate them.

A maximum likelihood procedure is described which allows the measurement of the relative rates of the production of several intermediate resonant states leading to the same final state. This method is then generalized to allow measurement of the parameters of the decay angular distributions of these resonances as well as their relative rates.

This procedure is first applied to the reaction $K^- p \to p \bar{K}^o \pi^-$. The production of non-negligible amounts of Y^*_1 (1660), Y^*_1 (1765), $N^*_{3/2}$ (1238), $N^*_{1/2}$ (1520), N^* (1688) and $K^*_{1/2}$ (892) are observed at all beam momenta, and production of $K^*_{1/2}$(1400) is also observed at the higher beam momenta. The total cross sections for the production of these resonances are presented as a function of center of mass energy. The most copiously produced resonance, $K^*_{1/2}$ (892) is studied in more detail. Its differential cross section and the parameters of its decay angular distribution are measured as a function of production angle and center of mass energy.

Next the likelihood procedure is applied to the reaction $K^- p \to p \bar{K}^o \pi^o \pi^-$, where production of the well known resonances:

$N^*_{3/2}$ (1238), $K^*_{1/2}$ (892) and $K^*_{1/2}$ (1400) is observed. In addition associated production of $K^*_{1/2}$ (892) $N^*_{3/2}$ (1238) is observed. Also there is an enhancement in the $\bar{K}^o \pi^o \pi^-$ mass spectrum at a mass of 1280 MeV with a full width at one half maximum of 50 MeV. The total cross sections for the production of these resonant states as a function of center of mass energy are presented. The associated production of K^* (892), N^* (1238) is analyzed further. Its differential cross section and parameters of the joint decay angular distribution are measured as a function of production angle and center of mass energy.

The last reaction to be studied is $K^- p \rightarrow n \bar{K}^o \pi^+ \pi^-$ where Y^*_0 (1520), $N^*_{3/2}$ (1238) and $K^*_{1/2}$ (892) are produced. Associated production of $K^*_{1/2}$ (892), $N^*_{3/2}$ (1238) is also observed but in insufficient quantity to allow a detailed analysis. The total cross sections for the production of these resonances as a function of center of mass energy is presented.

The $K \pi \pi$ mass spectra in the four particle final states are studied, and the nature of the observed enhancements in $\bar{K}^o \pi^o \pi^-$ investigated.

Finally, theoretical models for the reactions $K^- p \rightarrow K^{*-}_{1/2}$ (892) p and $K^- p \rightarrow K^*_{1/2}$ (892) $N^*_{3/2}$ (1238) are considered. The experimental measurements of the first reaction are compared to the predictions of the absorbative peripheral model with pseudoscalar and vector meson exchange,[45] and to a Regge pole model.[47] The results of the experimental analysis on the second reaction are compared to the predictions of the absorbative peripheral model with pseudoscalar meson exchange[61] and to a quark model.[51]

II The Beam

The beam used in this experiment has been described in detail elsewhere [9-13] and only its general features and those details pertinent to this analysis will be presented here.

The beam was derived from an internal copper target in the west quadrant of the Bevatron. The beam transport system involved two stages of separation employing bending magnets to split the beam into momentum components, glass cathode spectrometers to separate it into its velocity components and quadrupole magnets to focus the desired components through well defined slits and the undesired components away from these slits. In most of its features this beam differed little from those used in earlier K^- exposures except that tolerances were more critical since at the higher beam momenta it was running close to the upper limit of K^-'s produced at the target.

An unusual feature of this beam was the use of tilted mass slits to account for chromatic aberration. Due to low K^- flux produced at the target at the higher momentum settings a large momentum bite was necessary to provide sufficient flux at the bubble chamber. This introduces severe chromatic aberration which is accounted for by separating the momentum components with a bending magnet and tilting the mass slits toward the horizontal beam line.

At the highest momentum settings, the beam produced typically 6 to 7 K^- mesons per Bevatron pulse with 1.5×10^{12} protons incident on the target and a momentum bite of two percent ($\Delta p/p = .02$). Both flux and purity improved at the lower momentum settings.

III Data Reduction

The bubble chamber photographs were scanned on the Alvarez Group SP-4 scanning projectors. At these energies many different final states are possible and the first classification of events is made as to the topology of the visible bubble tracks. The reactions studied here come from the two pronged plus vee topology sketched in figure 1. The scanners also recorded the position of each event found in the chamber and other indicative information.[14]

After the K^-p interactions are located on the film by the scanning process, the bubble tracks are measured in at least two views on digitized projection microscopes. Alvarez Group MP-2c and MP-2d "Frankensteins" and SMP projectors[15] were used for this experiment. The measured points as well as other indicative information were recorded on magnetic or punched paper tape.

This information is then processed by several computer codes. First a code called PANAL[16] checks the measurement information for obvious inconsistencies and reformats the data for the next computer code called PACKAGE.[17-20] This program is divided into two parts which perform different functions. The first part, called PANG, has coded into it a detailed knowledge of the optical system and magnetic field in the bubble chamber, and makes a reconstruction of each bubble track in space, and calculates the position, momenta and orientation of each track along with errors. This information is then treated by the second part of the PACKAGE code, called KICK. This routine tries to fit the event to all possible reactions consistent with its topology. In the case of the two pronged plus vee topology a hypothesis is made

for the particle whose decay gave rise to the vee. The alternatives are either $\overline{K}^o \rightarrow \pi^+\pi^-$ or $\Lambda \leftrightarrow p\ \pi^-$.[21] For each, a mass is assigned accordingly to each track, its energy computed from this mass and the measured momenta, and the constraints of energy and momentum conservation applied. A least squares fit is performed in which the measurable quantities are varied so as to be as close as possible to their measured values and satisfy the constraints of energy and momentum conservation. Since the $\overline{K}^o$ (or Λ) is a neutral particle it leaves no track in the bubble chamber so that its momentum from curvature is not known. However its direction is known from the relative positions of the two vertices of the event. Thus one of the constraint equations must be used to calculate this missing information, and there are three constraints left to be satisfied.

Using the fit from the vee, various hypotheses made as to the production vertex. If there are no missing neutrals at the production vertex the fit has four constraints. If there is one missing neutral particle there is one constraint left and a fit is still possible. If more than one neutral particle is produced no fit is possible and only the missing momentum and energy can be calculated.

The reactions studied in this report are:

$K^- p \rightarrow p \overline{K}^o \pi^-$	4 constraint fit at primary vertex
$K^- p \rightarrow p \overline{K}^o \pi^- \pi^o$	1 constraint fit at primary vertex
$K^- p \rightarrow \overline{K}^o \pi^+ \pi^- n$	1 constraint fit at primary vertex.

The output from the PACKAGE program is run through two more computer codes WRING[22] and AFREET[23] which reformat the PACKAGE output. Finally the data is treated by DST-EXAM.[24] Using the information

from PACKAGE, this routine selects the "best" hypothesis for the event, determines whether this hypothesis is ambiguous with others, and outputs the various physical quantities for the "best" hypothesis as well as relevant bookkeeping information. Thus the output from DST-EXAM constitutes the "reduced" data which is used for all further analysis.

Decision making is performed by DST-EXAM as follows. For each hypothesis for each vertex, PACKAGE returns the chi square for the attempted least squares fit. Decisions in DST-EXAM are based on the confidence level, which is the probability of obtaining a chi square greater than or equal to the one observed, provided the hypothesis is correct. The confidence level has the property that its distribution is flat if the chi square distribution is correct.[25] Since confidence level takes into account the number of constraints, hypotheses with different numbers of constraints can be compared directly. The observed chi square distributions are not correct, however, since PACKAGE underestimates the errors in the measurables. In order to make the confidence level distributions as flat as possible, the chi square for each hypothesis is multiplied by an empirical factor which depends upon the number of constraints.[26]

DST-EXAM forms a chi square and number of constraints for each hypothesis for the entire event in the following manner:

$$\chi^2_H = \sum_{i=1}^{N} \chi^2_i \, F(n_i) \quad , \quad n_H = \sum_{i=1}^{N} n_i$$

where χ^2_H is the chi square for the event, N is the number of vertices (equal to two for the two pronged plus vee topology), χ^2_i is the chi square for each vertex, F is the empirical factor for each vertex, and n_H is the number of constraints for the entire event. The confidence level for χ^2_H and n_H is calculated for each hypothesis.

Chi squares for missing mass hypotheses are also calculated in DST-EXAM on the basis of a minimum missing energy.[27] A probability for a missing mass vertex is computed as:

$$P(MM) = f\, P(E, E_{min}) \prod_{i=1}^{N_f} (1 - P_f)$$

where P(MM) is the probability for the missing mass hypothesis, f is an overall empirical factor (0.2 for this experiment), E is the missing energy for the event, E_{min} is the minimum missing energy for the missing mass hypothesis, N_f is the number of successful non-missing mass fits, and P_f is the probability for each such successful fit. $P(E, E_{min})$ is defined as follows:

$$P(E, E_{min}) = \begin{cases} 1.0 \text{ for } E > E_{min} + \sigma_E \\ e^{-\left(\frac{E - E_{min} - \sigma_E}{\sigma_E}\right)^2} \text{ for } E < E_{min} + \sigma_E \end{cases}$$

where σ_E is the error on the missing energy. P (MM) is converted to a chi square by assuming it has one constraint.

An event was considered acceptable if there was at least one hypothesis for it with a confidence level greater than one half of one percent (.005). An event was considered ambiguous if more than one

hypothesis had such a confidence level and the largest confidence level was less than three times as large as the next highest. The "best" hypothesis is defined as the one with the highest confidence level for the event.

IV Biases

A) The Beam

Contamination of π^- mesons in the beam can cause biases to the data from their interactions in the bubble chamber. From counting three pronged decays of K^- and beam tracks, the contamination of non K^- to the beam was estimated to be around 20 °/o at 2.70 GeV/c and about 10 °/o at the lower momenta.

A more accurate determination of π^- contamination was obtained by fitting the zero pronged two vee events to the associated production hypothesis $\pi^- p \rightarrow K^o \Lambda$. This is a four constraint fit. From the number of fits obtained and the cross section for associated production at these energies the path length of π^- in the film can be determined for each momentum. Table 1 gives the results of this analysis.[28] The π^- contamination is seen to increase with increasing beam momentum becoming most serious at 2.7 GeV/c.

With the exception of 2.7 GeV/c the contamination to the two pronged plus vee topology from π^- interactions is seen (from Table 1) to be negligible. At 2.7 GeV/c this contamination is marginal but not serious. Thus, this bias has been neglected in the rest of this analysis.

B) Scanning

Scanners can introduce biases by not finding events that are on the film or by misclassifying those that they do find. This can bias total cross sections as well as angular correlations since events of certain configurations are harder to find or more easily misclassified. To minimize these effects the film is scanned twice at separate times by

separate scanners. The results of these scans are compared and those conflicts that are found to exist are resolved. One can estimate the bias to the total cross section measurement by comparing the two scans and determining the efficiency for finding events on the film.

Scanners are more inclined to miss events with the following configurations: the production plane of the primary vertex is near the vertical, or the decay plane of the vee is near vertical. These biases can be detected by histogramming the angle of the production or decay plane with respect to the vertical direction. Figure 2 shows these histograms. As can be seen this bias is small in this experiment and may be neglected.

Two more configurations are more easily missed or misclassified by scanners. These are 1) the $\overline{K}^o$ decays very close to the primary vertex and may be confused with the primary vertex itself or 2) the $\overline{K}^o$ decays far from the primary vertex and might be missed altogether. Those events in the first category will be misclassified as four pronged events and those of the second as two pronged events.

The first possibility is most easily detected by histogramming the length of the $\overline{K}^o$. If there is no bias of this type, this plot should be consistent with the well known exponential decay law. If there is a bias then the plot will deviate from this exponential at shorter length. Figure 3 shows this plot for shorter length $\overline{K}^o$ events in this experiment. As can be seen the histogram deviates drastically from an exponential for very short $\overline{K}^o$ lengths. Thus this bias is seen to be serious for this data.

The bias against very long lenth $\overline{K}^o$ can be detected by measuring the mean life of the $\overline{K}^o$ as a function of an imposed long length cutoff. If this bias is present, the measured mean life will decrease as the long length cutoff is increased. Figure 4 shows the results of these measurements. The line band indicates the world averaged value for the $\overline{K}^o$ lifetime and its error.[29] As can be seen there seems to be no measurable decrease in the measured K^o_1 mean life as the long length cutoff is increased. Of course, those events where the $\overline{K}^o$ leaves the chamber are misclassified, but it is possible to correct for this, as is described below.

The effects of the last two biases can be reduced by introducing a fiducial volume in the chamber for the decay vertex. All events whose decay vertex lies outside this fiducial volume will be rejected, and all those inside will be weighted with the inverse probability that they would have decayed inside the fiducial volume. The fiducial volume is chosen so as to exclude events with configurations that are badly biased. The fiducial volume excludes fixed regions near the periphery of the chamber, and surrounding the primary vertex of each event a cylindrical region of radius ℓ capped top and bottom by sections of a sphere of radius twice ℓ. Figure 5 shows a sketch of the excluded region surrounding each primary vertex.

The probability for the $\overline{K}^o$ to decay inside the allowed fiducial volume is given by $P = e^{-\frac{\ell}{\eta c \tau}} - e^{-\frac{L}{\eta c \tau}}$,

where ℓ is the distance from the primary vertex to the inside fiducial volume boundary along the direction of the $\overline{K}^o$, L is the distance to the outside fiducial volume boundary, η is the momentum of the $\overline{K}^o$ divided by its mass, c is the speed of light and γ is the mean life of the K^o_1. The weight of an event is then $W = 1/P$ and the corrected number of events in a sample is $N = \sum_{i=1}^{M} W_i$ where M is the number of events in the sample and Wi is the weight for the ith event in the sample.

The fixed outside region was determined from an a priori consideration of those parts of the chamber that are hard to see, hard to measure or where turbulence is a problem. The short length cutoff, or inner fiducial volume boundary parameter "ℓ" can be determined by plotting the total corrected number of events as a function of "ℓ". Starting with a small cutoff length, as it is increased the sum of weights for the events should increase until a length is reached where the bias is no longer present. Increasing it further should cause the sum of the event weights to remain approximately constant. The nominal cutoff length ℓ, is that length where the sum of the weights stops increasing.

Figure 6 shows these plots separately for each beam momentum exposure and separately for the three and four particle final states. These plots exhibit the expected behavior described above. The arrows show the value chosen for the given sample plotted. Table 2 gives the value of the nominal short length cutoff ℓ chosen for each sample as well as the correction it gives to the total number of events in the sample.

C) Measurement and Spatial Reconstruction

Biases can come from measurement since events with particular spatial configurations are harder to measure than others and have less chance of a successful spatial reconstruction. Vertices near the edge of the chamber or with short or steeply dipping tracks are examples. To help reduce this bias a fiducial volume for the primary vertex was imposed to exclude fixed regions near the edge of the chamber and where events are difficult to measure.

An event which fails to be successfully spatially reconstructed by PANG is remeasured and processed a second time. If the event fails a second time it is remeasured again and reprocessed a third time and so on. This procedure keeps the number of these small. The bias to total cross sections can be accounted for since these events are identified and not lost. The bias to angular distributions is small since most of these errors are due to operator mistakes, and is neglected here.

D) Kinematic Fitting and Ambiguities

Two types of biases are introduced to the data by the kinematic fitting stage of data reduction.

First events may fail to fit any reaction hypothesis. This is usually due to poor measurement and subsequent spatial reconstruction. These events are treated in the same manner as events which fail spatial reconstruction. They are remeasured and processed a second time and so on. These events are accounted for in the same manner as those which fail spatial reconstruction. The bias to angular correlations here is also small and is neglected.

The most serious bias introduced in kinematic fitting comes from events that fit well a reaction hypothesis which is not the reaction which gave rise to the event. This bias can go both ways. Events may be lost due to their fitting another hypothesis better or events may be added to the sample because they fit its hypothesis better than the correct one. This bias effects both total cross sections and angular distributions since "faking ability" is strongly correlated to both the reaction hypothesis and the kinematic configuration of the event.

Contamination (and/or loss) can come from two sources: lambda hypotheses and other $\overline{K}^o$ hypotheses. Λ contamination can be most easily detected by plotting the decay angle of the $\overline{K}^o$ in its rest frame. If there are no biases from Λ contamination this distribution should be consistent with isotropy. Figure 7 shows this distribution separately for the one and four constraint reactions. The four constraint events are seen to be consistent with an isotropic distribution but the one constraint events show a sharp peak in the extreme forward direction.

This excess of events in the forward direction is contaminated from Λ events. The four constraint events are seen to be free of this contamination. For the events which fit one constraint hypotheses best, the Λ contamination as identified in the forward peak, amounts to approximately 7 $^{o}/o$ of the total sample.

Removal of the Λ contamination can proceed in two ways. First, one can try to decide which are the Λ events by looking at the relative ionization of the positive track at the vee. It is possible to separate a proton from a π^{+} by the ionization of its bubble track, if the particle has a momentum in the laboratory of less than one BeV/c. Approximately one-half of the events in this sample have vees whose positive track is less than one BeV/c in the laboratory.

Approximately one-half of the events ambiguous with Λ hypotheses were inspected on the scan table. Approximately one-half of these could be resolved. Of those events that could be resolved by ionization at the scan table, all appeared to be Λ decays.

Another procedure to try to remove Λ contamination is to alter the decision making in DST-EXAM to better separate between Λ and $\overline{K}^{o}$ hypotheses. Figure 8 shows the $\overline{K}^{o}$ decay angle for various decision making criteria. As can be seen, almost all of the Λ contamination can be removed while discarding only a very few legitimate $\overline{K}^{o}$ events by giving a Λ assignment to any event which has a confidence level for a Λ production hypothesis greater than .001, even though it has a higher confidence level for a one constraint $\overline{K}^{o}$ production hypothesis. This was the criterion subsequently used. As Figure 8 shows, this lowers the Λ contamination to the one constraint $\overline{K}^{o}$ events to less than one

percent.

Contamination (and/or loss) also can come from other $\overline{K}^{o}$ hypotheses. This type of bias is not so easily detected as that from the Λ contamination. The ambiguous events provide a clue to the effects these biases since we expect these events to have higher contamination from wrong hypotheses than the unambiguous ones. The four constraint events contain less than one percent ambiguities. These are all ambiguous between the $K^{-} p \rightarrow p \overline{K}^{o} \pi^{-}$ hypothesis and either a one constraint or missing mass hypothesis. Since it is harder to fit four constraint hypotheses than either one constraint or missing mass hypothesis, these events are assumed to belong to the four constraint sample. Since there are <1 $^{o}/o$ ambiguities, the possible biases introduced by contamination to the four constraint events is negligible.

Separation of hypotheses is more difficult in the case of the one constraint reactions. Table 3 shows a histogram of the ambiguous reaction hypotheses for both one constraint reactions considered in this report. As can be seen, ambiguities with the four constraint hypothesis are small in both cases. The principle ambiguities are between the two one constraint hypotheses and the missing mass hypotheses corresponding to the other one constraint reactions.

These ambiguities can be investigated by looking at the ionization of the positive track at the primary vertex. Almost all events in these reactions have the momentum of this track less than one GeV/c in the laboratory. Thus all of these ambiguities can be resolved at the scanning table, in principle. In practice this is a large job,

since these few events are scattered throughout all of the rolls of film in the experiment.

In order to estimate the actual contamination resulting from these ambiguities, all of these ambiguous events which existed three or more per roll were looked at on the scan table. This accounted for around one-half of these ambiguous events in the sample. This scan showed that 27 °/o of the ambiguous events which fit $K^- p \rightarrow p \bar{K}^o \pi^- \pi^o$ were really examples of the reaction $K^- p \rightarrow n \bar{K}^o \pi^+ \pi^-$ or $K^- p \rightarrow \bar{K}^o \pi^+ \pi^-$ + missing mass. 33 °/o of the ambiguous events which fit best $K^- p \rightarrow n \bar{K}^o \pi^+ \pi^-$ were really $K^- p \rightarrow p \bar{K}^o \pi^o \pi^-$ or $K^- p \rightarrow p \bar{K}^o \pi^-$ + missing mass. This amounts to 2.2 °/o of the total sample of $K^- p \rightarrow p \bar{K}^o \pi^o \pi^-$ and 3.7 °/o of $K^- p \rightarrow n \bar{K}^o \pi^+ \pi^-$. This then is an estimate of the actual contamination to these samples from the wrong reaction.

The next step was to correct those events which had been identified from the ambiguity scan as having been assigned the wrong reaction hypothesis and adding them to the correct sample. This reduced the contamination to 1.1 °/o and 1.3 °/o respectively for the reactions $K^- p \rightarrow p \bar{K}^o \pi^o \pi^-$ and $K^- p \rightarrow n \bar{K}^o \pi^+ \pi^-$.

In order to see if this contamination could produce any sharp effects to the data, the events which were seen to have been assigned the wrong reaction hypothesis as a result of the special ambiguity scan were studied in detail. The results of this study showed that there was no serious bunching of these events in any kinematic measurable and that the above contaminations could produce no measurable effects to the data.

As a final check on the data Figure 9 shows missing mass plots

for the one constraint and missing mass events. As can be seen the possible loss to (or contamination from) missing mass hypotheses is small.

V Total Cross Sections

One of the most fundamental measurements concerning a reaction is its rate or frequency of occurrence. This may be parameterized by the mean free path for the reaction, which is the average distance a beam particle travels in the target material before suffering the particular type of reaction. This average distance may be evaluated by

$$\lambda = \frac{L}{N}$$

where λ is the mean free path, L is the total pathlength the beam particles travel in the target material and N is the total number of reactions of the specific type. Reaction rates are usually parameterized by the cross section for the reaction, which is related to the mean free path by

$$\lambda = \frac{1}{n\sigma}$$

where n is the density of targets in the target material, and σ is the reaction cross section. Solving for the cross section one obtains

$$\sigma = \frac{N}{nL} .$$

A) Pathlength

In experiments where the beam consists of K^- mesons, the pathlength of the K^- in the hydrogen bubble chamber for each momentum can be inferred from the number of three pronged decays of the beam K^- observed in the chamber. An event with a three pronged topology in the hydrogen bubble chamber can only result from a beam K^- decay. Thus the pathlength of K^- in the beam can be determined in this manner even if the beam contains other particles.

The pathlength of K^- in a sample of hydrogen bubble chamber

photographs is given by

$$L = N_\gamma \frac{P_{K^-} c \tau_{K^-}}{m_{K^-} B_\gamma} \qquad (1)$$

where L is the pathlength, N_γ is the number of events with three pronged topology in the sample, P_{K^-} is the momentum of the incident K^- mesons through the chamber,[35] C is the velocity of light, τ_{K^-} is the mean life of the K^- meson, m_{K^-} is the rest mass of the K^- meson, and B_γ is the branching ratio for the three pronged decay of the K^- meson.

The problem of evaluating the pathlength thus reduces to counting the number of three pronged events in each exposure and determining the efficiency for finding events with this topology.

The efficiency for finding three pronged events was determined by rescanning samples of film distributed throughout the experiment. This rescan was compared to the original scan and all conflicts were resolved at the scan table. An effiency factor for the original scan can then be determined as[71]

$$E = 1 + \frac{N_I - N_M}{N_T} \qquad (2)$$

where E is the efficiency factor, N_I is the number of events in the sample that the original scan called three pronged that were actually of another topology, N_M is the number of three pronged events that were missed on the original scan or misclassified on the original scan as another topology. N_T is the total number of events in the sample found on the original scan. This efficiency factor depends very little on incident beam momentum and depends mostly on the individual who performed

the scan. Thus one average efficiency was calculated for all of the beam momentum exposures. The efficiency factor for three pronged events on the original scan was found to be .977 ± .016. The error results from the statistical uncertainty of the sample chosen to be conflicted against the original scan.

The pathlength at each momentum is then determined using eqn. 1. Table 4 gives the number of three pronged events found on the original scan, the estimate of the actual number of three pronged events, estimated by using the number found on the original scan and the efficiency factor, and the pathlength for each momentum. Also table 4 gives the values and errors of the various quantities entering into eqn. 1. The errors in the pathlength come from the statistical errors in the number of three pronged events at each momentum, the statistical errors in the efficiency calculation and the errors in the various quantities entering into eqn. 1.

B. The Numerator

Counting the number of events of a given reaction is more difficult than counting the number of events of a given topology, since the complete data reduction system is needed, to separate the various reaction hypotheses, rather than just the scan information. As discussed in the previous chapter the biases that enter into the data reduction system are complex and harder to understand than just the scanning biases. Also there is a residue of events at each momentum for which no fitted information exists. These are events which for some reason have never been measured, or having been measured once, or several times, fail to be successfully spatially reconstructed by PANG or kinematically fitted

to a reaction hypothesis in KICK. Since these events constitute a select sample, their composition among the various reaction hypotheses may not be the same as the sample of events for which fitted information exists.

Since the reactions studied here all come from the two pronged plus vee topology, the number of events with this topology at each momentum was first determined using the scan information only. Then the kinematic fitted information was used to evaluate the fraction of each reaction composing this topology.

The number of two pronged plus vee events was determined in the same manner as the three pronged events described above. An efficiency factor was evaluated by rescanning a portion of the film, comparing the results with the original scan and resolving all conflicts at the scan table. The efficiency factor (as defined in eqn. 2) for the two pronged plus vee topology was found to be $1.0 \pm .03$. Here again the error results from the statistical uncertainty of the sample chosen for the conflict.

The number of two pronged plus vee events resulting from interactions of the π^- contamination in the beam, shown in table 1, was subtracted from the total estimated number of two pronged plus vee events at each momentum.

Table 5 gives the estimated number of two pronged plus vee events at each momentum and the number of these resulting from K^- interactions obtained by subtracting the π^- induced events. The errors result from the error in the efficiency factor.

Next the fitted information was used to estimate the fraction

of two pronged plus vee events that constitute the reactions studied here. The number of events for which no fitted information exists differs for the various momenta. 2.45 GeV/c and 2.70 GeV/c are the most completed exposures in that they have the smallest fraction of non-fitted events and 2.1 GeV/c is the least complete. 2.58 and 2.61 GeV/c are slightly more complete than 2.1 GeV/c but much less than 2.45 or 2.70 GeV/c. This presents a problem since the passing rate of the various reaction hypotheses, as a function of the number of times the failing events are remeasured and reprocessed, is different. Thus the relative fractions of the various reactions in the fitted events changes as more of the difficult to process events finally pass and are added to the sample.

In order to estimate this effect, the relative fractions of the various reaction hypotheses in the passing events were studied as a function of the number of measurement passes made on the failing events for the most completed momenta (2.45 and 2.70 GeV/c.). It was found that each $\overline{K}^{o}$ hypothesis increased its fraction of the whole two pronged plus vee sample from the first to the third measurement pass by approximately 7 °/o. Since this increase is so nearly the same for all three reactions at both momenta, the average of the six values was chosen to be used for extrapolating those momenta where less than three processing passes were made. This average value is .076 ± .013 where the error is taken to be the root mean square deviation of the six values.

Finally these fractions must be corrected for the differences in short length and chamber escape corrections of the vee, for the different reactions at the various momenta, as shown in table 2.

Table 6 and figure 10 give the results for the total cross section for each of the three reactions $K^- p \rightarrow p \bar{K}^o \pi^-$, $K^- p \rightarrow p \bar{K}^o \pi^- \pi^o$, and $K^- p \rightarrow n \bar{K}^o \pi^+ \pi^-$ for each beam momentum. The errors result from combining in an uncorrelated way the statistical errors in the numbers of events used, the estimated errors in the various calculated efficiencies, and the pathlength error.

VI The Maximum Likelihood Analysis

A common property to the reactions studied here is the copious production of many different resonant processes all leading to the same final state. An interesting problem is to determine the relative rates of production of these resonance processes. Also, it is interesting to be able to measure the rate for associated resonance production as separated from the corresponding single resonance production; for example $K^- p \to K^* N^*$ as distinct from $K^- p \to K^* N \pi$ and $K^- p \to N^* K \pi$. Also it would be helpful to be able to take into account the effects of the decay angular correlations due to the spin alignments of the resonances when measuring the rates, or conversely, take into account the effects of competing resonance production when measuring the decay correlation coefficients of the resonances.

These problems are approached here through the method of maximum likelihood fitting. The method requires the construction of a model which predicts the total rate for the reaction. The model depends upon the measurables of the events and parameters which do not depend explicitly on the event measurables. The problem is to find the values of these parameters that best describe the experiment. These values are said to be the most probable values of the parameters as measured by the experiment. Let $F(X_1 \ldots X_N; \alpha_1 \ldots \alpha_M)$ represent the frequency function for events of the experiment as predicted by the model. This frequency function depends upon the event measurables $X_1 \ldots X_N$, and the model parameters $\alpha_1 \cdots \alpha_M$.

The first step is to convert this frequency function into a differential probability by normalizing it.

$$P(x_1 \cdots x_N; \alpha_1 \cdots \alpha_M) = \frac{F(x_1 \cdots x_N; \alpha_1 \cdots \alpha_M)}{\int F(y_1 \cdots y_N; \alpha_1 \cdots \alpha_M)\, dy_1 \cdots dy_N}$$

where the region of integration is the allowed values of the event measurables $X_1 \ldots X_n$. Using this probability density function, one calculates the probability that the model would have predicted each event. The product of these probabilities gives the probability that the model would have predicted the experiment. The Maximum Likelihood Theorem[30] states that those values of the parameters which maximize this probability are the most likely values of these parameters, that in the limit of a very large number of events, these most likely values approach the true values of the parameters, and furthermore there is no other method of estimation that is more accurate. This is of course provided that the model is correct and $P(X_1 \ldots X_n;\ \alpha_1 \cdots \alpha_M\ )$ is the true normalized distribution function for the events.

The problem then is to maximize the function $L(\alpha_1 \cdots \alpha_M)$ where

$$L(\alpha_1 \cdots \alpha_M) = \prod_{i=1}^{N} P(X_1^i \cdots X_n^i; \alpha_1 \cdots \alpha_M)$$

where N is the total number of events in the experiment and $X_1^i \ldots X_n^i$ are the particular values of $X_1 \ldots X_n$ for the ith event. Since the logarithm of a quantity varies montonically as the quantity, one can just as well

seek the maximum of the function

$$w(\alpha_1 \cdots \alpha_M) = \log L(\alpha_1 \cdots \alpha_M) = \sum_{i=1}^{N} \log P(x_1^i \cdots x_n^i ; \alpha_1 \cdots \alpha_M)$$

the error matrix for the parameters $\alpha_1 \cdots \alpha_M$ is given by the inverse of the second derivative matrix of w evaluated at the maximum[31]

$$\overline{\Delta\alpha_i \Delta\alpha_j} = \left(\frac{\partial^2 w}{\partial\alpha_k \partial\alpha_\ell} \right)^{-1}_{ij} \Bigg/ \alpha_1^0 \cdots \alpha_M^0$$

where $\alpha_1^0 \cdots \alpha_M^0$ are the values of the parameters at the maximum of the likelihood function L (or w).

The problem is then to construct a frequency function which gives the rate for the final state, parameterized in terms of the relative rates of the intermediate state resonance processes. This can be done as follows:

$$P(x_1 \cdots x_n ; \alpha_1 \cdots \alpha_M) = \sum_{i=1}^{M} \alpha_i \frac{BW(x_1 \cdots x_n)}{\int BW(y_1 \cdots y_n)\, dy_1 \cdots dy_n}$$

$$+ \left(1 - \sum_{i=1}^{M} \alpha_i\right) \frac{1}{\int dy_1 \cdots dy_n} \qquad (1)$$

Here $X_1 \ldots X_n$ are the components of the four vectors for the final state particles, $\alpha_1 \cdots \alpha_M$ are the relative rates of the resonance processes and BW is a Breit-Wigner function describing the resonance process. The normalization integrations are carried out over the allowed regions of phase space only. Thus the integral in the denominator of the last term is just the total phase space for the reaction and those of the other terms are total phase space weighted with the appropriate Breit-Wigner resonance function.

Each term in the sum represents one of the final state resonance processes and the last term represents the final state with no intermediate resonance formation. In order that the entire probability density can be normalized the constraint is imposed that the relative rates add to one. This is satisfied by making the fractional rate of the last term one minus the sum of all other fractional rates.

Equation 1 is a sum of rates, one for each resonance process. This assumes that the amplitudes which describe the production of these resonance states do not interfere. Thus, this frequency function can only be used when interferences are small. This need not be true in general, and if equation 1 is used as the model to describe the final state interactions it must be shown that interference effects are small in the particular final state being studied.

The mass and width of each resonance process enter as parameters in equation 1 through the Breit-Wigner functions, and thus they may also be solved for, as well as the relative rates.

Decay angular correlations of the resonance processes can be taken into account simply, if it is assumed (and this need not be

a priori true) that the production and decay amplitudes do not interfere. The total rate for the production and decay of the resonance state then becomes the product of the production rate and the decay rate. This may be parameterized as

$$\lambda(\alpha; M,\Gamma; C_1 \cdots C_K) = \alpha\, BW(M,\Gamma)\, I(C_1 \cdots C_K)$$

where λ is the rate for the production and decay of the resonant state, α is the fraction of the resonant state in the whole final state, M and Γ are the mass and width of the resonance, and I is the decay angular distribution which is parameterized by the coefficients $C_1 \ldots C_K$. These $C_1 \ldots C_K$ may be the spin density matrix elements or coefficients of a spherical harmonic expansion of the decay angular distribution.

The general probability density (neglecting interference effects) will then have the form

$$P(x_1 \cdots x_m; \alpha_1 \cdots \alpha_M; M_1 \cdots M_m; \Gamma_1 \cdots \Gamma_m; C_1 \cdots C_K)$$

$$= \sum_{i=1}^{m} \alpha_i \frac{BW(M_i \Gamma_i; x_1 \cdots x_m)\, I_i(C_1^i \cdots C_K^i; x_1 \cdots x_m)}{\int BW(M_i \Gamma_i; y_1 \cdots y_m)\, I_i(C_1^i \cdots C_K^i; y_1 \cdots y_m)\, dy_1 \cdots dy_m}$$

$$+ \left(1 - \sum_{i=1}^{m} \alpha_i\right) \frac{1}{\int dy_1 \cdots dy_m} \qquad (2)$$

where $\alpha, M, \Gamma,$ X and I have the same meanings as above and C is the j^{th} coefficient of the ith resonance's decay angular distribution. Again the normalization integrations are carried out over the kinematically allowed regions of phase space.

Any or all of the parameters may be variables of the fit or constants. The logarithm of the total likelihood function is formed and then the maximum is found in the space of the varied parameters. After a solution is found the second derivative matrix is evaluated and inverted to obtain the error matrix.

The maximum likelihood method allows one to solve for the most likely values of the parameters of a model, but gives no information as to how well the model fit the data. There is no analog in likelihood fitting to the chi-square in the least squares method. In order to get an estimate of how well the model fits the data, one must make projections of the measurables of the events and compare these projections with what the model predicts for these projections.

The predictions of the solution for distributions of event measurables may be calculated numerically or with Monte Carlo techniques. The numerical calculations are in general very difficult, so for the general applications Monte Carlo procedures were used. This procedure consists in generating a large number of random events and weighting each one by its probability as predicted by the probability density function using the solution values for the parameters. Histograms of measurables from the weighted Monte Carlo events can then be compared with those of the data upon which the fit was performed. Discrepancies between the weighted Monte Carlo histograms and the

corresponding histograms of the data would indicate failures of the model.

There is one very special application where the solution predictions can be calculated numerically. This is for two particle mass projections in three particle final states. Here the Dalitz plot density can be inferred directly from the probability density function. The mass projections can then be calculated by integrating this density between the kinematic limits of the Dalitz plot in the perpendicular direction to the projection axis.

Failures of the model, as described by equation 2, could come about by not including all of the resonance effects in the final state, by inserting the wrong resonance parameters (i.e. incorrect mass and/or width), by using the incorrect resonance line shape, by using an incorrect parameterization of the decay angular distribution or from the presence of non-negligible interference effects. These possible failures of this model must be investigated by comparing the data to the predictions of the maximum likelihood solution, before the solution can be regarded as a measurement of the parameters.

This model (as described by equation 2) was used in conjunction with the computer code MURTLEBERT[32] to perform the maximum likelihood analysis described in this report. MURTLEBERT constructs the likelihood function from the frequency function, performs the search for maximum, calculates the error matrix, and compares the predictions of the solution to the data for various projections of the event measurables.

VII . The Reaction $K^- p \rightarrow p\bar{K}^0\pi^-$

This reaction has been studied by several experiments both below and above the energy range of this experiment.[36-41] The total cross section for this reaction at each beam momentum setting of this experiment is given in table 6 and shown in figure 10. Figure 22 shows the total cross section for this reaction as a function of K^- beam momentum as measured by several experiments (including this one) in the momentum range .6 to 5.5 GeV/c. The total cross section for this reaction is seen to increase very rapidly from threshold reaching a maximum around 2 GeV/c and then decreasing to approximately one fifth of its maximum value of 5.5 GeV/c.

In figure 22 the data points for 2.58 and 2.61 GeV/c are combined into a single data point at 2.60 GeV/c. In the rest of this report data from these two exposures are combined to form a single sample, referred to as "2.60 GeV/c".

Figures 11 through 20 graphically summarize this final state. Figure 11 histograms the three two particle invariant masses for each beam momentum sample. Figures 12 through 15 show these invariant mass distributions for various cuts on the production cosines of the corresponding particle pairs. Figure 16 displays the Dalitz plots for this reaction at each beam momentum. Figure 17 shows Chew-Low plots for each particle pair at each momentum.

As these figures show, the reaction is dominated by the production of the $K^*_{\frac{1}{2}}(892)$. Production of this resonance accounts for approximately sixty percent of the final state at each momentum. The abundance

of $K^*_{\frac{1}{2}}$ (892) and its very high signal to noise ratio make this reaction an excellent one for studying the production and decay properties of this resonance. This is the subject of the next section of this report. The rest of this section will discuss the final state as a whole, including a study of the other resonant states produced.

Figure 18 shows the two particle invariant mass distributions at each momentum, for which events in a mass band about the mass of the $K^{*-}_{\frac{1}{2}}$ (892) have been removed. Events were included in the plot only if their $\overline{K}^o\pi^-$ invariant mass squared was less than .64 GeV squared or greater than 1.0 GeV squared. Figure 19 displays the two particle invariant mass distributions, with $K^{*-}_{\frac{1}{2}}$ (892) events similarly removed, for various production cosine cuts of the particle pairs. Figure 20 shows the Chew-Low plots for this reaction with the $K^*_{\frac{1}{2}}$ (892) events removed.

These figures show evidence for the production of Y^*_1 (1660), Y^*_1 (1765), $N^*_{3/2}$ (1238), N^* (1520), N^* (1680) as well as $K^*_{\frac{1}{2}}$ (892).

There is also a broad enhancement in the $\overline{K}^o\,\pi^-$ mass spectrum in the region of 1250 to 1450 MeV. A study of the four particle final state reaction $K^-p \rightarrow p\,\overline{K}^o\,\pi^-\pi^o$ (discussed in a later section) shows clearly resolved enhancements in the $K\pi\pi$ mass spectra at 1280 and 1410 MeV each with a width of approximately 50 MeV. This suggests that the broad enhancement in the $\overline{K}^o\pi^-$ mass spectrum in the three particle final state could be the two particle decay modes of these enhancements, if they are resonances. The enhancement at 1410 MeV has been seen in many experiments in both the $K\pi$ and $K\pi\pi$ mass spectra[42] and has been

identified as an isospin one-half resonance with spin parity two plus. Both of these enhancements are studied in detail in a later section.

Direct channel partial wave analysis of π p scattering has shown that the 1520 MeV and 1680 MeV enhancements are complex structures where several partial wave amplitudes go through resonances.[43] Thus it is not known which or how many of them are appearing in the 1520 and 1680 MeV enhancements in the πp mass distributions in this final state. The narrow width of the 1680 MeV enhancement suggests that it is mainly composed of the isospin one-half spin-parity $5/2^+$, $N^*_{\frac{1}{2}}$ (1688). The The 1520 MeV πp enhancement in this final state is not large enough to give any indication of its composition.

In order to estimate the relative fractions of the various resonances produced in this final state the maximum likelihood analysis described in the previous section was applied to the data. A model employing non-interfering resonance rates and Lorentz invariant phase space was fitted to the data at each momentum. Resonant terms representing the Y^*_1 (1660), Y^*_1 (1765), $N^*_{3/2}$ (1238), N^* (1520), N^* (1688), $K^*_{\frac{1}{2}}$ (892), and K^* (1280) were included for all momenta. A term representing the $K^*_{\frac{1}{2}}$ (1400) was also included in all momenta above 2.1 GeV/c. Decay angular correlations were included for the $K^*_{\frac{1}{2}}$ (892) only, since the other resonances have such small rates compared to it.

The decay angular distribution for the $K^{*-}_{\frac{1}{2}}$ (892) was parameterized as $I(\hat{k}) = Y_0^0 + C_1 Y_2^0(\hat{k}) + C_2 \mathrm{Re} Y^2_2(\hat{k}) + C_3 \mathrm{Re} Y^1_2(\hat{k})$, where I is the intensity along the direction $\hat{k}$ which is a unit vector in the direction of the $\overline{K}^0$ in the $\overline{K}^0\pi^-$ rest frame. The coordinate

system in the $\overline{K}^{o}\pi^{-}$ rest frame was chosen to have the z-axis parallel to the final state proton, the y-axis along the production normal, and the x-axis chosen so as to have a right handed coordinate system.

The masses and widths of the resonant terms were set to their world average values[29] except for the N^{*} (1688) and $K^{*-}_{\frac{1}{2}}$ (892). The mass and width of these two resonances were made parameters of the maximum likelihood fits at each momentum except 2.1 GeV/c where the mass and width of the N^{*} (1688) was set to the average of the solution values for the other momenta.

Tables 7 and 8 present the maximum likelihood solutions at each momenta. Table 7 gives the solution values for the fractions of each resonant term and the $K^{*}_{\frac{1}{2}}$ (892) decay correlation parameters at each momentum. Table 8 gives the solution values for the varied masses and widths at each momentum. These values should not be taken as attempts to measure these quantities, since no attempt was made to include the detailed systematic effects which could alter these values.

Figure 21 compares the maximum likelihood solutions to invariant mass projections and $\overline{K}^{o}\pi^{-}$ azimuth angle for each momentum. This is the azimuth angle of the plane defined by the $\overline{K}^{o}\pi^{-}$ about the direction of the $\overline{K}^{o}\pi^{-}$ system. This angle is independent of the Dalitz plot density and can be written as

$$I(\varphi) = 1 + f(K^{*})\, C_2\, \frac{\sqrt{30}}{6} \cos 2\varphi,$$

where $f(K^{*})$ is the fraction of K^{*} (892) in the final state and C_2 is the coefficient of ReY^{2}_{2} in the parameterization of the $K^{*}_{\frac{1}{2}}$ (892) decay angular distribution.

As figure 21 shows, the projected distributions as predicted by the maximum likelihood solutions represent the data satisfactorily at all momenta. Thus it appears that the model of non-interfering resonances and Lorentz invariant phase space characterize well these final state interactions. Any interference effects or non-resonant final state interactions cannot be detected from these distributions.

The solutions show that the fraction of $K^*_{\frac{1}{2}}$ (892) in the final state is decreasing with increasing beam momentum, while the fraction of Y^*_1 (1765), $K^*_{\frac{1}{2}}$ (1400), and K^* (1280) are increasing. The fractions of the other resonant states are staying roughly constant. Since the total cross section for this reaction is decreasing rapidly in this beam momentum range, the total cross sections for the production of Y^*_1 (1660), $N^*_{3/2}$ (1238), N^* (1520), N^* (1688), and $K^*_{\frac{1}{2}}$ (892) are also decreasing rapidly. The total cross sections for Y^*_1 (1765), K^* (1280), and $K^*_{\frac{1}{2}}$ (1400) production are staying approximately constant or slightly increasing in this beam momentum range.

The maximum likelihood solution values for the width of the N^*(1688) reflect the fact that the enhancement seen here seems somewhat narrower than the corresponding πp direct channel effects. However the phenomenon seen here is difficult to relate to the πp direct channel resonances, and using a Breit-Wigner line shape characterized by a single mass and width is at best a phenomenological approximation.

VIII. The Reaction $K^- p \rightarrow K^{*-}_{\frac{1}{2}}(892)\, p$

As observed in the last section, $K^{*}_{\frac{1}{2}}(892)$ production accounts for approximately sixty percent of the $p\bar{K}^0\pi^-$ final state at all momenta. This large sample of resonance events coupled with the very small background provides an excellent opportunity to study the production and decay properties of this resonant state.

For this study the upper three beam momentum exposures, 2.45, 2.60, and 2.70 GeV/c are combined to form a single sample with large statistics, so that these production and decay properties could be studied for many finely divided production cosine intervals.

Figure 23 shows the total cross section for this reaction as measured by several experiments. The data points representing this experiment were obtained by multiplying the total cross section for the reaction $K^- p \rightarrow \bar{K}^0\pi^-$ at each momentum by the fraction of $K^{*-}_{\frac{1}{2}}(892)$ produced at that momentum, as determined by the maximum likelihood solutions. The total cross section for the reaction $K^- p \rightarrow K^{*-}_{\frac{1}{2}}(892)\, p$ is seen from figure 23 to rise very rapidly from threshold to a maximum value of about 1.3 millibarns at around 1.8 GeV/c incident K^- momentum, and then fall slowly to approximately .2 millibarns at 5.5 GeV/c.

Figure 24 shows the center of mass production angular distribution of the $K^{*-}_{\frac{1}{2}}(892)$ for 2.1 GeV/c and the upper momentum sample. In both samples this distribution is highly peripheral becoming more so at the higher momenta. Events plotted had $\bar{K}^0\pi^-$ invariant mass squared in an interval .706 to .884 GeV^2. This selection introduces approximately

five percent non-K^{*-} events into the sample.

In analyzing the K^* production and decay properties, it has been customary to use events within a given $(\overline{K}^o\pi^-)$ mass interval around the $K^{*-}_{\frac{1}{2}}(892)$ mass. The mass interval is chosen as a compromise between minimizing contamination from non-K^* events and minimizing statistical errors. One is forced to include some "background" events. The assumption of noninterference of background amplitudes with the K^* production and decay amplitudes is essential for this analysis, but even the "noninterfering background" will cause errors in the determination of the K^* production and decay parameters.

The arbitrariness of limits on the mass cut has been avoided, and the effect of noninterfering background has been accounted for, by using the maximum-likelihood method described in section VI.

As in the last section, the decay angular distribution of the $K^{*-}_{\frac{1}{2}}(892)$ was parameterized as

$$I(\hat{k}) = Y^o_o + C_1 Y^o_2(\hat{k}) + C_2 \mathrm{Re}\, Y^2_2(\hat{k}) + C_3 \mathrm{Re}\, Y^1_2(\hat{k}),$$

however, the coordinate system, in the rest frame of the $\overline{K}^o\pi^-$, for this analysis is chosen differently. The z-axis is chosen along the direction of the incident K^-, the y-direction along the production normal, and the x-axis so as to make a right-handed coordinate system. This coordinate system (referred to as the "t-channel" coordinate system) reduces the decay angular distribution of the $K^{*-}_{\frac{1}{2}}(892)$ to particularly simple forms for definite spin parities in the crossed channels. For example, spin-parity 0^- in the t-channel predicts

$$I(\alpha, \varphi) \sim \cos^2\alpha ,$$

where α and φ are the polar and azimuthal angles of $\hat{k}$ in the t-channel

coordinate system. The corresponding distribution for spin parity 1^- in the t-channel would be

$$I(\alpha,\varphi) \sim \sin^2\alpha\,(1 + b\cos 2\varphi)$$

where b is a parameter determined by the dynamics of the baryon vertex.

The above expression for the $K^{*-}_{\frac{1}{2}}$ (892) decay angular distribution neglects the "illegal" decay correlations of the K^*, i.e., those prohibited by angular momentum and parity conservation. This assumes that the K^* decays as a free particle and that there is no interference between the K^* production and decay and other processes.

To determine the production angular distribution and decay correlation coefficients as a function of production angle, the data was divided at the two momentum samples into intervals in the production angle of the $\overline{K}^o\pi^-$ system. The intervals were chosen to include approximately 100 K^* events in each. Maximum-likelihood solutions were obtained for each of these intervals.

Figures 29 through 32 and tables 9 through 11 give the results of these solutions for both momentum samples. Table 9 gives the number of events in each of the production cosine intervals for 2.1 GeV/c, the fraction of $K^{*-}_{\frac{1}{2}}$ (892) in each interval, the differential cross section, and decay correlation parameters averaged over the interval. Table 10 gives the same for the higher momentum sample. Table 11 gives the decay correlation parameters averaged over all production angles for the two momentum samples. Figures 29 and 30 plot the differential cross section for the two momentum samples as a function of center of mass production cosine. Figures 31 and 32 plot the decay correlation

coefficients for the two momentum samples as a function of center of mass production cosine.

Since the maximum-likelihood solutions are based on a model not necessarily representative of the data, the solutions are compared to the data in figures 25 through 28. Events selected for these plots were required to have an effective $\overline{K}^{o}\pi^{-}$ mass squared in the range .706 to .884 GeV^2, in addition to the $\overline{K}^{o}\pi^{-}$ production angular interval indicated. This mass cut has introduced an estimated fraction of background events amounting to 5 $^{o}/_{o}$ at the most forward cos θ intervals and 25 $^{o}/_{o}$ at the most backward. The distributions shown refer only to the decay of the K^{*}, but these distributions should be quite sensitive to the effects of interference between the K^{*} production and decay amplitude and other amplitudes. Specifically, any asymmetries with respect to reflection about $\varphi = 0$ and 180^{o} or, after averaging over φ, about $\cos\alpha = 0$ are not accounted for in the model.

Figure 25 contains plots of the decay polar cosine, $\cos\alpha$, and azimuth angle, φ, for all production angles at the two momentum samples. The solid curves are the predictions of the likelihood solutions which take the form

$$I(\cos\alpha) = N\left[1 + C_1 \frac{\sqrt{5}}{2}(3\cos^2\alpha - 1)\right]$$

$$I(\varphi) = N\left[1 + C_2 \frac{\sqrt{30}}{6}\cos 2\varphi\right]$$

where N normalizes to the total number of events in the plot. Figure 26 similarly compares the predictions of the likelihood solutions to the data for each of the production angle intervals at 2.1 GeV/c and figures 27 and 28 the same for the higher momentum sample.

The overall agreement between the solutions and the data is fairly good for both momentum samples. The consistency between the data and the likelihood solutions based on this simple model suggest that the K^* produced in the reaction studied here is essentially free from interference, and can be used to test theoretical models of production and decay which assume production of a free K^*.

Qualitative features of the decay distributions of figures 27 and 28 for the upper momentum sample show the following:

(a) In the extreme forward direction there is a strong $\cos^2\alpha$ distribution and a somewhat flat azimuth distribution. This is characteristic of pseudoscalar exchange in the production process.

(b) In the intermediate and backward directions there are strong $\sin^2\alpha$ polar distributions and 1-b $\cos 2\varphi$ azimuth distributions, characteristic of vector exchange.

(c) Between these two regions, there is a relatively flat polar distribution and a moderate 1-b $\cos 2\varphi$ azimuth distribution, which may result from a combination of pseudoscalar and vector exchange. Although somewhat more limited in statistics, the data at 2.1 GeV/c exhibit the same general features.

These qualitative features of the data have been predicted by Jackson et al.[1] using a meson-exchange model with corrections for competing channels. Donohue[45] discusses, in detail, the results of a previous report of this experiment[46] within the framework of this model. Kiadalov and Karnakov[47] discuss the results of the previous report within the framework of a Regge Pole model.

IX. The Reaction $K^- p \rightarrow p\bar{K}^o \pi^o \pi^-$

The total cross section for this reaction at each beam momentum setting of this experiment is given in table 6 and shown in figure 10. As can be seen, this reaction proceeds with approximately one-half the rate of the corresponding three particle final state reaction in the energy range of this experiment.

Figure 33 shows the total cross section for this reaction in the energy range, 1.2 to 3.5 GeV/c as measured by several experiments. The cross section is seen to be relatively constant at about 40 microbarns in the region below 1.5 GeV/c. The cross section begins to rise very rapidly in the region of the $\bar{K}^*(892)$ $N^*(1238)$ threshold, and continues to rise rapidly in the energy range of this experiment, leveling off somewhat at the higher beam momentum settings. At energies above this experiment the cross section appears to be constant or slightly decreasing. Thus from the energy spectrum of the total cross section alone it is clear that associated production of $\bar{K}^*$ (892) N^* (1238) will be very important in this reaction in the energy range of this experiment.

This becomes even clearer in Figures 34 through 37 where the invariant mass squared of the ten two and three particle combinations are shown for each momentum. Copious production of N^* (1238), K^{*-} (892), and $\bar{K}^{*o}$ (892) is observed at all momenta.

Two small but significant enhancements are also observed at high mass values in the $\bar{K}^o \pi^o \pi^-$ mass squared spectra, corresponding to mass values of 1280 and 1400 MeV each about 50 MeV wide. The latter is

associated with a three particle decay mode of the $K^*_{\frac{1}{2}}$ (1400). The enhancement at 1280 MeV does not correspond to any well known resonance, and for the purpose of this section is treated in a phenomenological manner. The $K\pi\pi$ mass spectra

are studied in detail in a later section of this report.

Maximum likelihood fits to this final state were made at each momentum setting using a model of non-interfering resonance production and Lorentz invariant phase space. Resonance processes employed were:

(1) associated production of $K^{*-}_{\frac{1}{2}}$ (892) $N^{*+}_{3/2}$ (1238), (2) associated production of $\bar{K}^{*o}_{\frac{1}{2}}$ (892) $N^{*o}_{3/2}$ (1238), (3) unassociated production of N^{*+} (1238), (4) unassociated production of N^{*o} (1238), (5) unassociated production of $\bar{K}^{*o}$(892), (6) unassociated production of K^{*-} (892), and (7) production of the two $K\pi\pi$ enhancements at 1280 and 1400 MeV. At 2.1 GeV/c. the 1400 MeV $K\pi\pi$ enhancement was not included since this momentum is below threshold for its production.

The masses and widths of these resonances were allowed to vary as parameters of the fits for each momentum to allow for possible systematic effects which might cause mass shifts, since this reaction is only singly constrained in the kinematic fitting. All masses and widths of the well known resonances were consistent with the world averaged values.[29] The masses and widths of the $K\pi\pi$ enhancements were obtained by performing the maximum likelihood fit to the 2.60 and 2.70 GeV/c samples combined, varying these masses and widths as parameters of the fit. The values so obtained are given in table 13

and were used in the likelihood fits for each separate momentum.

Table 12 gives the results of the maximum likelihood solutions at each beam momentum, and the solid curves superimposed on the histograms of Figures 34 through 37 show the predictions of these solutions for the invariant mass squared projections.

The predictions of the maximum likelihood solutions for these mass squared projections represent the data well at all momenta. Thus from these comparisons it seems that the final state is well represented by this simple model.

The $\bar{K}^{*}_{\frac{1}{2}}$ (892) $N^{*}_{3/2}$ (1238) final state provides additional consistency checks on the model, since it is in a pure isospin one state. This requires that the rate for $K^{-}p \rightarrow \bar{K}^{*o}_{\frac{1}{2}}$ (892) $N^{*o}_{3/2}$ (1238) be one fourth that for $K^{-}p \rightarrow K^{*-}_{1/2}$ (892) $N^{*+}_{3/2}$ (1238), provided there are no interference effects. Inspection of table 12 shows that the solutions at all momenta are each consistent with this requirement, however, the rates for $\bar{K}^{*o}$ N^{*o} are systematically one to two standard deviations below one fourth the rate for K^{*-} N^{*+} production at all momenta. Including K^{*} N^{*} decay correlations does not change these results.[49] This effect could be the result of interference between the two amplitudes. If so, this would imply that interference effects are of the order of five to ten percent between these two amplitudes, which are comparable to the statistical uncertainties.

The results of the maximum likelihood solutions for the fraction of unassociated production of N^{*o} (1238) were consistent with zero at all momenta and are not included in table 12.

The results of the likelihood solutions show that the fraction of $\overline{K}^{*}_{\frac{1}{2}}$ (892) $N^{*}_{3/2}$ (1238) in the final state is decreasing rapidly with increasing beam energy. The fractions of single resonance production are all staying constant or increasing. Since the total cross section for this final state is increasing rapidly in this energy region, the total cross section for associated resonance production K^{*} (892) N^{*} (1238) is roughly constant while that for single resonance production is increasing rapidly.

X . The Reaction $K^-p \rightarrow n\bar{K}^o\pi^+\pi^-$

This reaction proceeds at a slightly lower rate than the proton four particle final state at all momenta in this experiment, as is seen in table 6 and figure 10. Figure 38 shows the total cross section for this reaction as measured by several experiments, both below and above the beam energy range of this experiment. In the energy range below the $\bar{K}^*_{\frac{1}{2}}$ (892) $N^*_{3/2}$ (1238) threshold, the cross section for this reaction is roughly double that for the $p\bar{K}^o\pi^o\pi^-$ final state. In the region of the $\bar{K}^*_{\frac{1}{2}}$ (892) $N^*_{3/2}$ (1238) threshold, the cross section for this reaction also rises rapidly, but not nearly as rapidly as the $p\bar{K}^o\pi^o\pi^-$ final state. Past the $\bar{K}^*_{1/2}$ (892) $N^*_{3/2}$(1238) threshold region, the $p\bar{K}^o\pi^o\pi^-$ final state emerges with the larger total cross section and remains so throughout the energy range of this experiment. Thus it appears from these total cross section measurements that the associated resonance production of $\bar{K}^*_{\frac{1}{2}}$(892) $N^*_{3/2}$ (1238) does not dominate the n $\bar{K}^o\pi^+\pi^-$ final state to the extent it does the $p\bar{K}^o\pi^o\pi^-$ one.

As mentioned in the previous section $\bar{K}^*_{1/2}$ (892) $N^*_{3/2}$ (1238) is in a pure isospin one state. This requires that it contribute $2\frac{1}{2}$ times as much to the $p\bar{K}^o\pi^o\pi^-$ final state as it does to the $n\bar{K}^o\pi^+\pi^-$ one. This is verified by the energy behavior of the these two cross sections in the $K^*_{\frac{1}{2}}$ (892) $N^*_{3/2}$ (1238) threshold region.

Figures 39 through 42 show the invariant mass squared spectra of the ten two and three particle combinations for this final state at each beam momentum. Copious production of Y^{*o}_{o} (1520), $N^{*+}_{3/2}$ (1238),

$N^{*-}_{3/2}$ (1238), and $K^{*-}_{\frac{1}{2}}$ (892) is observed at all beam momenta. There is no evidence from these mass spectra of any other pronounced resonance production in this final state. In particular, the $K\pi\pi$ enhancements observed in the $p\bar{K}^{o}\pi^{o}\pi^{-}$ final state, appear to be much less pronounced in this one.

Maximum likelihood fits were performed on this final state in a similar manner as the other four particle final state. The model employed included associated production of $K^{*-}_{\frac{1}{2}}$ (892) $N^{*+}_{3/2}$ (1238) and unassociated resonance production of Y^{*o}_{o} (1520), $N^{*+}_{3/2}$ (1238), $N^{*-}_{3/2}$ (1238), and $K^{*-}_{\frac{1}{2}}$ (892). As in the previous section, the masses and widths of these resonances were made parameters of the fits to account for possible systematic effects, but the solution values for all of them were consistent with the world averaged values.[29]

Table 14 gives the results of the maximum likelihood solutions for the amounts of the resonance processes at each momentum, and the solid curves superimposed on figures 39 through 42 show the predictions of these solutions for the corresponding mass squared projections. These solid curves follow the data histograms very closely, and this simple model, representing the above four resonances, seems to give a good account of the mass projections.

As discussed above, the reaction $K^{-}p \rightarrow \bar{K}^{*}_{\frac{1}{2}}$ (892) $N^{*}_{3/2}$ (1238) must contribute $2\frac{1}{2}$ times as much to the $p\bar{K}^{o}\pi^{o}\pi^{-}$ final state than to the $n\,\bar{K}^{o}\,\pi^{+}\pi^{-}$ one. This allows the prediction of the number of $\bar{K}^{*}_{\frac{1}{2}}$ (892) $N^{*}_{3/2}$ (1238) events in the $n\bar{K}^{o}\pi^{+}\pi^{-}$ final state, knowing the number in the $p\bar{K}^{o}\pi^{o}\pi^{-}$ final state. Put another way, it gives a

consistency check between the maximum likelihood solutions on the final states.

Table 15 allows a comparison between the likelihood solutions of the two four particle final states for the fraction of $\overline{K}^{*}_{\frac{1}{2}}$ (892) $N^{*}_{3/2}$ (1238). Inspection of table 15 shows that the solutions at each momentum are consistent with the isospin constraint, but the number of $\overline{K}^{*}_{\frac{1}{2}}$ (892) $N^{*}_{3/2}$ (1238) events in the n $\overline{K}^{o}\pi^{+}\pi^{-}$ final state is about a standard deviation or so less than would be predicted from the likelihood solutions on the $p\overline{K}^{o}\ \pi^{o}\pi^{-}$ final state at each momentum. This same type of effect is observed in the $p\overline{K}^{o}\ \pi^{o}\pi^{-}$ final state between the two decay modes of the $\overline{K}^{*}_{\frac{1}{2}}$ (892) $N^{*}_{3/2}$ (1238) there. Here, the effect is approximately the same size, and is comparable with the statistical uncertainties.

To the extent that these discrepancies are significant, they represent an inadequacy of the model, and this model of non-interfering resonance production and Lorentz invariant phase space should be regarded as an approximation, and representing the invariant mass spectra should not be the only test of its success.

The results of the maximum likelihood solutions indicate that the fractions of Y_{o}^{*o} (1520), $N^{*+}_{3/2}$ (1238), and $N^{*-}_{3/2}$ (1238) are decreasing in the energy range of this experiment while the fraction of $K^{*-}_{1/2}$ (892) seems to be increasing. However, none of these trends is very marked, and since the total cross section for the final state is increasing rapidly in this energy range, so are the cross sections for these single resonance productions.

XI . The Reaction $K^- p \rightarrow \bar{K}^*_{\frac{1}{2}}(892)\, N^*_{3/2}(1238)$

As observed in the preceding two sections, the pseudo-two particle reaction $K^- p \rightarrow \bar{K}^* N^*$ dominates the two four particle final states of this experiment, accounting for approximately 40 $^o/_o$ of the $p\bar{K}^o\pi^o\pi^-$ final state and 20 $^o/_o$ of the $n\bar{K}^o\pi^+\pi^-$ one. These final states afford an opportunity to study the production and decay properties of this reaction as a function of center of mass energy and production angle. Associated resonance production has been the subject of considerable theoretical interest, since these reactions give rise to many experimentally measurable quantities and thus provide excellent tests for dynamical models of the production process.[51-53] The reaction $K^- p \rightarrow K^* N^*$ has been studied at lower energies[38,50] and the corresponding reaction $K^+ p \rightarrow K^* N^*$ has also been studied in several experiments, at energies both below and above this experiment.[54-57]

The total cross section for $K^- p \rightarrow K^* N^*$ as measured by this experiment at each beam momentum is given in table 16. The cross section at each momentum was determined by evaluating the cross sections for each of the decay modes observed in this experiment, and performing a least squares fit to these cross sections applying the constraints of isospin convervation. The results were then corrected for other charged states and decay modes not observed in this experiment. Figure 43 shows the total cross section for $K^- p \rightarrow \bar{K}^* N^*$ as measured by several experiments. The errors are large, but a clear trend is seen. The total cross section rises from threshold rapidly, and continues to rise to a maximum of approximately 1.7 millibarns in the region of

2.45 GeV/c. The cross section then begins to fall, going to about 1.3 millibarns at 2.70 GeV/c. Figure 44 shows the production angular distribution at each beam momentum. Events for these plots were selected by making cuts on the invariant masses of the $p\pi^o$ and $K^o\pi^-$ and the background from non-$K^{*-}N^{*+}$ events is estimated to be about 20 $^o/_o$ at 2.1 GeV/c increasing with higher beam momentum to around 35 $^o/_o$ at 2.70 GeV/c. These production angular distributions are seen to become progressively more peripheral as the center of mass energy is increased. At energies lower than this experiment,[38,50] the production angular distribution is seen not to be very peripheral at all. Thus it appears that this reaction follows the usual trend for two particle reactions, having flat (s-wave) production angular distributions near threshold and becoming more and more forward peaked with increasing energy. At 2.1 GeV/c this reaction is already moderately peripheral, and by 2.70 GeV/c almost all K^*N^* events have production cosine greater than .8.

The joint decay angular distribution for K^*N^* may be written[58]

$$I(\hat{e}\,\hat{p}) = 1 + \sum_{i=1}^{19} C_i Z_i(\hat{e}\,\hat{p})$$

where $\hat{e}$ is a unit vector in the direction of the $\bar{K}^o$ and $\hat{p}$ a unit vector in the direction of the proton. The coordinate systems for the decay of the K^* and N^* are defined differently. $\hat{e}$ is expressed in the "t-channel" coordinate system in the rest frame of the K^* with the beam K^- direction as the quantization axis. $\hat{p}$ is also expressed in the "t-channel" coordinate system but in the rest frame of the N^* with the target proton direction as the quantization axis. The 19 correlation

functions, $Z_i(\hat{e}\,\hat{p})$ may be chosen in a number of ways, and table 17 gives the set chosen for this experiment. Each of these functions has the following properties:

$$\int Z_i(\hat{e}\,\hat{p})\, d\hat{e}\, d\hat{p} = 0 \quad ; \quad \int |Z_i(\hat{e}\,\hat{p})|^2 d\hat{e}\, d\hat{p} = 16\pi^2$$

The coefficients of these correlation functions, C_i, are independent of the decay variables, and are determined by the dynamics of the production process. Thus the C_i^S are in general functions of center of mass energy and scattering angle. Along with the differential cross section, these coefficients provide 20 measurables as a function of energy and momentum transfer which any dynamical model must describe. Thus, this reaction can provide a very rigorous test for any theory of its production.

With the limited statistics of this experiment it is not possible to measure all 19 coefficients as a function of energy and production angle. Some of the coefficients may be measured independently of the others by integrating $I(\hat{e}\,\hat{p})$ over one or several of the decay angles. For example:

$$I(\hat{e}) = \int I(\hat{e}\,\hat{p})\, d\hat{p} = 1 + \sum_{i=1}^{3} C_i Z_i(\hat{e})$$

$$I(\hat{p}) = \int I(\hat{e}\,\hat{p})\, d\hat{e} = 1 + \sum_{i=4}^{6} C_i Z_i(\hat{p})$$

$$I(e_3) = \int I(\hat{e}\,\hat{p})\, d\hat{p}\, d\varphi_e = 1 + C_1 Z_1(e_3)$$

$$I(p_3) = \int I(\hat{e}\,\hat{p})\, d\hat{e}\, d\varphi_p = 1 + C_4 Z_4(p_3)$$

$$I(e_3 p_3) = \int I(\hat{e}\,\hat{p})\, d\phi_e\, d\phi_p = 1 + c_1 Z_1(e_3) + c_4 Z_4(p_3) + c_7 Z_7(e_3 p_3)$$

$$I(\phi_e) = \int I(\hat{e}\,\hat{p})\, d\hat{p}\, de_3 = 1 + c_2 \frac{\sqrt{30}}{6} \cos 2\phi_e$$

$$I(\phi_p) = \int I(\hat{e}\,\hat{p})\, d\hat{e}\, dp_3 = 1 + c_4 \frac{\sqrt{30}}{6} \cos 2\phi_p$$

$$I(\phi_e \phi_p) = \int I(\hat{e}\,\hat{p})\, de_3\, dp_3 = 1 + c_2 \frac{\sqrt{30}}{6} \cos 2\phi_e + c_5 \frac{\sqrt{30}}{6} \cos 2\phi_p + c_{11} \frac{5}{6} \cos 2\phi_e \cos 2\phi_p + c_{19} \frac{5}{6} \sin 2\phi_e \sin 2\phi_p$$

where $\hat{e} = (e_1 e_2 e_3)$, $\hat{p} = (p_1 p_2 p_3)$, $\phi_e = \tan^{-1}\left(\frac{e_2}{e_1}\right)$ and $\phi_p = \tan^{-1}\left(\frac{p_2}{p_1}\right)$.

Thus C_1, C_2, and C_3 correspond to the uncorrelated K^* decay parameters, C_4, C_5, and C_6 to the uncorrelated N^* decay parameters, and C_7 gives rise only to a correlation between the polar decay angles of the two resonances. After integrating over all polar angles, C_2 and C_5 give rise to the uncorrelated azimuthal decay angular distributions of the K^* and N^*, while C_{11} and C_{19} serve to correlate these two azimuthal angles. Thus of the 19 joint decay angular distribution coefficients, the 9 coefficients C_1, C_2, C_3, C_4, C_5, C_6, C_7, C_{11}, and C_{19} are in relatively simple integrated distributions, each involving only a few coefficients. Thus it is possible within the limited statistics of this experiment to measure these 9 coefficients as a function of energy and production angle.

In order to account for the background in a systematic manner and avoid having to impose mass cuts, the maximum likelihood technique of section IX was applied to the $p\bar{K}^o\pi^o\pi^-$ final state, however, here the $K^{*-}N^{*+}$ resonance process was given a joint decay angular distribution. The $\bar{K}^{*o}N^{*o}$ process in the same final state and the $K^{*-}N^{*+}$ resonance process in the $n\bar{K}^o\pi^+\pi^-$ final state are produced in insufficient quantity to allow an analysis of their decay correlations.

The decay angular distributions employed were $I(\hat{e})$, $I(\hat{p})$, $I(e_3\ p_3)$ and $I(\varphi_e\ \varphi_p)$ as defined above. Maximum likelihood solutions were obtained at each momentum for each of these joint decay angular distributions. The results of these solutions are given in table 18 and displayed in figure 45. For those coefficients which appear in more than one distribution, the solution which gave the smallest

statistical error was used. However in all of these cases the solution values and errors for the same coefficients in different decay angular distributions were very nearly equal.

The solution values for most of the decay correlation coefficients show no marked energy dependence, the exceptions being C_2 and C_{19} which appear to be decreasing with increasing energy.

In order to see if these solution values and, indeed, the model itself represent the data, the predictions of the solutions for various projections of $I(\hat{e}\,\hat{p})$ are compared to the data in figures 46 through 49. The projections chosen are related to the decay correlation coefficients as follows:

$$I(e_3) = 1 + C_1 \frac{\sqrt{5}}{2}(3e_3^2 - 1) \qquad I(p_3) = 1 + C_4 \frac{\sqrt{5}}{2}(3p_3^2 - 1)$$

$$I(\phi_e) = 1 + C_2 \frac{\sqrt{30}}{6}\cos 2\phi_e \qquad I(\phi_p) = 1 + \frac{\sqrt{30}}{6} C_5 \cos 2\phi_p$$

$$I[(e_1 + e_3)/\sqrt{2}] = 1 + \frac{3}{4}\sqrt{5}\,C_1 - \frac{\sqrt{30}}{8} C_2 + \frac{\sqrt{15}}{12} C_3 + \frac{1}{2}\left(\frac{3}{2}\sqrt{5}\,C_1 + \frac{3}{4}\sqrt{30}\,C_2 - \frac{\sqrt{15}}{2} C_3\right)\left(\frac{e_1 + e_3}{\sqrt{2}}\right)^2$$

$$I[(e_1 - e_3)/\sqrt{2}] = 1 + \frac{3}{4}\sqrt{5}\,C_1 - \frac{\sqrt{30}}{8} C_2 - \frac{\sqrt{15}}{12} C_3 + \frac{1}{2}\left(\frac{3}{2}\sqrt{5}\,C_1 + \frac{3}{4}\sqrt{30}\,C_2 + \frac{\sqrt{15}}{2} C_3\right)\left(\frac{e_1 - e_3}{\sqrt{2}}\right)^2$$

$$I[(\rho_1+\rho_3)/\sqrt{2}] = 1+\frac{3}{4}\sqrt{5}\,c_4 - \frac{\sqrt{30}}{8}c_5 + \frac{\sqrt{15}}{12}c_6 + \frac{1}{2}\left(\frac{3}{2}\sqrt{5}\,c_4 + \frac{3}{4}\sqrt{30}\,c_5 - \frac{\sqrt{15}}{2}c_6\right)\left(\frac{\rho_1+\rho_3}{\sqrt{2}}\right)^2$$

$$I[(\rho_1-\rho_3)/\sqrt{2}] = 1+\frac{3}{4}\sqrt{5}\,c_4 - \frac{\sqrt{30}}{8}c_5 - \frac{\sqrt{15}}{12}c_6 + \frac{1}{2}\left(\frac{3}{2}\sqrt{5}\,c_4 + \frac{3}{4}\sqrt{30}\,c_5 + \frac{\sqrt{15}}{2}c_6\right)\left(\frac{\rho_1-\rho_3}{\sqrt{2}}\right)^2$$

$$I(\phi_e+\phi_p) = (\phi_e+\phi_p)\left[1+\frac{5}{12}(c_{19}-c_{11}) + \frac{5}{6}(c_{11}-c_{19})\cos^2(\phi_e+\phi_p) + \frac{5}{24}(c_{11}+c_{19})\frac{\sin 2(\phi_e+\phi_p)}{\phi_e+\phi_p}\right]$$

$$I(\phi_e-\phi_p) = [\pi/2-(\phi_e-\phi_p)]\left[1-\frac{5}{12}(c_{11}+c_{19}) + \frac{5}{24}(c_{11}-c_{19})\frac{\sin 2(\phi_e-\phi_p)}{\pi/2-(\phi_e-\phi_p)} + \frac{5}{6}(c_{11}+c_{19})\cos^2(\phi_e-\phi_p)\right]$$

$$I(e_3;\,|\rho_3|>.5) = 1+\frac{3}{8}\sqrt{5}\,c_4 + (c_1+\frac{3}{8}\sqrt{5}\,c_7)\frac{\sqrt{5}}{2}(3e_3^2-1)$$

$$I(e_3;\,|\rho_3|<.5) = 1-\frac{3}{8}\sqrt{5}\,c_4 + (c_1-\frac{3}{8}\sqrt{5}\,c_7)\frac{\sqrt{5}}{2}(3e_3^2-1)$$

$$I(\rho_3;\,|e_3|>.5) = 1+\frac{3}{8}\sqrt{5}\,c_1 + (c_4+\frac{3}{8}\sqrt{5}\,c_7)\frac{\sqrt{5}}{2}(3\rho_3^2-1)$$

$$I(\rho_3;\,|e_3|<.5) = 1-\frac{3}{8}\sqrt{5}\,c_1 + (c_4-\frac{3}{8}\sqrt{5}\,c_7)\frac{\sqrt{5}}{2}(3\rho_3^2-1)$$

Each of the nine coefficients solved for appears in at least two of the above 14 projections. Figures 46 through 49 histogram these projections for events with $p\pi^o$ invariant mass in a band centered at the N^* mass and $\bar{K}^o\pi^-$ mass in a band centered at the K^* mass at each momentum. The contamination to these samples from non-K^*N^* events is least at 2.1 GeV/c where it is around 20 $^o/_o$ and gets progressively larger with increasing beam momentum reaching 35 $^o/_o$ at 2.70 GeV/c. The solid curves superimposed on the histograms represent the predictions of the solution for the K^*N^* decay correlation parameters at that momentum normalized to the number of events in the plot. Note that all polar iosine distributions are folded about cos Θ = 0, and all azimuthal angular distributions are folded twice, first about $\varphi = \pi$ and then about $\varphi = \frac{\pi}{2}$.

The predictions of the maximum likelihood solutions for the joint decay angular correlation coefficients appear to give an adequate description of these projections of the data, considering the large number of non-K^*N^* events in the plots. The most serious discrepancies arise in those projections which involve the N^* polar cosine at 2.60 and 2.70 GeV/c. There is an excess of events in the region of small p_z at these two momenta. This is due to the presence of the 1280 MeV $\bar{K}^o\pi^o\pi^-$ enchancement in the non-K^*N^* background events in the samples histogrammed.

Any structure in the $K^*\pi$ invariant mass will reflect directly into the N^* decay polar cosine distribution and vice versa. A 1280 MeV enhancement in $K\pi\pi$ invariant mass with a width of 50 MeV will give

rise to a bump in the N^* decay polar distribution at $P_3 \simeq .2$ with a full width of $\Delta P_3 \simeq .1$ at 2.6 and 2.7 GeV/c. Folding about $P_3 = 0$ would cause an enhancement of events from $P_3 = 0$ to $P_3 = .3$ in the N^* polar cosine distribution. Calculations were made to estimate the amount of the 1280 MeV enhancement that would be present in the K^*N^* background. The results agree well with the size of the observed enhancement in the N^* decay polar cosine distribution at 2.60 and 2.70 GeV/c. The maximum likelihood procedure takes into account this effect by specifically including it in the model (as well as all other non-negligible resonances which might distort any of the K^*N^* decay angular distributions). The discrepancy arises only because the events in the mass cut are not a pure K^*N^* sample while the solution values for the decay correlation parameters are for K^*N^* events only.

In order to study the dependence of the differential cross section and decay angular correlation parameters on center of mass scattering angle, maximum likelihood fits were made on events in several production cosine intervals. For this analysis 2.60 and 2.70 GeV/c events were combined to form a single sample at the higher momenta while 2.1 GeV/c events were used as a sample at lower momenta. Because of its small number of events, the 2.45 GeV/c sample was not included in this part of the analysis. Also due to lack of statistics, only the production cosine dependence of C_1, C_4, and C_7 was studied at 2.1 GeV/c. However, the production angle dependence of all nine coefficients studied above, were measured as a function of production angle for the upper momentum sample.

Table 19 gives the results of the maximum likelihood fits at various production cosine intervals for the decay angular distribution coefficients at 2.1 GeV/c, and table 20 the same for the upper momentum sample. Table 21 gives the fraction of K^*N^* events in each interval and the differential cross section for K^*N^* production, averaged over the production angle interval. These results are displayed in figures 50, 51, and 52.

The differential cross section for $K^-p \rightarrow \bar{K}^*N^*$ is clearly seen to be much more forward peaked at the higher momenta that at 2.1 GeV/c. Also the solutions show that $\bar{K}^*N^*$ events are much more forward peaked than the non-$\bar{K}^*N^*$ ones at the upper momenta, while this is not the case for 2.1 GeV/c. Also, with the possible exception of C_4, the decay angular correlation coefficients show no marked dependence on production angle at 2.1 GeV/c. At the upper momentum several of the measured decay angle correlation coefficients show a dependence on the production angle. C_1, C_3, C_5, and C_{19} seem to show production angle dependencies at the upper momenta, while the others show no significant change with production angle. The most interesting production angle dependence is that of C_{19} which is consistent with zero in the forward direction, then decreases to almost -1 at $\cos\theta_p = .8$ and then is again consistent with zero in the region $.6 \leq \cos\theta_p \leq 0$. C_1, C_3, and C_5 all seem to monotonically decrease with increasing production angle.

Figure 53 compares the predictions of the maximum likelihood solutions for relevant projections of I $(\hat{e}\ \hat{p})$, with the data, for the production angle intervals at 2.1 GeV/c. Here again, the events were chosen to be plotted on the basis of cuts on the $p\pi^o$ and $\overline{K}^o\pi^-$ invariant masses (as well as the corresponding production angle cuts). The background from non-K^*N^* events is about 20 $^o/_o$ for the forward two production cosine intervals, and 35 $^o/_o$ for the backward one. Figure 54 compares the solutions for the azimuth angle correlations with the relevant projections of the data at the upper momenta. Here the fraction of non-K^*N^* events in the samples plotted is around 15 $^o/_o$ in the most forward production cosine interval, and increases monotonically with increasing production angle to about 50$^o/_o$ in the most backward. Figures 55 through 59 compare the likelihood solutions for the K^*N^* decay angle coefficients with the relevant projections of the data for the five production angle intervals at the upper momenta where C_1, C_2, C_3, C_4, C_5, C_6, and C_7 were solved. Here again, the fraction of non-K^*N^* events in the samples plotted runs from 15 $^o/_o$ in the most forward directions to around 50 $^o/_o$ in the backward one.

The predictions of the maximum likelihood solutions represent fairly well the projections of the data for most all of the production cosine intervals. The comparisons are clearly better in the forward production cosine intervals where the data plotted contains less non-K^*N^* background, than in the less forward ones, where this background is higher. In particular the enhancement in the N^* polar cosine distribution near $p_3 = 0$ becomes much more visible as the production angle

and thus the non-$K^{*}N^{*}$ background in the samples plotted increases.

XII. Theoretical Models

Much theoretical attention has been given to quasi-two-particle reactions in which one or both of the reaction products are resonances. The reactions $K^- p \rightarrow K^{*-}_{\frac{1}{2}}(892)\, p$ and $K^- p \rightarrow \overline{K}^{*}_{\frac{1}{2}}(892)\, N^{*}_{3/2}(1238)$, experimentally studied in this report, are examples of these quasi-two-particle reactions. This section will compare the measurements of this experiment, on these reactions, with predictions of various theoretical models.

The two most successful models for describing the properties of quasi-two-particle reactions at intermediate energies, (2 to 10 GeV/c incident beam momentum) have been the single meson exchange model with absorptive corrections[1], [3], [7], [45] (loosely termed the absorptive model) and the Regge pole model.[5], [6], [47] Both models assume that the amplitudes responsible for these reactions are dominated by contributions from the crossed or t-channel, and background from s-channel effects is small. Both models have enjoyed considerable success in describing many properties of the production and decay of unstable particles produced in quasi-two-particle reactions.

A) The Absorptive Peripheral Model

This model has its roots in the analogy of the strong interactions to quantum electrodynamics. The strong interactions responsible for these reactions are assumed to result from exchanges of strongly interacting particles in the same sense that the electromagnetic interactions between charged particles can be described by their exchange of photons. This assumes that quantum field theory can be

applied to the strong interactions, that the interaction Legrangian for the strong interactions is similar to electrodynamics, and the first order terms (The Born amplitudes) dominate in the expansion of the S-matrix. The contribution of the absorptive peripheral model is to modify the Born amplitudes by accounting for the absorptive effects of competing channels, similar to the introduction of complex phase shifts to account for competing channels in elastic scattering.

The prescription assumed by this model to account for the absorptive effects is given by the matrix equation

$$M_{fi} = S_{ff}^{1/2} B_{fi} S_{ii}^{1/2}$$

where B_{fi} is the unmodified Born amplitude for the reaction, S_{ii} and S_{ff} are the elastic scattering S-matrix elements in the initial and final states, and M_{fi} is the modified or absorbed amplitude for the reaction. In applications of the model S_{ff} and S_{ii} are assumed to be diagonal, helicity preserving, and purely diffractive. S_{ii} can then be inferred from elastic scattering data. Since no experimental data exist for elastic scattering of resonant states, it is usually assumed that their elastic scattering amplitudes have slightly larger range than stable particle scattering, and sufficient strength so as to completely absorb the lowest partial wave.

Jackson and Donohue [45], [46] have performed a detailed comparison of the absorptive peripheral model predictions to the data of this experiment for the reaction $K^- p \to K^{*-}_{\frac{1}{2}}(892)\, p$, employing a mixture of pseudoscalar and vector exchange. With this model, each helicity amplitude for $K^{*-}_{\frac{1}{2}}(892)$ production may be written (suppressing the

the helicity indices).

$$M_{K^{*-}} = g_{K^*K\pi^o} G_{pp\pi^o} M^P - f_{K^*KV^o} (G^V_{ppV^o} M^V + G^T_{ppV^o} M^T)$$

where M^P is the pseudoscalar exchange amplitude and M^V and M^T are the exchange amplitudes corresponding to vector and tensor coupling of the vector meson to the nucleon. $g_{K^*K\pi^o}$ and $G_{pp\pi^o}$ are the coupling constants of the pion to the K^*K and pp vertices; $f_{K^*KV^o}$ is the coupling constant of the vector meson to the K^*K vertex and $G^V_{ppV^o}$ and $G^T_{ppV^o}$ are the vector and tensor coupling constants of the vector meson to the nucleon.

Donohue [45] defines

$$x = \frac{f_{K^*KV^o} G^V_{ppV^o}}{g_{K^*K\pi^o} G_{pp\pi^o}} \quad \text{and} \quad y = \frac{f_{K^*KV^o} G^T_{ppV^o}}{g_{K^*K\pi^o} G_{pp\pi^o}}$$

The amplitude for $K^{*-}_{\frac{1}{2}}(892)$ production can then be written

$$M_{K^{*-}} = g_{K^*K\pi^o} G_{pp\pi^o} (M^P - x M^V - y M^T).$$

$g_{K^*K\pi}$ is known from the width of the $K^*_{\frac{1}{2}}(892)$ and $G_{pp\pi^o}$ is known from pion nucleon interactions. The coupling constants associated with the vector exchange amplitudes are not known experimentally, and must be fit to the data. x and y as defined above appear quadratically in the differential cross section and in fourth order in the chi square

$$\chi^2 = \sum_{i=1}^{N} \left[\left(\frac{d\sigma}{d\Omega}\right)_i^{exp.} - \left(\frac{d\sigma}{d\Omega}\right)_i^{theo.} \right]^2 / \Delta_i^2(exp.).$$

The procedure of Jackson and Donohue was to select the values of x and y which gave the lowest value of the x^2 for the differential cross section at 2.64 GeV/c and use these values to predict the differential cross section at 2.1 GeV/c and the decay correlation parameters at both momenta.

Figure 60 shows a contour map of the χ^2 for the differential cross section at 2.64 GeV/c as a function of x and y. Two regions are seen to have χ^2 less than 100 (for 16 data points). These have $x \lesssim \pm 2.5$. positive x corresponds to constructive interference between the pion exchange amplitude and the vector coupling part of the vector exchange amplitude, while negative x corresponds to negative interference. The differential cross section is relatively insensitive to y because the tensor coupling amplitude M^T is not as large as the vector coupling term M^V at small momentum transfer, and thus cannot interfere as much with the pion exchange amplitude. For constructive interference between the pion and vector exchange amplitudes the differential cross section will rise rapidly in the extreme forward direction where the pion exchange amplitude is large, while for destructive interference the differential cross section will turn over and decrease in the extreme forward direction. The data at 2.64 GeV/c clearly rise in the extreme forward direction favoring constructive interference. The region near x =-2.5 in the χ^2 contour map shows a dip because it fits the data at larger production angles where there is no pion exchange amplitude to interfer with. The region near x = 2.5 has a much deeper valley because it fits the differential cross section at both large and small momentum transfers.

Figure 61 compares the predictions of the model for (x,y) = (2.5, 1.1) with the differential cross section and decay correlation parameters as measured in this experiment.[46] The experimental data points for the decay correlation parameters are given in terms of the

spin density matrix elements for the $K^*_{\frac{1}{2}}$ (892), which are linearly related to the decay correlation coefficients defined earlier by:

$$C_1 = \frac{3\rho_{00}-1}{\sqrt{5}}\,,\quad C_2 = -\frac{12}{\sqrt{30}}\,\rho_{1-1}\,,\ \text{and}\ C_3 = \frac{12}{\sqrt{15}}\,\mathrm{Re}\,\rho_{10}$$

The predictions of the model represent the production angle (or momentum transfer) dependence of the differential cross section and decay correlation parameters well at all momenta but predicts too small a total cross section at 2.1 GeV/c. This difficulty in predicting the absolute cross sections of reactions where vector exchange is involved is well known. The problem stems from the fact that the exchange of a particle of spin J yields a Born amplitude with an energy dependence S^J, where S is the square of the center of mass energy. The cross section thus goes as S^{2J-1}. This predicts that the total cross sections for reactions where vector exchange occurs will increase without bound with increasing beam energy. Absorption as used here cannot effect this energy dependence. Since all resonance production cross sections decrease with increasing energy, models employing vector exchange cannot hope to give the correct energy dependence of the cross section.

The reaction $K^-p \rightarrow \bar{K}^*_{\frac{1}{2}}$ (892) $N^*_{3/2}$ (1238) is an excellent one to test predictions of the absorptive peripheral model since its qualitative features appear to result from the domination of the pion exchange amplitude. This is not surprising since the pion and K^- are strongly coupled to the K^* and the pion and proton are also strongly coupled to the N^*. The unmodified Born amplitude for single pion exchange predicts no joint decay correlations between the K^* and N^*,

and only the coefficients of $\cos^2\theta_{K^*}$ and $1 + 3\cos^2\theta_{N^*}$ for the individual decay distributions non-vanishing. Since the analysis of Section XI indicates the existence of joint decay correlations between the K^* and N^* as well as other non-zero coefficients for the individual decay distributions, it is of interest to see if the absorptive correction to the one pion exchange peripheral model can account for them. Since all of the coupling constants in the problem are known, the absorptive peripheral model with one pion exchange is able to make absolute predictions of the differential cross section and combined decay angular correlations and no fitting is necessary. (72)

Before discussing the detailed predictions of the pion exchange absorptive model for this reaction it is of interest to compare the experimental results for the joint decay angular distribution in the extreme forward direction with the purely kinematical restrictions placed upon them. In the special case of zero production angle there are in general only three non-vanishing helicity amplitudes. This requires that many of the joint decay angular distribution coefficients must vanish in the forward direction, and establishes relations between some that are not required to vanish.

These restrictions are most easily discussed in the spin density matrix formalism. The decay angular distribution of a resonance is determined by the spin density matrix.(59) For associated production of two resonances a joint spin density matrix is defined which determines the combined decay angular distributions of the two resonances.(60) Let $\rho^{K^*}_{mm'}$ and $\rho^{N^*}_{nn'}$ describe the spin populations of the K^* and N^* each in its own rest frame and $R_{mm';\,nn'}$ be the joint spin density matrix.

Then

$$\rho^{K^*}_{mm'} = \sum_n R_{mm';nn} \quad \text{and} \quad \rho^{N^*}_{nn'} = \sum_m R_{mm;nn'}$$

The joint decay angular distribution coefficients measured in Section XII are related to the spin density matrix elements by:

$$C_1 = \frac{3\rho^{K^*}_{00} - 1}{\sqrt{5}} \qquad C_2 = -\frac{12}{\sqrt{30}} \rho^{K^*}_{1-1} \qquad C_3 = \frac{12}{\sqrt{15}} \mathrm{Re}\, \rho^{K^*}_{10}$$

$$C_4 = \frac{1 - 4\rho^{N^*}_{33}}{\sqrt{5}} \qquad C_5 = -\frac{8}{\sqrt{10}} \mathrm{Re}\, \rho^{N^*}_{3-1} \qquad C_6 = \frac{8}{\sqrt{10}} \mathrm{Re}\, \rho^{N^*}_{31}$$

$$C_7 = \frac{1}{5} + \frac{1}{\sqrt{5}}(C_1 - C_4) - \frac{12}{5} R_{00;33}$$

$$C_{11} = \frac{24}{5\sqrt{3}} \mathrm{Re}\,(R_{1-1;-13} + R_{1-1;3-1})$$

$$C_{19} = \frac{24}{5\sqrt{3}} \mathrm{Re}\,(R_{1-1;-13} - R_{1-1;3-1})$$

Donohue[52] shows that in general

$$0 \leq R_{00;33} \leq \min\left[\tfrac{1}{2}\rho^{K^*}_{00}, \rho^{N^*}_{33}\right]$$

and in the special case of production in the forward direction (zero production angle)

$$R_{00;33} = 0, \quad \mathrm{Re}\, R_{1-1;-13} = 0, \quad \rho^{K^*}_{1-1} = 0$$

$$\mathrm{Re}\,\rho^{K^*}_{10} = 0, \quad \mathrm{Re}\,\rho^{N^*}_{3-1} = 0, \quad \mathrm{Re}\,\rho^{N^*}_{31} = 0 \quad \text{and}$$

$$|\,\mathrm{Re}\,R_{1-1;3-1}\,| \leq \sqrt{\tfrac{1}{2}\left(1 - \rho^{K^*}_{00} - 2\rho^{N^*}_{00}\right)\rho^{N^*}_{33}}$$

thus in the extreme forward direction

$$C_2 = 0, \quad C_3 = 0, \quad C_5 = 0, \quad C_6 = 0$$

$$C_7 = \frac{1}{5} + \frac{1}{\sqrt{5}}(C_1 - C_4), \quad C_{11} = -C_{19} \quad \text{and}$$

$$|\,C_{19}\,| \leq \frac{2}{5}\sqrt{1 + 2\sqrt{5}\,(C_4 - C_1) - 15\,C_4^2 + 10\,C_1 C_4}\,.$$

Furthermore, if the helicity amplitudes all have a common phase (as, for example, is assumed in the absorption model) then the inequality of the last relation becomes an equality. Since these relations are purely kinematical and do not depend on any dynamical model, they can be used as consistency checks on the most forward measurements of the joint decay angular distribution parameters

Inspection of Table 20 and Figure 52 shows that the maximum likelihood solutions for the joint decay correlation parameters in the forward most production angle bins are quite consistent with the kinematical restrictions above. C_2, C_3, C_5, and C_6 all approach zero

in the forward direction. Although $|C_{19}|$ is on the average much larger than C_{11}, in the forward direction C_{19} is quite consistent with $-C_{11}$. From the values and errors on C_1 and C_4 in the most forward production angle interval one obtains $1/5 + \sqrt{\frac{1}{5}}\ (C_1 - C_4) = .32 \pm .05$, which is in very good agreement with the measured value of C_7 in the most forward production angular interval $.29 \pm .09$.

In general, $C_7 \simeq \frac{1}{5} + \sqrt{\frac{1}{5}}\ (C_1 - C_4)$ at all measured production angles indicating a small value of $R_{00;33}$ even away from the forward direction. The inequality limiting the magnitude of C_{11} and C_{19} in the forward direction is impossible to test in this experiment since the expression under the radical is the difference of large quantities each with appreciable error. Thus the uncertainty in this upper limit is too large for its central value to have any meaning.

Jackson and Donohue[61] have calculated the predictions of the one pion exchange absorptive peripheral model for the differential cross section and joint decay angular distribution parameters at 2.64 GeV/c. The results are shown as solid curves superimposed upon plots of the measured values from this experiment in Figures 62 and 63. Figure 62 displays the differential cross section for the reaction $K^- p \rightarrow \bar{K}^*_{\frac{1}{2}}(892)\ N^*_{3/2}(1238)$ at 2.64 GeV/c with the prediction of the pion exchange absorptive model superimposed. The agreement between the predicted and measured values is excellent, especially since the model predicts both the shape and normalization of the solid curve. Thus the model describes well both the total cross

section and production angular distribution.

Figure 63 shows the one pion exchange absorptive peripheral model predictions for the joint decay angular correlation parameters measured in this experiment, superimposed upon the measured values. Qualitatively the agreement is excellent. The model predicts non-negligible values for C_1, C_4, C_6, and C_{11}, and C_{19}, and very small values for C_2, C_3, and C_5. It predicts that C_1, C_4, C_7, and C_{11} should have positive sign while C_6 and C_{19} should have negative sign. The predictions are born out in the data in the forward direction. Quantitatively the model also does very well in the extreme forward direction. The measurements in the most forward angular intervals agree well with the predictions for all decay correlation parameters measured. The model predicts the production angular dependence of C_2, C_4, C_6 and C_{11} excellently. The experimentally measured values for C_1, C_3, C_5, C_7, and C_{19} seem to decrease more rapidly with increasing production angle than the model predicts. Some of the assumptions involved in the absorptive peripheral model become less valid as production angle increases away from the forward direction, so that the minor disagreements between the model and the experimental measurements at increasing production angle are not surprising.

Donohue [45], [52] points out that the ability of the absorptive peripheral model with pion exchange to describe the experimentally observed joint polar cosine decay correlations in double resonance production in the past, [57], [62], [63] may stem from its ability

to describe the individual polar cosine distributions and from the fact that $R_{00;33}$ (which is kinematically constrained to be zero in the forward production direction) is slowly varying with production angle. Donohue suggests that a stringent test of the model would be a measurement of the only two joint spin density matrix elements (Re $R_{10;31}$ and Re $R_{1-1;3-1}$) which explicitly involve joint decay angle correlations, and are not required by kinematics to vanish at the forward production angle. Such measurements would test the models ability to describe joint decay angular correlations independent of its ability to describe the individual decay angular distributions.

The joint spin density matrix element Re $R_{1-1;3-1}$ is measured in this experiment throught its contribution to C_{11} and C_{19}. At small production angles

$$C_{19} \simeq -C_{11} \simeq -\frac{24}{5\sqrt{3}} \operatorname{Re} R_{1-1;3-1}$$

since $R_{1-1;-13}$ is kinematically required to be zero in the forward direction. Inspection of Figure 63 shows that in the most forward production angle interval (1 to .9), the absoprtive peripheral model prediction for C_{11} and C_{19} agree very well with the experimental measurements. Thus in the forward direction the absorptive peripheral model with single pion exchange gives an excellent account of the joint decay angular correlations as well as the individual decay angular distributions for this reaction at this energy.

B. The Regge Pole Model

Kaydalov and Karnakov [47] have applied a model of several Regge

poles to resonance production in pion nucleon and kaon nucleon reactions at intermediate energies.

Analytic continuation indicates that the t-channel helicity amplitudes for the reactions may be put as a sum over the singularities in the complex angular momentum plane as

$$M_{\lambda_{\bar{B}}\lambda_N,\lambda_M}(s,t) = \sum_i B^i_{\lambda_{\bar{B}}\lambda_N,\lambda_M}(t, \ln\tfrac{s}{s_0})(\tfrac{s}{s_0})^{\alpha_i(t)} + O[(\tfrac{s}{s_0})^{\nu}]$$

where $M_{\lambda_{\bar{B}}\lambda_N,\lambda_M}$ is the t-channel amplitude for $\lambda_{\bar{B}}$ helicity of the final state baryon, λ_N helicity of the initial state nucleon, and λ_M helicity of the final state meson. $\alpha_i(t)$ is the position of the i^{th} singularity in the complex j-plane and S_0 is the minimum physical value of S. B^i is a generalized residue function. The sum is to be taken over all singularities lying to the right of Re $j = \nu$.

In a model accounting only for poles in the j - plane this reduces to

$$M_{\lambda_{\bar{B}}\lambda_N,\lambda_M}(s,t) = \sum_k \xi_k(t)\, b^k_{\lambda_{\bar{B}}\lambda_N}(t)\, b^k_{\lambda_M}(t)\, (\tfrac{s}{s_0})^{\alpha_k(t)},$$

where the factorization of the residues of the poles has been taken into account. $\alpha_k(t)$ is the position of the k^{th} Regge pole and

$$\xi_k(t) = -[1 + P_j^k e^{-i\pi\alpha_k(t)}]/\sin\pi\alpha_k(t)$$

is the signature factor, P_j^k being the signature of the k^{th} pole. $b^k(t)$ is the residue function for each vertex. Each Regge pole has definite quantum numbers: signature P_j, parity P, isospin T, and G-parity G. Conservation of G and P require that the residue functions have the following properties:

$$b^k_{-\lambda_M} = (-1)^{\lambda_M} P^k P_j^k P_M (-1)^{S_M+1} b^k_{\lambda_M}$$

$$b^{\kappa}_{-\lambda_{\bar{B}}-\lambda_N} = (-1)^{\lambda_{\bar{B}}-\lambda_N} P^{\kappa} P_J^{\kappa} P_B (-1)^{S_B-1/2} b^{\kappa}_{\lambda_{\bar{B}}\lambda_N}$$

$$b^{\kappa}_{\lambda_{\bar{N}}\lambda_N} = (-1)^{T_{\kappa}} P_J^{\kappa} G_{\kappa} (-1)^{\lambda_{\bar{N}}-\lambda_N} b^{\kappa}_{\lambda_{\bar{N}}\lambda_N}$$

where P_M, P_B, S_M, and S_B are the parity and spin of the final state baryon and meson respectively. Using these properties and assuming that the dominant singularities have a definite value for the product PP_J. Kaydalov and Karnakov derive for the helicity amplitudes

$$M_{-\lambda_{\bar{B}}-\lambda_N,\lambda_M} = (-1)^{\lambda_{\bar{B}}-\lambda_N} P P_J P_B (-1)^{S_B-1/2} M_{\lambda_{\bar{B}}\lambda_N,\lambda_M}$$

$$M_{\lambda_{\bar{B}}\lambda_N,-\lambda_M} = (-1)^{\lambda_M} P P_J P_M (-1)^{S_M+1} M_{\lambda_{\bar{B}}\lambda_N,\lambda_M}$$

while if the dominate singularities have a definite value for the product $(-1)^T P_J G$ then

$$M_{\lambda_{\bar{N}}\lambda_N,\lambda_M} = (-1)^T P_J G (-1)^{\lambda_{\bar{N}}-\lambda_N} M_{\lambda_N\lambda_{\bar{N}},\lambda_M}.$$

The possible contributing Regge poles are divided into two classifications: poles of type a which have the properties $PP_J = +1$ and $(-1)^T P_J G = +1$, and poles of type b which have $PP_J = -1$ and $(-1)^T P_J G = +1$. Poles of type a would be, for example, P, P', ρ, A_2, ω, and φ Regge poles while poles of the type b would be the π and B poles.

Using the relations above between the helicity amplitudes and the general relation connecting the final state vector meson's spin density matrix to the helicity amplitudes

$$\rho_{\lambda\mu}(s,t) = \frac{1}{N} \sum_{\lambda_{\bar{B}}\lambda_N} M^{(s,t)}_{\lambda_{\bar{B}}\lambda_N,\lambda} M^{*(s,t)}_{\lambda_{\bar{B}}\lambda_N,\mu}$$

Kaydalov and Karnakov obtain:

$$\rho_{11} = \frac{2}{N}\left[|M^{a}_{\frac{1}{2}\frac{1}{2},1}|^2 + |M^{a}_{\frac{1}{2}-\frac{1}{2},1}|^2 + |M^{b}_{\frac{1}{2}\frac{1}{2},1}|^2 \right]$$

$$\rho_{1-1} = \frac{2}{N}\left[|M^{a}_{\frac{1}{2}\frac{1}{2},1}|^2 + |M^{a}_{\frac{1}{2}-\frac{1}{2},1}|^2 - |M^{b}_{\frac{1}{2}\frac{1}{2},1}|^2 \right]$$

$$\rho_{00} = \frac{2}{N}|M^{b}_{\frac{1}{2}\frac{1}{2},0}|^2 \qquad \rho_{10} = \frac{2}{N} M^{b}_{\frac{1}{2}\frac{1}{2},1} M^{b*}_{\frac{1}{2}\frac{1}{2},0}$$

where $M^{a(b)}_{\lambda\bar{N}\lambda N,\lambda M}$ are the contributions to the t-channel helicity amplitudes from poles of type a and b respectively and N is a normalization factor ($\sum_{\lambda} \rho_{\lambda\lambda} = 1$) which gives

$$N = \sum_{\lambda\bar{B}\lambda N,\lambda} |M_{\lambda\bar{B}\lambda N,\lambda}|^2 = [s-(m_N-\mu)^2][s-(m_N+\mu)^2]\frac{d\sigma}{dt}$$

m_N is the mass of the target while μ is the mass of the beam particle. These expressions show that ρ_{00} and ρ_{10} can only come from poles of type b while ρ_{11} and ρ_{1-1} can arise from both types of poles. Also, these relations imply

$$\rho_{00}(\rho_{11} - \rho_{1-1}) = 2|\rho_{10}|^2$$

for both pole types.

Assuming a small contribution from the B pole, the behavior of the spin density matrix elements for the $K^{*-}_{\frac{1}{2}}(892)$ in the reaction $K^- p \rightarrow K^{*-} p$, can be deduced soley from the contribution of the π^0 meson Regge pole even though there is considerable contribution to the production amplitudes from other poles. ρ_{00} is obtained from

$$\rho_{00} = \left(\frac{d\sigma}{dt}\right)^{0}_{\pi} \Big/ \frac{d\sigma}{dt}$$

where $$\left(\frac{d\sigma}{dt}\right)^{o}_{\pi} = |M^{\pi}_{\frac{1}{2}\frac{1}{2},0}|^2 / 2m_N^2 E$$

and $d\sigma/dt$ is the experimentally observed differential cross section. E is the energy of the K^- in the Lorentz system. The helicity amplitudes for the π^omeson Regge pole contribution may be explicitly expressed as

$$M^{\pi}_{\frac{1}{2}\frac{1}{2},0} = C^{\pi}_{0}(E)\sqrt{-t}\; \xi_{\rho\pi}(t)[t-(m_{K^*}-m_K)^2][t-(m_{K^*}+m_K)^2]\, e^{\lambda^{\pi}_{0}(E)t}$$

$$M^{\pi}_{\frac{1}{2}\frac{1}{2},1} = -C^{\pi}_{1}(E)\, t\, \xi_{\pi}(t)\alpha_{\pi}(t)[t-(m_{K^*}-m_K)^2][t-(m_{K^*}+m_K)^2]\, e^{\lambda^{\pi}_{1}(E)t}$$

The E- dependence of the parameters is written:

$$C^{\pi}_{\lambda}(E) = C^{\pi}_{\lambda}(E_o)\left(\frac{E}{E_o}\right)^{\alpha_{Re}(0)} \quad \text{and} \quad \lambda^{\pi}_{\lambda}(E) = \lambda^{\pi}_{\lambda}(E_o) + \alpha'_{\pi}(0)\ln\frac{E}{E_o}.$$

The π^opole trajectory is approximated by a straight line and $C^{\pi}_{o}(E_o)$ is obtained by extrpolating $M^{\pi}_{\frac{1}{2}\frac{1}{2},0}$ to the π^omeson pole $t = m^2_{\pi}$, and using the $K^-\pi^o K^{*-}$ and $p\,\pi^o p$ coupling constants. Kaydalov and Karnakov obtain the other parameters of the pion pole by fitting the differential cross section for the reaction $K^+ n \rightarrow K^{*o}_{\frac{1}{2}}(892)\,p$ at 2.3 GeV/c [64], in which they assume only the π, A_2, and ρ poles contribute.

Using the relation connecting ρ_{10} to the helicity amplitudes and the above explicit expressions for the π^o meson Regge pole amplitudes one obtains:

$$\rho_{10} = \frac{C^{\pi}_{1}\sqrt{-t}\;\alpha_{\pi}(t)\; e^{-(\lambda^{\pi}_{1}-\lambda^{\pi}_{o})t}}{C^{\pi}_{o}[t-(m_{K^*}-m_K)^2][t-(m_{K^*}+m_K)^2]}\,\rho_{oo}$$

ρ_{10} is real if the only dominate pole of type b is the π^o meson. ρ_{1-1} can then be obtained from the relation connecting the spin density matrix elements, which becomes

$$\rho_{1-1} = \rho_{11} - \frac{2\rho_{10}^2}{\rho_{00}} = \frac{1-\rho_{00}}{2} - \frac{2\rho_{10}^2}{\rho_{00}}$$

Thus, knowing the experimentally measured differential cross section and the contribution of the π° meson Regge pole, all of the spin density matrix elements of the $K^{*-}_{\frac{1}{2}}(892)$ in this reaction can be explicitly calculated. The parameters entering into the expression for the π° meson contribution to the helicity amplitudes have been determined from other experiments involving different reactions at different energies.

Figure 64 compares the predictions of this model to the experimental measurements for the reaction $K^- p \to K^*_{\frac{1}{2}}(892)\, p$ at 2.64 GeV/c. Figure 64a shows the experimentally measured differential cross section. The solid line is just a smooth curve drawn through the data points. The dashed curve is the pion Regge pole contribution $(\frac{d\sigma}{dt})^\circ_\pi$ as calculated by Kaydalov and Karnakov. Figure 64b shows the experimental data for ρ_{00} and the prediction of the model, which is just the ratio of the dashed and solid curves of Figure 64a. Figures 64c and 64d display the experimentally measured data points for Re ρ_{10} and ρ_{1-1}, along with the predictions of the model as derived from ρ_{00} using the relations above.

As seen from figure 64, the correspondence between the data and the predictions of the model is excellent, especially since these predictions are not fits to this data. The fact that the parameters entering into the model were determined with different reactions at different energies, and these parameters obviously describe this data, argues strongly for the general validity of the Regge pole model.

In order for the model to predict the differential cross section, the relative contributions to the helicity amplitudes from the various poles of type a must be known. Since there is a large number of such poles that may contribute to this reaction, a fit to the differential cross section would involve too many parameters to be practial for this data. However, when additional data at different energies becomes available for both K^+p and K^-p interactions then these relative contributions can be measured.

C. The Quark Model

Bialis, Gula, and Muryn [51] have considered the problem of double resonance production in the generalized quark model of high energy scattering. They derive the following form for the joint decay angular distribution of the two resonances:

$$16\pi^2 W(\theta_\alpha \Phi_\alpha; \theta_\beta \Phi_\beta) = 1 + A(2X_\alpha + X_\beta) + \tfrac{1}{2}(\tfrac{1}{2} - A) X_\alpha X_\beta + \tfrac{3}{2}(\tfrac{1}{2} + A) \mathrm{Re}\, Y_\alpha \mathrm{Re}\, Y_\beta + B[(4 + X_\beta)\mathrm{Re}\, Y_\alpha + (2 + X_\alpha)\mathrm{Re}\, Y_\beta] + C\, \mathrm{Im}\, Y_\alpha \mathrm{Im}\, Y_\beta + D\, \mathrm{Re}\, Z_\alpha \mathrm{Re}\, Z_\beta + F\, \mathrm{Im}\, Z_\alpha \mathrm{Im}\, Z_\beta$$

where $X = 1 - 3\cos^2\theta$, $Y = \sin^2\theta\, e^{2i\varphi}$, $Z = \sin 2\theta\, e^{i\varphi}$ and the index α denotes the vector meson while the index β refers to the isobar.

The five parameters, A, B, C, D, and F depend upon the assumed quark-quark interaction and are different for different reactions. Since this model predicts that the joint decay angular distribution can be described by only five independent parameters, it provides relations between the 19 joint decay angular distribution parameters. Some of these relations can be tested by this experiment for the

reaction $K^- p \rightarrow K^*_{\frac{1}{2}}(892)\ N^*_{3/2}(1238)$.

The above expression for the joint decay angular distribution implies the following relations between the joint decay angular correlation coefficients measured in this experiment: $C_1 = 2\ C_4$, $C_2 = 2\ C_5$, $C_3 = C_6 = 0$, $C_7 = 1/5 + (1/\sqrt{5})\ C_4$, and $C_{11} = 1/5 - (1/2)\ C_7$. These relations imply that the individual decay angular distribution for the $K^*_{\frac{1}{2}}(892)$ will be twice as pronounced as that for the $N^*_{3/2}(1238)$, that the $\Theta_K^*\ \Theta_N^*$ joint correlation follows directly from the individual angular distributions as well as the $\cos 2\Phi_K^* \cos 2\Phi_N^*$ part of the $\Phi_K^*\ \Phi_N^*$ joint correlation. Also the joint decay correlation coefficients C_1, C_4, C_7 and C_{11} all depend only upon the single quark interaction parameter A.

These rather stringent conditions can be tested by inspecting Tables 18, 19, and 20 or Figures 45, 51, and 52. The model appears to fail rather badly at 2.1 GeV/c where C_4 is generally larger than C_1. However, at the higher momenta the model seems to give a better account of the data, especially in the extreme forward direction where it seems to describe the data rather well. Since the relativistic corrections necessary for the description of spin are neglected in the quark model, it may be that in the extreme forward direction these corrections are minimal, allowing the quark model to give a good description of the data.

Acknowledgements

An experiment of this size requires the effort and assistance of many people. The following is an incomplete list of those who were instrumental in the progress of this work.

The K63 beam was designed and built under the direction of Dr. Joesph Murray. The bubble chamber crews were directed by Robert Watt. The scanning and measuring staff for this experiment was coordinated by Michael Hoffman and Lisa Becker was the librarian.

I would like to acknowledge the help of my colleagues on the K63 experiment, and especially thank Alan Rittenberg and Drs. Philippe Eberhard and Morris Pripstein for many helpful discussions. I thank Professor J. D. Jackson and Drs. J. T. Donohue and Robert Huff for help on the theoretical aspects of this report.

I wish to thank Professor Ronald R. Ross for suggesting the topic for this work and for his advice and encouragement throughout its course.

It is customary to acknowledge also the help and encouragement of those who, while not directly connected with this experiment, have been instrumental to the students graduate career. To this end I thank Dr. Janos Kirz for my introduction to bubble chamber physics, Dr. Orin Dahl for many useful discussions and help with digital computer analysis, Dr. Frank Solmitz for helpful discussions concerning statistical methods, and Professor Luis W. Alvarez for his continued support.

This work was performed under the auspices of the United States Atomic Energy Commission.

Appendix

The High Mass $\bar{K}^o\pi^-$ and $\bar{K}^o\pi^o\pi^-$ Enhancements

In the general analyses of the reactions $K^-p \to p\,\bar{K}^o\pi^-$ and $K^-p \to p\bar{K}^o\pi^o\pi^-$, described in sections VII and IX, two rather narrow enhancements with masses at 1280 and 1400 MeV were included in the $\bar{K}^o\pi^-$ and $\bar{K}^o\pi^o\pi^-$ mass spectra of the respective reactions. This section will attempt to motivate that procedure.

Figure 65a shows the $\bar{K}^o\pi^o\pi^-$ mass squared distribution for all $p\,\bar{K}^o\pi^o\pi^-$ events in the experiment. The arrows indicate where other experiments have reported structure in $K\pi\pi$ mass spectra.[42] The bin width of .03 $(GeV)^2$ corresponds to the average resolution over the mass squared spectrum and represents a width of approximately 15 MeV in mass for the lower mass values and 10 MeV for the higher ones. Phase space for 2.1 GeV/c, which accounts for around one fourth of the events, ends at 1.8 $(GeV)^2$.

Figure 65b shows the same data with the predictions of the maximum likelihood solutions, assuming no $K\pi\pi$ enhancements, superimposed. These solutions were obtained at each momentum. The predictions of these solutions for the $\bar{K}^o\,\pi^o\pi^-$ mass spectrum were then added to construct the solid curve of Figure 60b. The sharp discontinuity at 1.8 $(GeV)^2$ from the 2.1 GeV/c events is evident. The curve systematically overestimates the data for lower mass squared values and underestimates it in the regions corresponding to mass values around 1280 and 1400 MeV.

The higher mass region may be more clearly seen in Figure 65c where the $\bar{K}^o\pi^o\pi^-$ mass squared distribution is plotted for 2.60 and 2.70

GeV/c. Both of these momenta are above threshold for the production of the $K^*_{1/2}$ (1400). Figure 65d shows the same data with the prediction of the maximum likelihood solutions superimposed, assuming no $K\pi\pi$ resonances. The curve is normalized to the total number of events inthe plot.

Clear enhancements are observed in the regions of 1280 and 1400 MeV. Each exhibits a full width a half maximum of approximately 50 MeV. These enhancements were incorporated into the general analysis of the $p\,\bar{K}^o\pi^o\pi^-$ final state described in SectionIX. The mass and width of these two enhancements were solved for at 2.60 and 2.70 GeV/c. combined, and these values were used to solve for the amounts at each of the momenta. Table 12 gives the solution values for the amounts of these two enhancements at each momenta. Table 13 gives their masses and widths as obtained from the maximum likelihood solutions on 2.60 and 2.70 GeV/c events.

Figures 65e and 65f show the data of figures 65a and 65c with the predictions of the maximum likelihood solutions including the $\bar{K}^o\pi^o\pi^-$ 1280 and 1400 MeV enhancements. Here again the curves are normalized to the total number of events. As can be seen, the inclusion of the 1280 and 1400 MeV enhancements, results in a much better correspondence to the $\bar{K}^o\pi^o\pi^-$ mass spectra.

Table 12 shows a large amount ($\simeq$ 9 %) of 1280 MeV enhancement at 2.1 GeV/c even though no clear cut bump in the $\bar{K}^o\pi^o\pi^-$ mass spectrum is observed. Figure 60g shows the $\bar{K}^o\pi^o\pi^-$ mass squared distribution for 2.1 GeV/c, with the prediction of the maximum likelihood solution assuming no 1280 MeV enhancement, and figure 60h the same except including the 1280 MeV enhancement. Clearly the inclusion of the $K\pi\pi$ 1280 MeV enhancement

in the model gives a better correspondence to the data.

Structure in the $N^*(1238)$ decay polar cosine distribution could give rise to structure in the $\bar{K}^o\pi^o\pi^-$ mass spectrum. This could give rise to bumps in the 1280 MeV region of the $\bar{K}^o\pi^o\pi^-$ mass at 2.1 GeV/c and in the 1400 MeV region at 2.60 and 2.70 GeV/c. However, the maximum likelihood solutions of Section XI , which included these decay correlations for the $N^{*+}_{3/2}(1238)$ associated with the $K^{*-}_{1/2}(892)$, gave nearly the same fractions for the $K\pi\pi$ enhancements as did the solutions of Section X which did not include them. Thus the $N^*_{3/2}(1238)$ decay correlations seem not to be responsible for these enhancements.

Figure 66a shows the $\bar{K}^o\pi^o\pi^-$ mass spectrum for events in the $\bar{K}^{*o}(892)$ mass region at 2.60 and 2.70 GeV/c. The enhancements at 1280 and 1400 MeV are clearly observed, and appear to be strengthened by the $\bar{K}^{*o}_{\frac{1}{2}}(892)$ mass selection. Figure 66b shows the $\bar{K}^o\pi^o\pi^-$ mass distribution for events in a mass interval centered around the $K^{*-}_{1/2}(892)$. Here again the enhancements at 1280 and 1400 MeV are seen, but are considerably less pronounced than for the $\bar{K}^{*o}_{1/2}(892)$ selection. This is to be expected for the $K^*_{1/2}(1400)$ since the branching ratio

$$R(T) = \frac{R(K^*_T \to K^{*-}_{1/2}(892)\,\pi^o)}{R(K^*_T \to K^{*o}_{1/2}(892)\,\pi^-)}$$

is one half for $T = \frac{1}{2}$ and two for $T = 3/2$. However, the enhancement at 1280 MeV is also much more associated with the $\bar{K}^{o*}(892)$ than the $K^{*-}_{1/2}(892)$. These simple considerations might suggest that, if the 1280 MeV enhancement is a resonance, then its isospin is one half.

However other effects can cause the two mass plots to differ.

First, the $N^*_{3/2}(1238)$ decay correlations reflect much more in the $K^{*-}_{1/2}(892)$ events than the $\overline{K}^{*o}_{1/2}(892)$ events since there is four times as much $N^*_{3/2}(1238)$ associated with the $K^{*-}_{1/2}(892)$, than with the $\overline{K}^{*o}_{1/2}(892)$. Also, since there is more $K^{*-}_{1/2}(892)$ than $\overline{K}^{*o}_{1/2}(892)$ in the final state, the reflection due to overlapping K^* is larger for the $\overline{K}^{*o}_{1/2}(892)$ events than for the $K^{*-}_{1/2}(892)$ ones. Also, for the case of the 1280 MeV enhancement, the $\rho(750)$ mass band exactly overlaps the two $K^*(892)$ mass bands where they overlap each other. Thus if this enhancement is also associated with $\rho(750)$, this will further complicate things. However, there is no significant enhancement in the $\pi^o\pi^-$ mass spectrum in the region of the ρ mass.[65] In addition, interference effects can further complicate the problem.

In order to allow for possible two particle decay modes, these enhancements were included in the general analysis of the $p\,\overline{K}^o\pi^-$ final state as $\overline{K}^o\pi^-$ resonances with the same masses and widths of the $\overline{K}^o\pi^o\pi^-$ effects. Table 7 shows that the solutions found non-negligible amounts for both enhancements in the three particle final state. The amount of $K^*_{1/2}(1400)$ found in the three particle final state is consistent with the world averaged value[29] for its two to three particle decay modes. The solutions for the three particle final state show as much 1280 MeV enhancement in the $\overline{K}^o\pi^-$ mass spectrum as the 1400 MeV one.

Clear resolution into two distinct peaks is not seen in the high mass region of the $\overline{K}^o\pi^-$ mass spectrum of the $p\,\overline{K}^o\pi^-$ final state. However a broad enhancement is clearly visible there. The association of this broad peak as two narrow enhancements is made solely from the information of the $p\,\overline{K}^o\pi^o\pi^-$ final state, and is clearly only an assumption.

Thus, the $\bar{K}^{o}\pi^{o}\pi^{-}$ mass spectra in this experiment show two statistically significant enhancements in the $\bar{K}^{o}\pi^{o}\pi^{-}$ mass at 1280 and 1400 MeV. The latter is associated with the well known $K^{*}_{1/2}(1400)$, although the width observed here is somewhat narrower than observed in other experiments.[66]

The enhancement at 1280 MeV is not easily associated with reported resonance phenomena. It could correspond to the reported $K^{*}(1320)$ enhancement[67] appearing at a somewhat lower mass or perhaps the $K^{*}(1215)$ (c-meson)[68] appearing at a somewhat higher mass.

It might also be a so far undiscovered resonance phenomenum or perhaps a "kinematic effect".[69],[70] However, it is difficult to imagine a possible kinematic mechanism that could produce such a narrow bump in the intermediate region of the $\bar{K}^{o}\pi^{o}\pi^{-}$ mass spectrum.

Footnotes and References

1. J.D. Jackson, J.T. Donohue, K. Gottfried, R. Keyser, and B.E.Y. Svensson, Phys. Rev. 139, B 428 (1965).
2. J.D. Jackson and H. Pilkuhn, Nuovo Cimento, 33, 906 (1964).
3. Ronald Omnes, Phys. Rev. 137, B 649 (1965).
4. M. Jacob and G.F. Chew, Strong Interaction Physics (W.A. Benjamin, Inc., New York, 1964).
5. S.C. Frautchi, Regge Poles and S-Matrix Theory (W.A. Benjamin Inc., 1963).
6. J.S. Ball and W.R. Fraser, Phys. Rev. Letters 14, 746 (1965).
7. K. Gottfried and J.D. Jackson, Physics Letters 8, 144 (1964).
8. A. Rosenfeld and W.E. Humphrey, Ann. Rev. Nucl. Sci. 13, 103 (1963).
9. J.J. Murray, J. Button-Shafer, F.T. Shively, G.H. Trilling, J.A. Kadyk, A. Rittenberg, D.M. Siegel, J.S. Linsey and D. Merrill, A separated 2.5 to 2.8 GeV/c K^- Beam at the Bevatron, Proceedings of 1964 International Conference on High Energy Physics, Dubna, Lawrence Radiation Laboratory Report UCRL 11426, July 1964 (unpublished).
10. D.W. Merrill, Design of the K63 Beam Using an Analog Computer, Alvarez Group Memo No. 519, July 1964.
11. S.M. Flatte, S.U. Chung, L. Hardy and R. Hess, K63: Changing the incident K^- Momentum from 2.7 GeV/c to 2.1 GeV/c, Alvarez Group Memo No. 524, August 1964.
12. J.J. Murray, D.M. Siegel and A. Rittenberg, Quadrupole Magnet Analysis and Shimming Alvarez Group Memo No. 518.

13. J.H. Friedman, D.M. Siegel, R.R. Ross, A study of K63 Beam Momenta using γ's Alvarez Group Memo No. 582.

14. R. Casey, O.I. Dahl, G.A. Smith, and L. Polissar, K63 Scanning Instructions, Alvarez Group Memo 456, July 1963.

15. P.G. Davey, R.I. Hulsizer, W.E. Humphrey, J.H. Munson, R.R. Ross, A.J. Schwemin, Rev. of Sci. Instruments 35, 1134 (1964).

16. M. Hutchinson, PANAL-Alvarez Group Program Alston, Berge, Braley et al (Revised), Alvarez Group Programming Memo P-358, Jan. 1963.

17. J.P. Berge, F.T. Solmitz, and H.D. Traft, Rev. of Sci. Instruments 32, 538 (1961).

18. A.H. Rosenfeld and J. Snyder, Digital Computer Analysis of Data from Bubble Chambers: IV. The Kinematic Analysis of Complete Events, Lawrence Radiation Laboratory Report UCRL Feb. 1961.

19. A.H. Rosenfeld, Reference Manual for KICK I.B.M. Program, Lawrence Radiation Laboratory Report UCRL 9099, May 1961.

20. F. Safier and C. Hansen, I.B.M. Program GUTS - Detailed Description and Flow, Lawrence Radiation Laboratory Report UCRL 9309, September 1960.

21. Electron, position pair production ($\gamma \rightarrow e^+e^-$) can also give rise to a vee in the bubble chamber. However, most of these can be identified at the scanning stage of data reduction and are discarded there. The pair production hypothesis was not included in attempting to fit vees in this analysis.

22. D. Johnson and O.I. Dahl, WRING and GENIE, Two Programs for Data Manipulations, Alvarez Group Programming Note P-5.

23. This routine was coded by O.I. Dahl to reformat WRING output for input to DST-EXAM.

24. O.I. Dahl, G. Kalbfleisch, and A. Rittenberg, DST-EXAM-2 and PI-63, K63 Data Analysis systems, Alvarez Group Programming Note P-54.

25. C.T. Draper, W.E. Humphrey, and R.R. Ross, Confidence Level for Events Adjusted by the Method of Least Squares with Constraints, Alvarez Group Memo No. 347, October 1961.

26. R.R. Ross, Elastic and Charge-Exchange Scattering of K^- Mesons in Hydrogen (Ph.D. Thesis), UCRL 9749, (Appendix A), June 1961.

27. This is due to Orin I. Dahl and is described in Ref. 24.

28. The π^- pathlength at each momentum was measured by P. Dauber (Private Communication)

29. A.H. Rosenfeld, A. Barbaro-Galtieri, W.J. Podolsky, L.R. Price, P. Soding, C.G. Wohl, M. Roos, and W. Willis, Rev. of Mod. Phys. 39, 1 (1967).

30. H. Cramer, Mathematical Methods of Statistics (Princeton University Press, 1946).

31. J. Orear, Notes on Statistics for Physicists, Lawrence Radiation Laboratory Report UCRL 8417, August 1958.

32. J.H. Friedman, MURTLEBERT, A general Program for Fitting Data by the Method of Maximum Likelihood, Alvarez Programming Memo P-156, November 1966.

33. L.M. Hardy, Analysis of Strange Particle Resonant States from π^-p Interactions (Ph.D. Thesis), UCRL 16788, July 1966.

34. R.I. Hess, Production of $K\bar{K}$ Pairs in $\pi^- p$ Interactions, (Ph.D Thesis), UCRL 16832, June 1966.

35. In general the beam K^- mesons suffer energy loss as they travel through the liquid hydrogen so that one beam track contributes pathlength to an interval of momenta rather than to one unique momentum. However, at the incident beam momenta in this experiment, the K^- mesons are minimum ionizing in hydrogen, and the momentum loss from one end of the bubble chamber to the other is small enough to be neglected.

36. P.L. Bastien and J.P. Berge, Phys. Rev. Letters 10, 188 (1963).

37. S.G. Wojcicki, Phys. Rev. 135, B 484 (1964).

38. L.T. Smith, Resonance Production in $K^- p$ Interactions at 1.80 to 1.95 GeV/c, (Ph.D. Thesis), Unpublished.

39. R. Barloutand, A. Leveque, C. Louedec, J. Meyer, P. Schlein, A. Verglas, J. Bradier, M. Demoulin, J. Goldberg, B.P. Gregory, P. Krejbich, C. Pelletier, M. Ville, E.S. Gelsema, J. Hoogland, J.C. Kluyver, and A.G. Tenner, Phys. Letters 12, 352 (1964).

40. Birmingham, Glasgow, London (I.C.), Oxford, Rutherford Collaboration, Proceedings of 1967 International Conference on High Energy Physics, Heidelberg, Germany.

41. F.L. Schweingruber, K^* Production in High Energy $K^- p$ Interactions (Ph.D. Thesis), June 1967, (Unpublished).

42. For a good summary see Gerson Goldhaber, Rapporteur Talk, "Boson Resonances," in Proceedings of the XIII International Conference on High Energy Physics, Berkeley, September 1966.

43. For a good summary see Robert D. Tripp, "Baryon Resonances," Estratto da Rendiconti della Scuola Internazionale di Fisica E. Fermi XXXIII Corso.

44. M. Alston, L.W. Alvarez, P.E. Eberhard, M. Good, W. Graziano, H. Ticho, S. Wojcicki, Phys. Rev. Letters 6, 300 (1961).

45. J.T. Donohue, "Calculations on Production Reactions using the Absorptive Peripheral Model", (Ph.D. Thesis), Unpublished (1967)

46. J.H. Friedman and R.R. Ross, Phys. Rev. Letters 16, 485 (1966)

47. A.B. Kaydalov and B.M. Karnakov, "Regge Poles and the Production of Resonances in πN and $\bar{K}N$ Collisions," Institute of Theoretical and Experimental Physics, State Committee on the Use of Atomic Energy of the U.S.S.R., Report No. 520, Moscow 1967.

48. S. Wojcicki, M. Alston, and G. Kalbfleisch, Phys. Rev. 135, B 495 (1964).

49. See Section XI for a complete study of $K^{*}N^{*}$ combined decay correlations.

50. P. Dauber, "A Study of Selected Final States in $K^{-}p$ Scattering at GeV/c." (Ph.D. Thesis), Unpublished (1966).

51. A. Bialas, A. Gula, and M. Muryn, Phys. Letters 24B, 428 (1967).

52. J.T. Donohue, "Joint Decay Correlations in Double Resonance Production," CERN Report TH. 749 (1967).

53. I. Bender, V. Linke, and H.J. Rothe, "Study of Angular Decay Correlations for the Process $\pi + N \rightarrow \quad + N^{*}$ in the Regge Pole Model I", Institute fur Hochenergiephysik der Universitate Heidelberg Internal Report (1967).

54. G. Goldhaber, "Proceedings of Athes Conference on Resonant Particles," p. 80 (1963).

55. M. Ferro-Luzzi, R. Gorge, Y. Goldschmidt-Clermont, V.P. Henri, B. Jongljans, D.W.G. Leith, G.R. Lynch, F. Muller, and J.M. Perreau, Nuovo Cimento 39, 417 (1965).

56. F. Grard, J. Debaisieu, J. Henghebaert, L. Pape, and R. Windmolders, paper presented at the 1964 International Conference on High Energy Physics, Dubna, August 5-15, 1964.

57. G. Goldhaber, J. Brown, I. Butterworth, S. Goldhaber, A. Hirata, J.A. Kadyk, B. Shen, G.H. Trilling, Phys. Letters 18, 76 (1965).

58. S.M. Berman and R.J. Oaks, Phys. Rev. 135, B 1034 (1964).

59. K. Gottfried and J.D. Jackson, Nuovo Cimento 33, 309 (1964).

60. H. Pilkuhn and B.E.Y. Svensson, Nuovo Cimento 38, 518 (1965).

61. J.D. Jackson and J. Donohue (Private communication).

62. Aachen-Berlin-CERN Collaboration, Phys. Letters 22, 533 (1966).

63. Brussels-CERN Collaboration, CERN Preprint 66-18 (1966).

64. S. Goldhaber, J.L. Brown, I.Butterworth, G. Goldhaber, A.A. Hirata, J.A. Kadyk, and G.H. Trilling, Phys. Rev. Lett. 15, 737(1965).

65. This does not rule out possible association of these enhancements with the ρ -meson. The $\pi^{o}\pi^{-}$ mass spectrum in the region of the ρ mass has a falling background and the ρ has a large width. Thus a few percent ρ in the final state would not produce an observable peak in the $\pi^{o}\pi^{-}$ mass distribution.

66. The world averaged value (Ref. 29) for the width of the $K^{*}_{1/2}(1400)$ is $\sim$ 90 MeV.

67. B. C. Shen, I. Butterworth, C. Fu, G. Goldhaber, S. Goldhaber, S. Hagopian, and G. Trilling, "K^+p Interactions at 4.6 GeV/c. and Evidence for a $K^*(1320)$ Resonance", Paper 7b.16, XIIIth Int. Conf. on High Energy Physics (1966).

68. R. Armenteros, D. N. Edwards, T. Jacobsen, L. Montanet, A. Shapira, J. Vandermeulen, Ch. D'Andlau, A. Astier, P. Baillon, J. Cohen-Ganouna, C. Ghesquiere, and P. Rivet, Phys. Letters 9, 207 (1964).

69. R. T. Deck, Phys. Rev. Lett. 13, 169 (1964).

70. U. Maor and T. O'Halloran, Jr., Phys. Letters 15, 281 (1965).

71. This expression is correct only to first order, however, the inaccuracy introduced by neglecting terms of higher order is negligible here.

72. The elastic scattering amplitudes for the reaction $K^* N^* \rightarrow K^* N^*$ are unknown and the assumptions discussed above are made concerning them. If these assumptions are not made then these elastic scattering amplitudes must be parameterized, and the parameters fited to the data.

Tables

Table 1

π^- pathlength, ratio of π^- to K^- pathlength and ratio of π^- to K^- induced events in the two pronged plus vee topology.

Momentum GeV/c.	π^- pathlength[28] ev./mb.	π^-/K^- total	π^-/K^- (*) 2 pronged + V
2.1	173±70	.03±.01	.003
2.45	150±77	.07±.04	.006
2.58	590±165	.15±.04	.014
2.61	1040±260	.15±.04	.014
2.7	1180±260	.34±08	.031

(*) The numbers in this column were calculated using the central values of column three, and the ratio of cross sections for $\pi^- P \longrightarrow$ 2 pronged + V[33],[34] in this energy range.

Table 2

Optimum short length cutoff parameter "l" for inner fiducial volume boundry, for the three and four particle final states at each momentum, and the correction it produces to the total cross section.

Momentum GeV/c.	3 particle final state centimeters	Fractional correction	4 particle final state centimeters	Fractional correction
2.1	.3	.041	.4	.059
2.45	.2	.042	.3	.058
2.58	.4	.042	.2	.060
2.61	.7	.060	.5	.047
2.7	.3	.040	.5	.062

Table 3

Distribution of ambiguities amoung the $\bar{K}^0$ hypothesises for the one constraint events

A. $K^- p \to p\bar{K}^0 \pi^0 \pi^-$ (5123 events total)

Reaction	Number of ambiguities with $K^- p \to p\bar{K}^0 \pi^0 \pi^-$
$K^- p \to p\bar{K}^0 \pi^-$	16
$K^- p \to n\bar{K}^0 \pi^+ \pi^-$	217
$K^- p \to p\bar{K}^0 \pi^-$ + missing mass	54
$K^- p \to \bar{K}^0 \pi^+ \pi^-$ + missing mass	179

B. $K^- p \to n K^0 \pi^+ \pi^-$ (4571 events total)

Reaction	Number of ambiguities with $K^- p \to n\bar{K}^0 \pi^+ \pi^-$
$K^- p \to p\bar{K}^0 \pi^0 \pi^-$	13
$K^- p \to p\bar{K}^0 \pi^+ \pi^-$	214
$K^- p \to p\bar{K}^0 \pi^-$ + missing mass	298
$K^- p \to \bar{K}^0 \pi^+ \pi^-$ + missing mass	22

Table 4

A. The number of three pronged events found on the original scan, the number estimated to be in the sample and the pathlength, at each momentum.

Momentum GeV/c.	Scanned three prongs	Estimated three prongs	Pathlength events/microbarn
2.1	6966	7129±157	6.656±.022
2.45	1810	1852±54	2.020±.007
2.58	3367	3445±86	3.960±.013
2.61	5786	5920±130	6.881±.021
2.7	2884	2951±77	3.548±.012

B. Values of the various constants entering into pathlength calculation[29] (see text).

$$L = N_\gamma \frac{P_{K^-} c \gamma_{K^-}}{m_{K^-} B_\gamma}$$

$P_{K^-} = 2.097 \pm .038,\ 2.45 \pm .04,\ 2.581 \pm .024$
$2.610 \pm .034,\ 2.70 \pm .035$ GeV/c.

$c = 2.997925 \times 10^{10}$ cm/sec., $\gamma_{K^-} = (1.235 \pm .006) \times 10^{-8}$ sec.

$m_{K^-} = .49382 \pm .00011$ GeV., $B_\gamma = .059 \pm .001$

Table 5

The total estimated number of two pronged plus vee events and those resulting from K^- interactions at each momentum.

Momentum GeV/c.	Total two pronged+V	K^- two pronged+V
2.1	29603	29514±974
2.45	9034	8980±296
2.58	17084	16845±556
2.61	30322	29897±987
2.7	15868	15376±507

Table 6

Total cross sections for the reactions $K^- p \to p\bar{K}^0 \pi^-$, $K^- p \to p\bar{K}^0 \pi^0 \pi^-$ and $K^- p \to n\bar{K}^0 \pi^+ \pi^-$ for each momentum as measured in this experiment. These values include corrections applied to the observed numbers of events for unobserved neutral decay modes of the K^0 (2.886).[29]

Momentum GeV/c.	$K^- p \to p\bar{K}^0 \pi^-$ millibarns	$K^- p \to p\bar{K}^0 \pi^0 \pi^-$ millibarns	$K^- p \to n\bar{K}^0 \pi^+ \pi^-$ millibarns
2.1	1.96±.11	.725±.043	.663±.040
2.45	1.74±.11	1.02±.068	.810±.057
2.58	1.50±.085	1.11±.066	.932±.056
2.61	1.52±.084	1.14±.065	1.10±.063
2.7	1.42±.079	1.22±.069	1.05±.061

Table 7a

Maximum likelihood solutions for the reaction $K^- p \to p\bar{K}^0 \pi^-$ employing the model of non-interfering resonance production and Lorentz invariant plase space. Decay angular correlations were included for the $K^{*-}_{1/2}(892)$ only.

Momentum GeV/c.	Fraction $Y^*_1(1660)$	Fraction $Y^*_1(1765)$	Fraction $N^*_{3/2}(1238)$	Fraction $N^*(1520)$	Fraction $N^*(1688)$	Fraction $K^*_{1/2}(892)$	Fraction $K^*(1280)$	Fraction $K^*_{1/2}(1400)$
2.1	.025±.010	.033±.014	.040±.015	.011±.015	.043±.013	.638±.017	.00±.005	------
2.45	.011±.013	.069±.020	.066±.020	.048±.022	.026±.015	.597±.024	.027±.014	.00±.006
2.60	.008±.006	.065±.011	.061±.010	.028±.010	.065±.011	.569±.011	.014±.007	.016±.005
2.7	.019±.011	.073±.020	.047±.015	.014±.018	.042±.017	.588±.022	.031±.013	.034±.011

Momentum GeV/c.	$K^*_{1/2}(892)$ Decay Angular Correlations		
	C_1	C_2	C_3
2.1	-.098±.032	-.327±.044	-.145±.040
2.45	-.145±.044	-.420±.065	-.197±.059
2.60	-.149±.023	-.478±.034	-.210±.031
2.7	-.179±.041	-.471±.063	-.179±.054

Table 7b

Total cross sections in microbarns for production of the principal resonances in the reaction $K^- p \to p\bar{K}^0 \pi^-$ as inferred from the total cross section for the final state (table 6) and the maximum likelihood solutions (table 7a).

Resonance	Beam Momenta (GeV/c.)			
	2.1	2.45	2.60	2.7
$Y_1^*(1660)$	49±20	19±23	12±9	27±16
$Y_1^*(1765)$	65±27	120±35	98±17	114±28
$N_{3/2}^*(1238)$	78±29	115±35	92±15	67±21
$N^*(1520)$	22±29	84±38	42±05	20±26
$N^*(1688)$	84±25	45±26	98±17	60±24
$K_{1/2}^*(892)$	1251±80	1040±80	859±40	835±55
$K^*(1280)$	0±10	47±24	21±11	44±18
$K_{1/2}^*(1400)$	-----	0±10	24±8	48±16

Table 8

Maximum likelihood solution values for the mass and width of the $K^*_{1/2}(892)$ and $N^*(1688)$. The errors are statistical only.

Momentum GeV/c.	Mass K^* GeV.	Width K^* GeV.	Mass N^* GeV.	Width N^* GeV.
2.1	.894±.001	.053±.003	------	------
2.45	.892±.002	.049±.004	1.676±.028	.050±.035
2.60	.892±.001	.046±.002	1.671±.009	.087±.021
2.7	.892±.001	.049±.003	1.667±.018	.066±.028

Table 9

Maximum likelihood solution values and differential cross section for the reaction $K^- p \rightarrow K^{*-}_{1/2}(892) p$ for the various production angle intervals at 2.1 GeV/c.

Interval	Number events	Fraction $K^{*-}_{1/2}(892)$	$\frac{d\sigma}{d\Omega}[K^{*-}_{1/2}(892)]$ mb/steradian	$K^{*-}_{1/2}(892)$ Decay Angular Correlation Coefficients		
				C_1	C_2	C_3
.97-1.0	190	.635±.057	.45±.05	.26±.12	-.13±.14	-.34±.13
.94-.97	163	.870±.051	.52±.05	.07±.10	-.31.14	-.01±.12
.90-.94	216	.821±.044	.49±.04	.09±.08	-.16±.10	-.13±.11
.86-.90	206	.819±.045	.46±.04	.08±.08	-.43±.11	-.09±.11
.80-.86	218	.768±.046	.31±.03	.01±.08	-.54±.11	-.24±.10
.70-.80	294	.862±.040	.28±.02	- .07±.06	-.50±.09	-.09±.09
.50-.70	351	.816±.056	.16±.01	- .28±.06	-.55±.09	.03±.07
.20-.50	287	.621±.052	.066±.007	- .16±.09	-.45±.15	.09±.12
-.20-.20	362	.460±.040	.048±.005	- .35±.07	-.06±.13	.06±.12
-1.0--.2	478	.300±.030	.022±.002	-.22±.10	-.13±.15	-.34±.13

Table 10

Maximum likelihood solution values and differential cross section for the reaction $K^- p \to K^{*-}_{1/2}(892) p$ for the various production angle intervals, 2.45, 2.60, and 2.70 GeV/c.

Interval	Number events	Fraction $K^{*-}_{1/2}(892)$	$\frac{d\sigma}{d\Omega}[K^{*-}_{1/2}(892)]$ mb/steradian	$K^{*-}_{1/2}(892)$ Decay Angular Correlation Coefficients		
				C_1	C_2	C_3
.99-1.0	141	.809±.057	.53±.06	.47±.10	-.22±.11	-.22±.13
.98-.99	173	.757±.052	.62±.06	.36±.09	-.17±.10	-.04±.13
.97-.98	173	.692±.050	.56±.06	.50±.09	-.19±.10	-.26±.12
.96-.97	134	.755±.051	.48±.05	.16±.10	-.43±.13	-.20±.13
.95-.96	147	.747±.055	.51±.06	.16±.11	-.61±.14	-.19±.14
.94-.95	136	.826±.045	.54±.05	.08±.09	-.53±.11	-.25±.10
.925-.94	175	.778±.045	.43±.04	.10±.08	-.39±.11	-.33±.12
.90-.925	329	.734±.033	.46±.03	.00±.07	-.57±.09	-.12±.08
.88-.90	213	.714±.041	.36±.03	-.11±.08	-.69±.10	-.01±.09
.86-.88	185	.795±.038	.35±.03	-.07±.08	-.62±.10	-.17±.09

Table 10 (cont.)

Interval	Number events	Fraction $K^{*-}_{1/2}(892)$	$\frac{d\sigma}{d\Omega}[K^{*-}_{1/2}(892)]$ mb/steradian	$K^{*-}_{1/2}(892)$ Decay Angular Correlation Coefficients		
				C_1	C_2	C_3
.84-.86	203	.795±.039	.38±.03	- .10±.08	-.52±.10	-.21±.09
.82-.84	160	.686±.052	.26±.03	- .07±.10	-.70±.14	-.01±.13
.78-.82	249	.721±.038	.21±.02	- .20±.07	-.78±.09	-.17±.09
.74-.78	200	.683±.060	.16±.02	- .22±.10	-.52±.15	.07±.15
.70-.74	183	.711±.045	.15±.01	- .01±.09	-.47±.12	-.15±.11
.65-.70	201	.623±.048	.12±.01	- .06±.10	-.47±.13	.07±.12
.60-.65	167	.678±.062	.11±.01	-.19±.10	-.69±.16	.05±.13
.40-.60	444	.542±.029	.058±.004	- .32±.05	-.48±.09	-.04±.08
.00-.40	663	.402±.028	.032±.003	-.36±.07	-.63±.11	.03±.07
-1.0-.0	838	.151±.030	.0065±.001	- .43±.10	-.50±.12	-.17±.11

Table 11

Maximum likelihood solutions for the $K^{*-}_{1/2}(892)$ decay angular correlation coefficients for all production angles.

Momentum GeV/c.	$K^{*-}_{1/2}(892)$ Decay Correlation Coefficients		
	C_1	C_2	C_3
2.1	$-.101 \pm .030$	$-.343 \pm .044$	$-.101 \pm .039$
2.45, 2.60, 2.7	$-.095 \pm .019$	$-.539 \pm .026$	$-.122 \pm .024$

Table 12a

Maximun likelihood solutions for the reaction $K^- p \rightarrow p\bar{K}^0 \pi^0 \pi^-$ employing the model of non-interfering resonance production and Lorentz invariant plase space.

Momentum GeV/c.	Fraction $K^{*-} N^{*+}$	Fraction $K^{*0} N^{*0}$	Fraction $N^{*+} K^0 \pi^-$	Fraction $\bar{K}^{*0} p\pi^-$	Fraction $K^{*-} p\pi^0$	Fraction $K^*(1280)$	Fraction $K^{*-}_{1/2}(1400)$
2.1	.397±.048	.089±.029	.073±.041	.034±.033	.107±.047	.088±.023	------
2.45	.440±.049	.026±.027	.068±.047	.083±.037	.023±.044	.010±.027	.024±.024
2.60	.308±.021	.051±.013	.067±.020	.121±.019	.131±.023	.050±.012	.042±.011
2.7	.242±.032	.039±.021	.086±.033	.155±.032	.165±.033	.027±.019	.046±.020

Table 12b

Total cross sections in microbarns for production of the principal resonance processes in the reaction $K^- p \to p\bar{K}^0 \pi^0 \pi^-$ as inferred from the total cross section for the final state (table 6) and the maximum likelihood solutions (table 12a).

Resonance Process	Beam Momentum (GeV/c.)			
	2.1	2.45	2.60	2.7
$K^{*-}_{1/2}(892)N^{*+}_{3/2}(1238)$	288±36	449±51	347±34	295±42
$\bar{K}^{*0}_{1/2}(892)N^{*0}_{3/2}(1238)$	65±21	27±28	57±15	48±26
$N^{*+}_{3/2}(1238)\ K^0\pi^-$	53±30	69±48	75±23	105±40
$K^{*0}_{1/2}(892)\ p\pi^-$	25±24	85±38	136±21	189±39
$K^{*-}_{1/2}(892)\ p\pi^0$	78±34	23±45	147±24	201±40
$K^*(1280)\ p$	64±17	10±28	56±14	33±23
$K^{*-}_{1/2}(1400)\ p$	-----	24±24	47±12	56±24

Table 13

The maximum likelihood solution values for the mass and width of the 1280 and 1400 MeV. enhancements in the $K^0\pi^0\pi^-$ mass spectra for 2.60 and 2.70 GeV/c. combined. Errors are statistical only.

Enhancement	Kππ(1280)	Kππ(1400)
Mass	1281±7 MeV.	1411±7 MeV.
Width	51±22 MeV.	43±13 MeV.

Table 14a

Maximum likelihood solutions for the reaction $K^- p \to n\bar{K}^0 \pi^+ \pi^-$ employing the model of non-interfering resonance production and Lorentz invariant phase space.

Momentum GeV/c.	Fraction $Y_0^{*0} \pi^+ \pi^-$	Fraction $K^{*-} N^{*+}$	Fraction $N^{*+} K^0 \pi^-$	Fraction $N^{*-} K^0 \pi^+$	Fraction $K^{*-} n\pi^+$
2.1	.083±.016	.151±.044	.095±.040	.348±.035	.220±.047
2.45	.127±.029	.211±.055	.008±.050	.246±.047	.217±.060
2.60	.066±.011	.114±.025	.066±.024	.254±.023	.315±.030
2.7	.062±.028	.118±.062	.100±.067	.230±.059	.289±.078

Table 14b

Total cross sections in microbarns for production of the principal resonance processes in the reaction $K^- p \to n\bar{K}^0\pi^+\pi^-$ as inferred from the total cross sections for the final state (table 6) and the maximum likelihood solutions (table 14a).

Resonance Process	Beam Momentum (GeV/c.)			
	2.1	2.45	2.60	2.7
$Y_0^*(1520)\ \pi^+\pi^-$	55±11	103±23	67±11	65±29
$K_{1/2}^{*-}(892)N_{3/2}^{*+}(1238)$	100±29	171±45	116±24	124±65
$N_{3/2}^{*+}(1238)\ K^0\pi^-$	63±27	6±41	67±24	105±70
$N_{3/2}^{*-}(1238)\ K^0\pi^+$	231±30	199±38	258±25	242±62
$K_{1/2}^{*-}(892)\ n\pi^+$	146±31	176±49	320±36	303±82

Table 15

Number of $K^*_{1/2}(892)N^*_{3/2}(1238)$ events in the $pK^0\pi^0\pi^-$ and $nK^0\pi^+\pi^-$ final states at each momentum.

Momentum GeV/c.	Final state	Number events	Fraction K^* N^*	Number K^* N^*
2.1	$pK^0\pi^0\pi^-$	1217	.486±.056	592±68
2.1	$nK^0\pi^+\pi^-$	1070	.151±.044	162±47
2.45	$pK^0\pi^0\pi^-$	527	.466±.056	246±30
2.45	$nK^0\pi^+\pi^-$	435	.211±.055	92±24
2.60	$pK^0\pi^0\pi^-$	2699	.359±.025	970±68
2.60	$nK^0\pi^+\pi^-$	2363	.114±.024	270±57
2.70	$pK^0\pi^0\pi^-$	1017	.281±.038	286±39
2.70	$nK^0\pi^+\pi^-$	868	.118±.062	112±54

Table 16

Total cross section for the reaction $K^- p \rightarrow K^*_{1/2}(892) N^*_{3/2}(1238)$ for each beam momentum as measured in this experiment. Corrections have been made for unobserved decay modes and charge states of the $K^*_{1/2}(892)$ and $N^*_{3/2}(1238)$.

Momentum GeV/c.	Total cross section $K^- p \rightarrow K^*_{1/2}(892) N^*_{3/2}(1238)$ Millibarns
2.1	1.19±.15
2.45	1.71±.23
2.60	1.41±.12
2.70	1.26±.20

Table 17

The orthoginal functions used to expand the joint decay angular distribution of the $K^*_{1/2}(892)$ $N^*_{3/2}(1238)$

$$I(\hat{e}\,\hat{p}) = 1 + \sum_{i=1}^{19} C_i Z_i(\hat{e}\,\hat{p})$$

where $\hat{e}$ is a unit vector along the direction of the $\bar{K}^0$ in the rest frame of the $\bar{K}^*_{1/2}(892)$ and $\hat{p}$ is a unit vector in the direction of the nucleon in the rest frame of the $N^*_{3/2}(1238)$. The coordinate system used in each rest frame is the "t-channel" coordinate system described in the text.

$$Z_1 = \sqrt{5}/2\,(3e_3^2-1) \qquad Z_2 = \sqrt{30}/4\,(e_1^2-e_2^2)$$

$$Z_3 = -\sqrt{15/2}\,e_1 e_3 \qquad Z_4 = \sqrt{5}/2\,(3p_3^2-1)$$

$$Z_5 = \sqrt{30}/4\,(p_1^2-p_2^2) \qquad Z_6 = -\sqrt{15/2}\,p_1 p_3$$

$$Z_7 = 5/4\,(3e_3^2-1)(3p_3^2-1)$$

$$Z_8 = \sqrt{150}/8\,(3e_3^2-1)(p_1^2-p_2^2)$$

$$Z_9 = -\sqrt{75/8}\,(3e_3^2-1)\,p_1 p_3$$

$$Z_{10} = \sqrt{150}/8\,(e_1^2-e_2^2)(3p_3^2-1)$$

$$Z_{11} = 30/16\,(e_1^2-e_2^2)(p_1^2-p_2^2)$$

$$Z_{12} = -15/4\,(e_1^2-e_2^2)\,p_1 p_3 \qquad Z_{13} = -\sqrt{75/8}\,e_1 e_3 (3p_3^2-1)$$

$$Z_{14} = -15/4\,(p_1^2-p_2^2)\,e_1 e_3 \qquad Z_{15} = 15/2\,e_1 e_3 p_1 p_3$$

$$Z_{16} = 15/2\,e_2 e_3 p_2 p_3 \qquad Z_{17} = -15/2\,e_2 e_3 p_1 p_2$$

$$Z_{18} = -15/2\,e_1 e_2 p_2 p_3 \qquad Z_{19} = 15/2\,e_1 e_2 p_1 p_2$$

Table 18

Decay angular distribution parameters for the reaction $K^- p \rightarrow \bar{K}^*_{1/2}(892)\, N^*_{3/2}(1238)$ averaged over all production angles at each momentum.

Coefficient	Beam Momentum (GeV/c.)			
	2.1	2.45	2.60	2.70
C_1	.25±.07	.24±.08	.32±.05	.29±.10
C_2	.37±.09	.31±.11	-.05±.06	.06±.14
C_3	-.11±.10	-.28±.12	-.22±.07	-.08±.14
C_4	.30±.07	.24±.08	.22±.05	.19±.10
C_5	.13±.09	-.01±.10	-.15±.06	-.02±.13
C_6	.12±.10	-.04±.11	-.02±.07	-.16±.15
C_7	.21±.08	.11±.09	.18±.05	.23±.10
C_{11}	-.01±.16	.23±.19	.23±.11	.25±.24
C_{19}	-.20±.17	.20±.18	-.41±.12	-.61±.24

Table 19

Decay angular distribution parameters for the reaction $K^- p \rightarrow \bar{K}^*_{1/2}(892)\, N^*_{3/2}(1238)$ at 2.1 GeV/c. averaged over several production cosine intervals.

Coefficient	Production Cosine Interval		
	1.0-.7	.7-0.0	0.0--1.0
C_1	.30±.13	.21±.10	.26±.12
C_4	.50±.14	.17±.10	.27±.11
C_7	.22±.14	.24±.11	.17±.12

Table 20

Decay angular distribution parameters for the reaction $K^- p \rightarrow \bar{K}^*_{1/2}(892)\, N^*_{3/2}(1238)$ for 2.60 and 2.70 GeV/c. averaged over several production cosine intervals.

Coefficient	Production Cosine Interval				
	1.0-.96	.96-.9	.9-.8	.8-.6	.6-0.0
c_1	.57±.09	.31±.08	.44±.10	.15±.09	.11±.12
c_2	-.20±.09	.07±.10	-.11±.12	.15±.13	-.02±.16
c_3	.07±.10	.04±.12	.03±.13	-.26±.14	-.63±.16
c_4	.30±.08	.21±.08	.24±.09	.20±.09	.26±.12
c_5	.01±.10	-.04±.10	-.10±.13	-.13±.12	-.28±.17
c_6	-.08±.11	.05±.12	-.16±.15	-.14±.13	-.21±.17
c_7	.29±.09	.10±.08	.30±.11	.04±.09	.19±.12
c_{11}	|—.26±.13—|		|—.34±.17—|		.01±.28
c_{19}	|—-.16±.13—|		|— -.90±.16—|		-.12±.28

Table 21

Differential cross section for the reaction $K^- p \to K^*_{1/2}(892) N^*_{3/2}(1238)$ averaged over several production cosine intervals.

Production cosine interval	Total weighted events	Fraction K^* N^*	mb/steradian
	A. 2.1 GeV/c.		
1.0-.7	362.0	.40±.08	.21±.04
.7-0.0	435.5	.51±.08	.14±.02
0.0--1.0	420.0	.33±.06	.06±.01
	B. 2.60 and 2.70 GeV/c.		
1.0-.96	346.2	.62±.05	1.22±.12
.96-.9	318.8	.65±.06	.78±.09
.9-.8	413.5	.44±.06	.41±.06
.8-.6	542.0	.45±.06	.27±.04
.6-0.0	1053.0	.19±.03	.07±.01

Figures

Figure 1

Sketch of the topology (two pronged plus vee) for the events studied in this report, as seen in the bubble chamber.

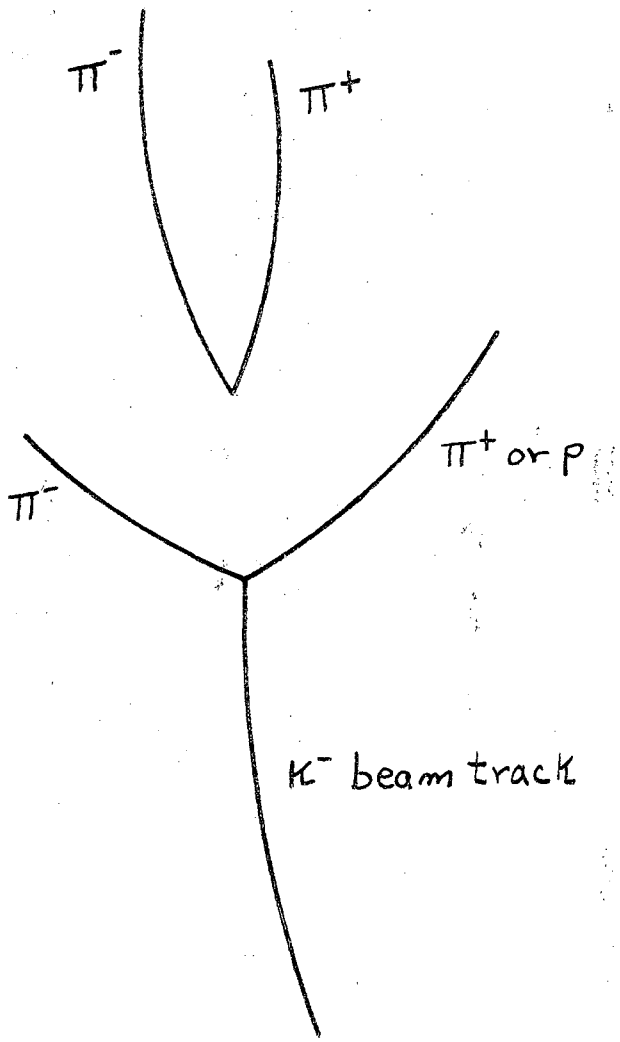

Figure 1

Figure 2

a) Dihedral angle between the plane, defined by the normal to the two pronged plane and the beam direction, and the plane, defined by the beam direction and the z-axis in the bubble chamber.

b) Dihedral angle between the plane, defined by the normal to the $\overline{K}^{o}$ decay plane and the beam direction, and the plane defined by the beam direction and the z-axis in the bubble chamber.

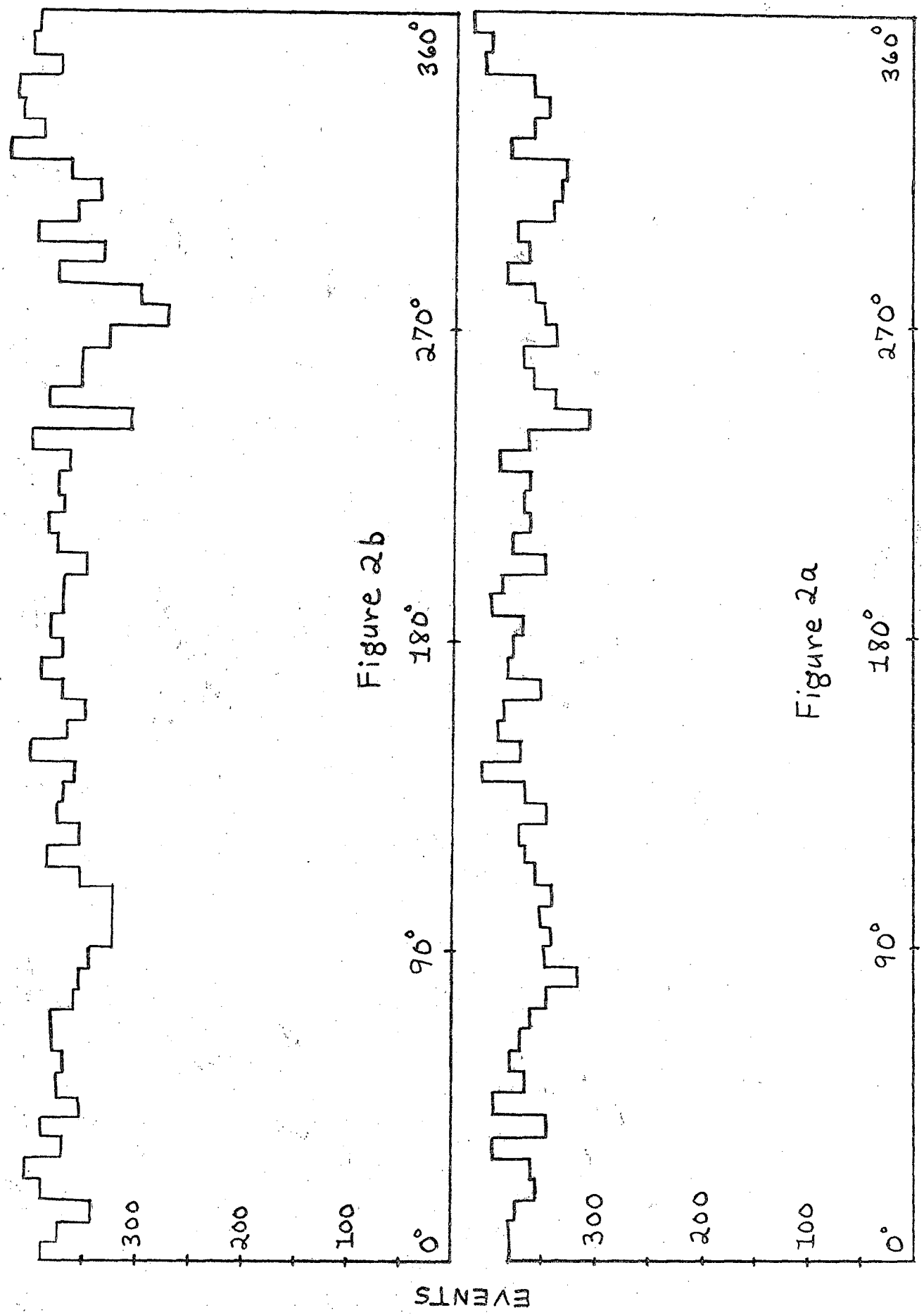
EVENTS
0°
100
200
300
90°
180°
270°
360°
Figure 2a
Figure 2b

Figure 3

Length of K_1^o for shorter length K_1^o events, to illustrate scanning bias against short length K_1^o events.

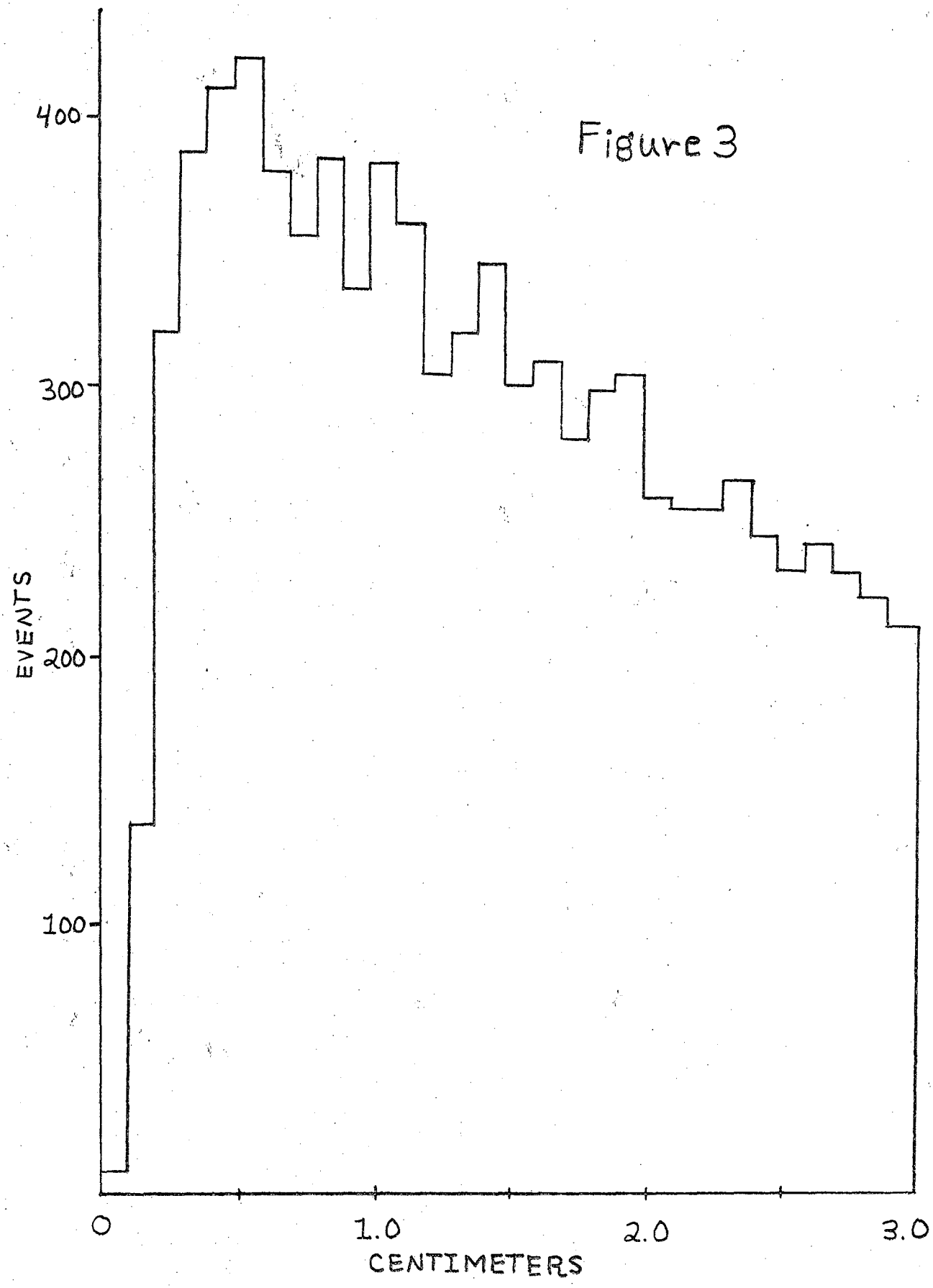

Figure 3

Figure 4

Measured mean life of K_1^o for various long length cutoffs on the length of the K_1^o, to test for scanning bias against long length K_1^o events. Short length cutoff used is described in the text. The point marked ∞ represents the results of the calculation for all events in the sample imposing the outer fiducial volume as the only long length cutoff. The errors are statistical only.

a) Three particle final state events

b) Four particle final state events

The solid band represents the world averaged value for the K_1^o mean life and error.[29]

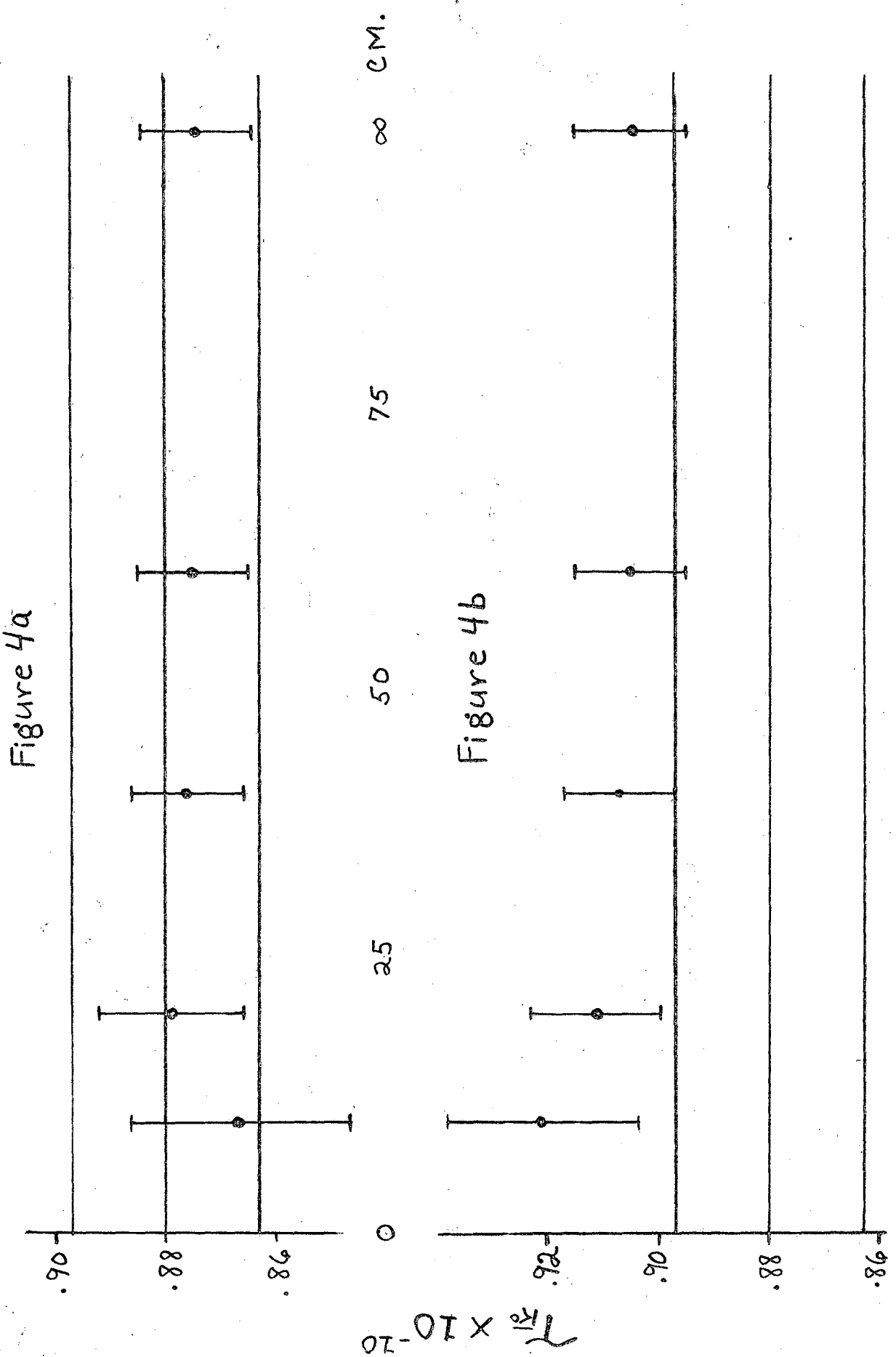
Figure 4a
Figure 4b
0
25
50
75
∞ cm.
.90
.88
.86
.92
.90
.88
.86
$\eta_{21} \times 10^{-20}$

Figure 5

Sketch of inner boundary of the fiducial volume surrounding each event. The parameter "ℓ" is loosely termed the short length cutoff in this report.

Figure 5

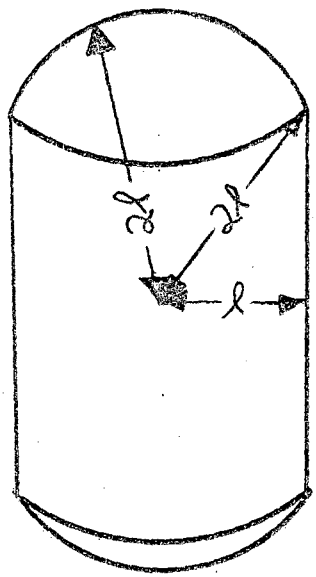

Figure 6

Total corrected number of events as a function of inner fiducial volume boundary parameter "ℓ". Arrows point to optimum values chosen. Outer fiducial volume boundary used is described in text.

a) 2.1 GeV/c. 3 particle final state

b) 2.1 GeV/c. 4 particle final state

c) 2.45 GeV/c. 3 particle final state

d) 2.45 GeV/c. 4 particle final state

e) 2.58 GeV/c. 3 particle final state

f) 2.58 GeV/c. 4 particle final state

g) 2.61 GeV/c. 3 particle final state

h) 2.61 GeV/c. 4 particle final state

i) 2.70 GeV/c. 3 particle final state

j) 2.70 GeV/c. 4 particle final state

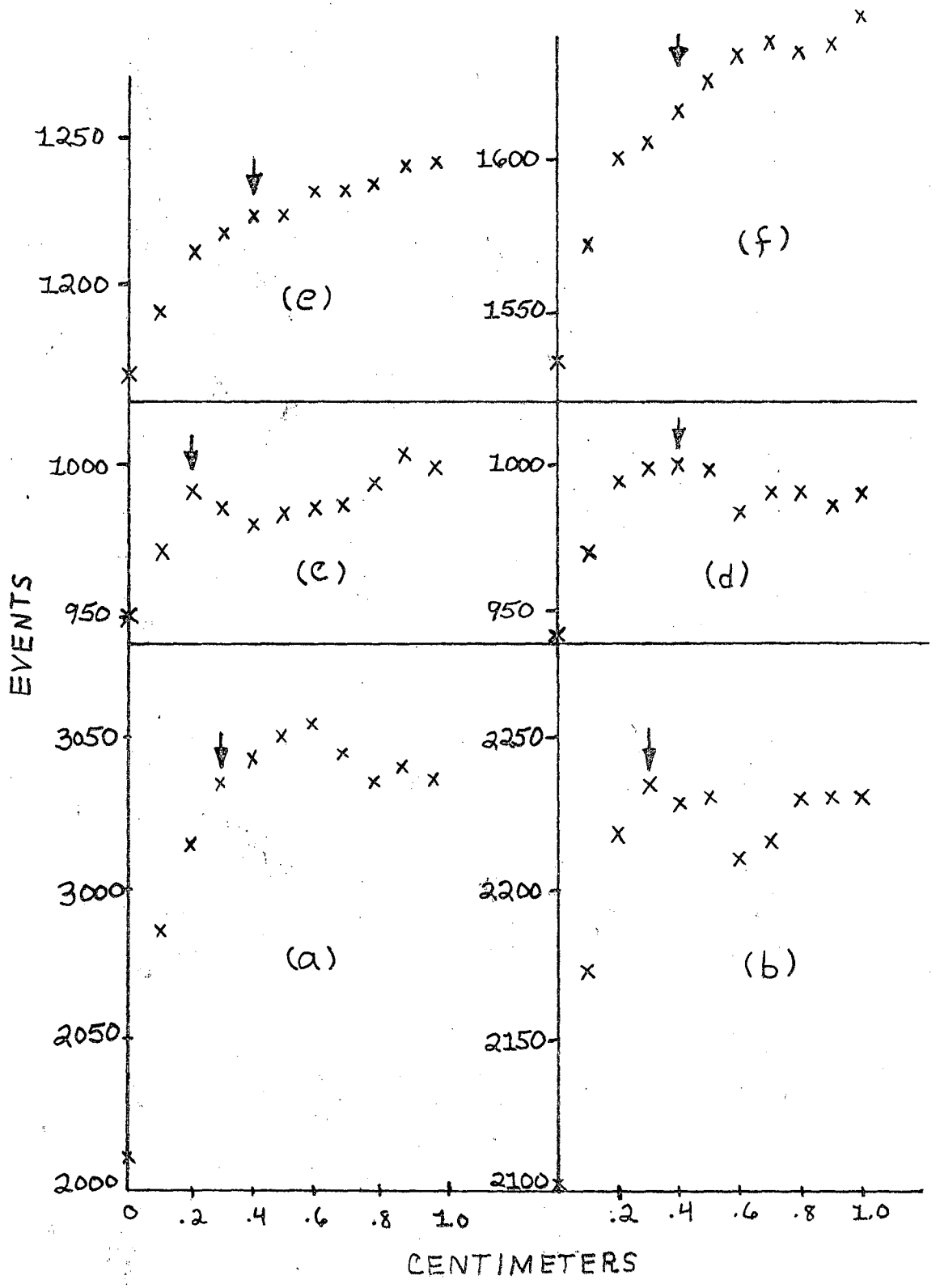
1250
1200
1600
1550
(e)
(f)
1000
950
1000
950
(c)
(d)
EVENTS
3050
3000
2250
2200
(a)
(b)
2050
2150
2000
2100
0
.2
.4
.6
.8
1.0
.2
.4
.6
.8
1.0
CENTIMETERS

Figure 6

Figure 6
(CONT.)

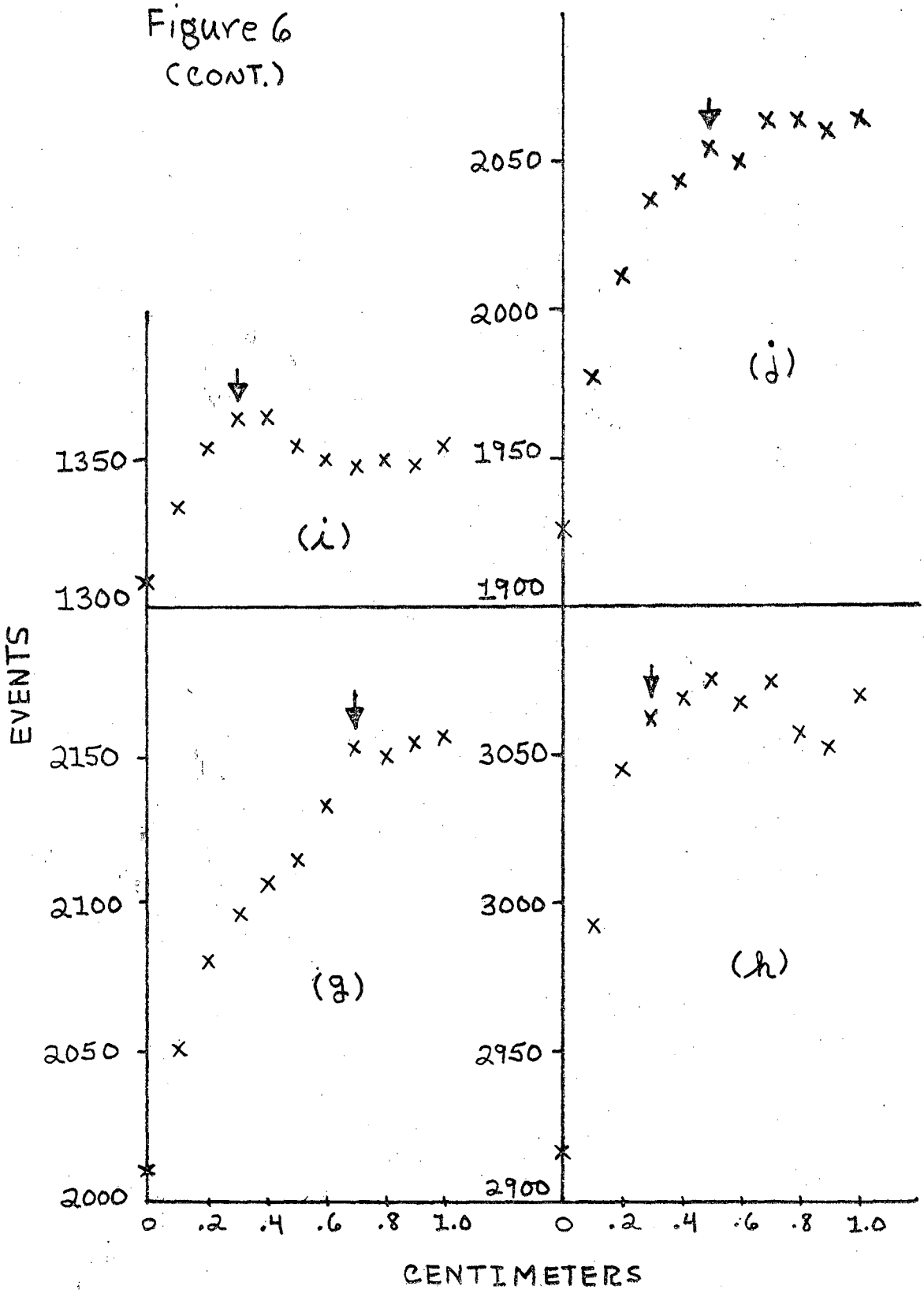

Figure 7

Decay angle of π^+ with respect to line of flight of K_1^o, in K_1^o rest frame.

a) 4 constraint events

b) 1 constraint events

Figure 7a

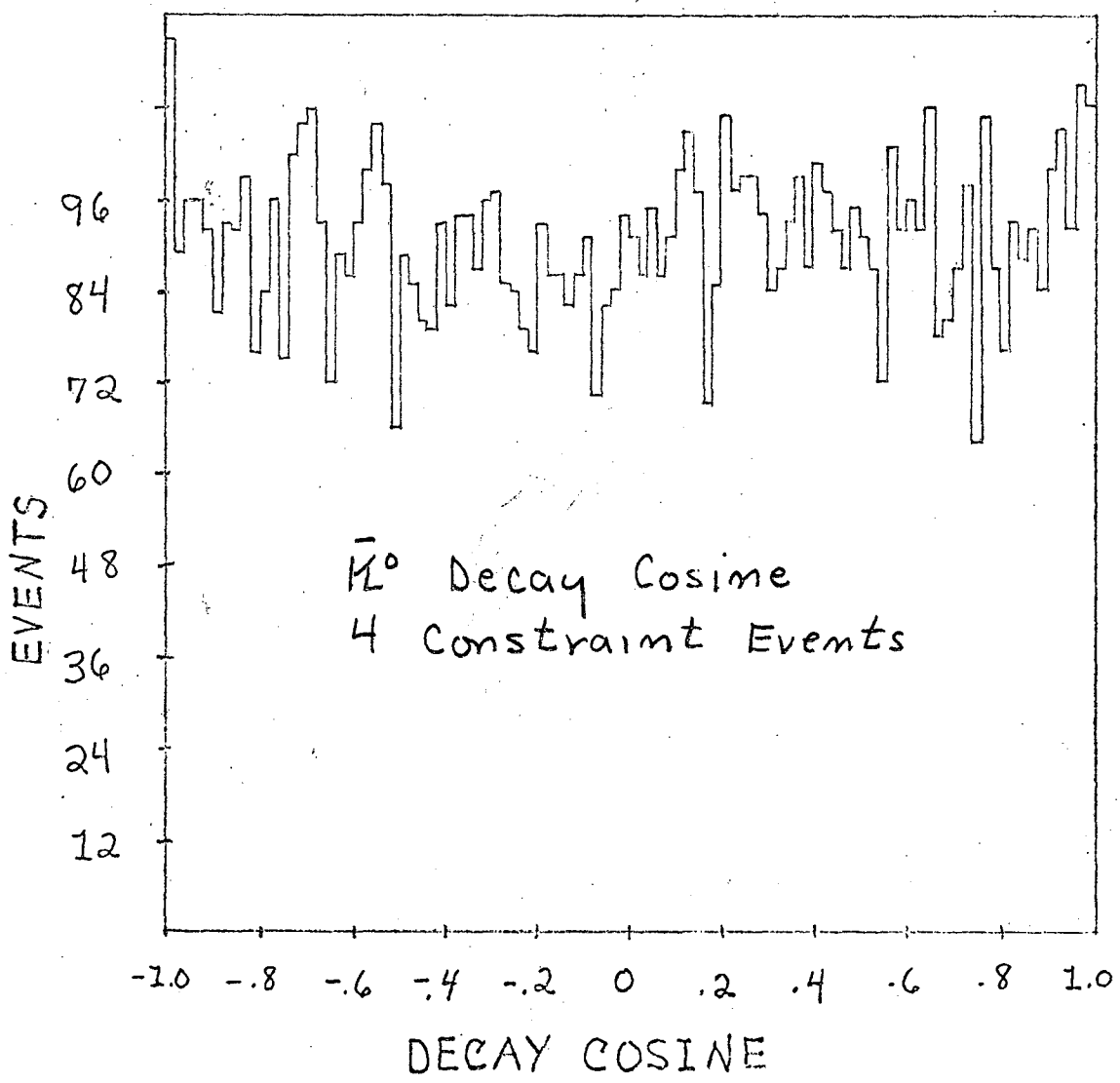
96
84
72
60
48
36
24
12
EVENTS
$\bar{K}^0$ Decay Cosine
4 Constraint Events
-1.0
-.8
-.6
-.4
-.2
0
.2
.4
.6
.8
1.0
DECAY COSINE

Figure 7b

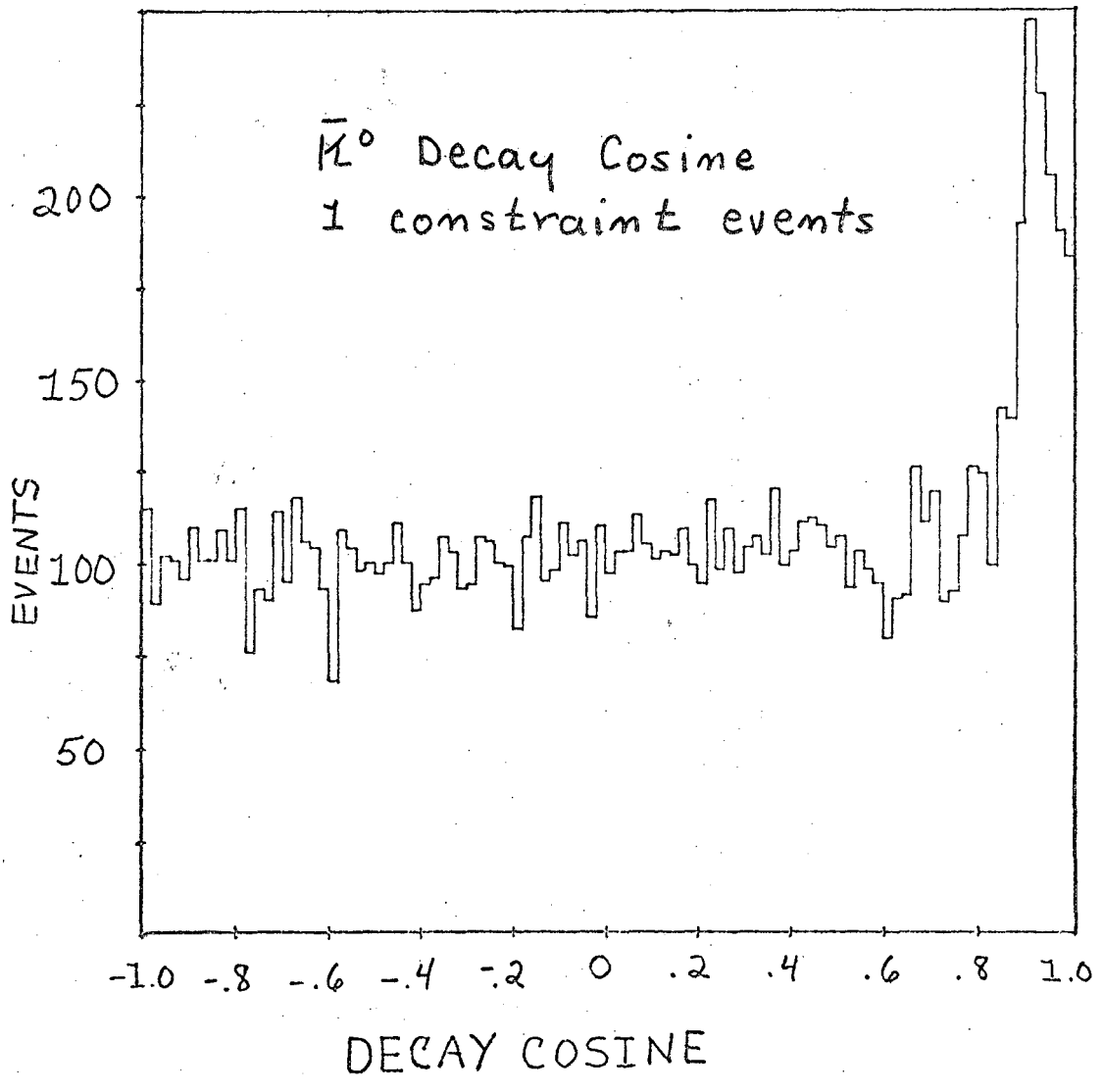
$\bar{K}^0$ Decay Cosine
1 constraint events
200
150
100
50
EVENTS
-1.0 -.8 -.6 -.4 -.2 0 .2 .4 .6 .8 1.0
DECAY COSINE

Figure 8

Decay angle of π^+ with respect to line of flight of K_1^o in K_1^o rest frame for 1 constraint events.

a) All events with highest confidence level for $\overline{K}^o$ hypothesis.

b) Same, except events with confidence level for Λ hypothesis greater than .005 removed.

c) Same, except events with confidence level for Λ hypothesis greater than .001 removed.

d) Events with confidence level for Λ hypothesis greater than .001. (difference between Fig. 8a and Fig. 8c).

Figure 8a

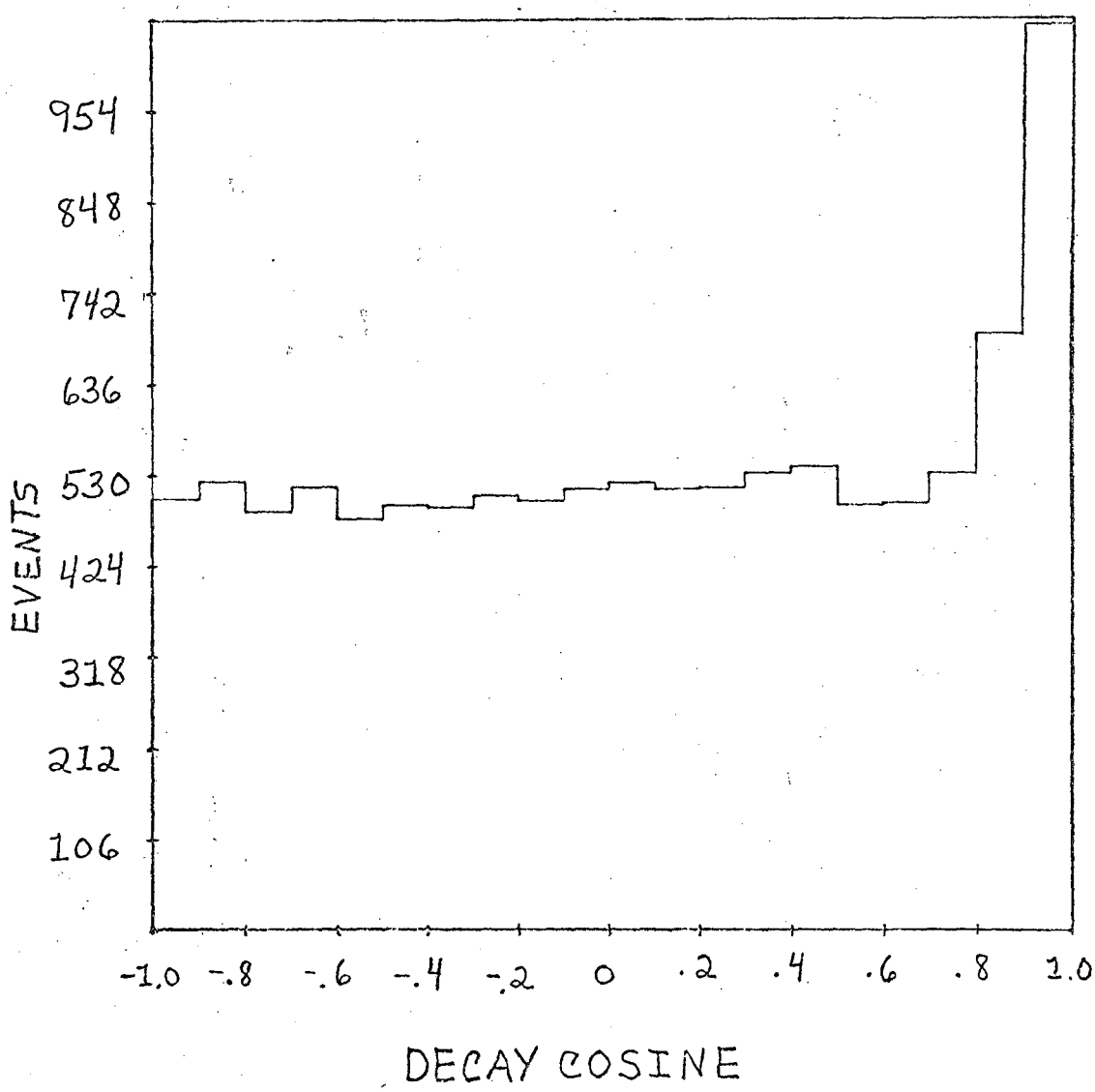
954
848
742
636
530
424
318
212
106
EVENTS
-1.0
-.8
-.6
-.4
-.2
0
.2
.4
.6
.8
1.0
DECAY COSINE

Figure 8b

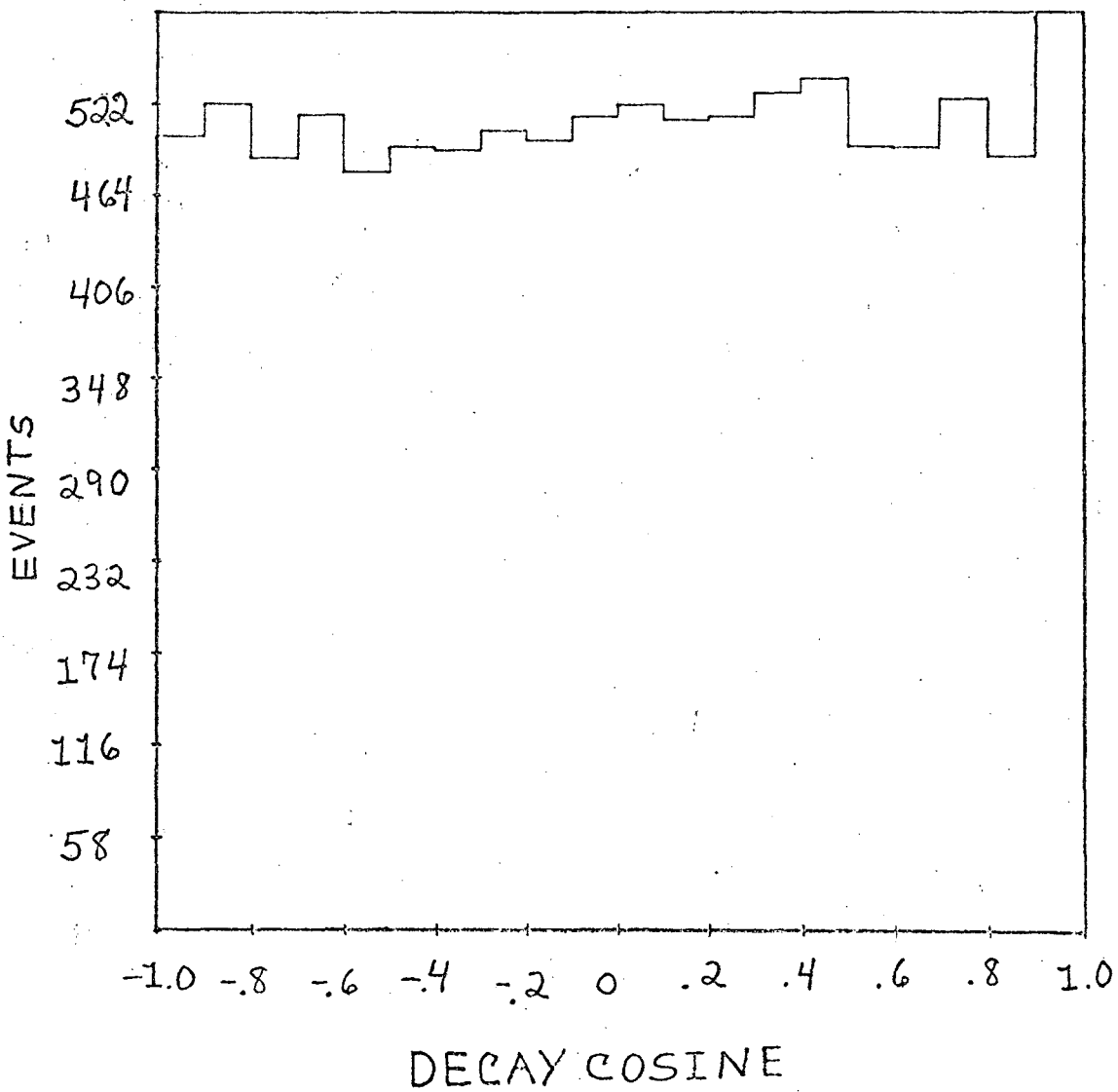
522
464
406
348
290
232
174
116
58
EVENTS
-1.0
-.8
-.6
-.4
-.2
0
.2
.4
.6
.8
1.0
DECAY COSINE

Figure 8c

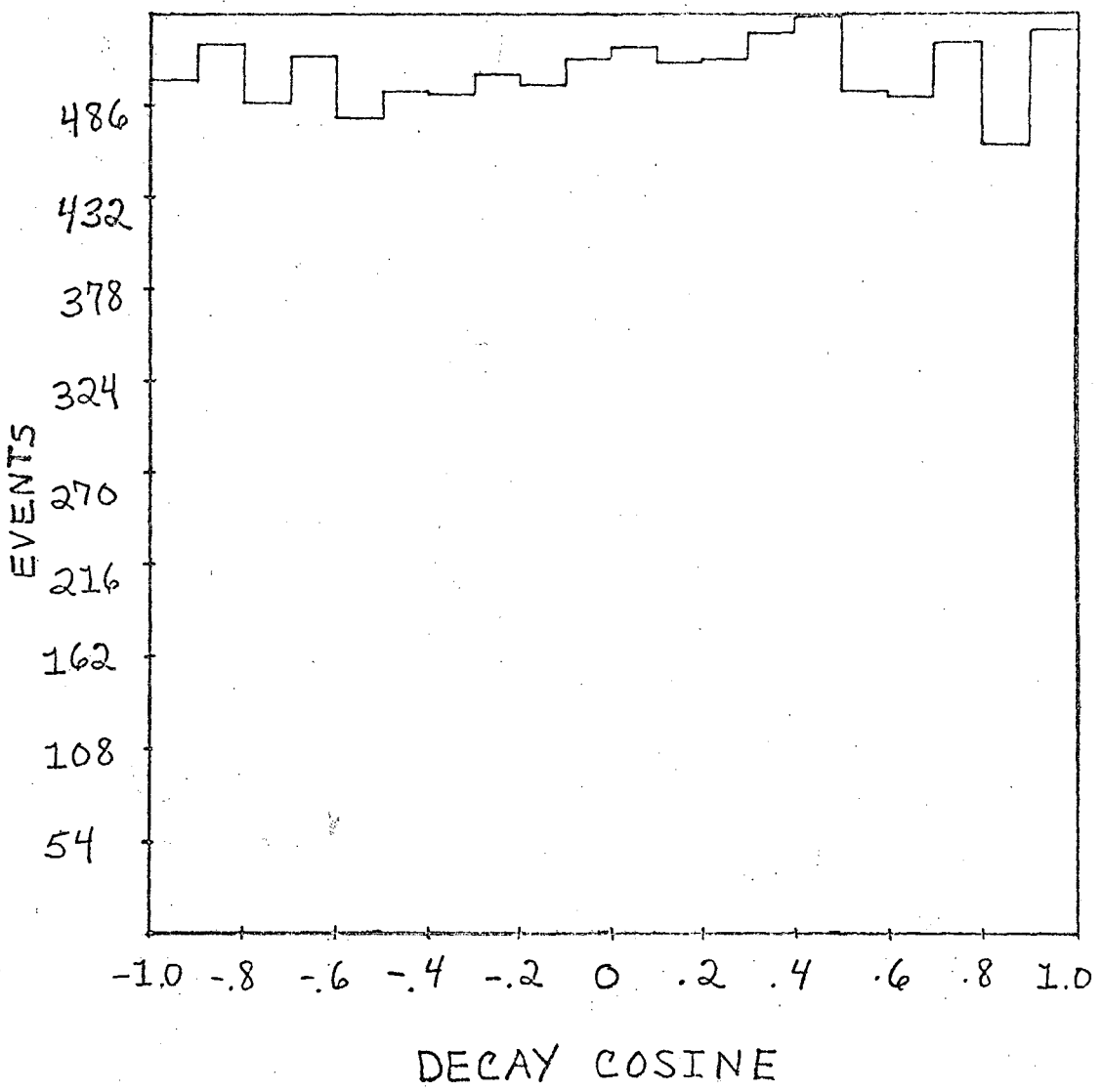
EVENTS
486
432
378
324
270
216
162
108
54
-1.0
-.8
-.6
-.4
-.2
0
.2
.4
.6
.8
1.0
DECAY COSINE

Figure 8d

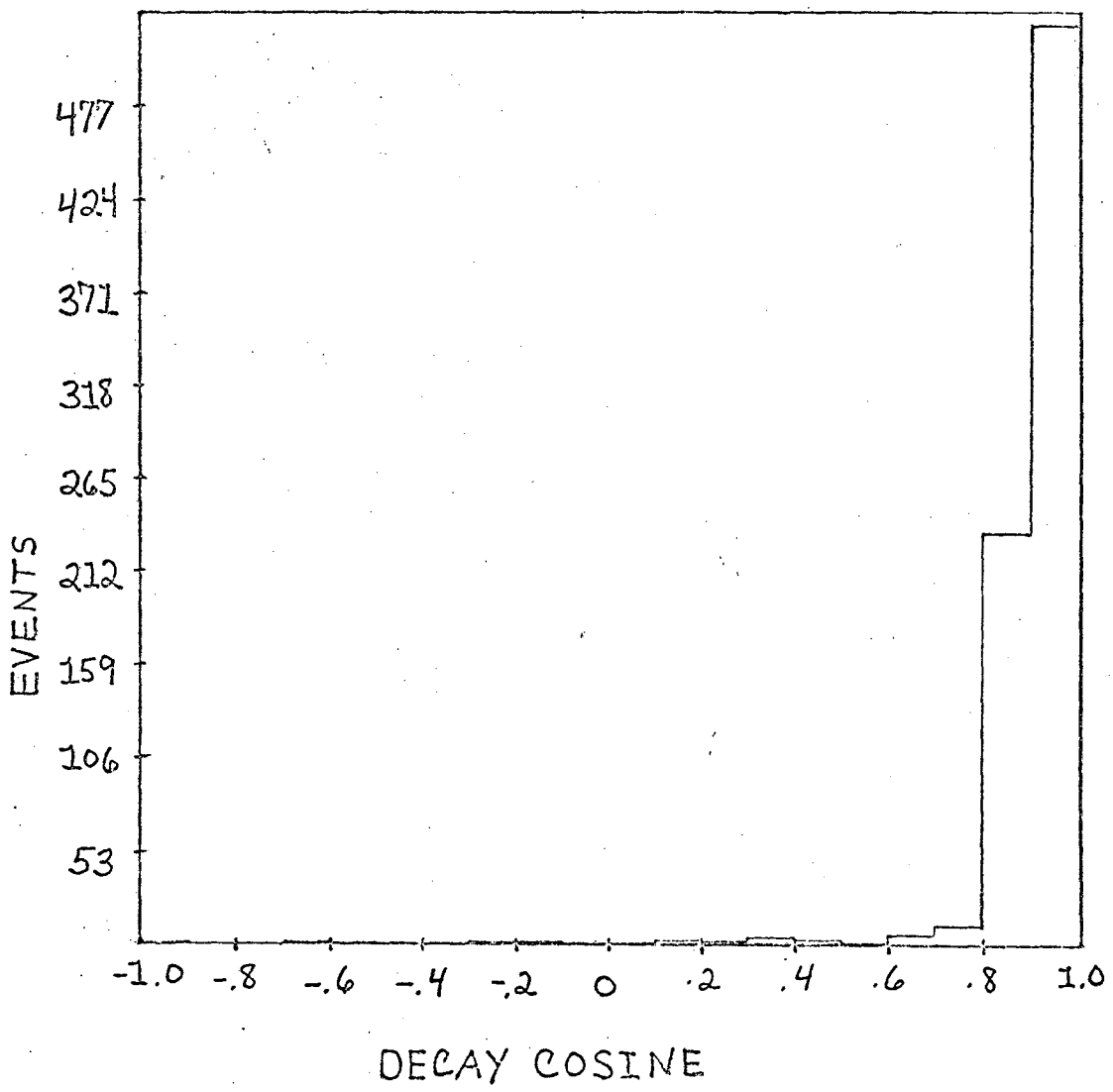
477
424
371
318
265
212
159
106
53
EVENTS
-1.0
-.8
-.6
-.4
-.2
0
.2
.4
.6
.8
1.0
DECAY COSINE

Figure 9

Missing mass squared plots for one constraint events.

a) Gaussian ideogram for events which fit best $K^- p \rightarrow p\overline{K}^0 \pi^0 \pi^-$

b) Histogram for same events

c) Histogram for events which best fit $K^- p \rightarrow p\overline{K}^0 \pi^-$ + missing mass.

d) Gaussian ideogram for events which fit best $K^- p \rightarrow \overline{K}^0 \pi^+ \pi^- n$

e) Histogram for same events

f) Histogram for events which best fit $K^- p \rightarrow \overline{K}^0 \pi^+ \pi^-$ + missing mass.

Figure 9a

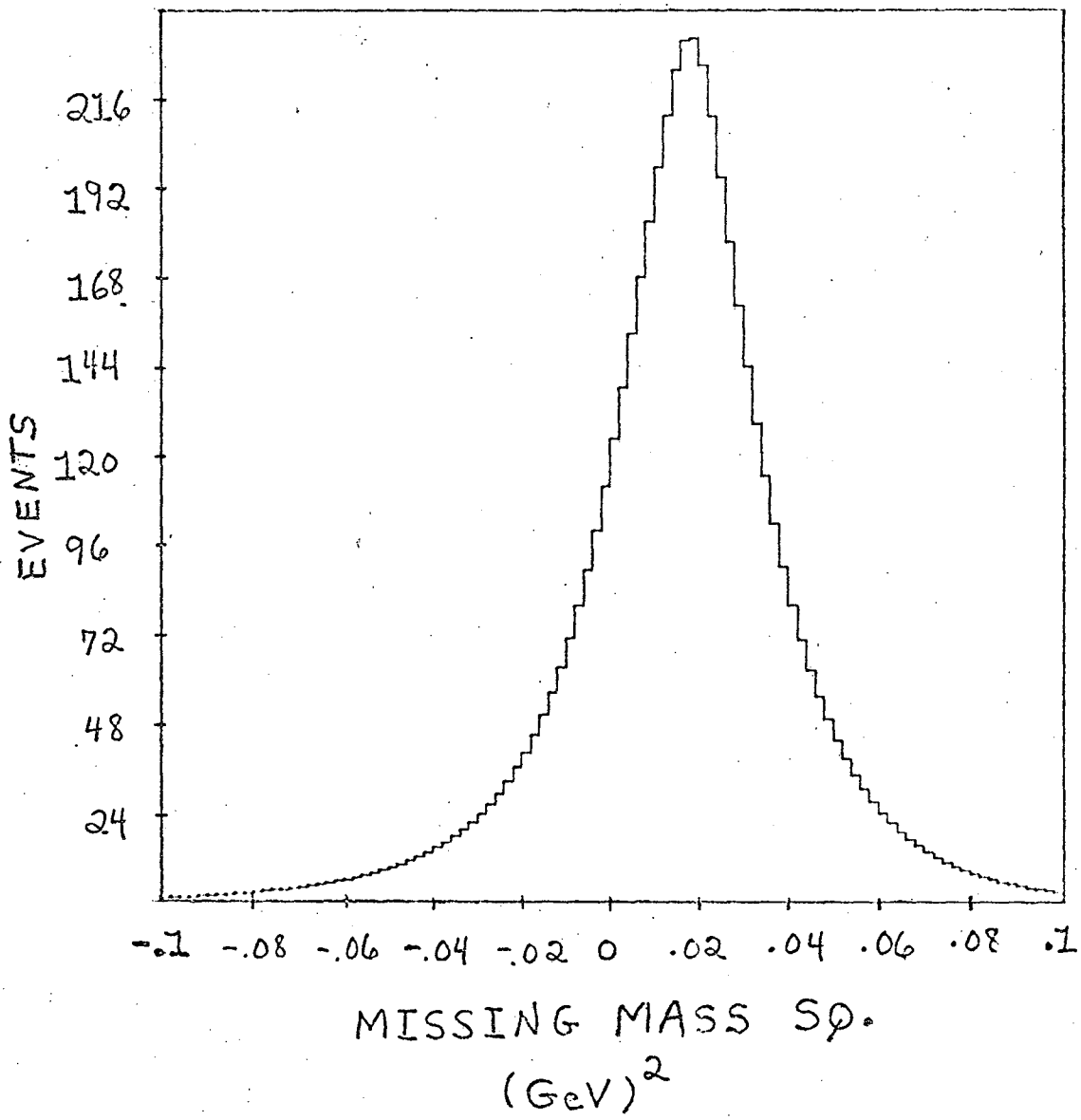
216
192
168
144
120
96
72
48
24
EVENTS
-.1
-.08
-.06
-.04
-.02
0
.02
.04
.06
.08
.1
MISSING MASS SQ.
(GeV)²

Figure 9b

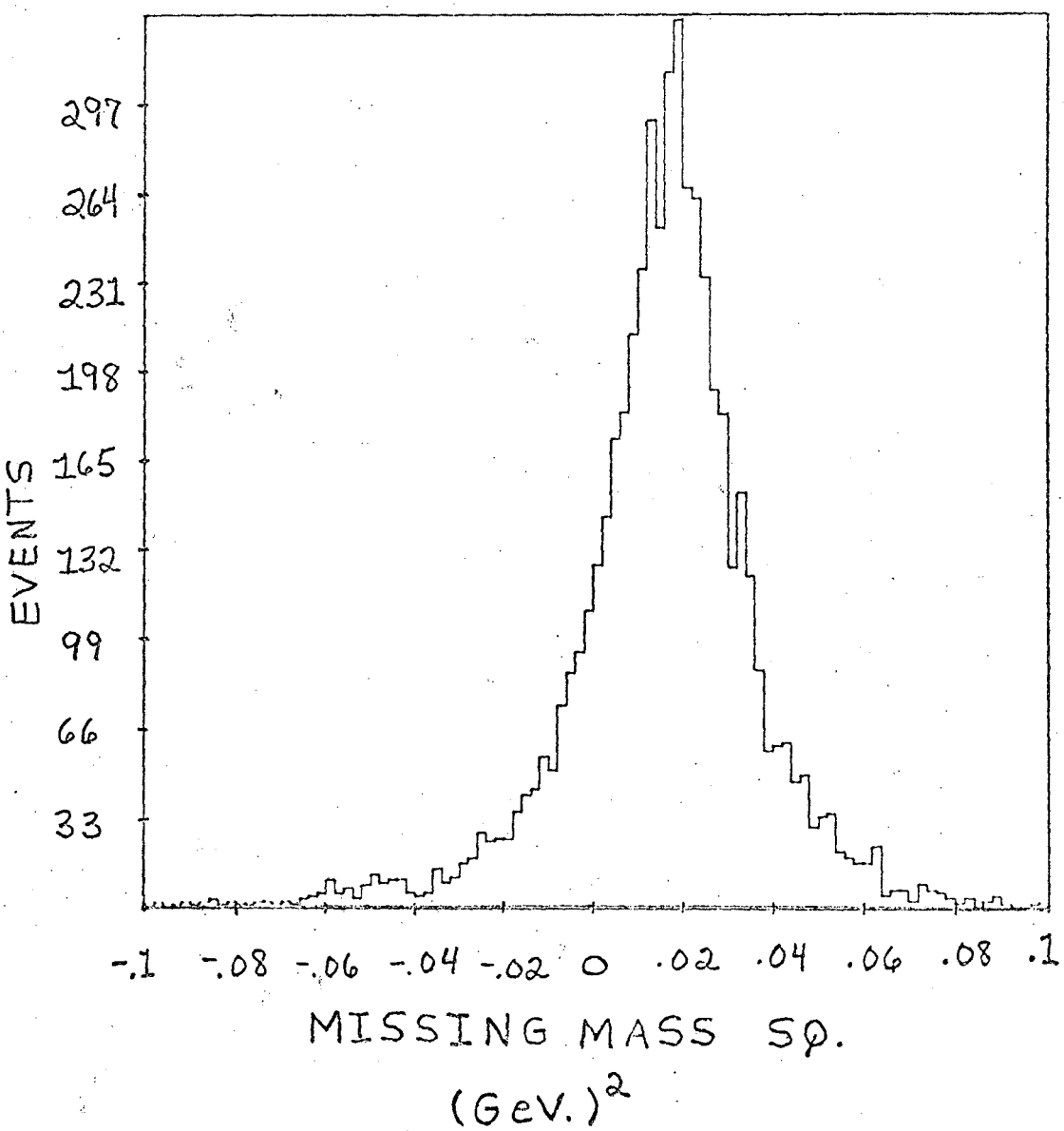
297
264
231
198
165
132
99
66
33
EVENTS
-.1
-.08
-.06
-.04
-.02
0
.02
.04
.06
.08
.1
MISSING MASS SQ.
(GeV.)²

Figure 9c

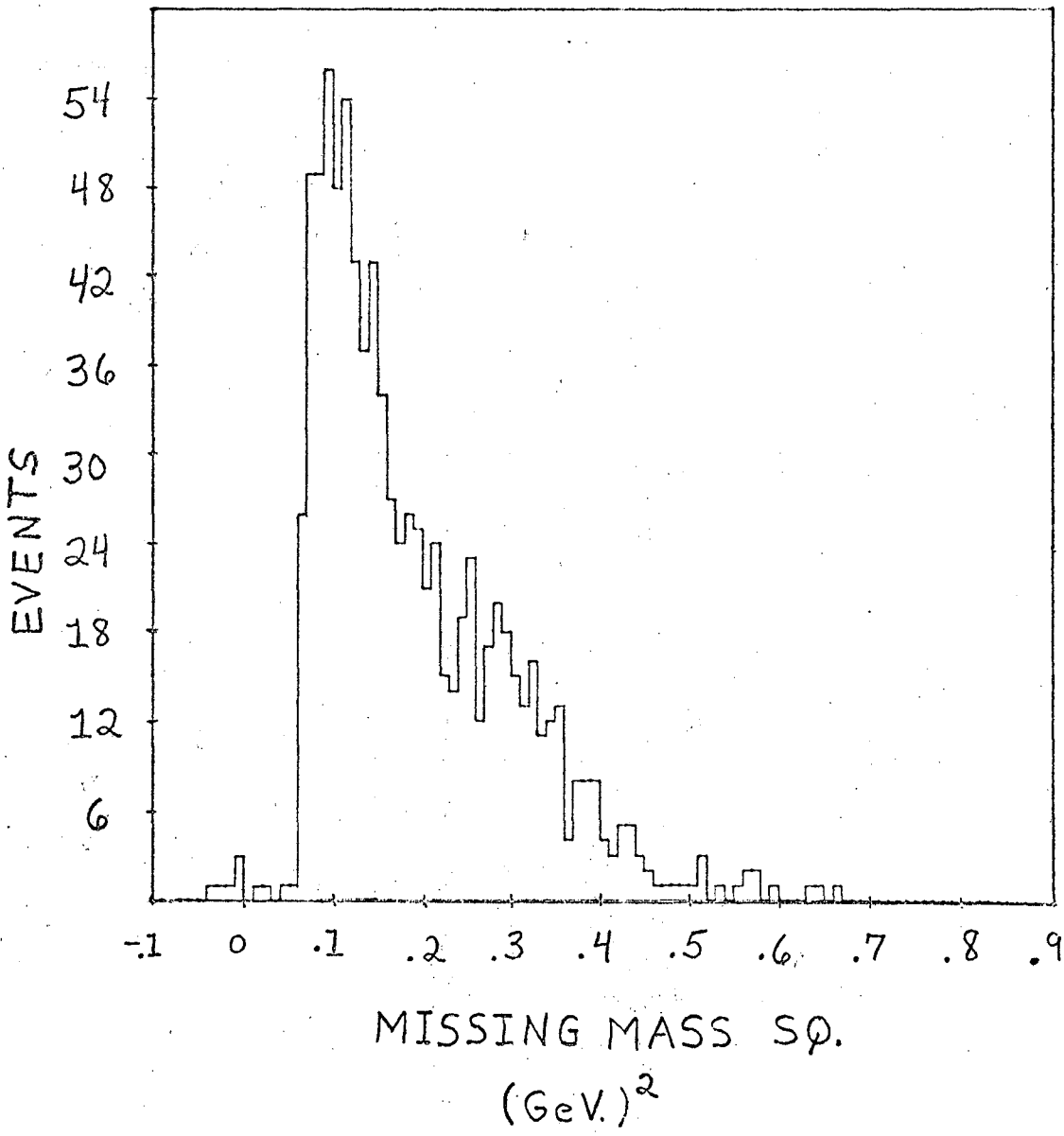
54
48
42
36
30
24
18
12
6
EVENTS
-.1
0
.1
.2
.3
.4
.5
.6
.7
.8
.9
MISSING MASS SQ.
(GeV.)²

Figure 9d

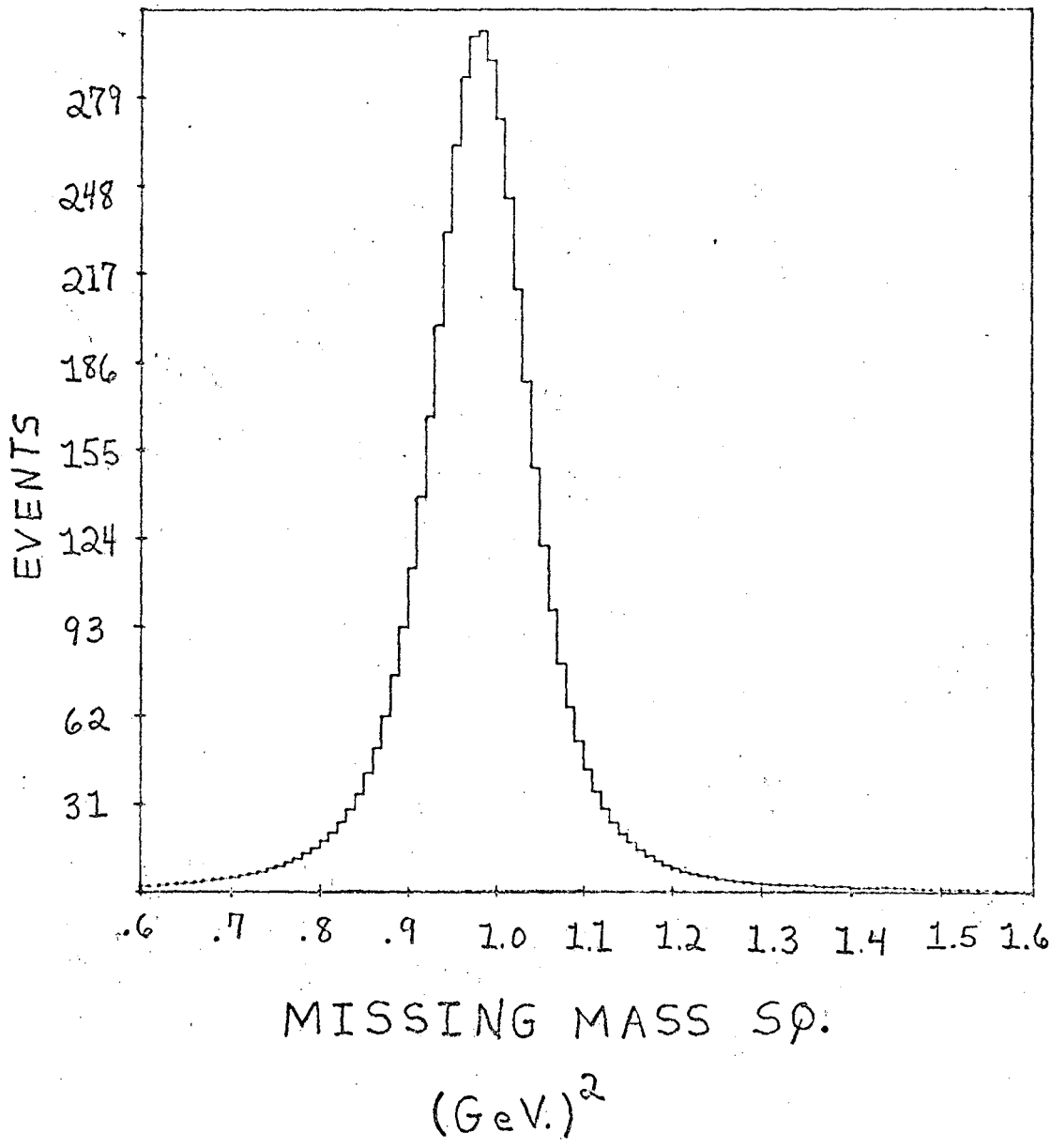
279
248
217
186
155
124
93
62
31
EVENTS
.6
.7
.8
.9
1.0
1.1
1.2
1.3
1.4
1.5
1.6
MISSING MASS SQ.
(GeV.)^2

Figure 9e

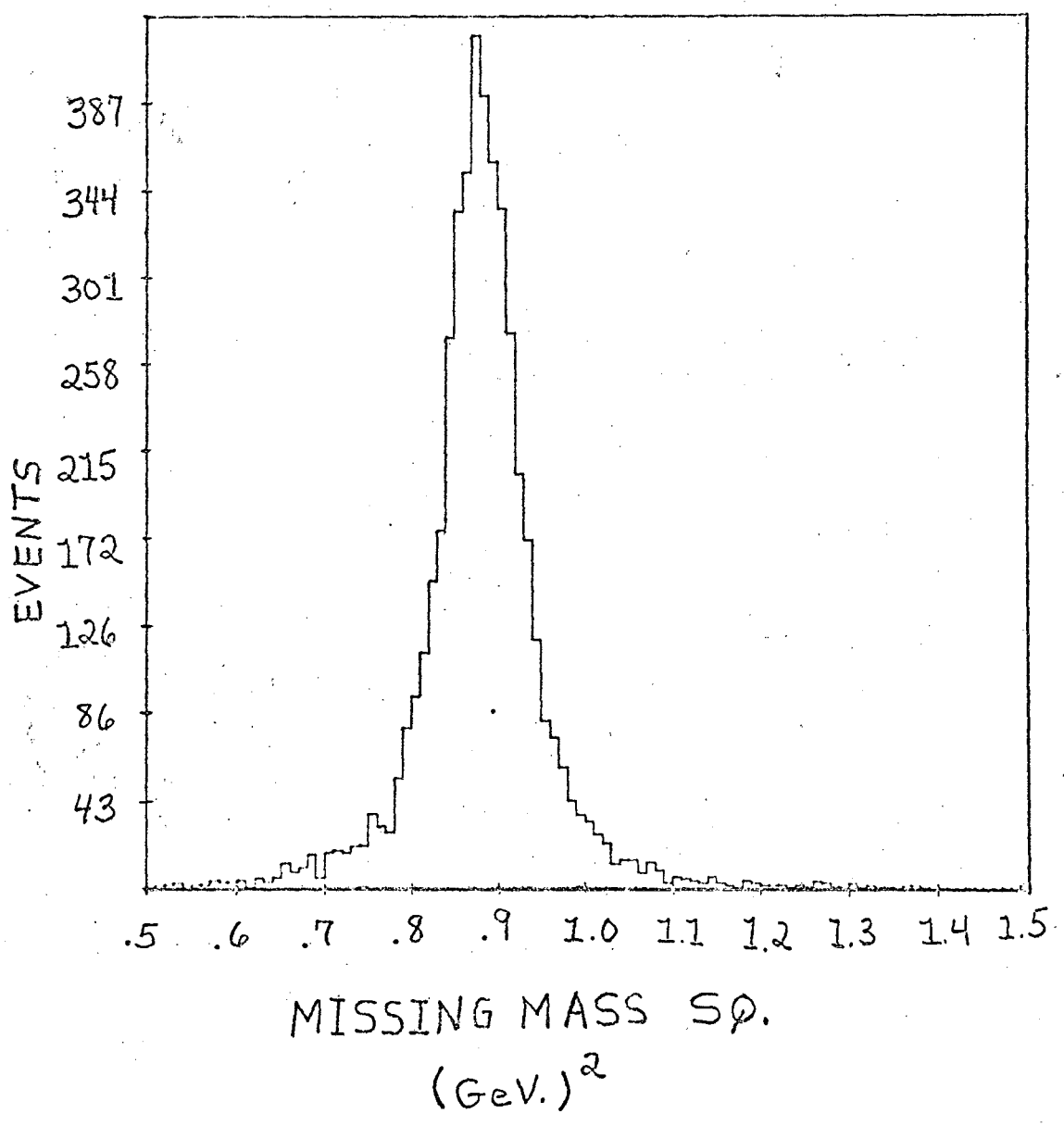
387
344
301
258
215
172
126
86
43
EVENTS
.5
.6
.7
.8
.9
1.0
1.1
1.2
1.3
1.4
1.5
MISSING MASS SQ.
(GeV.)²

Figure 9f

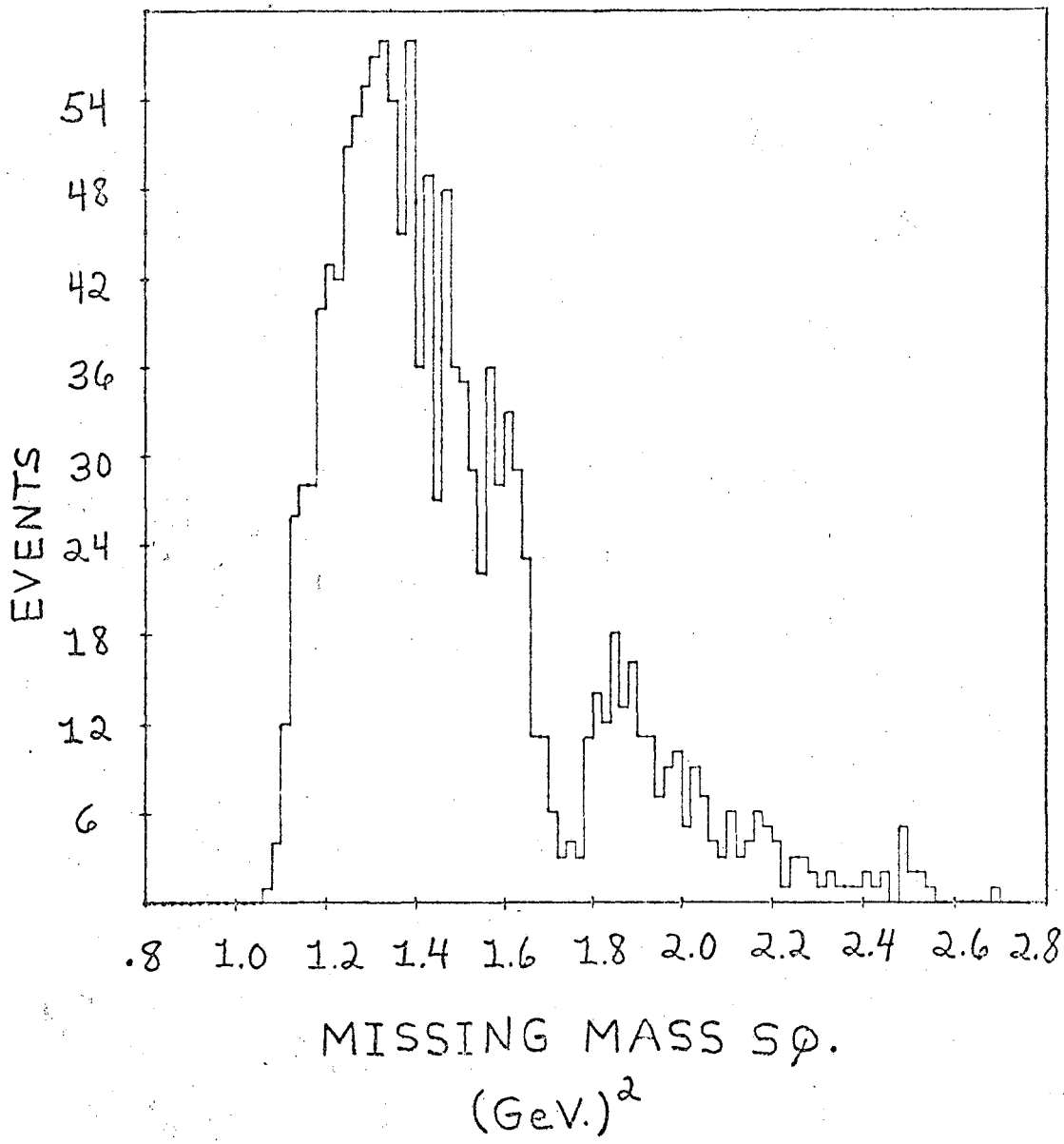
54
48
42
36
30
24
18
12
6
EVENTS
.8
1.0
1.2
1.4
1.6
1.8
2.0
2.2
2.4
2.6
2.8
MISSING MASS SQ.
(GeV.)²

Figure 10

Total cross sections for the reactions

a) $K^- p \rightarrow p\bar{K}^0 \pi^-$

b) $K^- p \rightarrow p\bar{K}^0 \pi^0 \pi^-$

c) $K^- p \rightarrow n\bar{K}^0 \pi^+ \pi^-$

as a function of incident K^- beam momentum as measured in this experiment. Points plotted include corrections for neutral decay modes of $\bar{K}^0$.

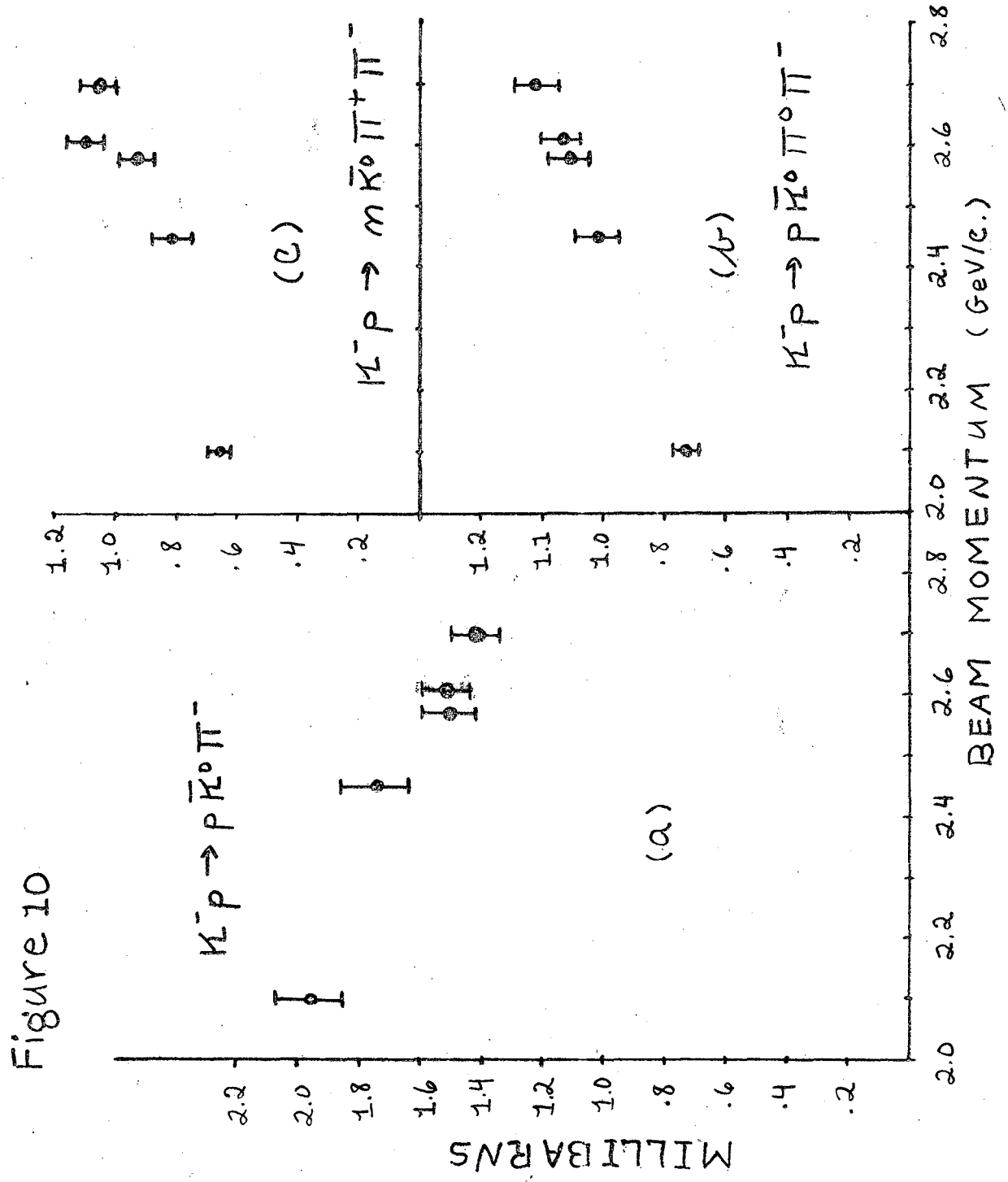
Total Cross Section
Figure 10
$K^- p \to p \bar{K}^0 \pi^-$
(a)
$K^- p \to n \bar{K}^0 \pi^+ \pi^-$
(c)
$K^- p \to p \bar{K}^0 \pi^0 \pi^-$
(b)
MILLIBARNS
BEAM MOMENTUM (GeV/c.)

Figure 11

The three two-particle invariant mass plots at each momentum for the reaction $K^- p \rightarrow p \overline{K}^0 \pi^-$.

a) $p\overline{K}^0$; 2.1 GeV/c

b) $p\pi^-$; 2.1 GeV/c

c) $\overline{K}^0\pi^-$; 2.1 GeV/c

d) $p\overline{K}^0$; 2.45 GeV/c

e) $p\pi^-$; 2.45 GeV/c

f) $\overline{K}^0\pi^-$; 2.45 GeV/c

g) $p\overline{K}^0$; 2.60 GeV/c

h) $p\pi^-$; 2.60 GeV/c

i) $\overline{K}^0\pi^-$; 2.60 GeV/c

j) $p\overline{K}^0$; 2.70 GeV/c

k) $p\pi^-$; 2.70 GeV/c

l) $\overline{K}^0\pi^-$; 2.70 GeV/c

Figure 11

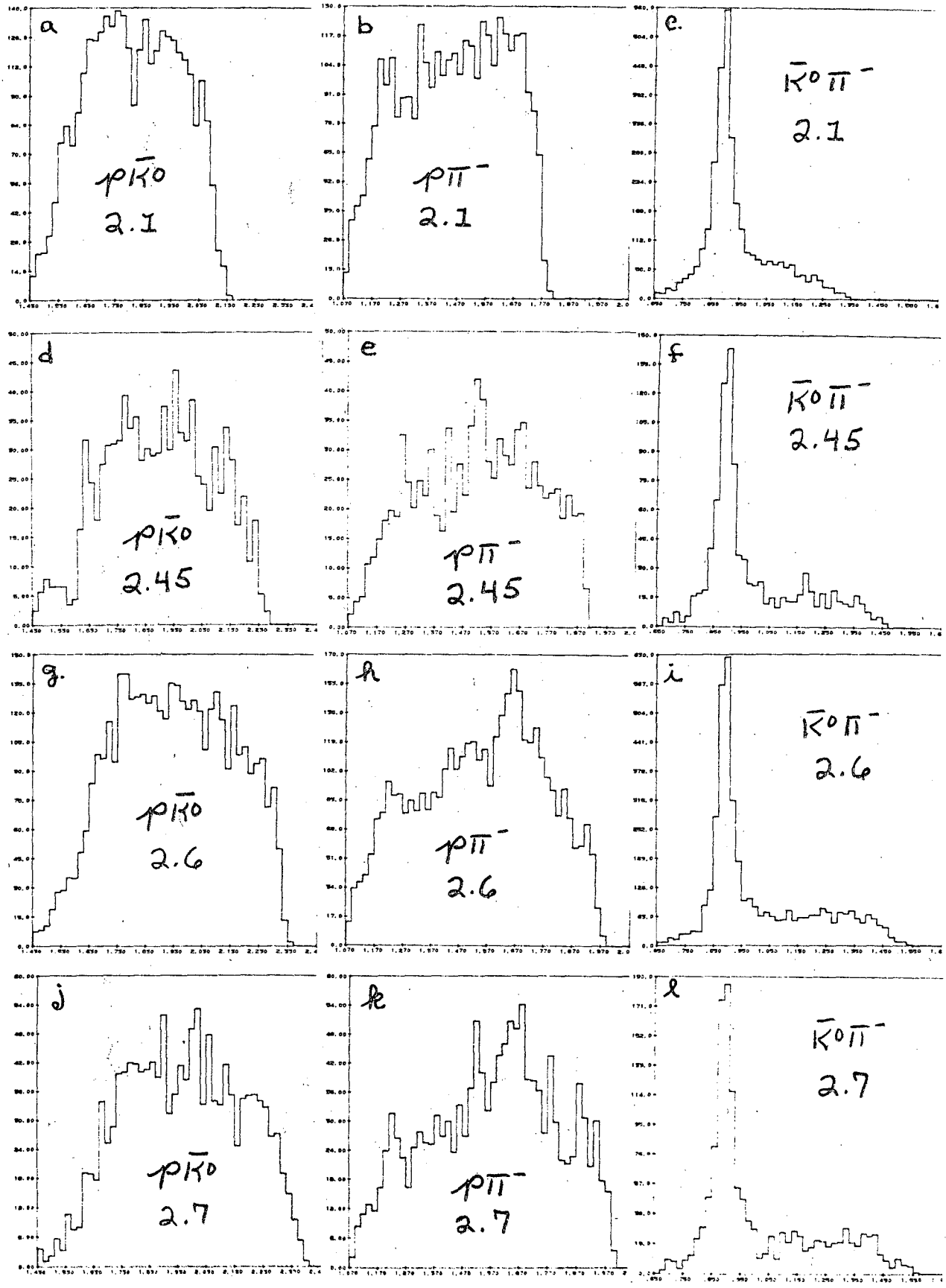

INVARIANT MASS

Figure 12

Invariant mass projections "M" for various cuts in production cosine "μ" for the reaction $K^- p \rightarrow p\bar{K}^0\pi^-$ at 2.1 GeV/c.

a) M $(p\bar{K}^0)$ for μ $(p\bar{K}^0$; beam) > .9

b) M $(p\bar{K}^0)$ for μ $(p\bar{K}^0$; beam) > .8

c) M $(p\bar{K}^0)$ for μ $(p\bar{K}^0$; beam) > .5

d) M $(p\bar{K}^0)$ for μ $(p\bar{K}^0$; target) > .9

e) M $(p\bar{K}^0)$ for μ $(p\bar{K}^0$; target) > .8

f) M $(p\bar{K}^0)$ for μ $(p\bar{K}^0$; target) > .5

g) M $(p\pi^-)$ for μ $(p\pi^-$; beam) > .9

h) M $(p\pi^-)$ for μ $(p\pi^-$; beam) > .8

i) M $(p\pi^-)$ for μ $(p\pi^-$; beam) > .5

j) M $(p\pi^-)$ for μ $(p\pi^-$; target) > .9

k) M $(p\pi^-)$ for μ $(p\pi^-$; target) > .8

l) M $(p\pi^-)$ for μ $(p\pi^-$; target) > .5

m) M $(\bar{K}^0\pi^-)$ for μ $(\bar{K}^0\pi^-$; beam) > .9

n) M $(\bar{K}^0\pi^-)$ for μ $(\bar{K}^0\pi^-$; beam) > .8

o) M $(\bar{K}^0\pi^-)$ for μ $(\bar{K}^0\pi^-$; beam) > .5

p) M $(K^0\pi^-)$ for μ $(\bar{K}^0\pi^-$; target) > .9

q) M $(\bar{K}^0\pi^-)$ for μ $(\bar{K}^0\pi^-$; target) > .8

r) M $(K^0\pi^-)$ for μ $(K^0\pi^-$; target) > .5

Figure 12

(a)

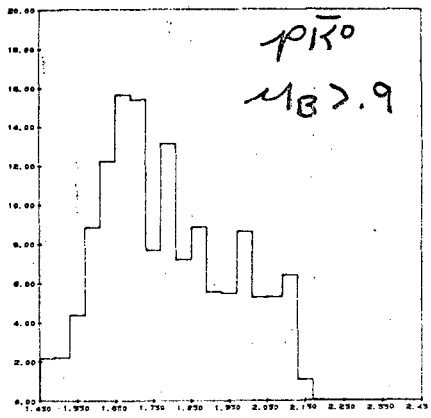

(d)

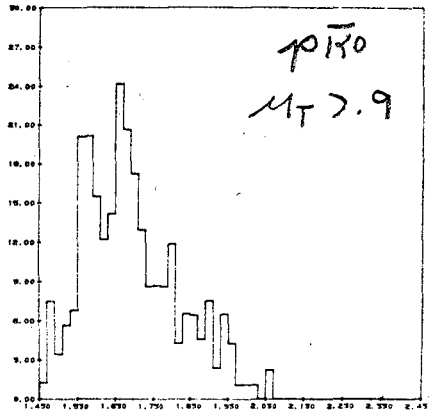

(b)

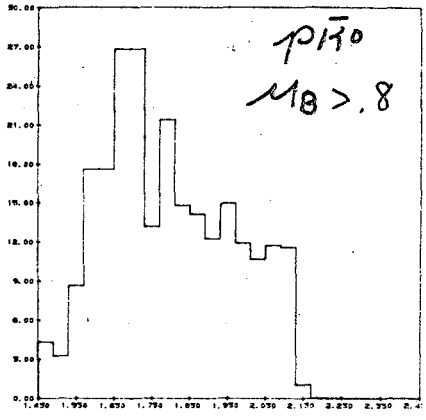

(e)

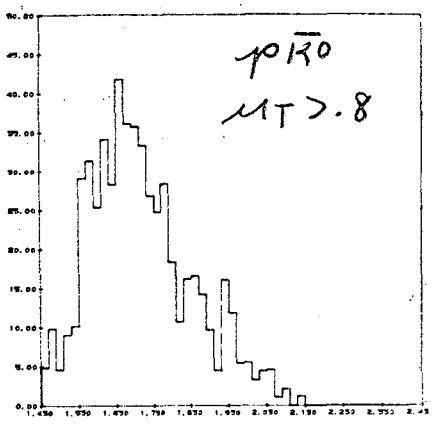

(c)

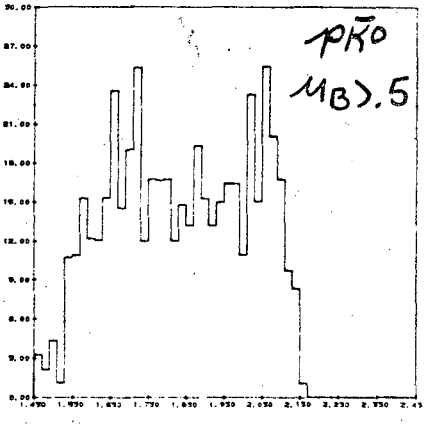

(f)

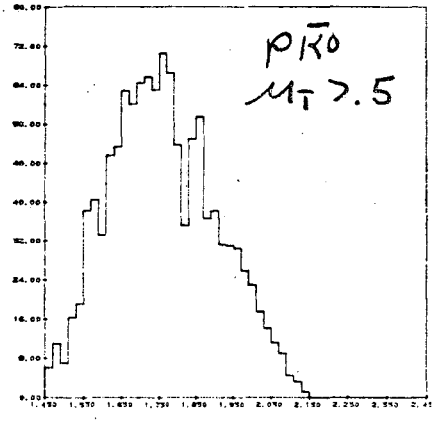

NUMBER OF EVENTS

INVARIANT MASS (GeV.)

Figure 12

(g)

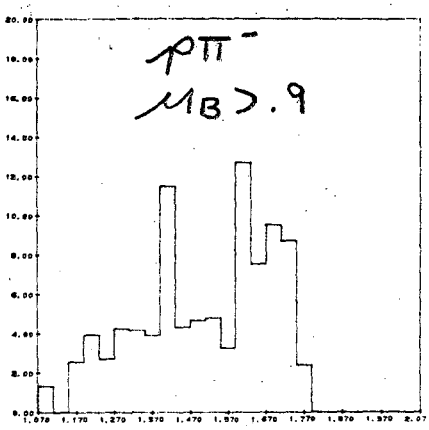

(j)

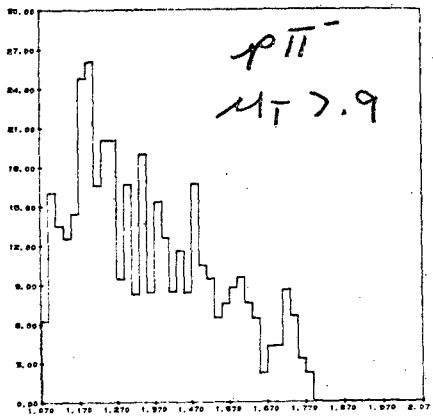

(h)

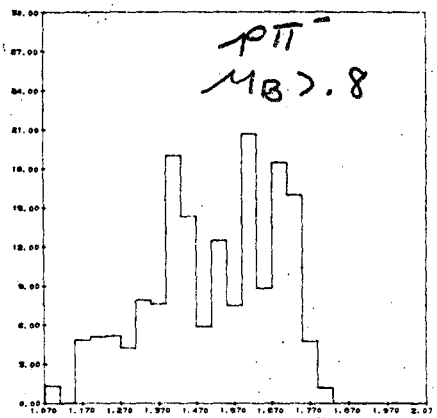

(k)

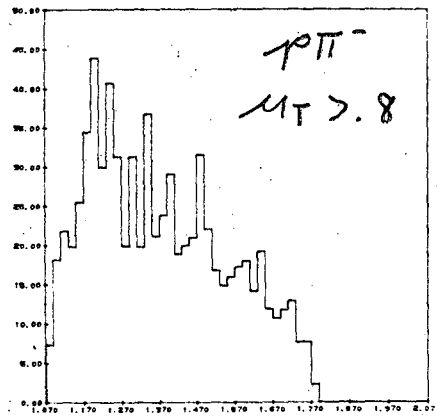

(i)

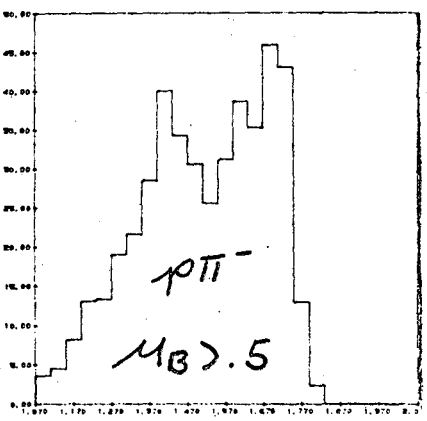

(l)

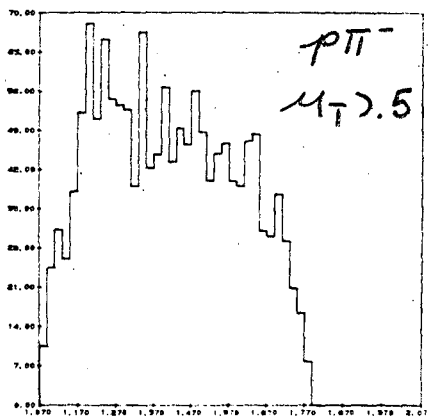

NUMBER OF EVENTS

INVARIANT MASS (GeV.)

Figure 12

(m)

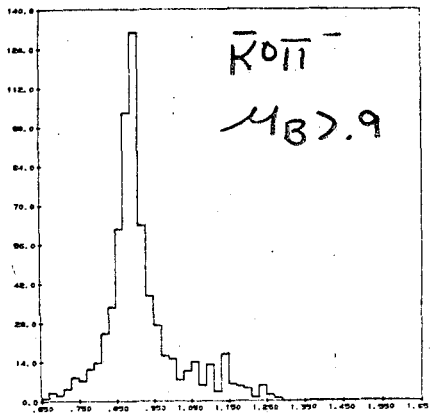

(p)

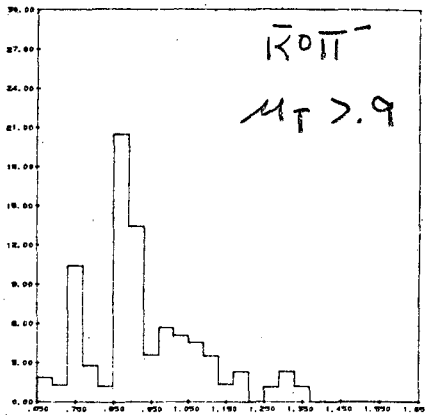

(n)

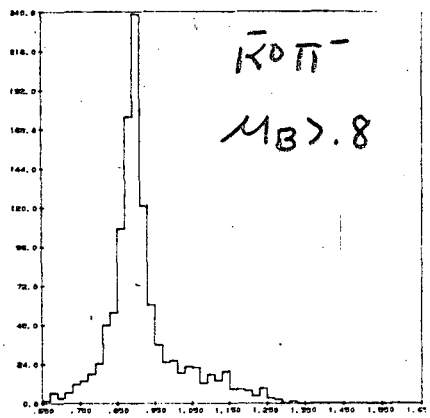

(q)

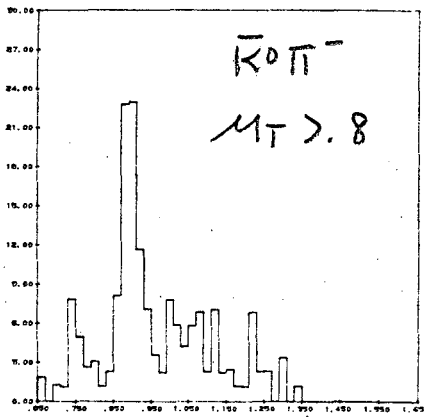

(o)

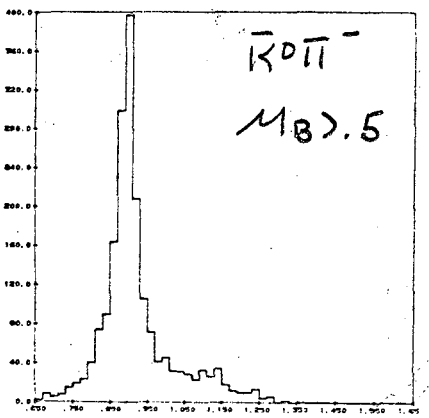

(r)

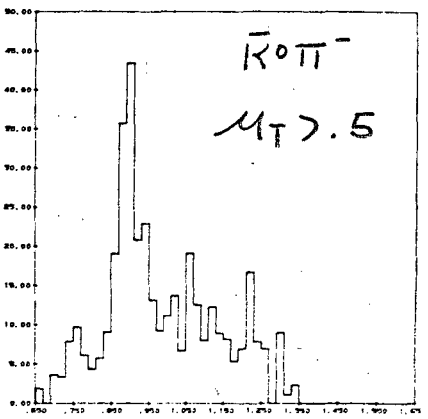

NUMBER OF EVENTS

INVARIANT MASS (GeV.)

Figure 13

Invariant mass projections "M" for various cuts in production cosine "μ" for the reaction $K^- p \rightarrow p\overline{K}^0 \pi^-$ at 2.45 GeV/c.

a) M $(p\overline{K}^0)$ for μ $(p\overline{K}^0$; beam) > .5

b) M $(p\overline{K}^0)$ for μ $(p\overline{K}^0$; target) > .5

c) M $(p\pi^-)$ for μ $(p\pi^-$; beam) > .5

d) M $(p\pi^-)$ for μ $(p\pi^-$; target) > .5

e) M $(\overline{K}^0\pi^-)$ for μ $(\overline{K}^0\pi^-$; beam) > .5

f) M $(K^0\pi^-)$ for μ $(\overline{K}^0\pi^-$; target) > .5

Figure 13

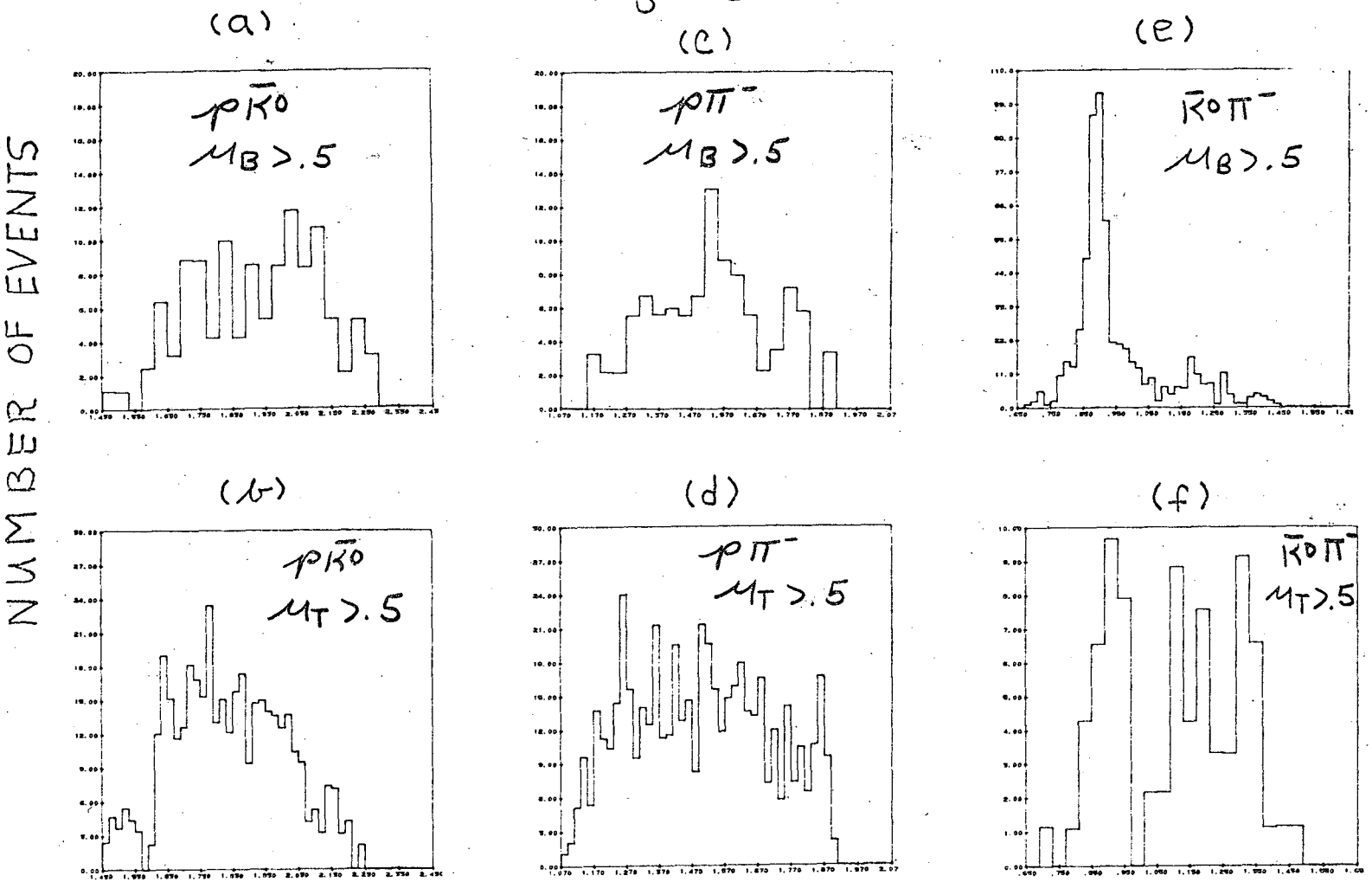
(a)
$p\bar{K}^0$
$M_B > .5$
(c)
$p\pi^-$
$M_B > .5$
(e)
$\bar{K}^0\pi^-$
$M_B > .5$
(b)
$p\bar{K}^0$
$M_T > .5$
(d)
$p\pi^-$
$M_T > .5$
(f)
$\bar{K}^0\pi^-$
$M_T > .5$
NUMBER OF EVENTS
INVARIANT MASS (GeV.)

Figure 14

Invariant mass projections "M" for various cuts in production cosine "μ" for the reaction $K^- p \to p\overline{K}^0\pi^-$ at 2.60 GeV/c.

a) M $(p\overline{K}^0)$ for μ $(p\overline{K}^0$; beam) > .9

b) M $(p\overline{K}^0)$ for μ $(p\overline{K}^0$; beam) > .8

c) M $(p\overline{K}^0)$ for μ $(p\overline{K}^0$; beam) > .5

d) M $(p\overline{K}^0)$ for μ $(p\overline{K}^0$; target) > .9

e) M $(p\overline{K}^0)$ for μ $(p\overline{K}^0$; target) > .8

f) M $(p\overline{K}^0)$ for μ $(p\overline{K}^0$; target) > .5

g) M $(p\pi^-)$ for μ $(p\pi^-$; beam) > .9

h) M $(p\pi^-)$ for μ $(p\pi^-$; beam) > .8

i) M $(p\pi^-)$ for μ $(p\pi^-$; beam) > .5

j) M $(p\pi^-)$ for μ $(p\pi^-$; target) > .9

k) M $(p\pi^-)$ for μ $(p\pi^-$; target) > .8

l) M $(p\pi^-)$ for μ $(p\pi^-$; target) > .5

m) M $(\overline{K}^0\pi^-)$ for μ $(\overline{K}^0\pi^-$; beam) > .9

n) M $(\overline{K}^0\pi^-)$ for μ $(\overline{K}^0\pi^-$; beam) > .8

o) M $(\overline{K}^0\pi^-)$ for μ $(\overline{K}^0\pi^-$; beam) > .5

p) M $(\overline{K}^0\pi^-)$ for μ $(\overline{K}^0\pi^-$; target) > .9

q) M $(\overline{K}^0\pi^-)$ for μ $(\overline{K}^0\pi^-$; target) > .8

r) M $(\overline{K}^0\pi^-)$ for μ $(\overline{K}^0\pi^-$; target) > .5

Figure 14

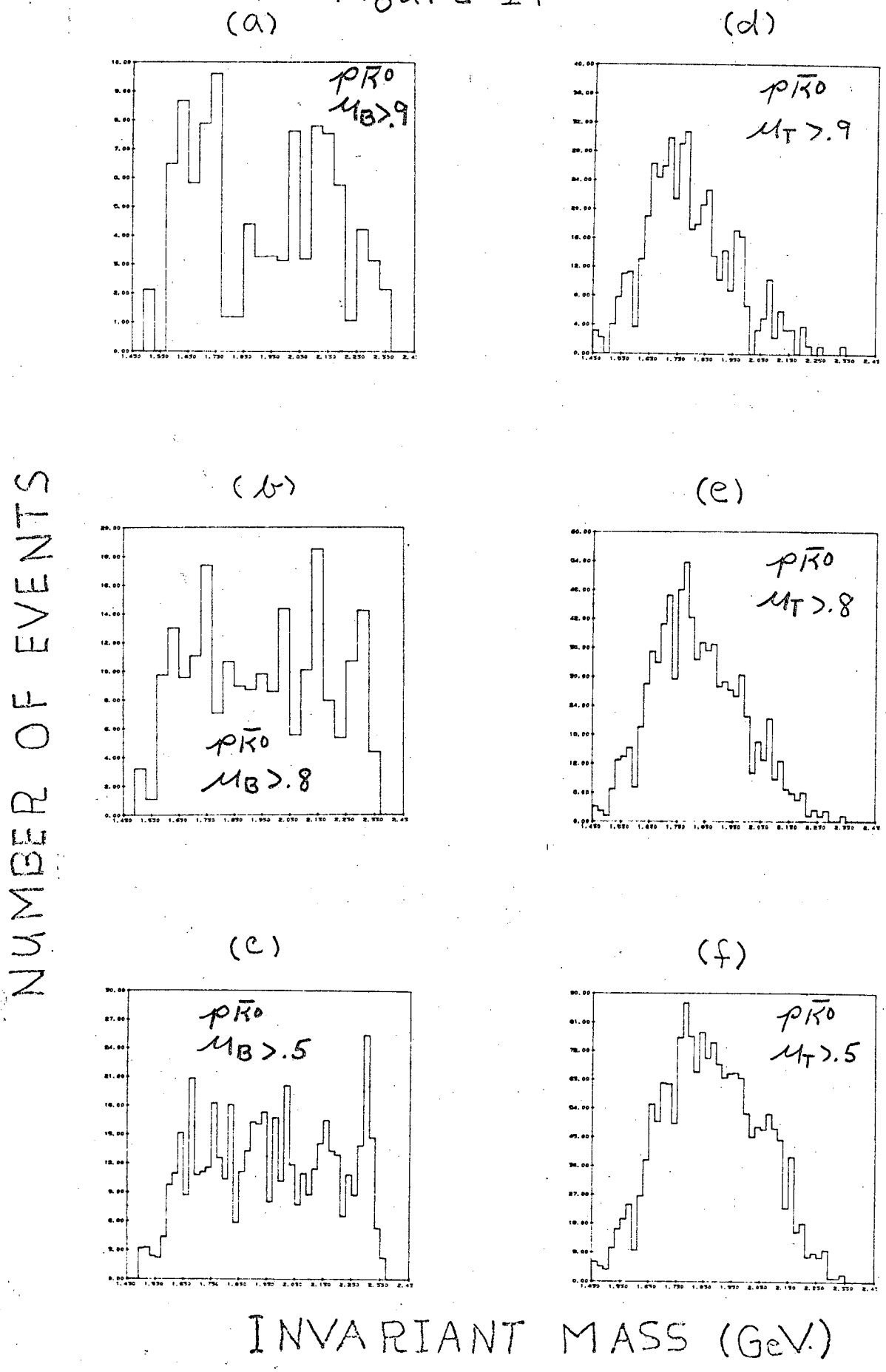
(a)
$p\bar{K}^0$
$\mu_B > .9$
(d)
$p\bar{K}^0$
$\mu_T > .9$
(b)
$p\bar{K}^0$
$\mu_B > .8$
(e)
$p\bar{K}^0$
$\mu_T > .8$
(c)
$p\bar{K}^0$
$\mu_B > .5$
(f)
$p\bar{K}^0$
$\mu_T > .5$
NUMBER OF EVENTS
INVARIANT MASS (GeV.)

Figure 14

(g)

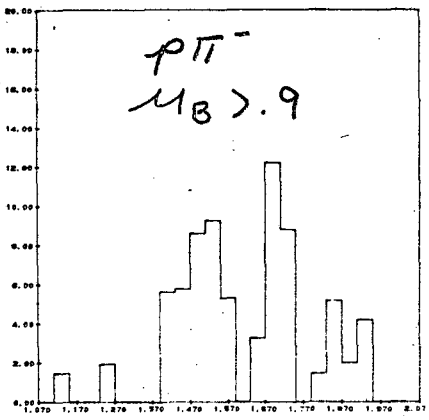

(j)

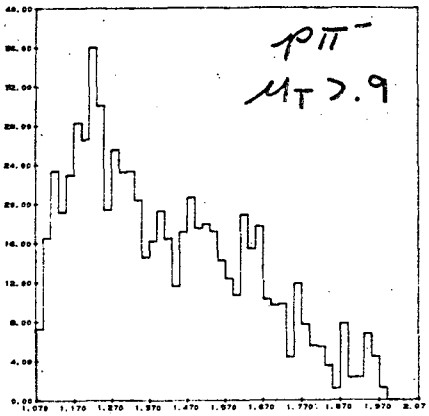

(h)

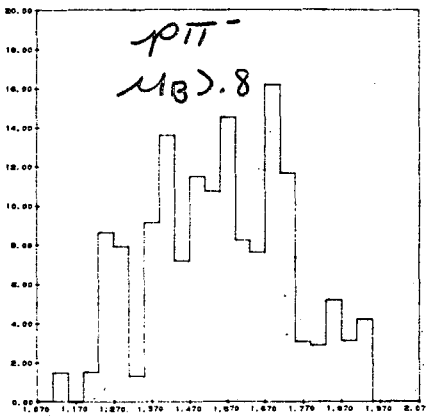

(k)

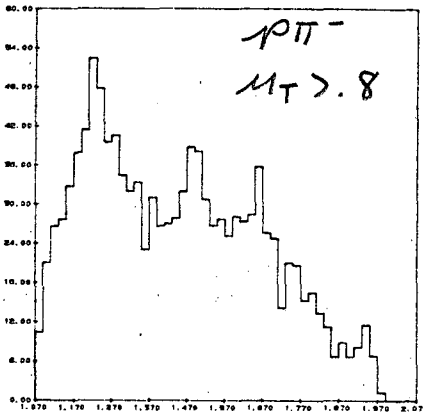

(i)

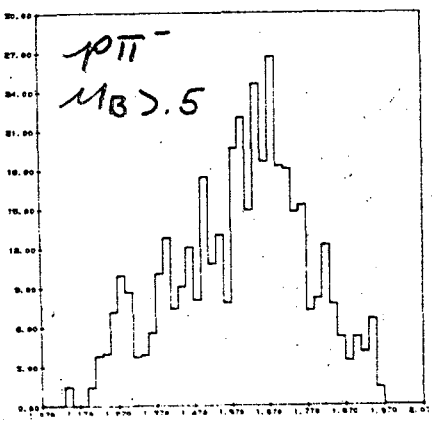

(l)

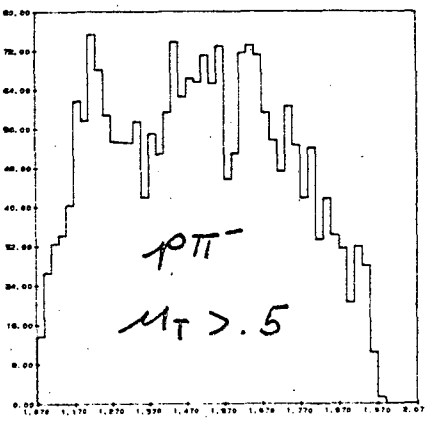

NUMBER OF EVENTS

INVARIANT MASS (GeV.)

Figure 14

(m)

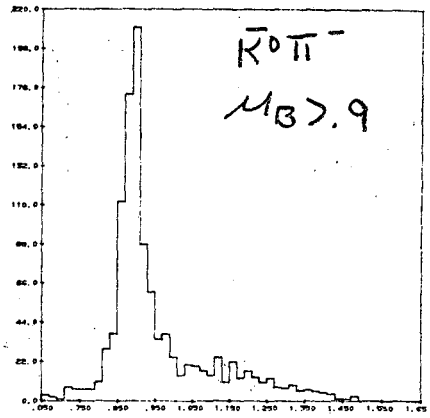

(p)

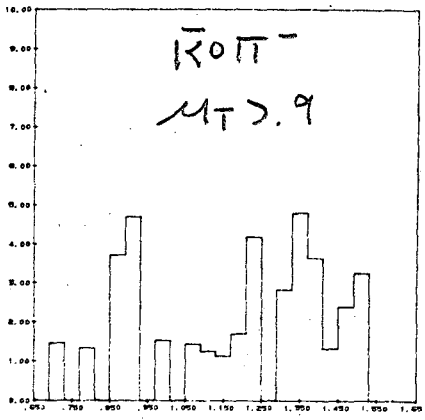

(n)

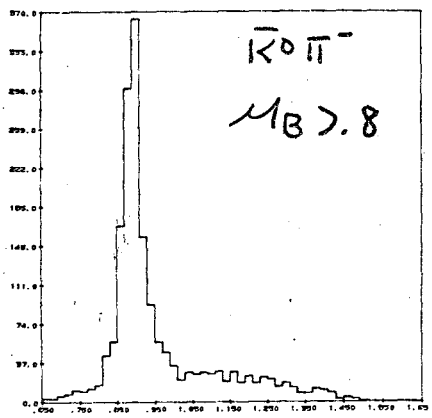

(q)

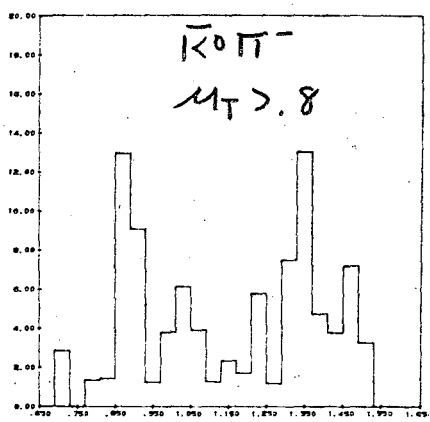

(o)

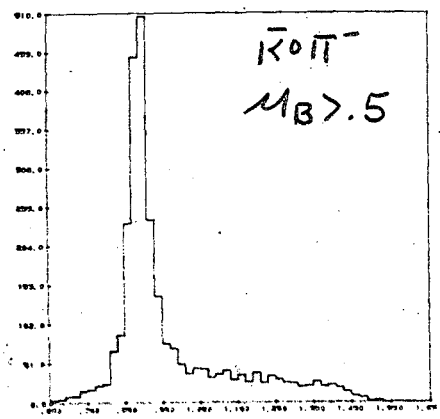

(r)

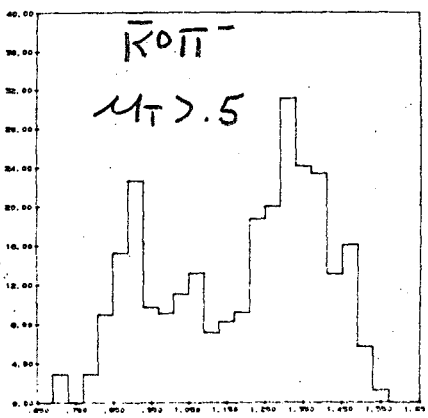

NUMBER OF EVENTS

INVARIANT MASS (GeV.)

Figure 15

Invariant mass projections "M " for various cuts in production cosine "μ" for the reaction $\bar{K}^- p \rightarrow p\bar{K}^0\pi^-$ at 2.70 GeV/c.

a) M $(p\bar{K}^0)$ for μ $(p\bar{K}^0$; beam) > .8

b) M $(p\bar{K}^0)$ for μ $(p\bar{K}^0$; beam) > .5

c) M $(p\bar{K}^0)$ for μ $(pK^0$; target) > .8

d) M $(p\bar{K}^0)$ for μ $(p\bar{K}^0$; target) > .5

e) M $(p\pi^-)$ for μ $(p\pi^-$; beam) > .8

f) M $(p\pi^-)$ for μ $(p\pi^-$; beam) > .5

g) M $(p\pi^-)$ for μ $(p\pi^-$; target) > .8

h) M $(p\pi^-)$ for μ $(p\pi^-$; target) > .5

i) M $(\bar{K}^0\pi^-)$ for μ $(\bar{K}^0\pi^-$; beam) > .8

j) M $(\bar{K}^0\pi^-)$ for μ $(\bar{K}^0\pi^-$; beam) > .5

k) M $(\bar{K}^0\pi^-)$ for μ $(\bar{K}^0\pi^-$; target) > .8

l) M $(\bar{K}^0\pi^-)$ for μ $(\bar{K}^0\pi^-$; target) > .5

Figure 15

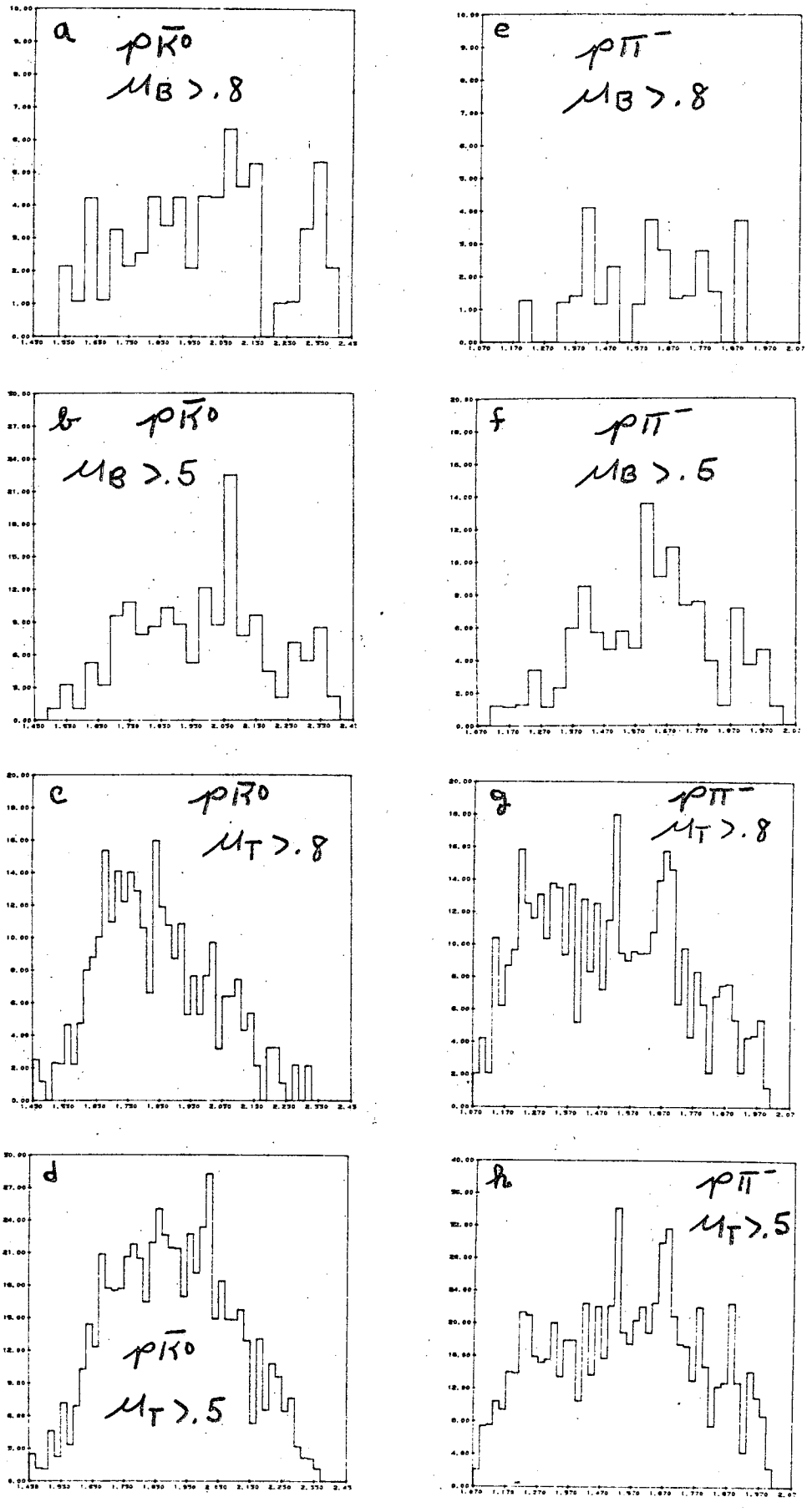
a
pK̄0
μB > .8
e
pπ⁻
μB > .8
b
pK̄0
μB > .5
f
pπ⁻
μB > .5
c
pK̄0
μT > .8
g
pπ⁻
μT > .8
d
pK̄0
μT > .5
h
pπ⁻
μT > .5
NUMBER OF EVENTS
INVARIANT MASS (GeV.)

Figure 15

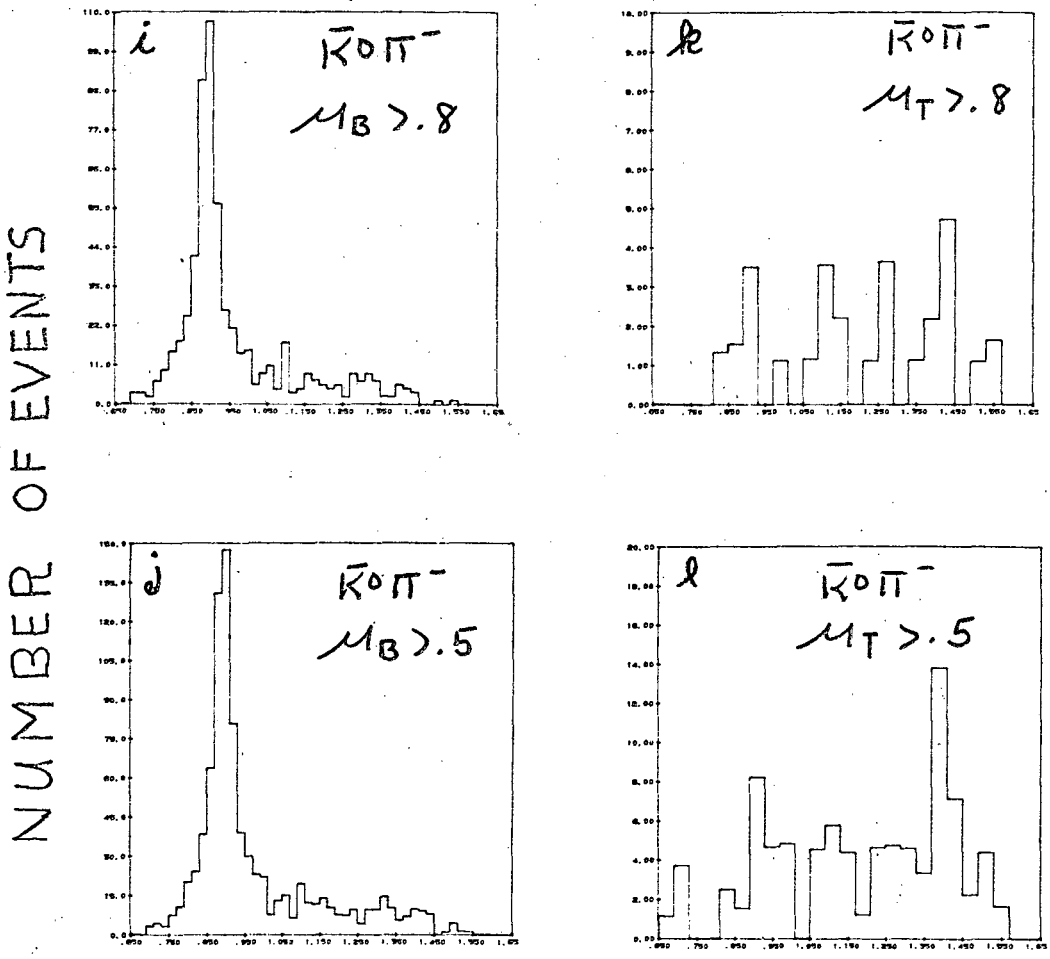
i
$\bar{K}^0\pi^-$
$\mu_B > .8$
k
$\bar{K}^0\pi^-$
$\mu_T > .8$
j
$\bar{K}^0\pi^-$
$\mu_B > .5$
l
$\bar{K}^0\pi^-$
$\mu_T > .5$
NUMBER OF EVENTS
INVARIANT MASS
(GeV.)

Figure 16

Dalitz plots for the reaction $\bar{K}^- p \rightarrow p\bar{K}^0\pi^-$ at each momentum.

a) $p\pi^-$ vs $p\bar{K}^0$, 2.1 GeV/c

b) $\bar{K}^0\pi^-$ vs $p\bar{K}^0$, 2.1 GeV/c

c) $\bar{K}^0\pi^-$ vs $p\pi^-$, 2.1 GeV/c

d) $p\pi^-$ vs $p\bar{K}^0$, 2.45 GeV/c

e) $\bar{K}^0\pi^-$ vs $p\bar{K}^0$, 2.45 GeV/c

f) $\bar{K}^0\pi^-$ vs $p\pi^-$, 2.45 GeV/c

g) $p\pi^-$ vs $p\bar{K}^0$, 2.60 GeV/c

h) $\bar{K}^0\pi^-$ vs $p\bar{K}^0$, 2.60 GeV/c

i) $\bar{K}^0\pi^-$ vs $p\pi^-$, 2.60 GeV/c

j) $p\pi^-$ vs $p\bar{K}^0$, 2.70 GeV/c

k) $\bar{K}^0\pi^-$ vs $p\bar{K}^0$, 2.70 GeV/c

l) $\bar{K}^0\pi^-$ vs $p\pi^-$, 2.70 GeV/c

Figure 16

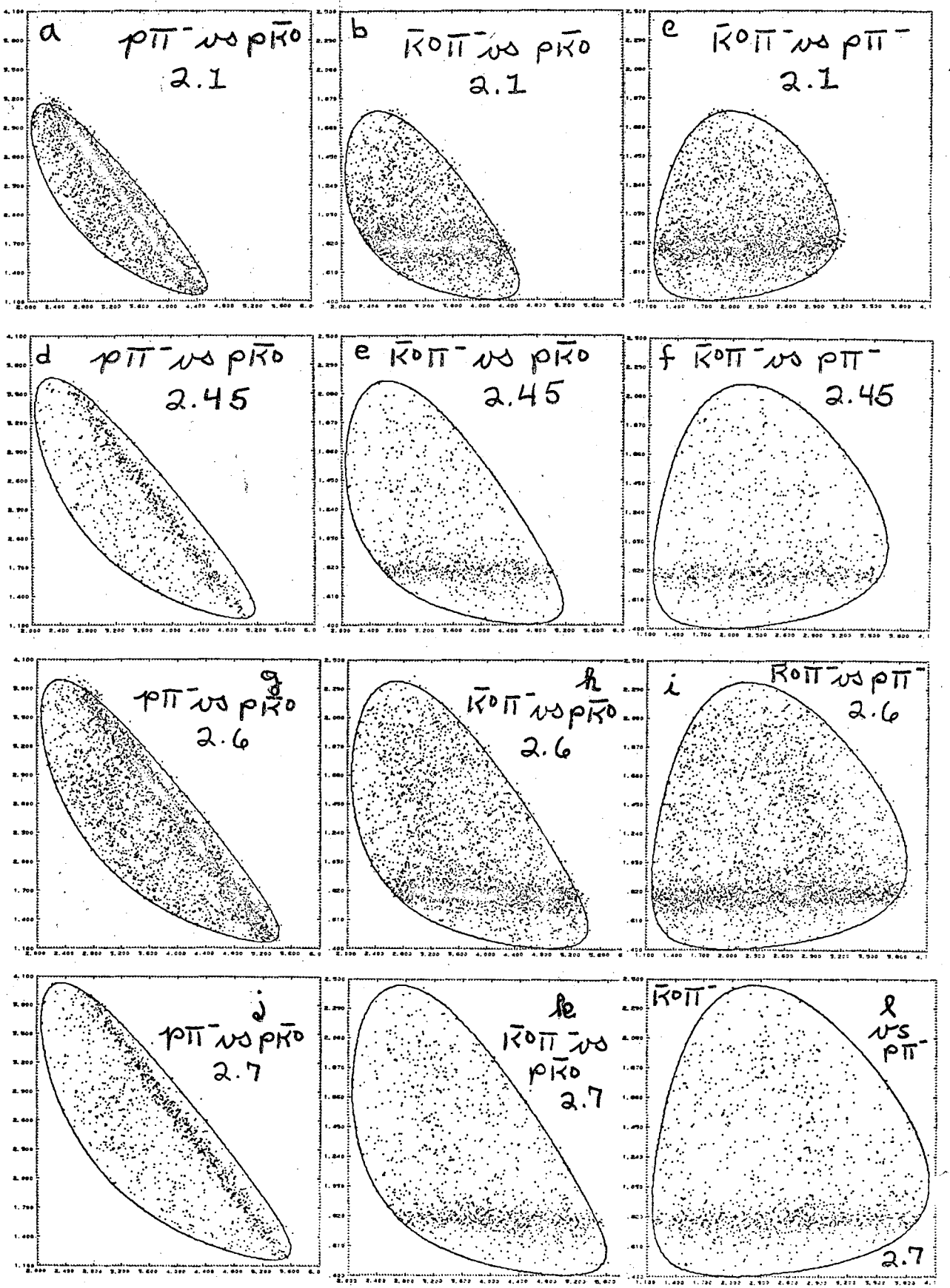
a
pπ⁻ vs pK̄⁰
2.1
b
K̄⁰π⁻ vs pK̄⁰
2.1
c
K̄⁰π⁻ vs pπ⁻
2.1
d
pπ⁻ vs pK̄⁰
2.45
e
K̄⁰π⁻ vs pK̄⁰
2.45
f
K̄⁰π⁻ vs pπ⁻
2.45
g
pπ⁻ vs pK̄⁰
2.6
h
K̄⁰π⁻ vs pK̄⁰
2.6
i
K̄⁰π⁻ vs pπ⁻
2.6
j
pπ⁻ vs pK̄⁰
2.7
k
K̄⁰π⁻ vs pK̄⁰
2.7
l
K̄⁰π⁻ vs pπ⁻
2.7

Figure 17

Chew-Low plots for the reaction $K^- p \rightarrow p\overline{K}^0\pi^-$ at each momentum.

a) $p\overline{K}^0$, 2.1 GeV/c

b) $p\pi^-$, 2.1 GeV/c

c) $\overline{K}^0\pi^-$, 2.1 GeV/c

d) $p\overline{K}^0$, 2.45 GeV/c

e) $p\pi^-$, 2.45 GeV/c

f) $\overline{K}^0\pi^-$, 2.45 GeV/c

g) $p\overline{K}^0$, 2.60 GeV/c

h) $p\pi^-$, 2.60 GeV/c

i) $\overline{K}^0\pi^-$, 2.60 GeV/c

j) $p\overline{K}^0$, 2.7 GeV/c

k) $p\pi^-$, 2.7 GeV/c

l) $\overline{K}^0\pi^-$, 2.7 GeV/c

Figure 17

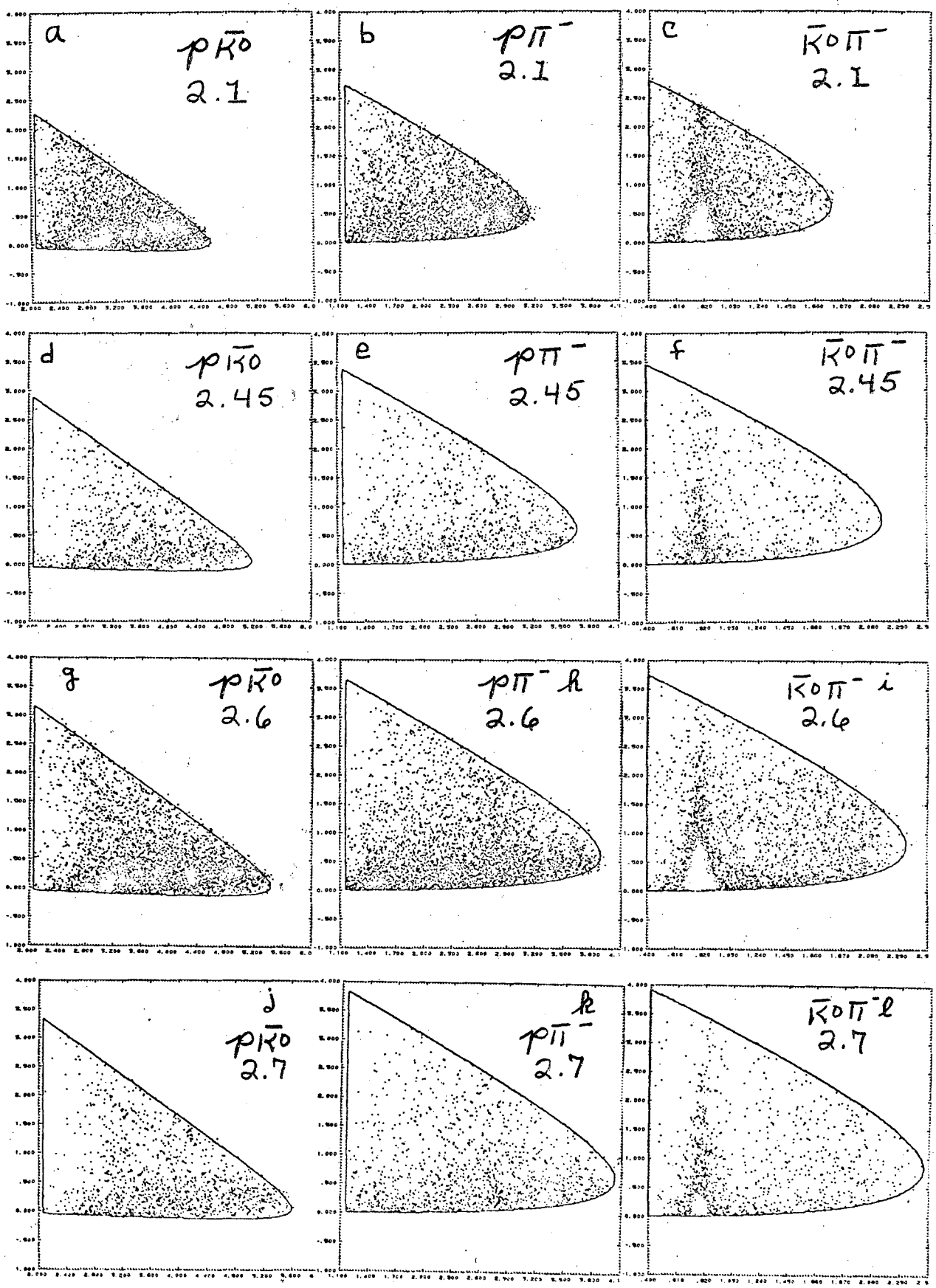
a
$p\bar{K}^0$
2.1
b
$p\pi^-$
2.1
c
$\bar{K}^0\pi^-$
2.1
d
$p\bar{K}^0$
2.45
e
$p\pi^-$
2.45
f
$\bar{K}^0\pi^-$
2.45
g
$p\bar{K}^0$
2.6
h
$p\pi^-$
2.6
i
$\bar{K}^0\pi^-$
2.6
j
$p\bar{K}^0$
2.7
k
$p\pi^-$
2.7
l
$\bar{K}^0\pi^-$
2.7

Figure 18

Invariant mass plots for each momentum with K^{*-} (892) events removed (M^2 $(\overline{K}^o\pi^-)$ $\angle$ .64 or M^2 $(\overline{K}^o\pi^-) > 1.0$)

a) M (pK^o) 2.1 GeV/c

b) M $(p\pi^-)$ 2.1 GeV/c

c) M $(p\overline{K}^o)$ 2.45 GeV/c

d) M $(p\pi^-)$ 2.45 GeV/c

e) M $(p\overline{K}^o)$ 2.60 GeV/c

f) M $(p\pi^-)$ 2.60 GeV/c

g) M $(p\overline{K}^o)$ 2.7 GeV/c

h) M $(p\pi^-)$ 2.7 GeV/c

Figure 18

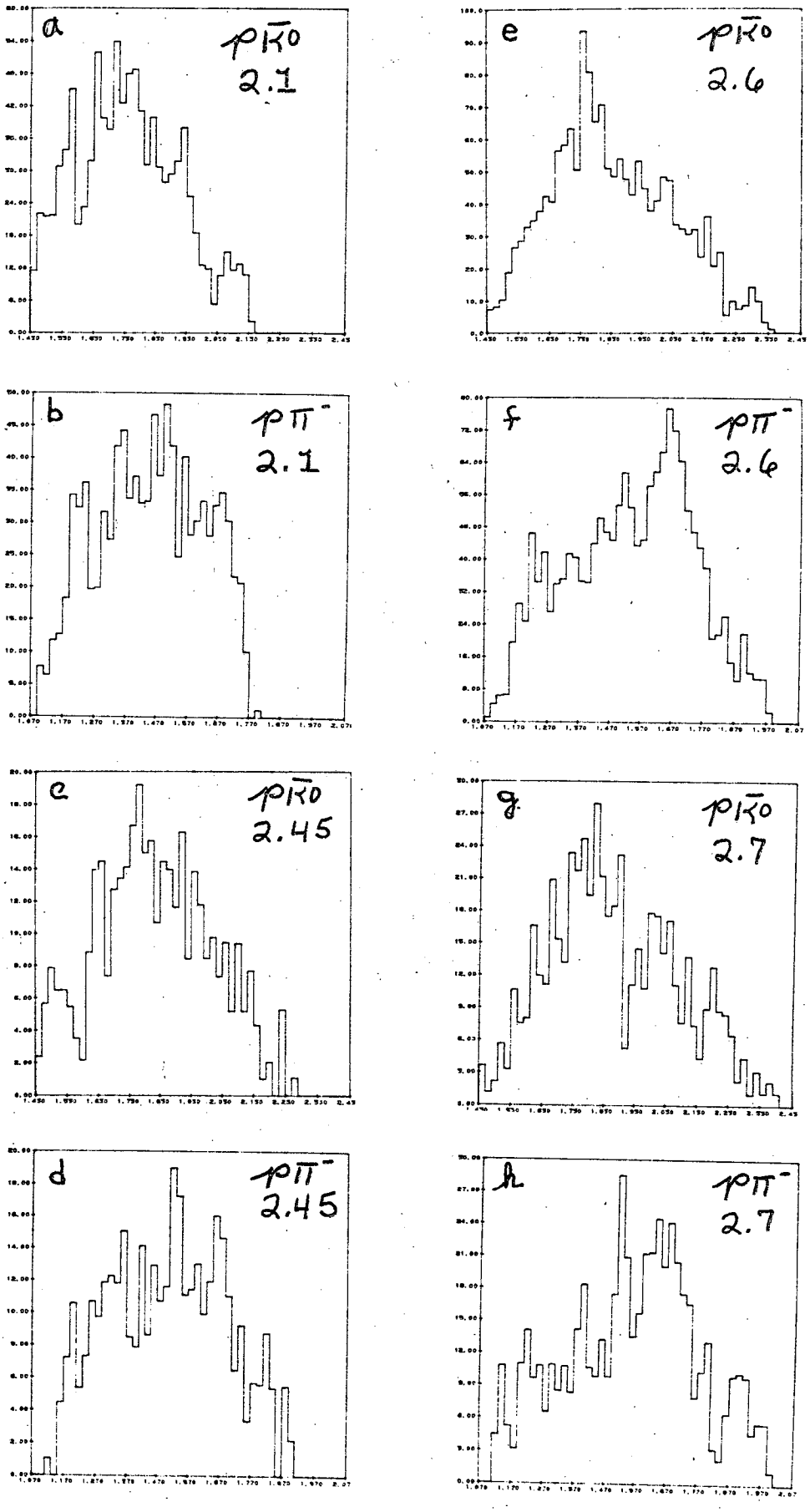
a
pK̄0
2.1
e
pK̄0
2.6
b
pπ⁻
2.1
f
pπ⁻
2.6
c
pK̄0
2.45
g
pK̄0
2.7
d
pπ⁻
2.45
h
pπ⁻
2.7
NUMBER OF EVENTS
INVARIANT MASS (GeV.)

Figure 19

Histograms of invariant mass "M" for various production cosine "μ" cuts at various momenta, for the reaction $K^- p \rightarrow p\overline{K}^0\pi^-$ with K^{*-} (892) events removed ($M^2(\overline{K}^0\pi^-) < .64$ or $M^2(\overline{K}^0\pi^-) > 1.0$).

a) M ($p\overline{K}^0$) ; μ ($p\overline{K}^0$, beam) > .8; 2.1 GeV/c

b) M ($p\overline{K}^0$) ; μ ($p\overline{K}^0$, beam) > .5; 2.1 GeV/c

c) M ($p\overline{K}^0$) ; μ ($p\overline{K}^0$, target) > .8; 2.1 GeV/c

d) M ($p\overline{K}^0$) ; μ ($p\overline{K}^0$, target) > .5; 2.1 GeV/c

e) M ($p\pi^-$) ; μ ($p\pi^-$, beam) > .8; 2.1 GeV/c

f) M ($p\pi^-$) ; μ ($p\pi^-$, beam) > .5; 2.1 GeV/c

g) M ($p\pi^-$) ; μ ($p\pi^-$, target) > .8; 2.1 GeV/c

h) M ($p\pi^-$) ; μ ($p\pi^-$, target) > .5; 2.1 GeV/c

i) M ($p\overline{K}^0$) ; μ ($p\overline{K}^0$, beam) > .8; 2.6 GeV/c

j) M ($p\overline{K}^0$) ; μ ($p\overline{K}^0$, beam) > .5; 2.6 GeV/c

k) M ($p\overline{K}^0$) ; μ ($p\overline{K}^0$, target) > .8; 2.6 GeV/c

l) M ($p\overline{K}^0$) ; μ ($p\overline{K}^0$, target) > .5; 2.6 GeV/c

m) M ($p\pi^-$) ; μ ($p\pi^-$, beam) > .8; 2.6 GeV/c

n) M ($p\pi^-$) ; μ ($p\pi^-$, beam) > .5; 2.6 GeV/c

o) M ($p\pi^-$) ; μ ($p\pi^-$, target) > .8; 2.6 GeV/c

p) M ($p\pi^-$) ; μ ($p\pi^-$, target) > .5; 2.6 GeV/c

q) M ($p\overline{K}^0$) ; μ ($p\overline{K}^0$, beam) > .5; 2.7 GeV/c

r) M ($p\overline{K}^0$) ; μ ($p\overline{K}^0$, target) > .5; 2.7 GeV/c

s) M ($p\pi^-$) ; μ ($p\pi^-$, beam) > .5; 2.7 GeV/c

t) M ($p\pi^-$) ; μ ($p\pi^-$, target) > .5; 2.7 GeV/c

Figure 19

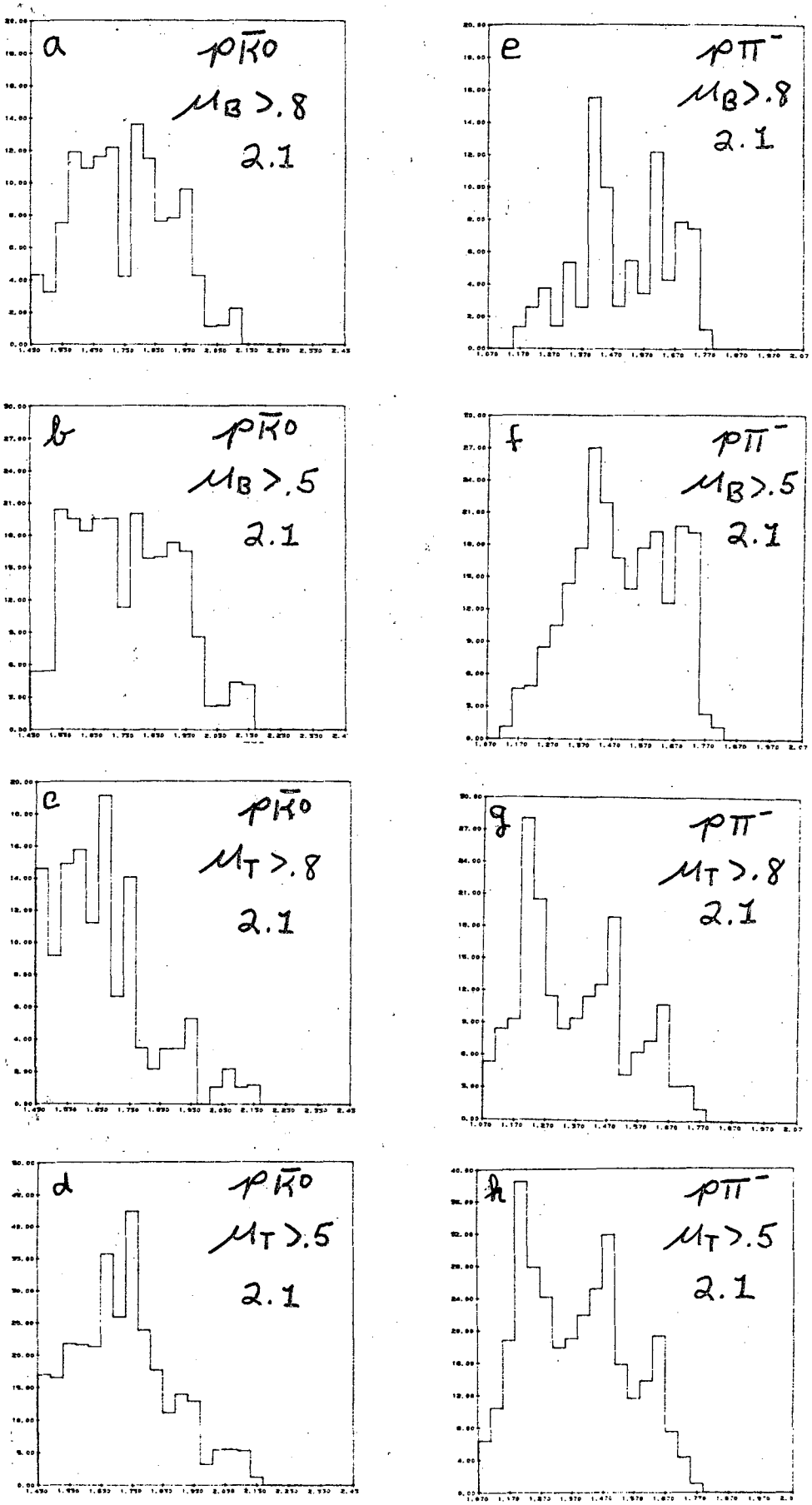
a
pK̄0
μB>.8
2.1
e
pπ⁻
μB>.8
2.1
b
pK̄0
μB>.5
2.1
f
pπ⁻
μB>.5
2.1
c
pK̄0
μT>.8
2.1
g
pπ⁻
μT>.8
2.1
d
pK̄0
μT>.5
2.1
h
pπ⁻
μT>.5
2.1
NUMBER OF EVENTS
INVARIANT MASS (GeV.)

Figure 19

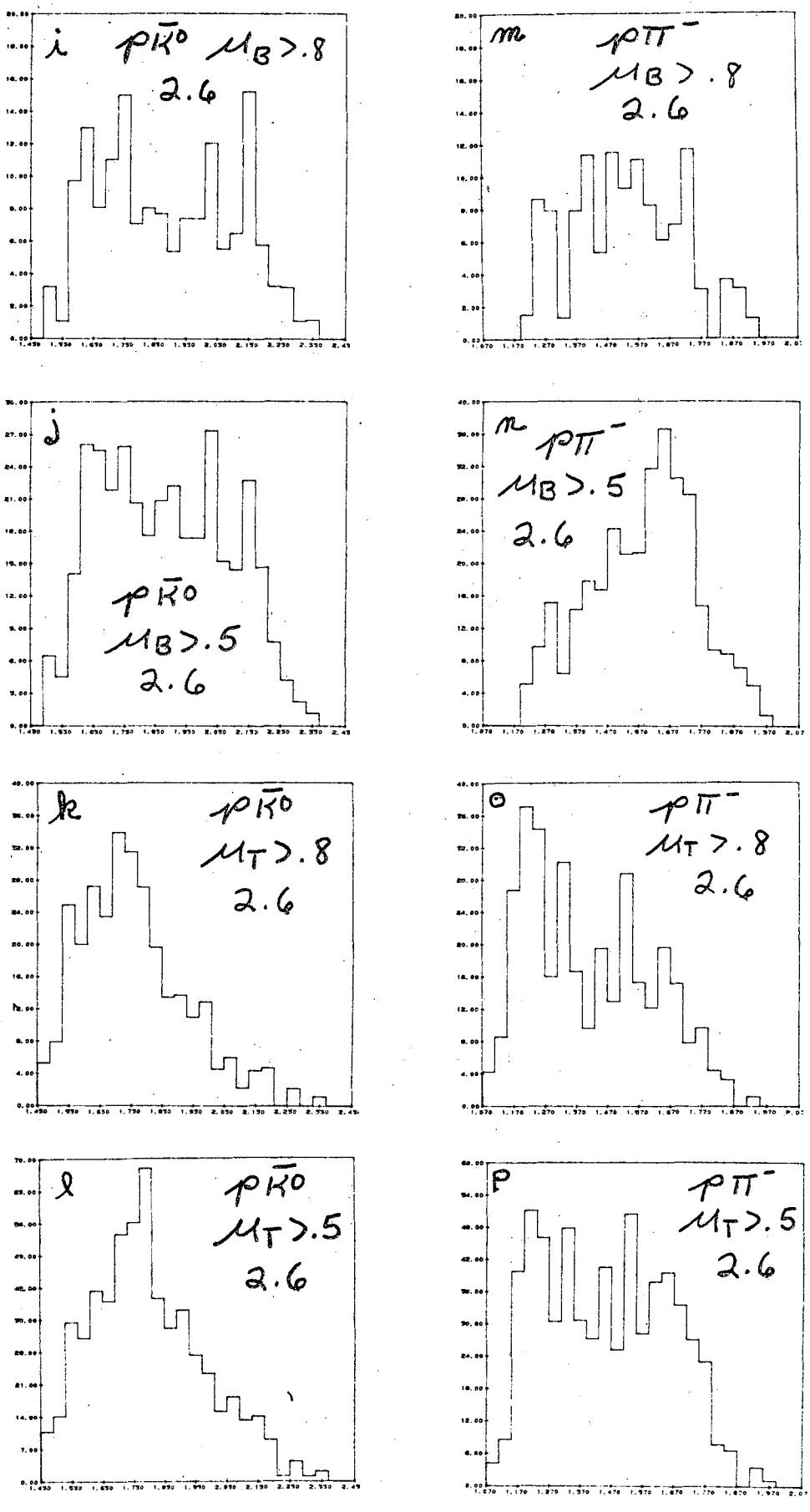
i pK⁰ μB>.8 2.6
m pπ⁻ μB>.8 2.6
j pK⁰ μB>.5 2.6
n pπ⁻ μB>.5 2.6
k pK⁰ μT>.8 2.6
o pπ⁻ μT>.8 2.6
l pK⁰ μT>.5 2.6
p pπ⁻ μT>.5 2.6
NUMBER OF EVENTS
INVARIANT MASS (GeV.)

Figure 19

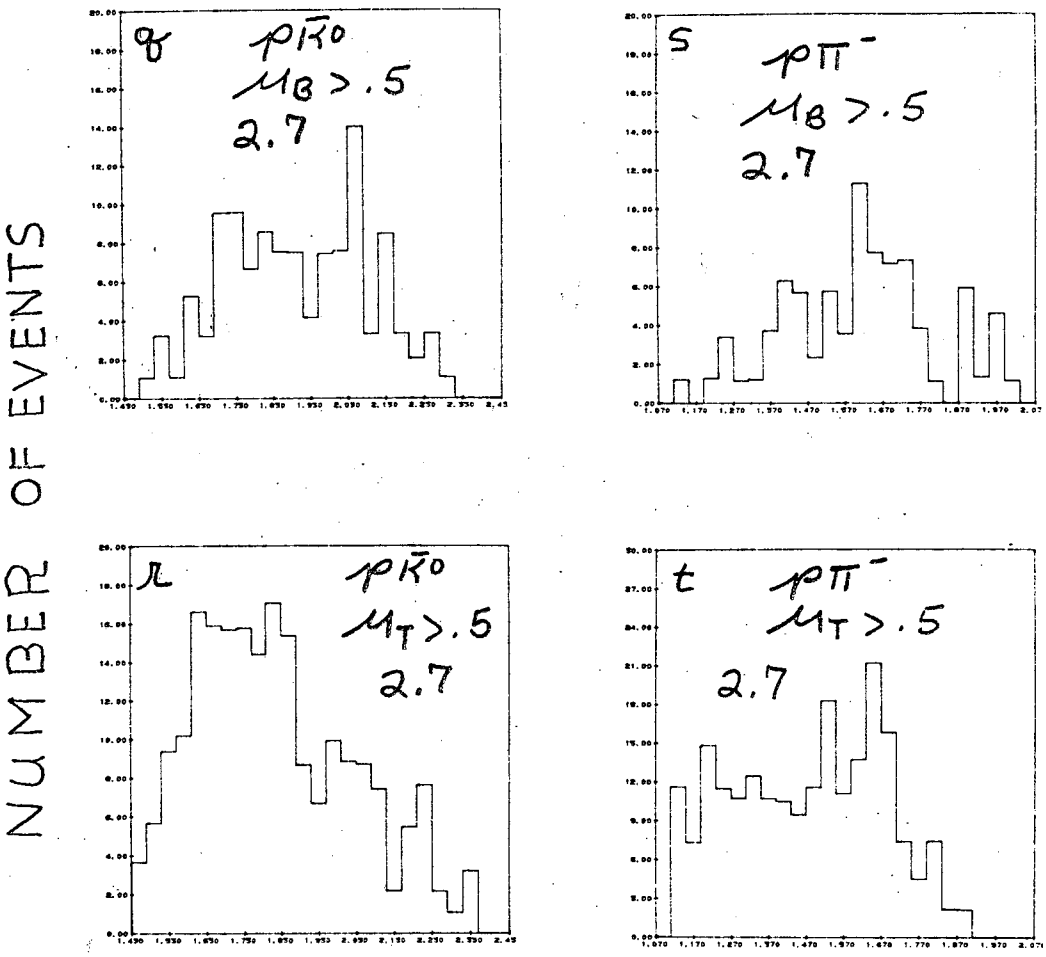
q
$p\bar{K}^0$
$\mu_B > .5$
2.7
s
$p\pi^-$
$\mu_B > .5$
2.7
r
$p\bar{K}^0$
$\mu_T > .5$
2.7
t
$p\pi^-$
$\mu_T > .5$
2.7
NUMBER OF EVENTS
INVARIANT MASS
(GeV.)

Figure 20

Chew-Low plots for the reaction $K^- p \rightarrow p\bar{K}^0\pi^-$ at each momenta with the K^{*-} (890) events removed (M^2 $(\bar{K}^0\pi^-) < .64$ or M^2 $(\bar{K}^0\pi^-) > 1.0$).

a) $p\bar{K}^0$; 2.1 GeV/c

b) $p\pi^-$; 2.1 GeV/c

c) $p\bar{K}^0$; 2.45 GeV/c

d) $p\pi^-$; 2.45 GeV/c

e) $p\bar{K}^0$; 2.60 GeV/c

f) $p\pi^-$; 2.60 GeV/c

g) $p\bar{K}^0$; 2.7 GeV/c

h) $p\pi^-$; 2.7 GeV/c

Figure 20

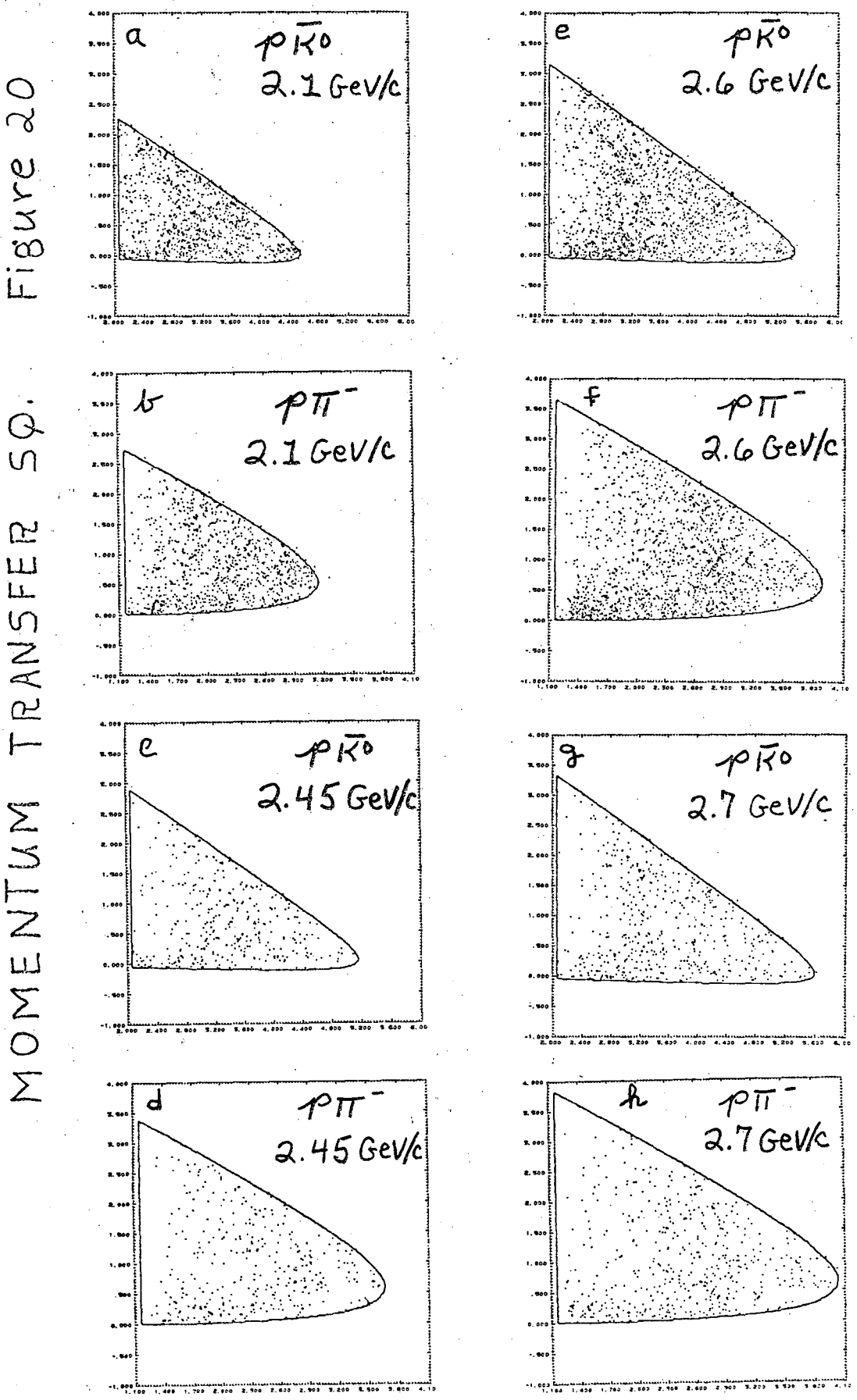
a
$p\bar{K}^0$
2.1 GeV/c
e
$p\bar{K}^0$
2.6 GeV/c
b
$p\pi^-$
2.1 GeV/c
f
$p\pi^-$
2.6 GeV/c
c
$p\bar{K}^0$
2.45 GeV/c
g
$p\bar{K}^0$
2.7 GeV/c
d
$p\pi^-$
2.45 GeV/c
h
$p\pi^-$
2.7 GeV/c
MOMENTUM TRANSFER SQ.
INVARIANT MASS SQ.

Figure 21

Comparisons of the data to the prediction of the maximum likelihood solution for the three invariant mass squared projections and the $\overline{K}^{o}\pi^{-}$ azimuth angle for the reaction $K^{-}p \rightarrow p\overline{K}^{o}\pi^{-}$ for each momentum.

a) $p\overline{K}^{o}$ invariant mass squared, 2.1 GeV/c.

b) $p\pi^{-}$ invariant mass squared, 2.1 GeV/c.

c) $K^{o}\pi^{-}$ invariant mass squared, 2.1 GeV/c.

d) $\overline{K}^{o}\pi^{-}$ azimuth angle, 2.1 GeV/c.

e) $p\overline{K}^{o}$ invariant mass squared, 2.45 GeV/c.

f) $p\pi^{-}$ invariant mass squared, 2.45 GeV/c.

g) $\overline{K}^{o}\pi^{-}$ invariant mass squared, 2.45 GeV/c.

h) $K^{o}\pi^{-}$ azimuth angle, 2.45 GeV/c.

i) $p\overline{K}^{o}$ invariant mass squared, 2.60 GeV/c.

j) $p\pi^{-}$ invariant mass squared, 2.60 GeV/c.

k) $\overline{K}^{o}\pi^{-}$ invariant mass squared, 2.60 GeV/c.

l) $\overline{K}^{o}\pi^{-}$ azimuth angle, 2.60 GeV/c.

m) $p\overline{K}^{o}$ invariant mass squared, 2.70 GeV/c.

n) $p\pi^{-}$ invariant mass squared, 2.70 GeV/c.

o) $\overline{K}^{o}\pi^{-}$ invariant mass squared, 2.70 GeV/c.

p) $\overline{K}^{o}\pi^{-}$ azimuth angle, 2.70 GeV/c

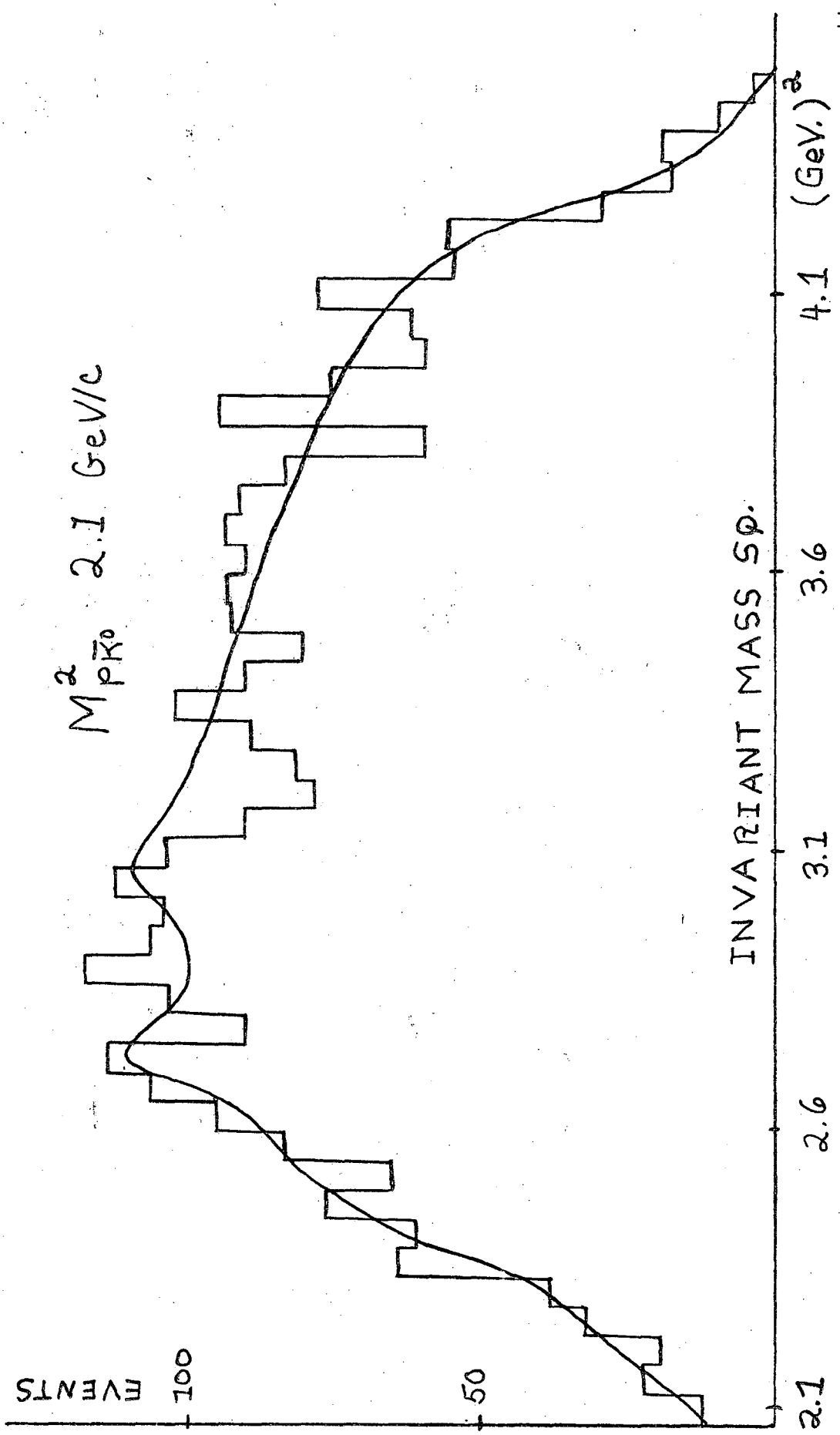
EVENTS
100
50
2.1
2.6
3.1
3.6
4.1
(GeV.)²
INVARIANT MASS SQ.
$M^2_{p\bar{K}^0}$ 2.1 GeV/c

Figure 21a

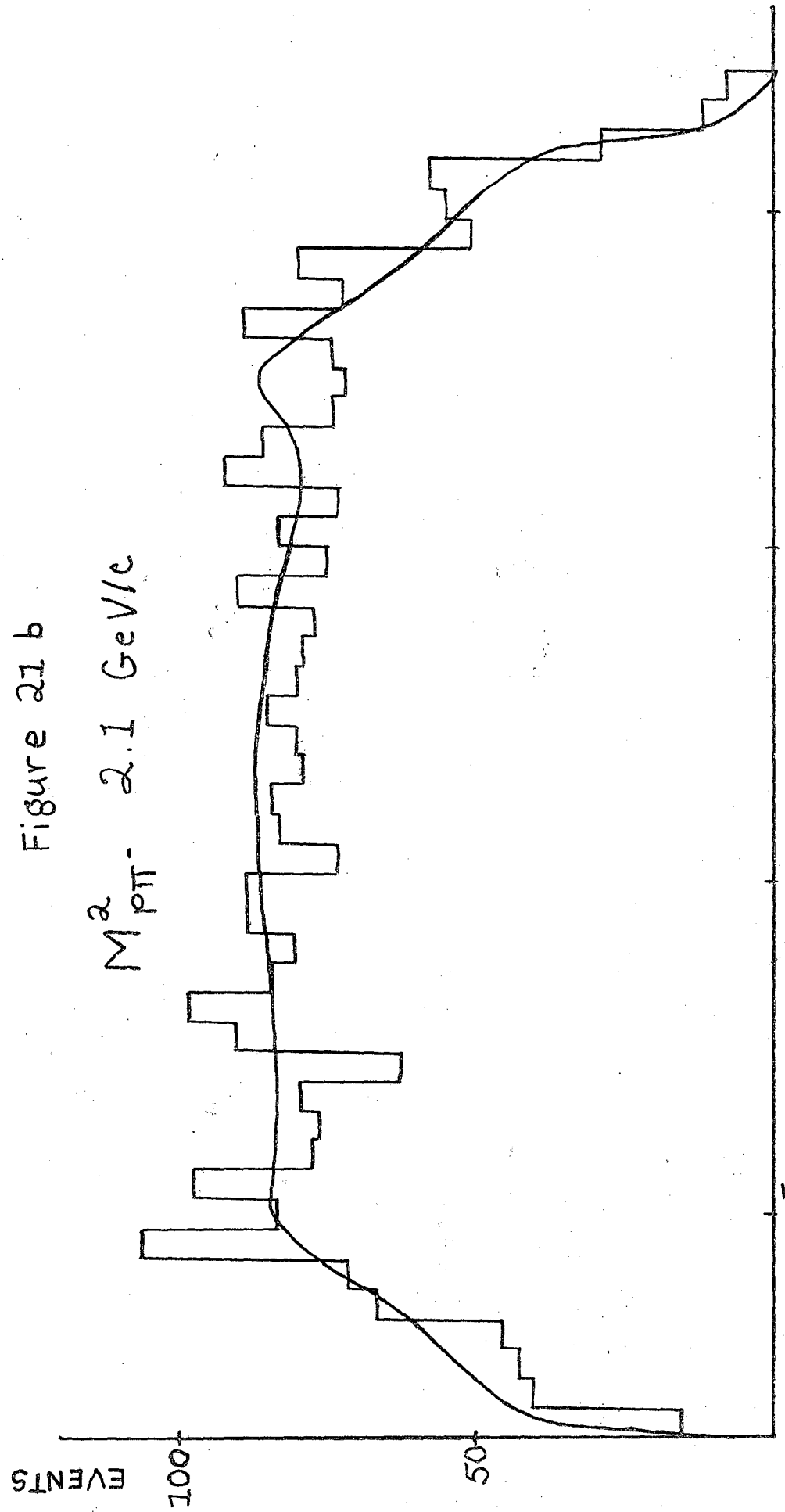

Figure 21 b

$M^2_{p\pi^-}$ 2.1 GeV/c

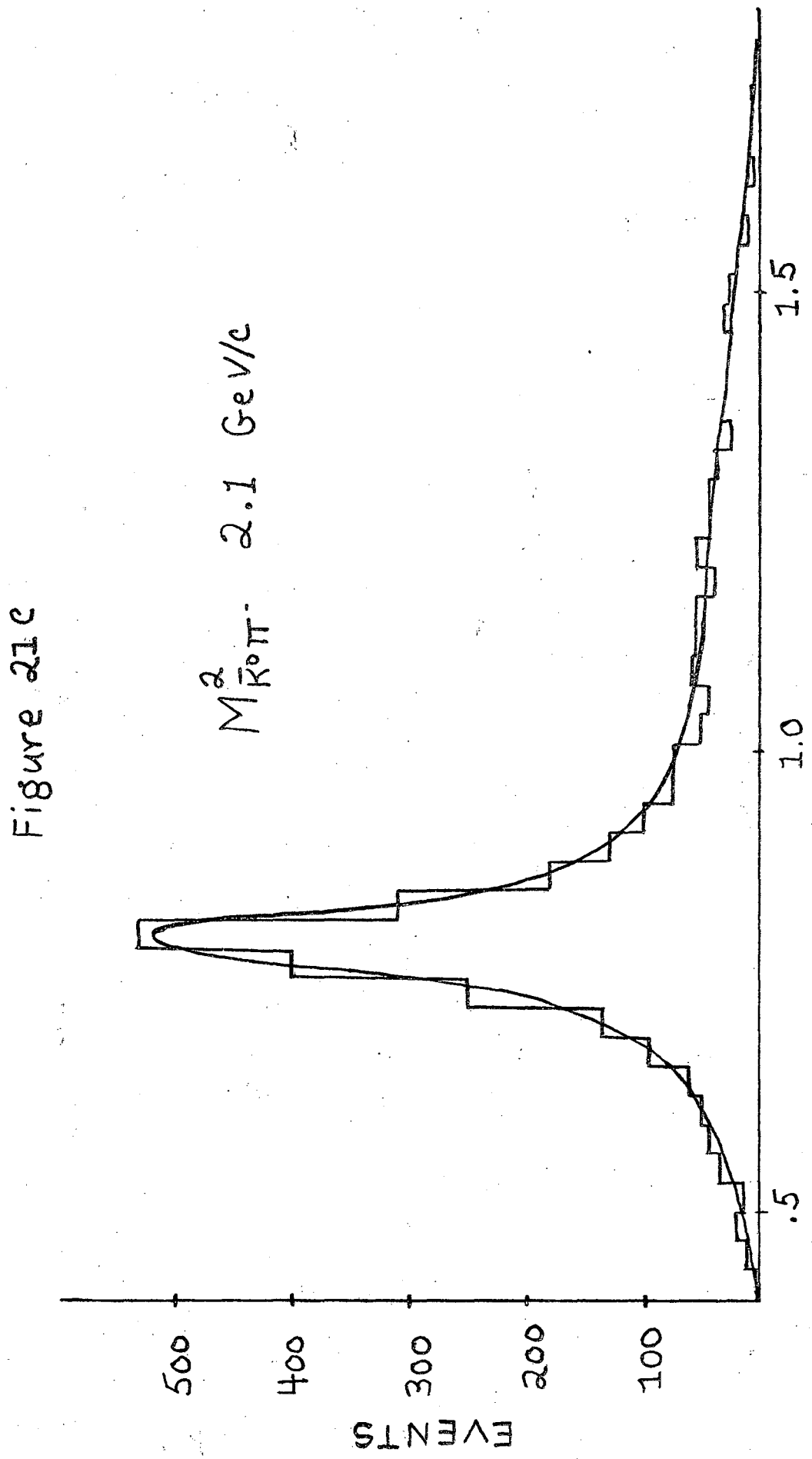
EVENTS
500
400
300
200
100
.5
1.0
1.5
INVARIANT MASS SQ. (GeV.)²
$M^2_{\bar{K}^0\pi^-}$ 2.1 GeV/c

Figure 21c

Figure 21d

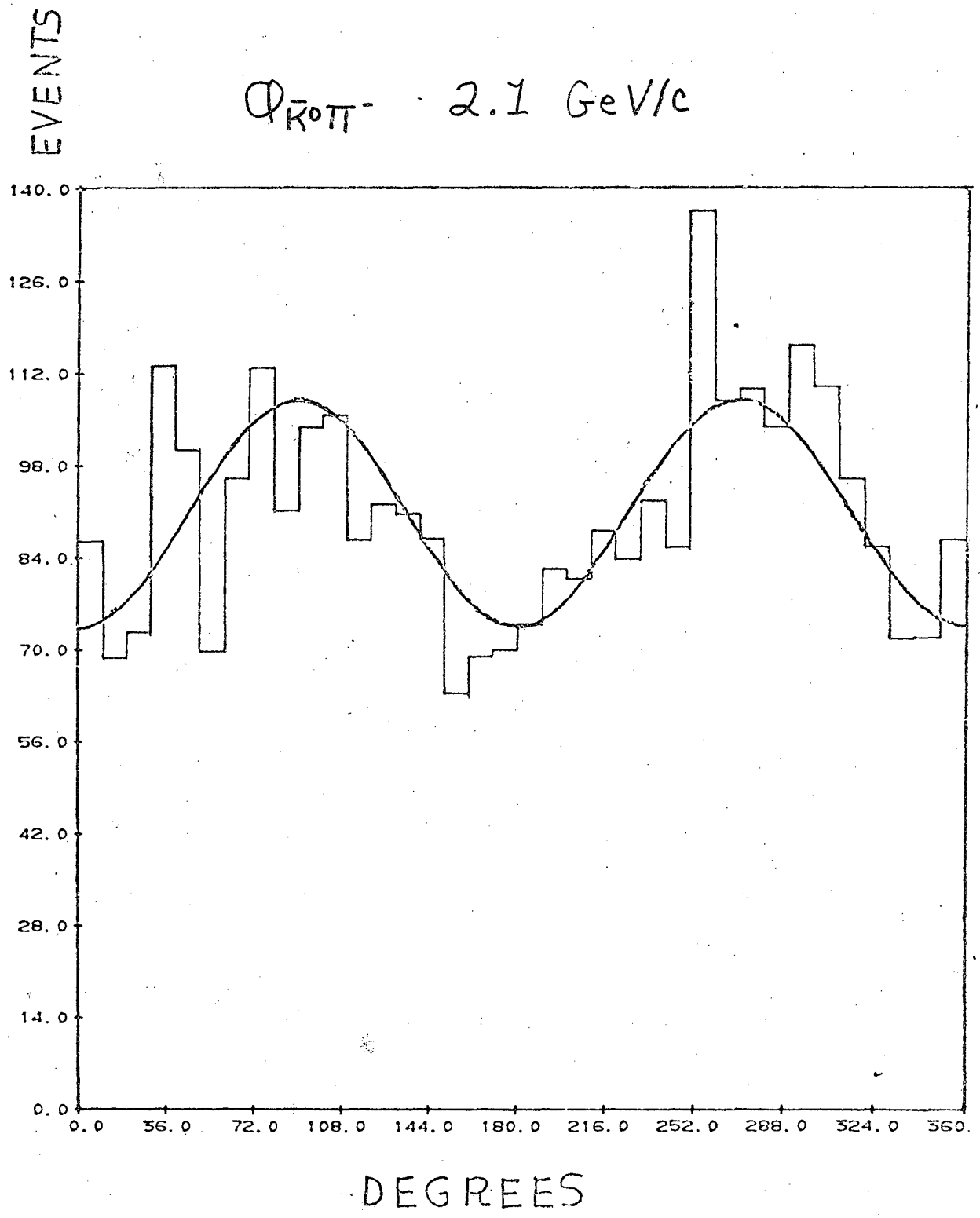
EVENTS
$Q_{\bar{K}^0\pi^-}$ 2.1 GeV/c
140.0
126.0
112.0
98.0
84.0
70.0
56.0
42.0
28.0
14.0
0.0
0.0
36.0
72.0
108.0
144.0
180.0
216.0
252.0
288.0
324.0
360.
DEGREES

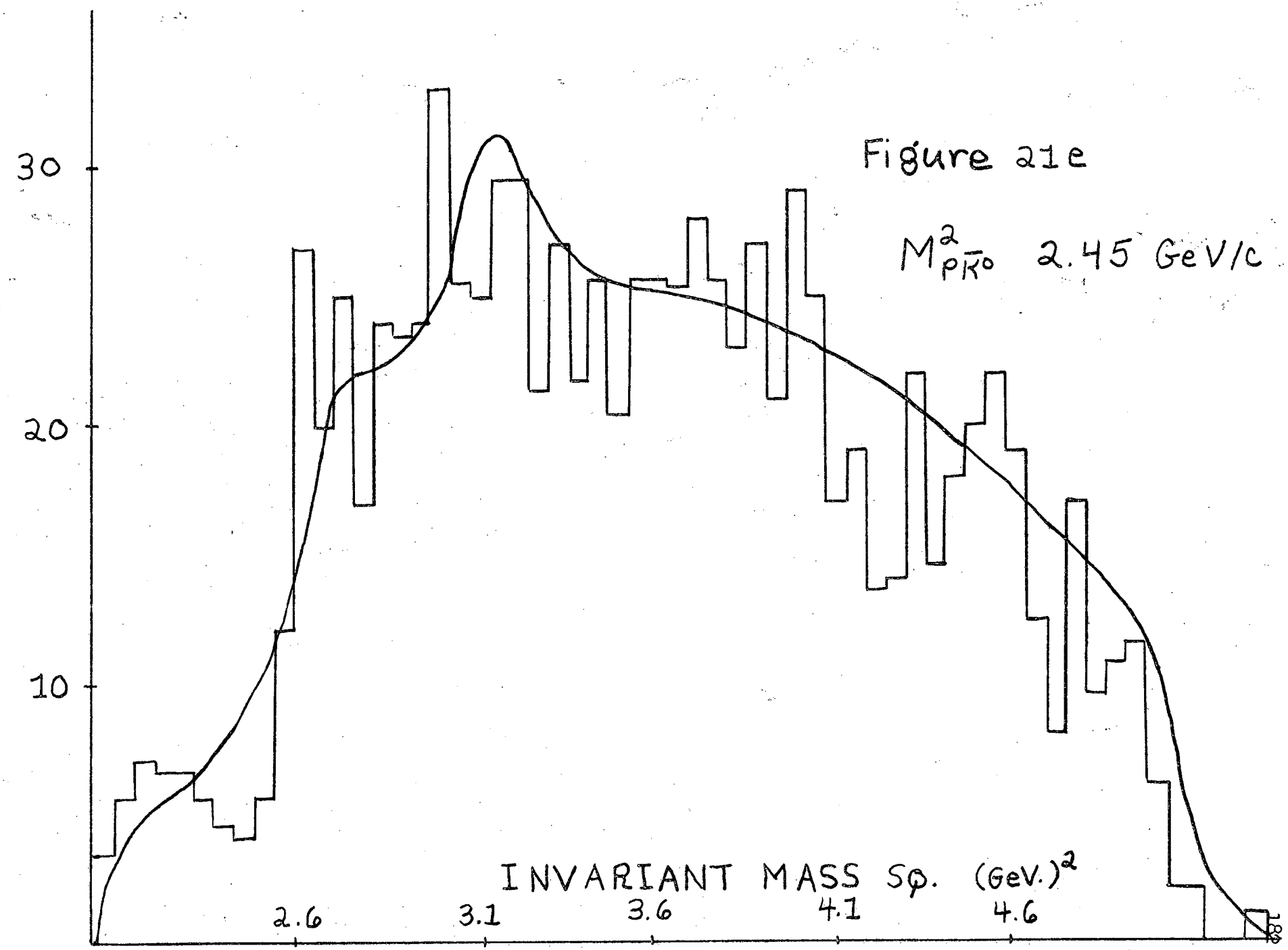

Figure 21e

$M^2_{PK^0}$ 2.45 GeV/c

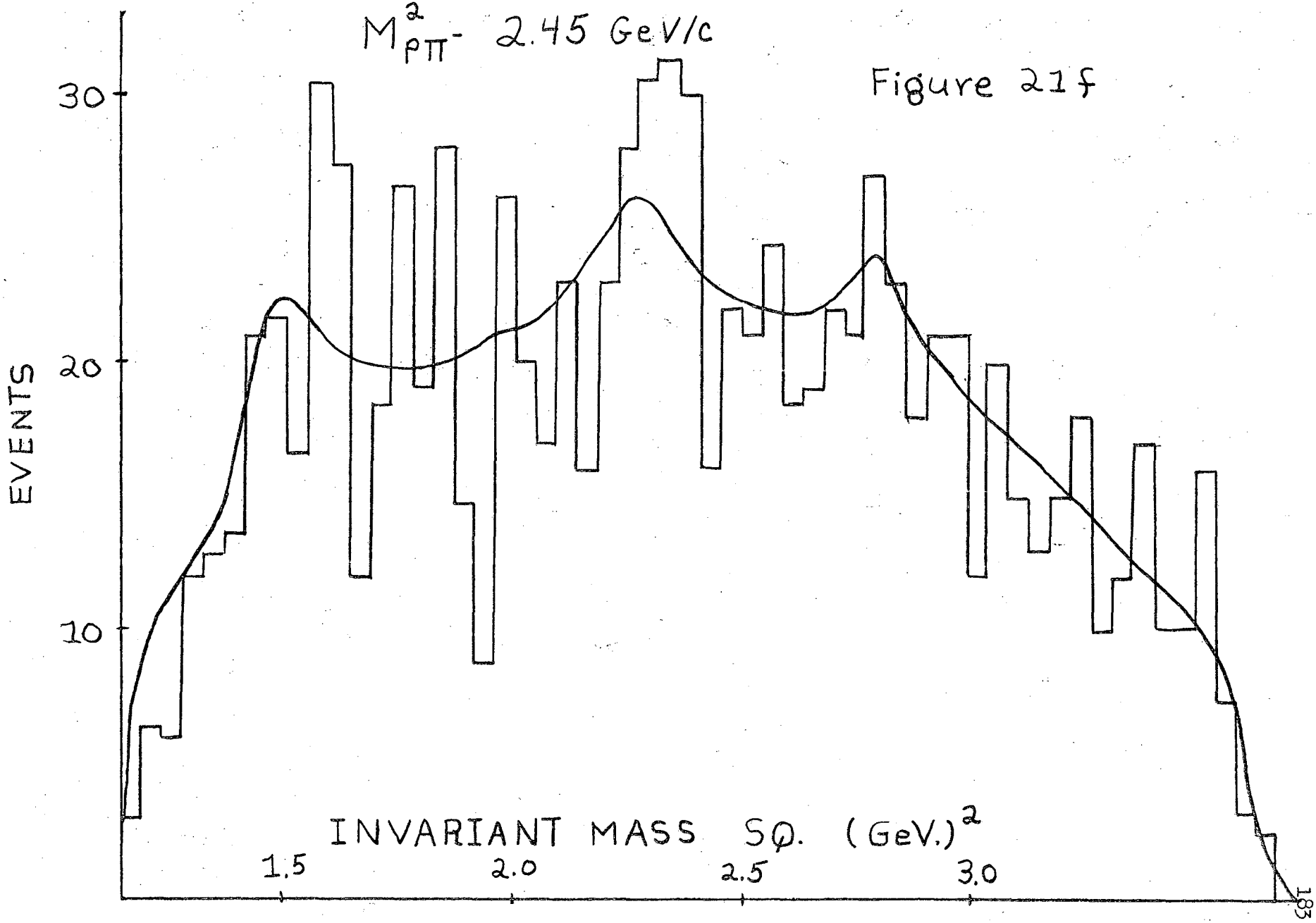
$M^2_{p\pi^-}$ 2.45 GeV/c
30
20
10
EVENTS
INVARIANT MASS SQ. (GeV.)^2
1.5
2.0
2.5
3.0
183

Figure 21f

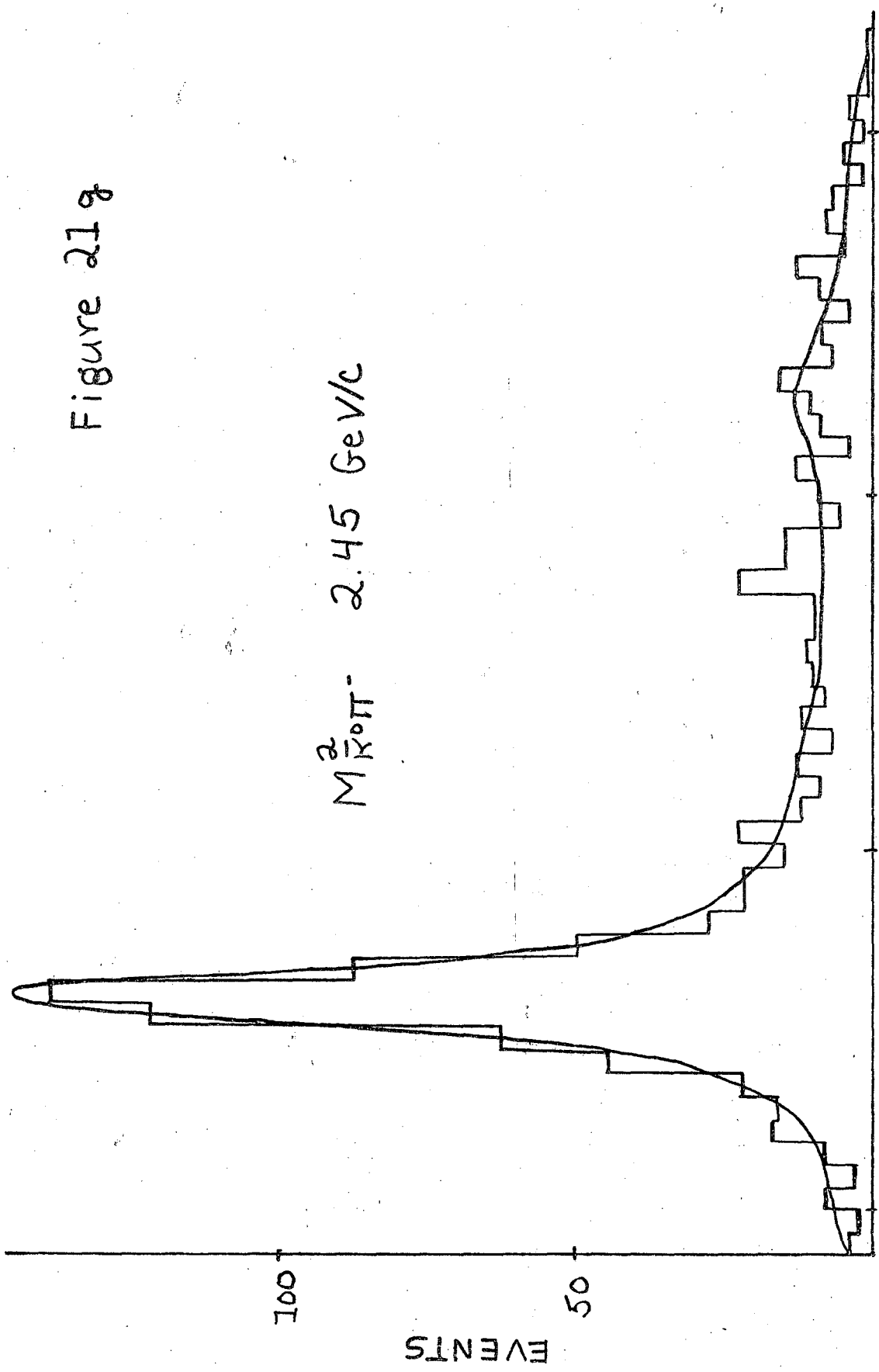
EVENTS
100
50
.5
(GeV)²
1.0 INVARIANT
1.5 MASS SQ.
2.0
$M^2_{\bar{K}^0\pi^-}$ 2.45 GeV/c

Figure 21g

Figure 21 h

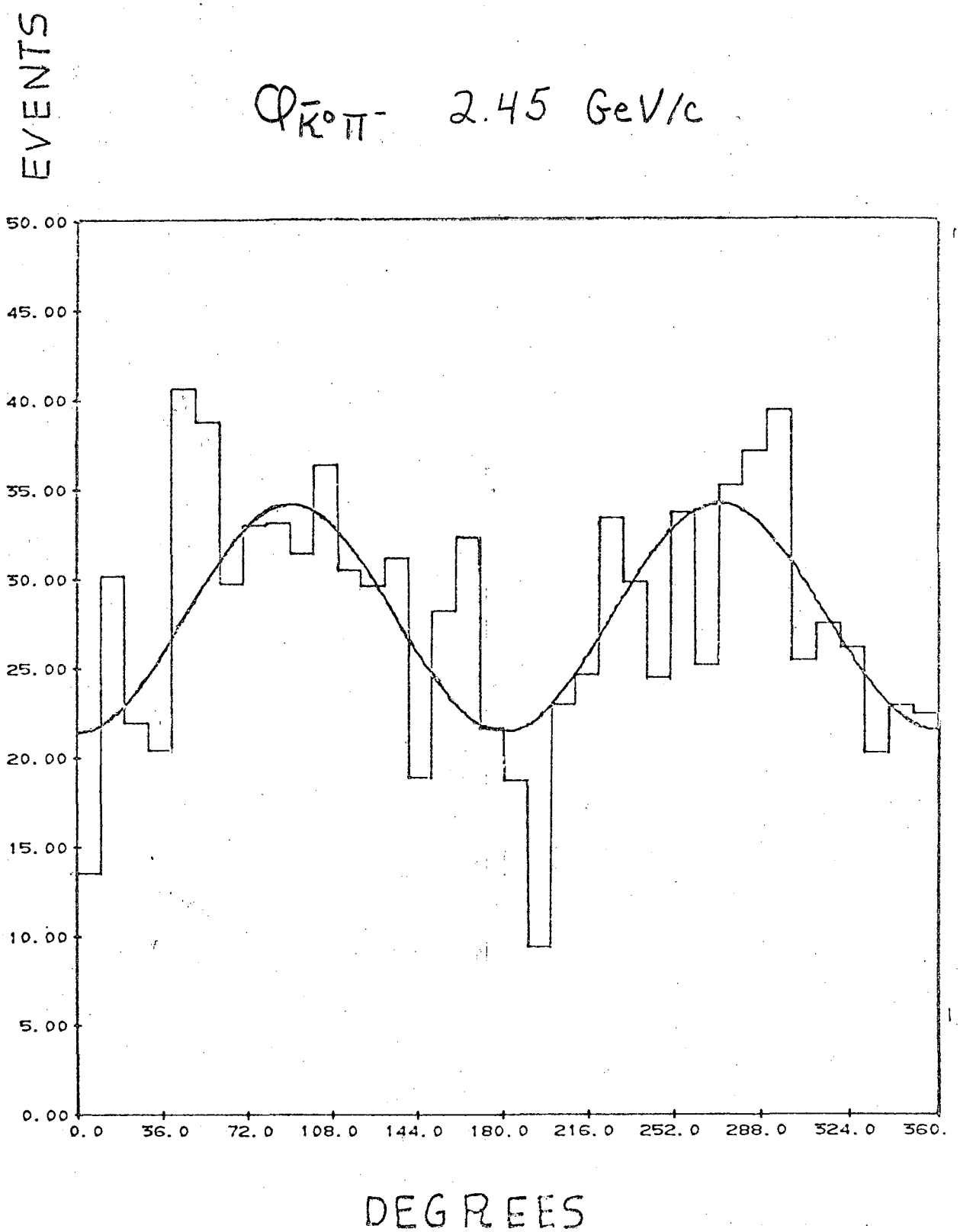
EVENTS
$\Phi_{\bar{K}^0\pi^-}$ 2.45 GeV/c
50.00
45.00
40.00
35.00
30.00
25.00
20.00
15.00
10.00
5.00
0.00
0.0
36.0
72.0
108.0
144.0
180.0
216.0
252.0
288.0
324.0
360.
DEGREES

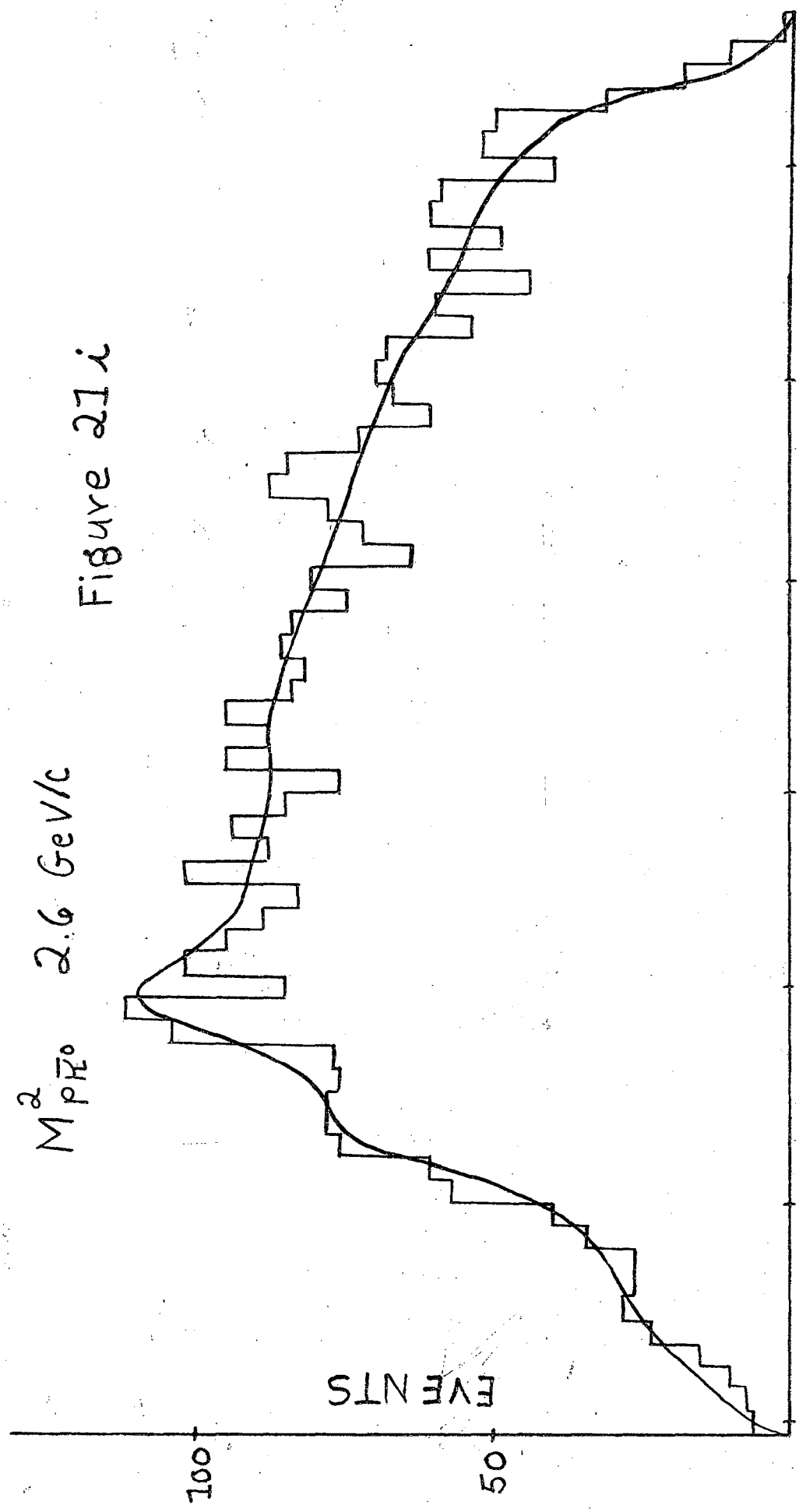
EVENTS
100
50
2.1
2.6
3.1
3.6
4.1
4.6
5.1
INVARIANT MASS SQ. (GeV.)²
$M^2_{p\bar{K}^0}$ 2.6 GeV/c

Figure 21i

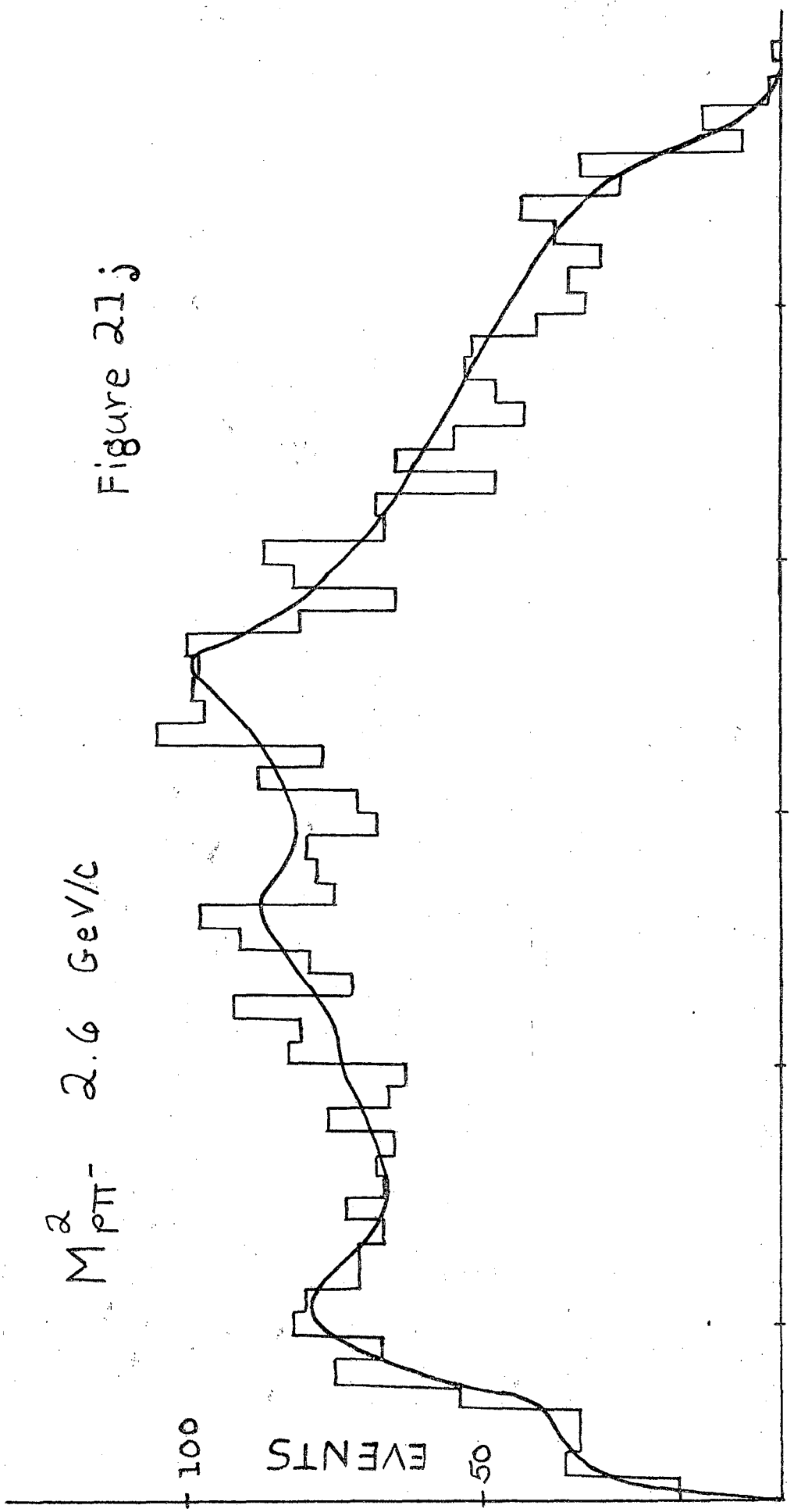
100
50
EVENTS
1.5
2.0
2.5
3.0
3.5
INVARIANT MASS SQ. (GeV.)^2
$M^2_{p\pi^-}$ 2.6 GeV/c

Figure 21 j

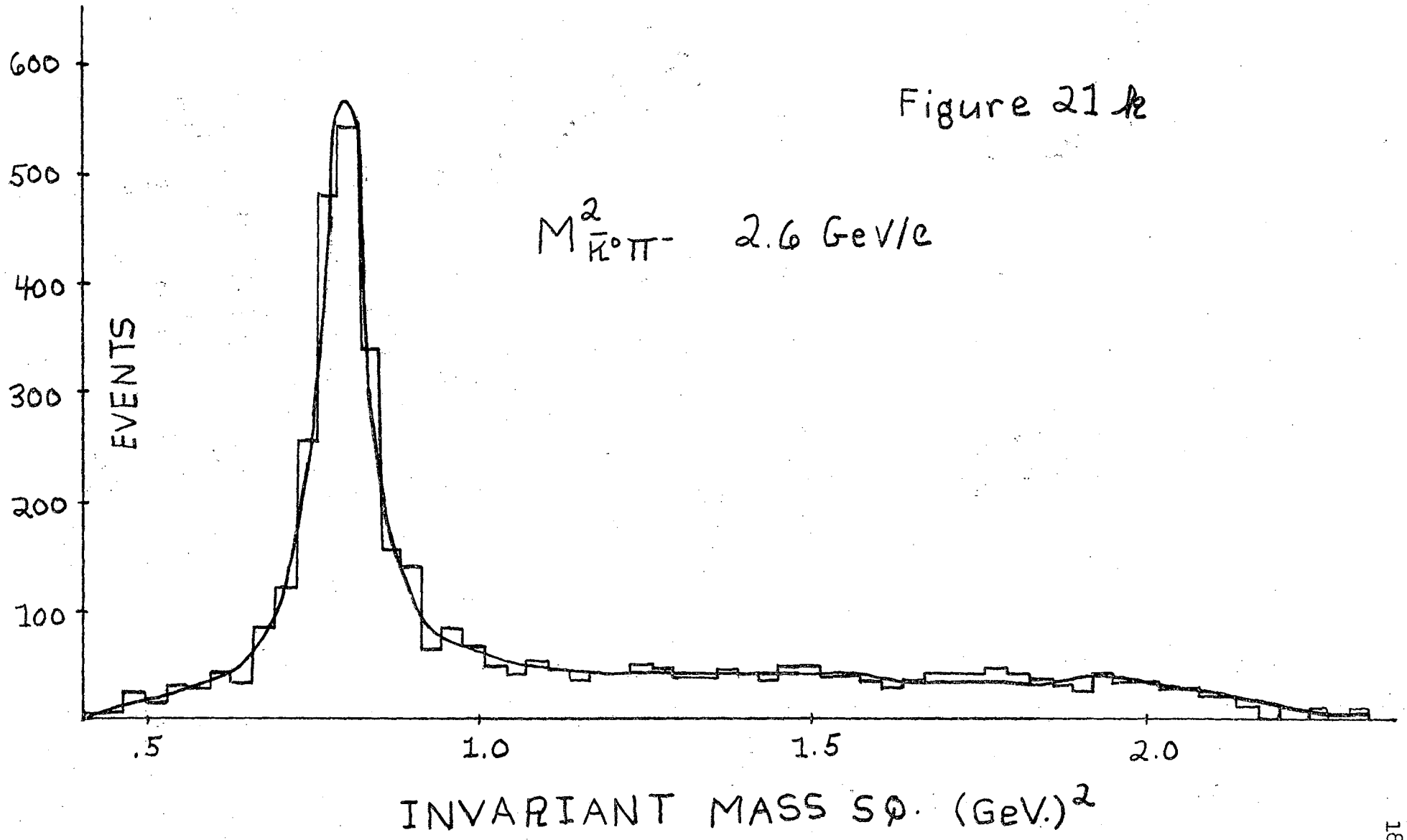
Figure 21 k
$M^2_{\bar{K}^0\pi^-}$ 2.6 GeV/c
600
500
400
300
200
100
EVENTS
.5
1.0
1.5
2.0
INVARIANT MASS SQ. (GeV.)^2

Figure 21 ℓ

$\Phi_{\bar{K}^0\pi^-}$ 2.6 GeV/c

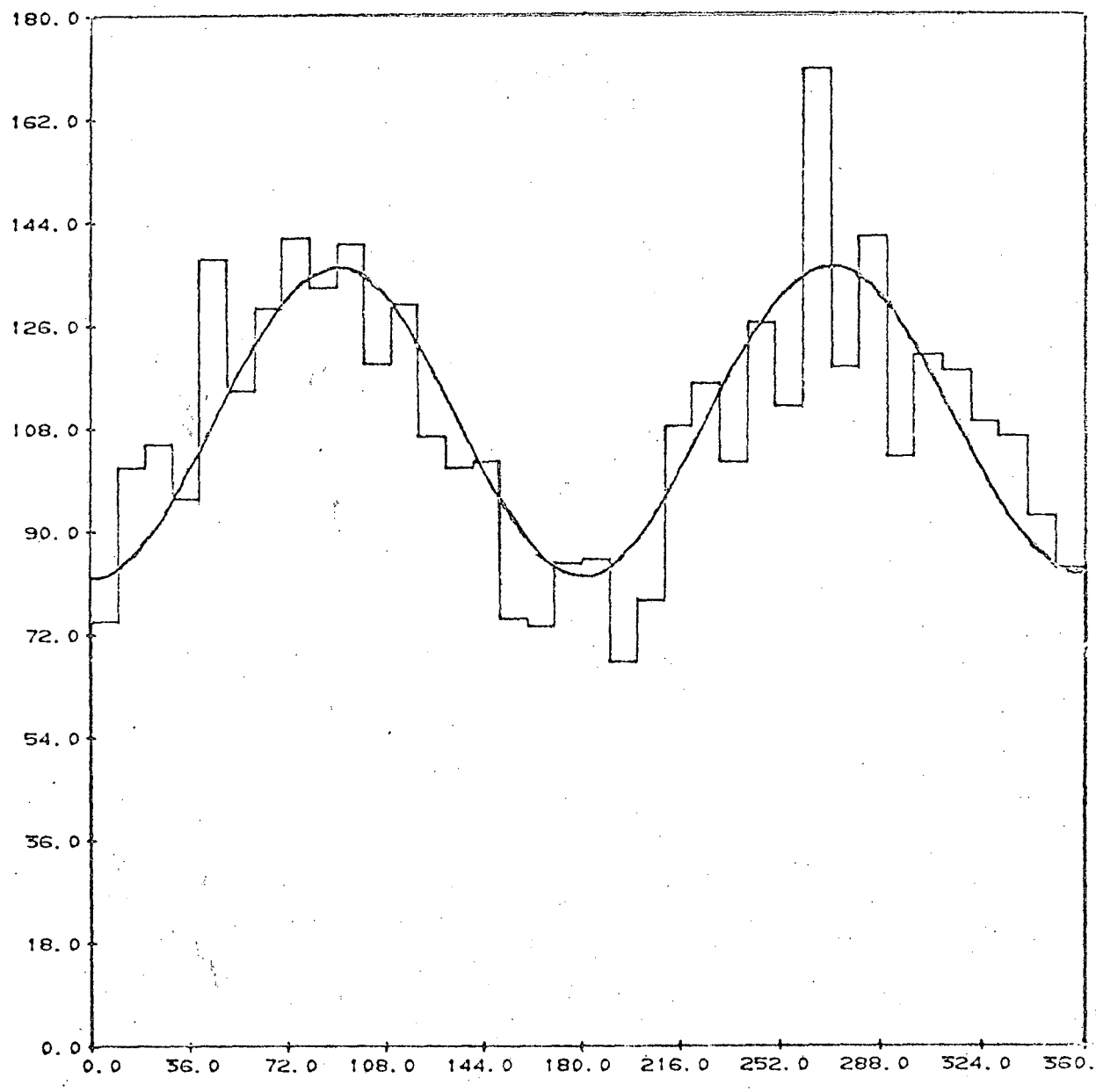

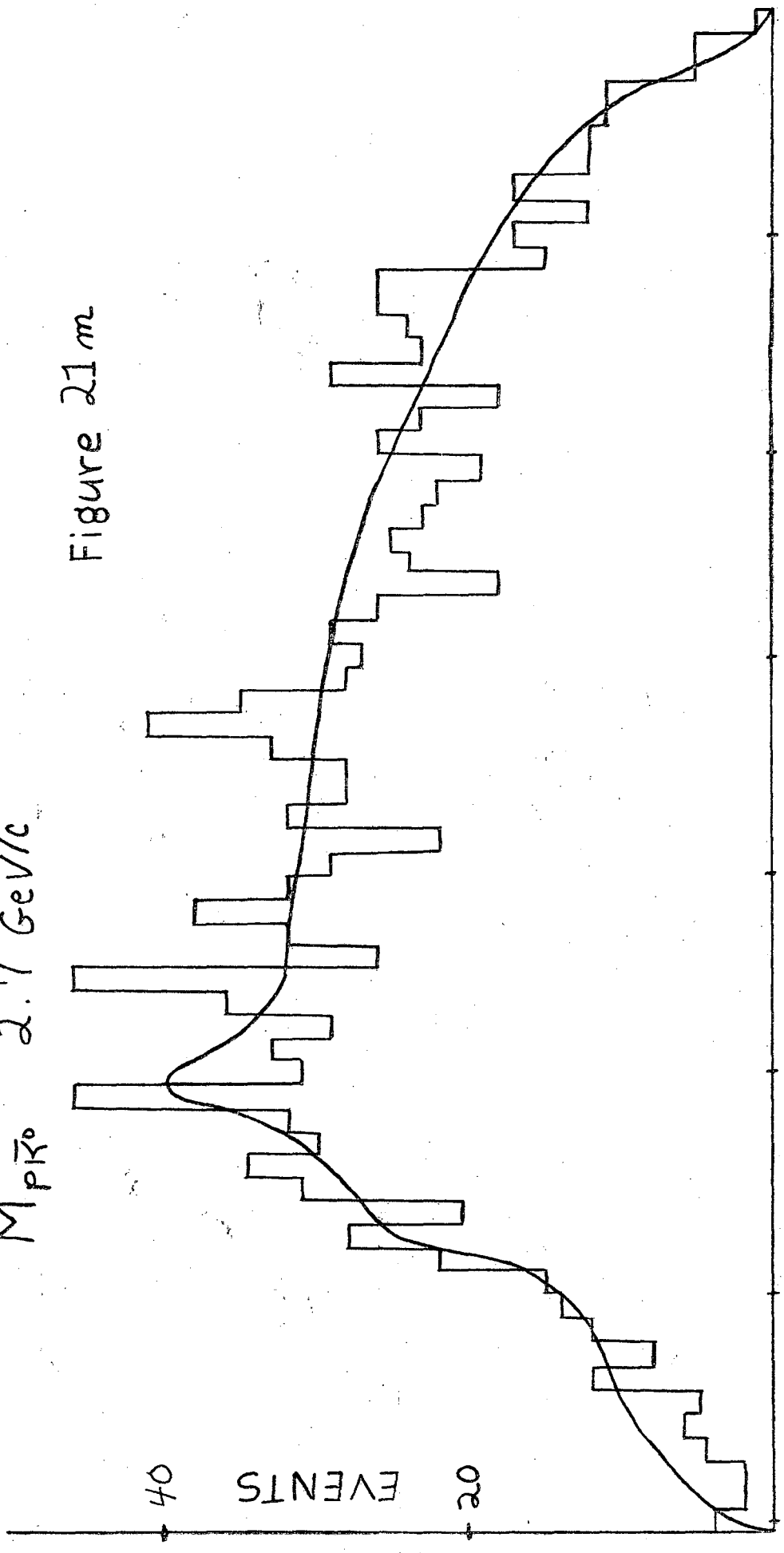
EVENTS
40
20
2.1
2.6
3.1
3.6
4.1
4.6
5.1
INVARIANT MASS SQ. (GeV.)²
$M^2_{p\bar{K}^0}$ 2.7 GeV/c

Figure 21 m

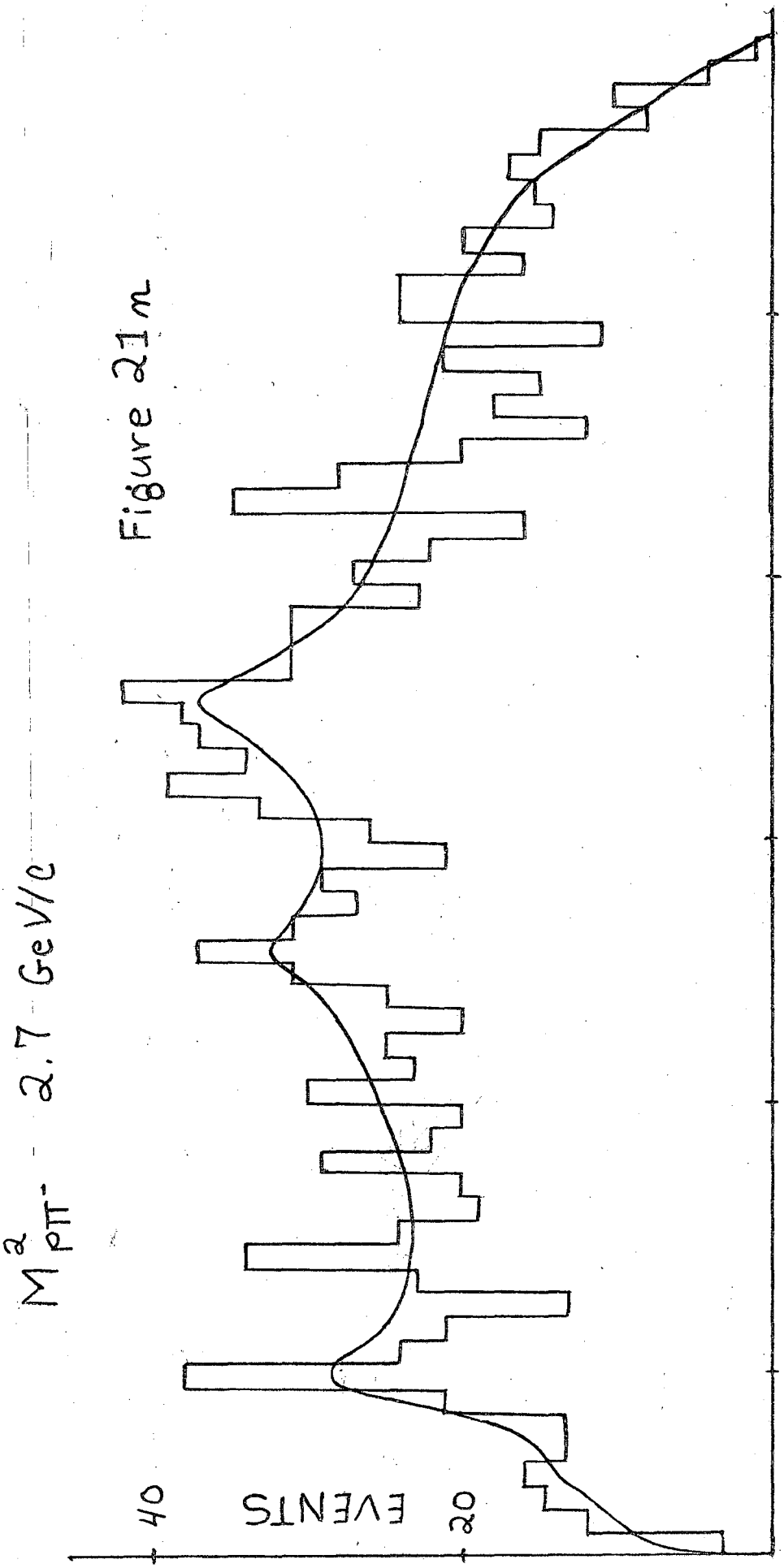
Figure 21m
$M^2_{p\pi^-}$ 2.7 GeV/c
EVENTS
40
20
1.5
2.0
2.5
3.0
3.5
INVARIANT MASS SQ. $(GeV.)^2$

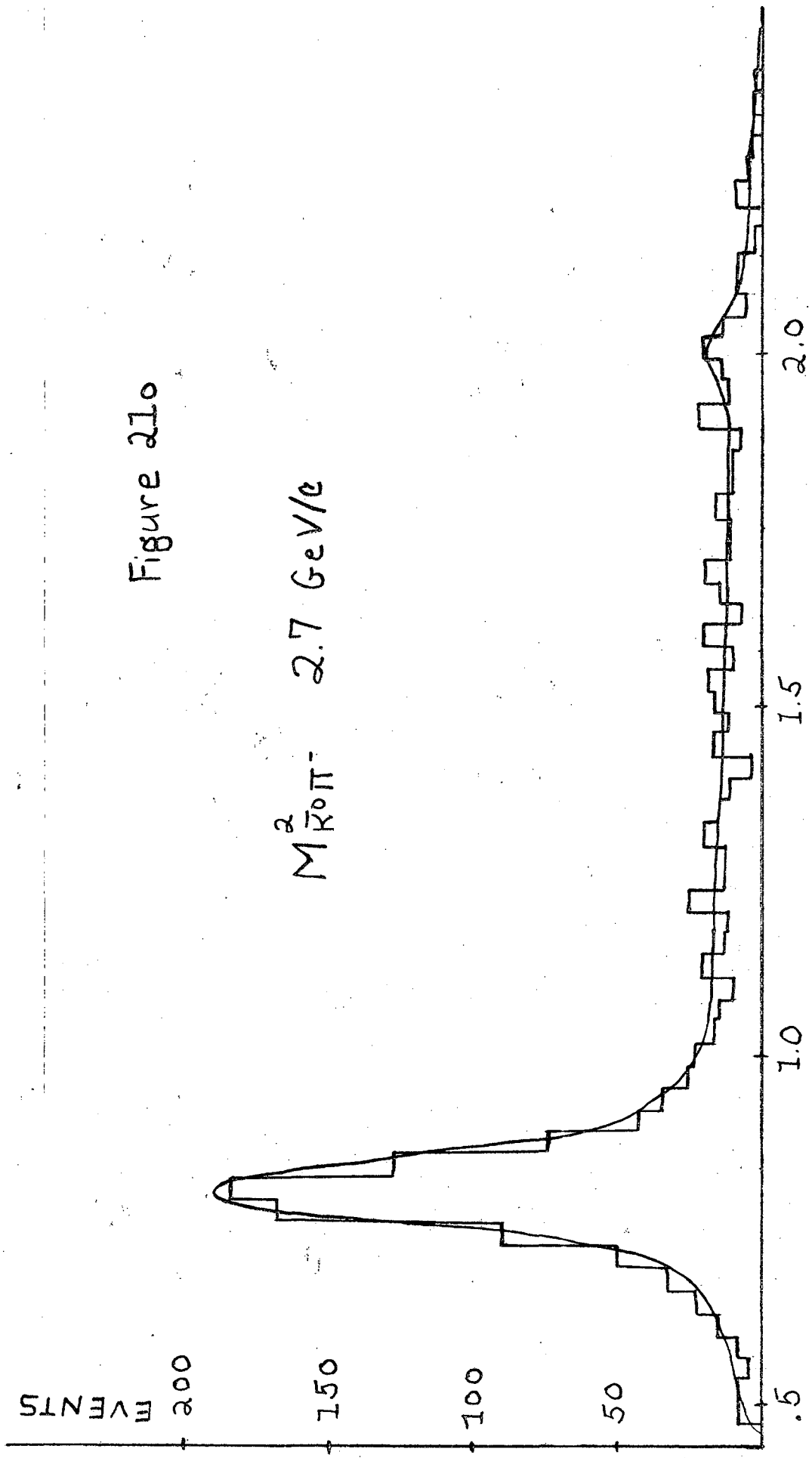

Figure 21o

$M^2_{\bar{K}^0\pi^-}$ 2.7 GeV/c

Figure 21 p

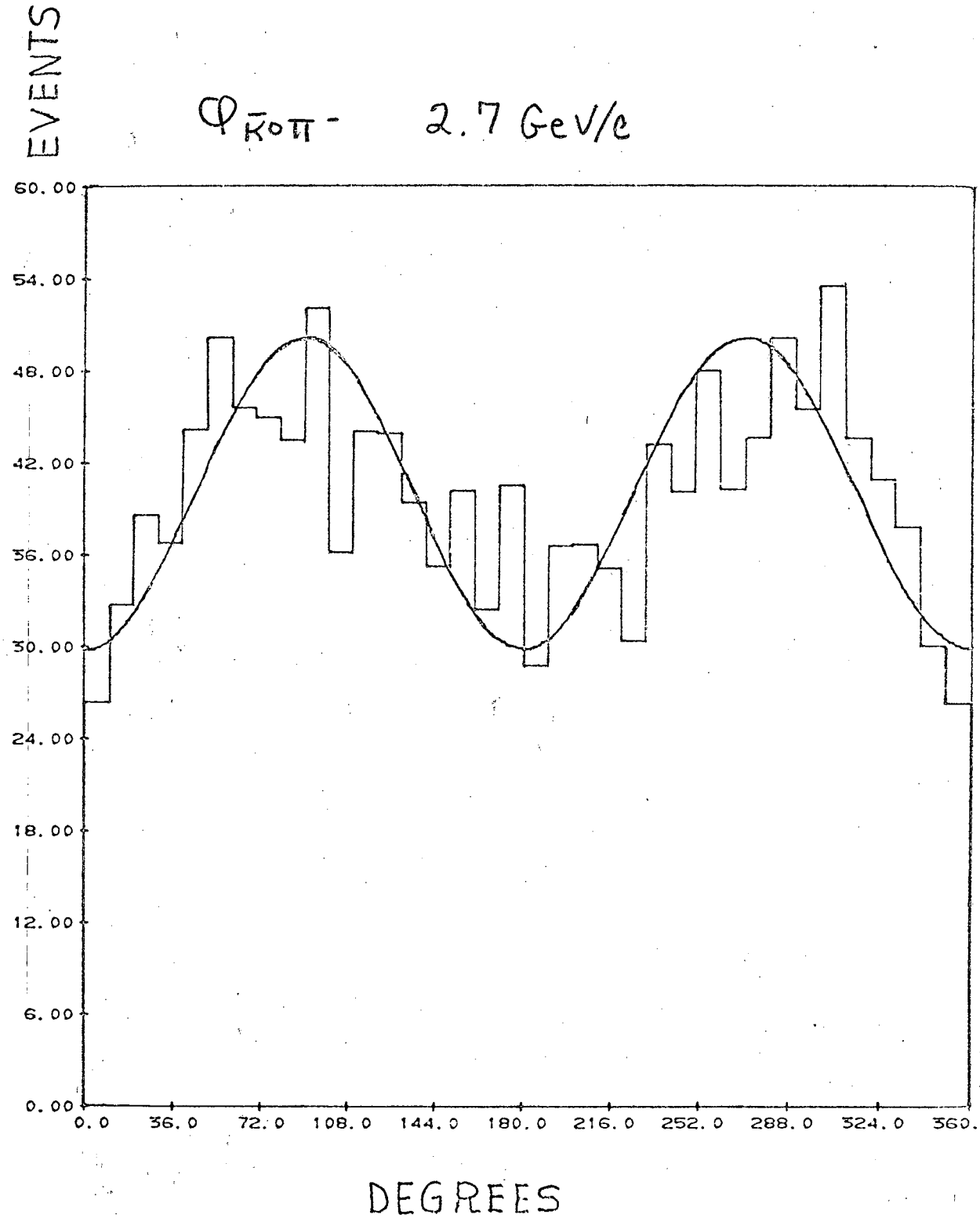
EVENTS
$\Phi_{K^0\pi^-}$ 2.7 GeV/c
60.00
54.00
48.00
42.00
36.00
30.00
24.00
18.00
12.00
6.00
0.00
0.0
36.0
72.0
108.0
144.0
180.0
216.0
252.0
288.0
324.0
360.
DEGREES

Figure 22

Total cross section for the reaction $K^- p \rightarrow p\overline{K}^0 \pi^-$ in the beam momentum range . 6 to 5.5 GeV/c as measured by several experiments.

□ Bastien and Berge (Ref. 36)

△ Wojcicki (Ref. 37)

○ Smith (Ref. 38)

□ R. Barloutand et al (Ref. 39)

▽ (Ref. 40)

● This experiment

▼ Schweingruber (Ref. 41)

▲ Alston et al (Ref. 44)

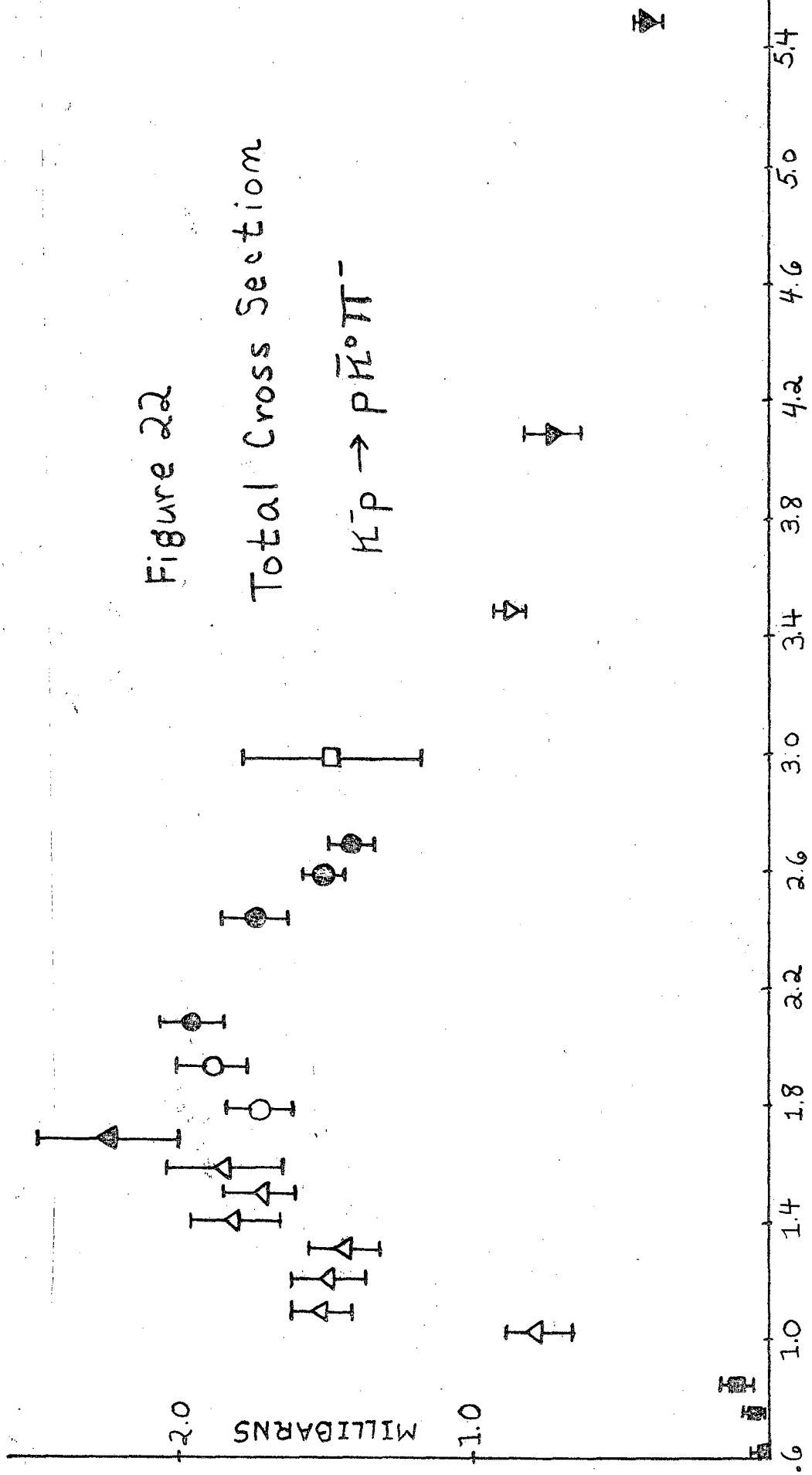
Figure 22
Total Cross Section
$K^- p \to p K^0 \pi^-$
MILLIBARNS
2.0
1.0
.6
1.0
1.4
1.8
2.2
2.6
3.0
3.4
3.8
4.2
4.6
5.0
5.4
K- BEAM MOMENTUM (GeV/c.)

Figure 23

Total cross section for the reaction $K^- p \rightarrow K^{*-} p$, $K^{*-} \rightarrow \bar{K}^0 \pi^-$, from threshold to 5.5 GeV/c beam momentum, as measured by several experiments.

△ Wojcicki (Ref. 37)

○ Smith (Ref. 38)

□ R. Barloutand et al (Ref. 39)

▽ (Ref. 40)

● This experiment

▽ Schweingruber (Ref. 41)

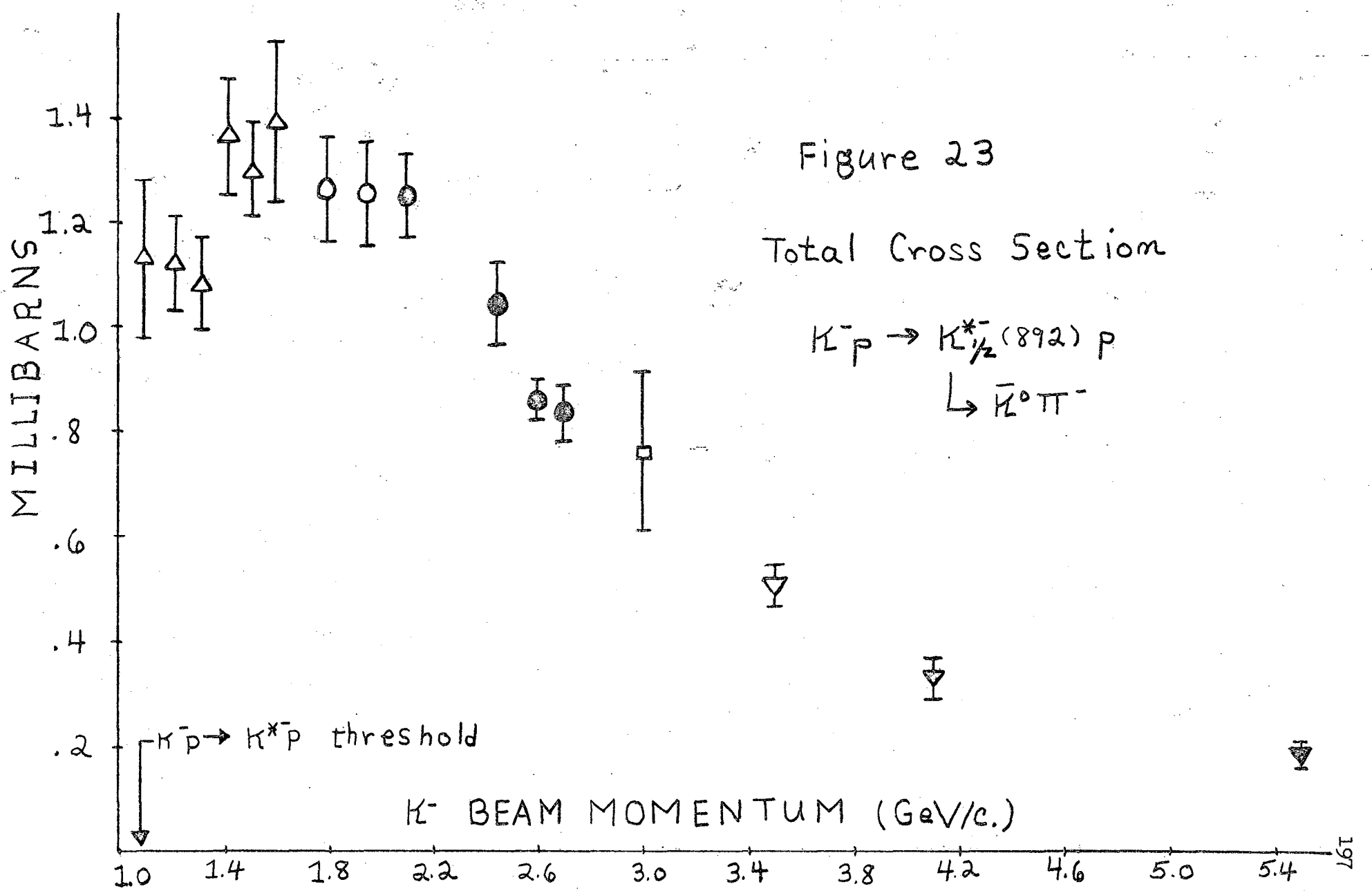

Figure 23

Total Cross Section

$K^-p \to K^{*-}_{1/2}(892)\,p$

$\hookrightarrow \bar{K}^0\pi^-$

Figure 24

Production cosine angular distribution for $\overline{K}^{o}\pi^{-}$ particle pair in the reaction $K^{-}p \rightarrow p\overline{K}^{o}\pi^{-}$ for events in the $\overline{K}^{o}\pi^{-}$ mass squared interval .706 to .884 GeV^{2}.

a) 2.1 GeV/c

b) 2.45, 2.60 and 2.70 combined

Figure 24

(a)

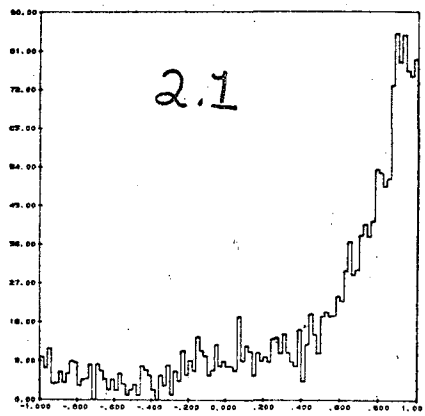

(b)

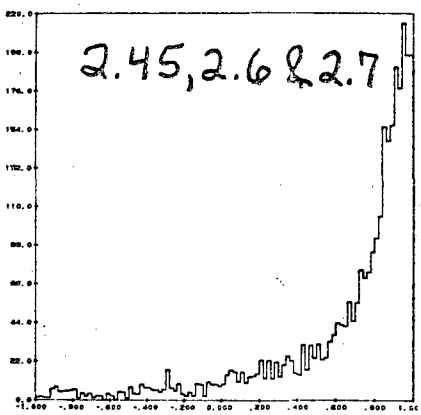

NUMBER OF EVENTS

PRODUCTION COSINE

Figure 25

Comparisons of the data to the predictions of the maximum likelihood solutions for $K^{*-}(892)$ polar and azimuthal decay angles in the reaction $K^- p \to K^{*-}_{\frac{1}{2}}(892)\, p$. Events plotted have $\bar{K}^0\pi^-$ invariant mass squared in the interval .706 to .884 GeV^2.

a) K^* polar decay angle cosine, 2.1 GeV/c

b) K^* azimuthal angle, 2.1 GeV/c

c) K^* polar decay angle cosine, upper momenta

d) K^* azimuthal angle, upper momenta

Figure 25

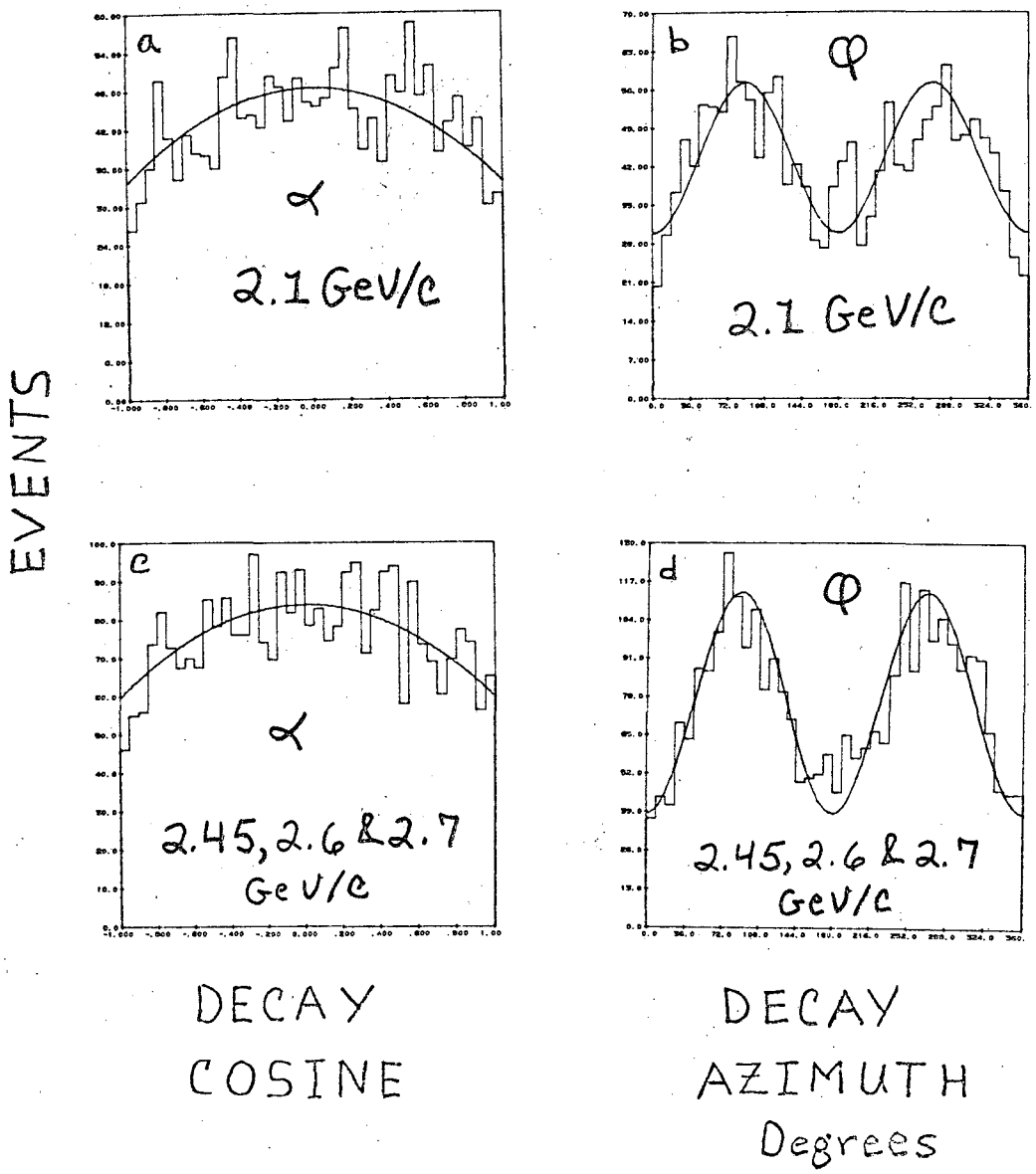
a
α
2.1 GeV/c
b
φ
2.1 GeV/c
c
α
2.45, 2.6 & 2.7 GeV/c
d
φ
2.45, 2.6 & 2.7 GeV/c
EVENTS
DECAY COSINE
DECAY AZIMUTH Degrees

Figure 26

Comparisons of the data to the predictions of the maximum likelihood solutions for $K^{*-}_{\frac{1}{2}}(892)$ decay polar cosine "α" and decay azimuthal angle "φ" in the reaction $K^- p \rightarrow K^{*-}_{\frac{1}{2}}(892)\, p$ at 2.1 GeV/c, for various intervals in the production cosine "μ" of the $K^{*-}_{\frac{1}{2}}(892)$. Events plotted have $\bar{K}^0\pi^-$ invariant mass squared in the interval .706 to .884 GeV^2.

Figure 26

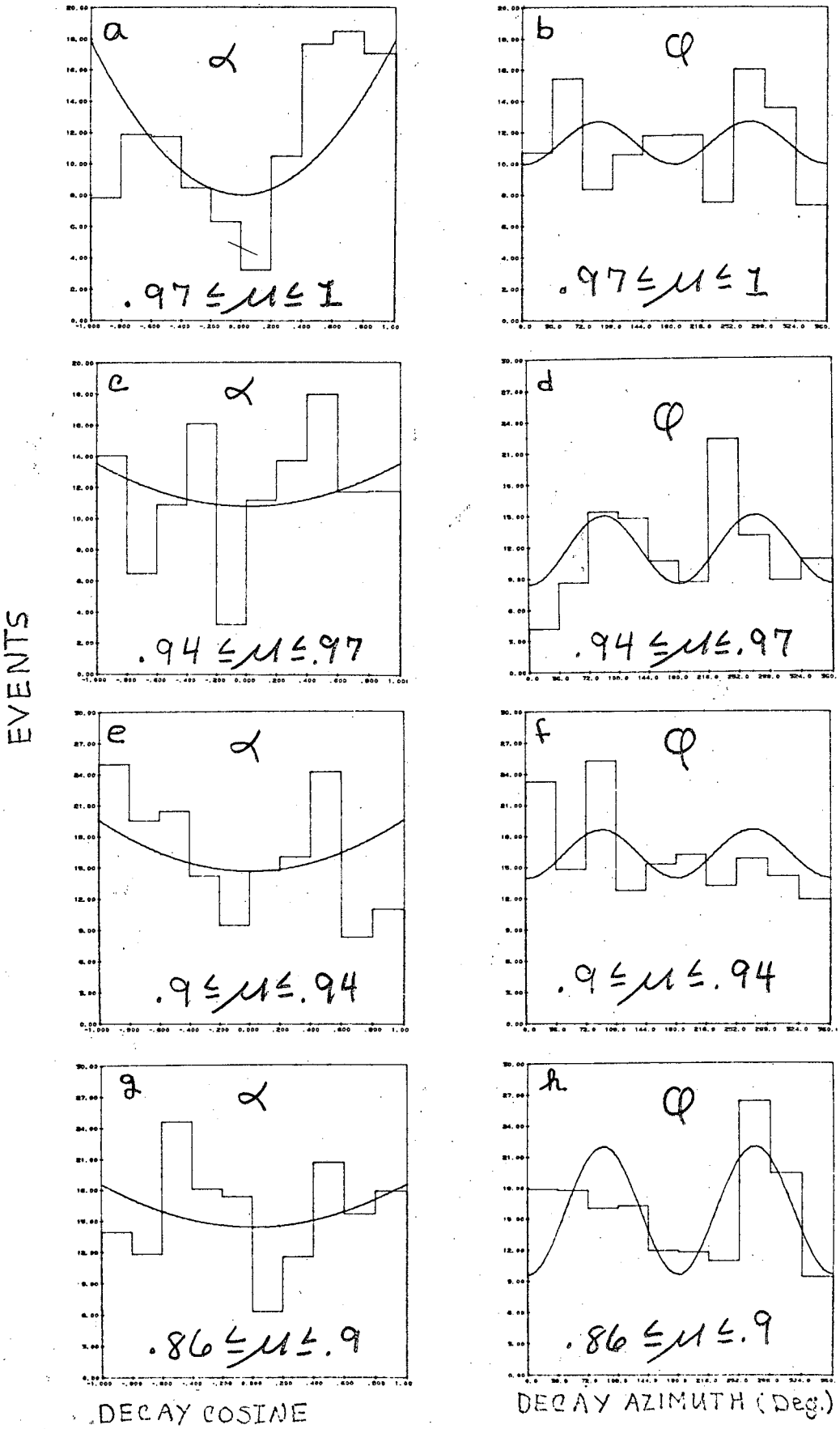
a
α
.97 ≤ μ ≤ 1
b
φ
.97 ≤ μ ≤ 1
c
α
.94 ≤ μ ≤ .97
d
φ
.94 ≤ μ ≤ .97
e
α
.9 ≤ μ ≤ .94
f
φ
.9 ≤ μ ≤ .94
g
α
.86 ≤ μ ≤ .9
h
φ
.86 ≤ μ ≤ .9
EVENTS
DECAY COSINE
DECAY AZIMUTH (Deg.)

Figure 26

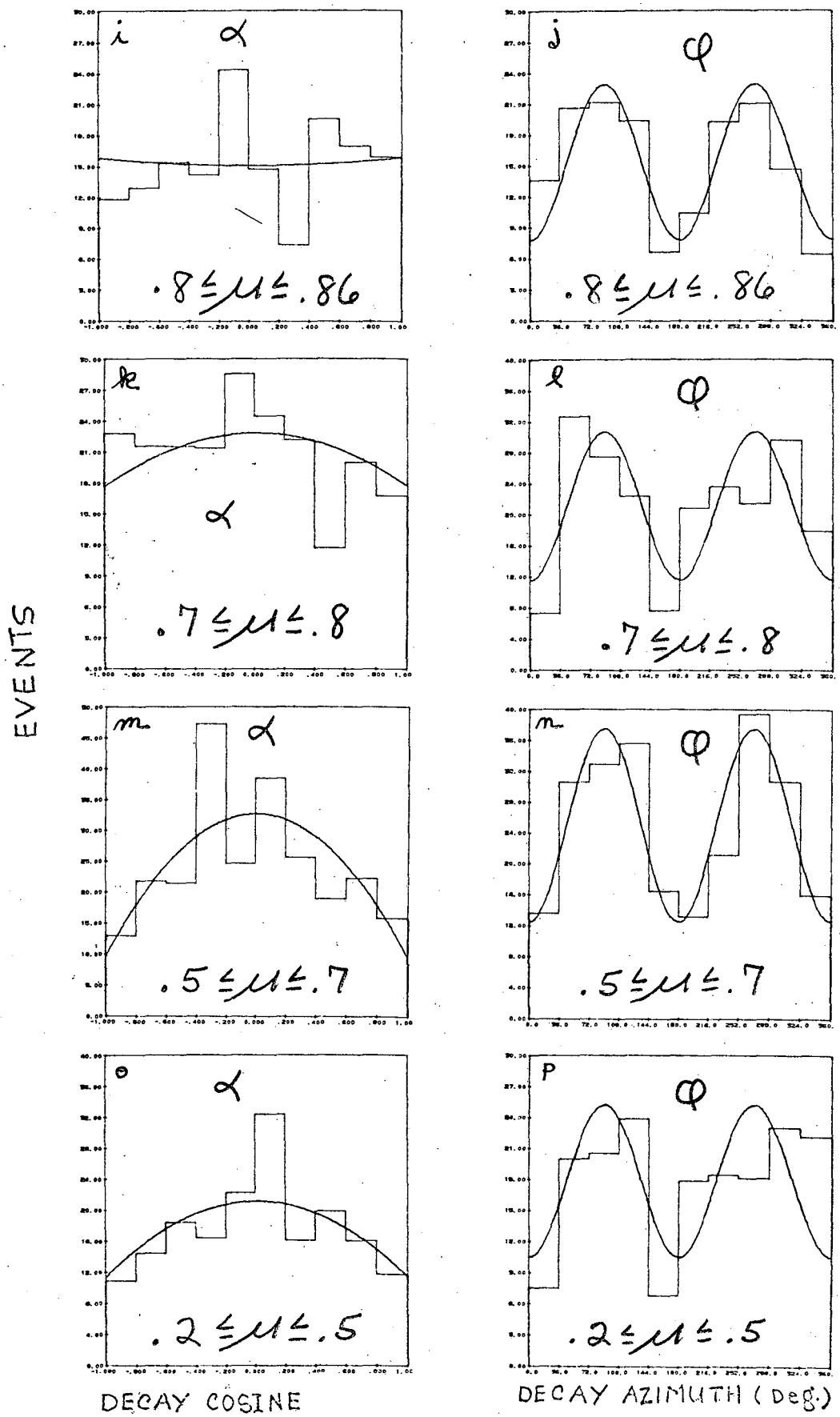
i
α
.8 ≤ μ ≤ .86
j
φ
.8 ≤ μ ≤ .86
k
α
.7 ≤ μ ≤ .8
l
φ
.7 ≤ μ ≤ .8
m
α
.5 ≤ μ ≤ .7
n
φ
.5 ≤ μ ≤ .7
o
α
.2 ≤ μ ≤ .5
P
φ
.2 ≤ μ ≤ .5
EVENTS
DECAY COSINE
DECAY AZIMUTH (Deg.)

Figure 26

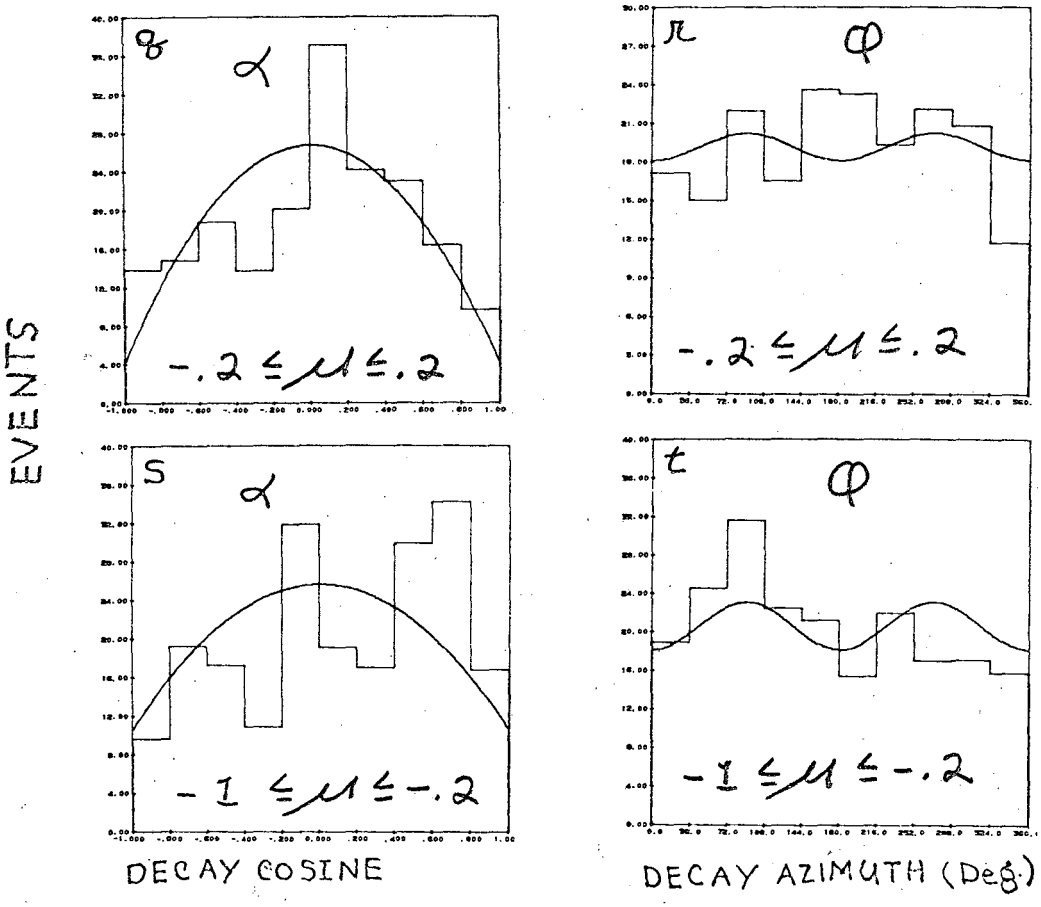
EVENTS
g
α
-.2 ≤ μ ≤ .2
π
φ
-.2 ≤ μ ≤ .2
S
α
-1 ≤ μ ≤ -.2
t
φ
-1 ≤ μ ≤ -.2
DECAY COSINE
DECAY AZIMUTH (Deg.)

Figure 27

Comparisons of the data to the predictions of the maximum likelihood solutions for the $K^{*-}_{\frac{1}{2}}$ (892) decay polar cosine " α " and decay azimuthal angle "φ" in the reaction $K^- p \rightarrow K^{*-}_{\frac{1}{2}}$ (892) p at the upper beam momenta, for the first ten intervals in the production cosine "μ" of the $K^{*-}_{\frac{1}{2}}$ (892). Events plotted have $\overline{K}^0\pi^-$ invariant mass squared in the interval .706 to .884 GeV^2.

Figure 27

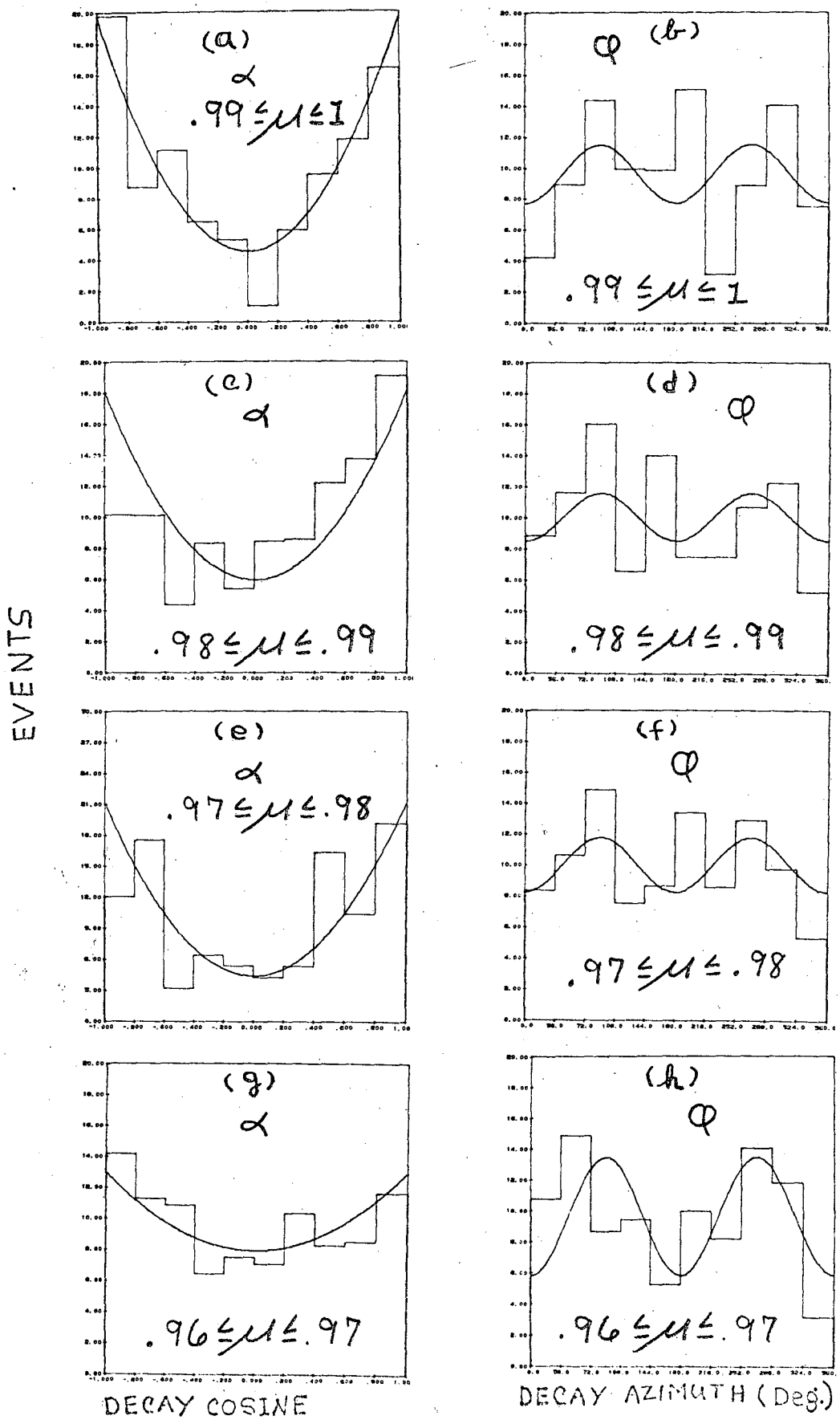
(a)
α
.99 ≤ μ ≤ 1
(b)
φ
.99 ≤ μ ≤ 1
(c)
α
.98 ≤ μ ≤ .99
(d)
φ
.98 ≤ μ ≤ .99
(e)
α
.97 ≤ μ ≤ .98
(f)
φ
.97 ≤ μ ≤ .98
(g)
α
.96 ≤ μ ≤ .97
(h)
φ
.96 ≤ μ ≤ .97
EVENTS
DECAY COSINE
DECAY AZIMUTH (Deg.)

Figure 27

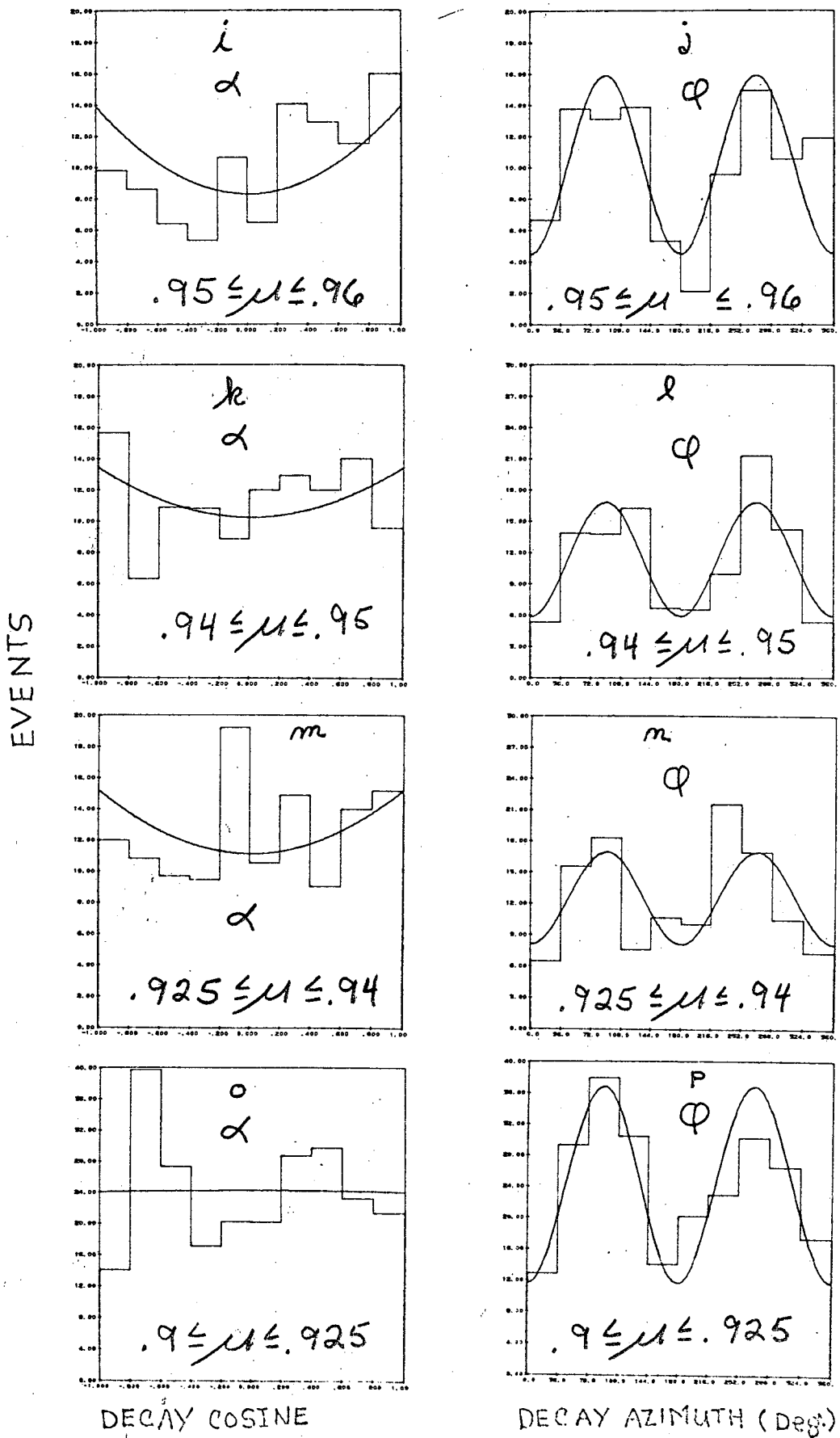
i
α
.95 ≤ μ ≤ .96
j
φ
.95 ≤ μ ≤ .96
k
α
.94 ≤ μ ≤ .95
l
φ
.94 ≤ μ ≤ .95
m
α
.925 ≤ μ ≤ .94
m
φ
.925 ≤ μ ≤ .94
o
α
.9 ≤ μ ≤ .925
P
φ
.9 ≤ μ ≤ .925
EVENTS
DECAY COSINE
DECAY AZIMUTH (Deg.)

Figure 27

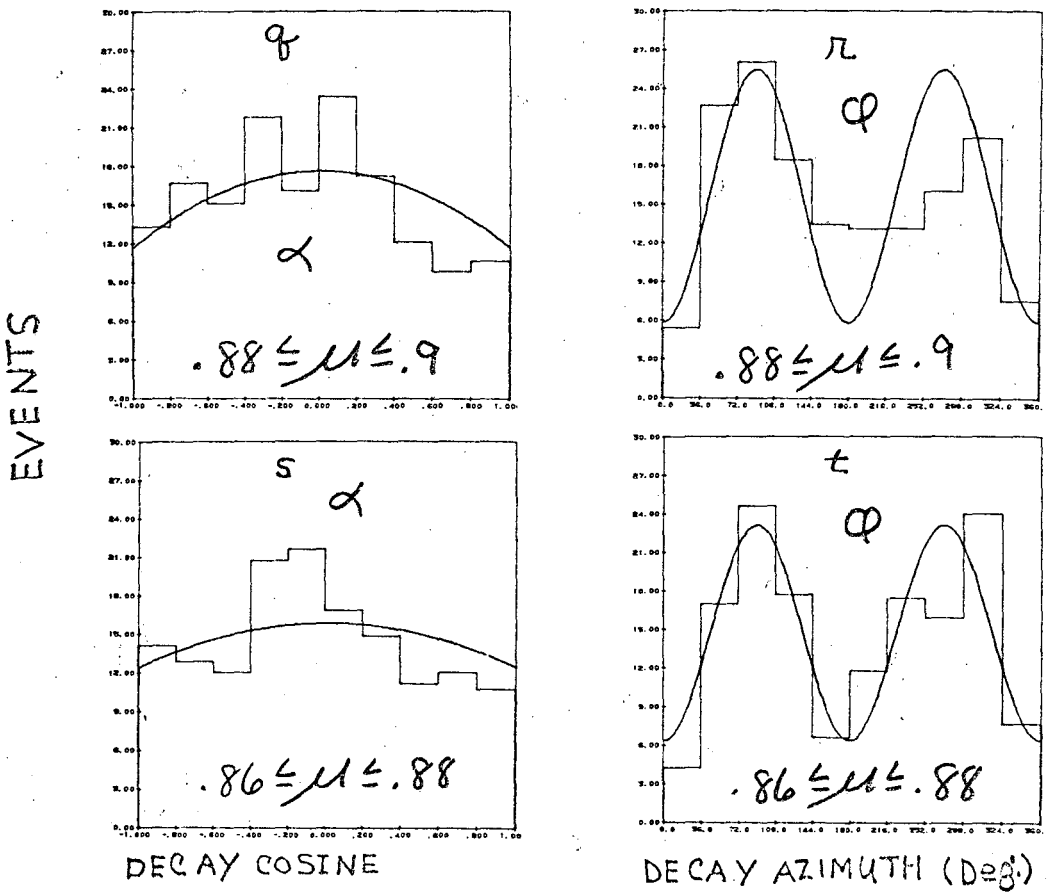
EVENTS
q
α
.88 ≤ μ ≤ .9
π
φ
.88 ≤ μ ≤ .9
s
α
.86 ≤ μ ≤ .88
t
φ
.86 ≤ μ ≤ .88
DECAY COSINE
DECAY AZIMUTH (Deg.)

Figure 28

Same as figure 27, except for the second ten $K^{*-}_{\frac{1}{2}}$ (892) production angle intervals.

Figure 28

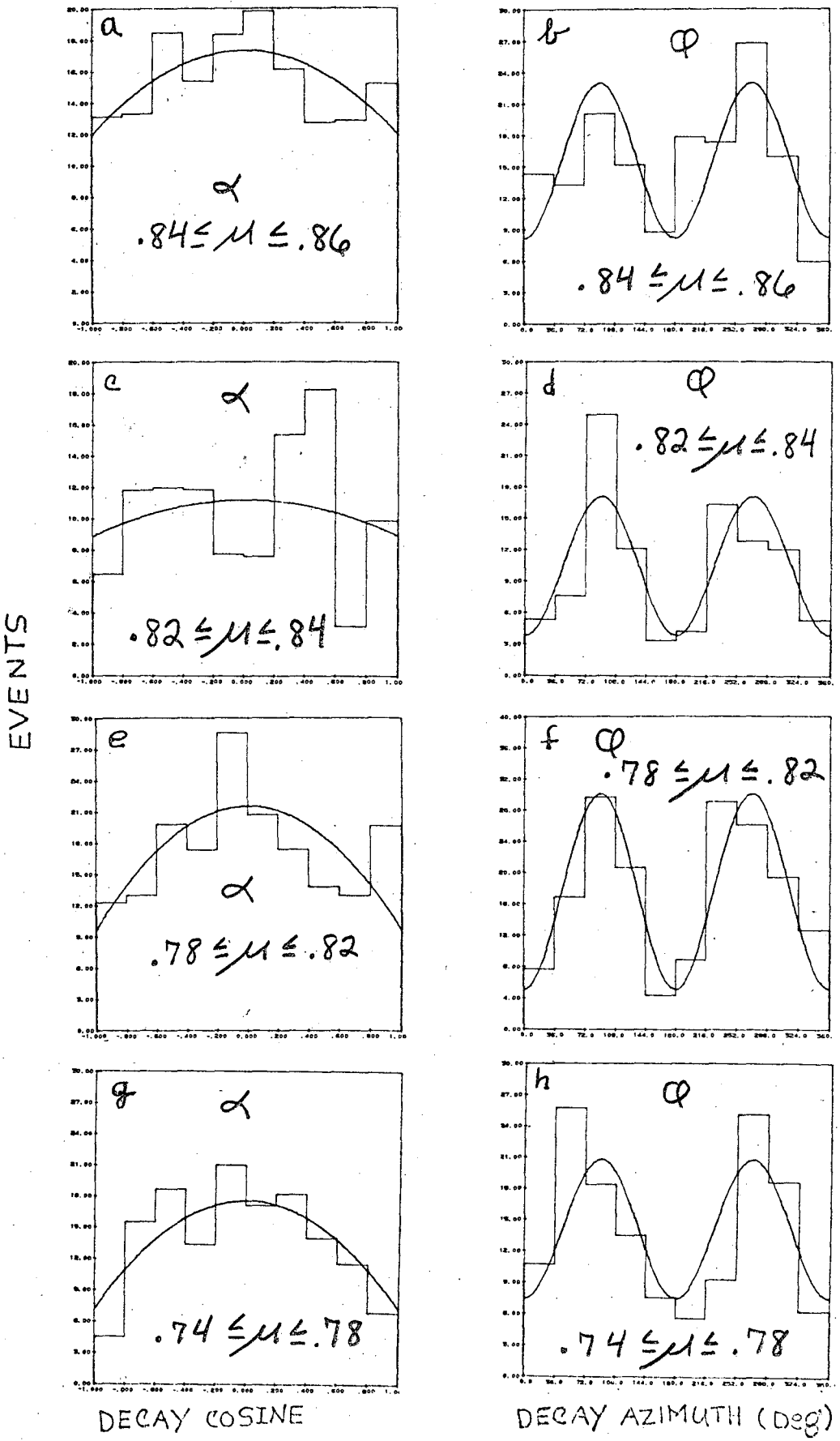
a
α
.84 ≤ μ ≤ .86
b
Φ
.84 ≤ μ ≤ .86
c
α
.82 ≤ μ ≤ .84
d
Φ
.82 ≤ μ ≤ .84
e
α
.78 ≤ μ ≤ .82
f
Φ
.78 ≤ μ ≤ .82
g
α
.74 ≤ μ ≤ .78
h
Φ
.74 ≤ μ ≤ .78
EVENTS
DECAY COSINE
DECAY AZIMUTH (Deg)

Figure 28

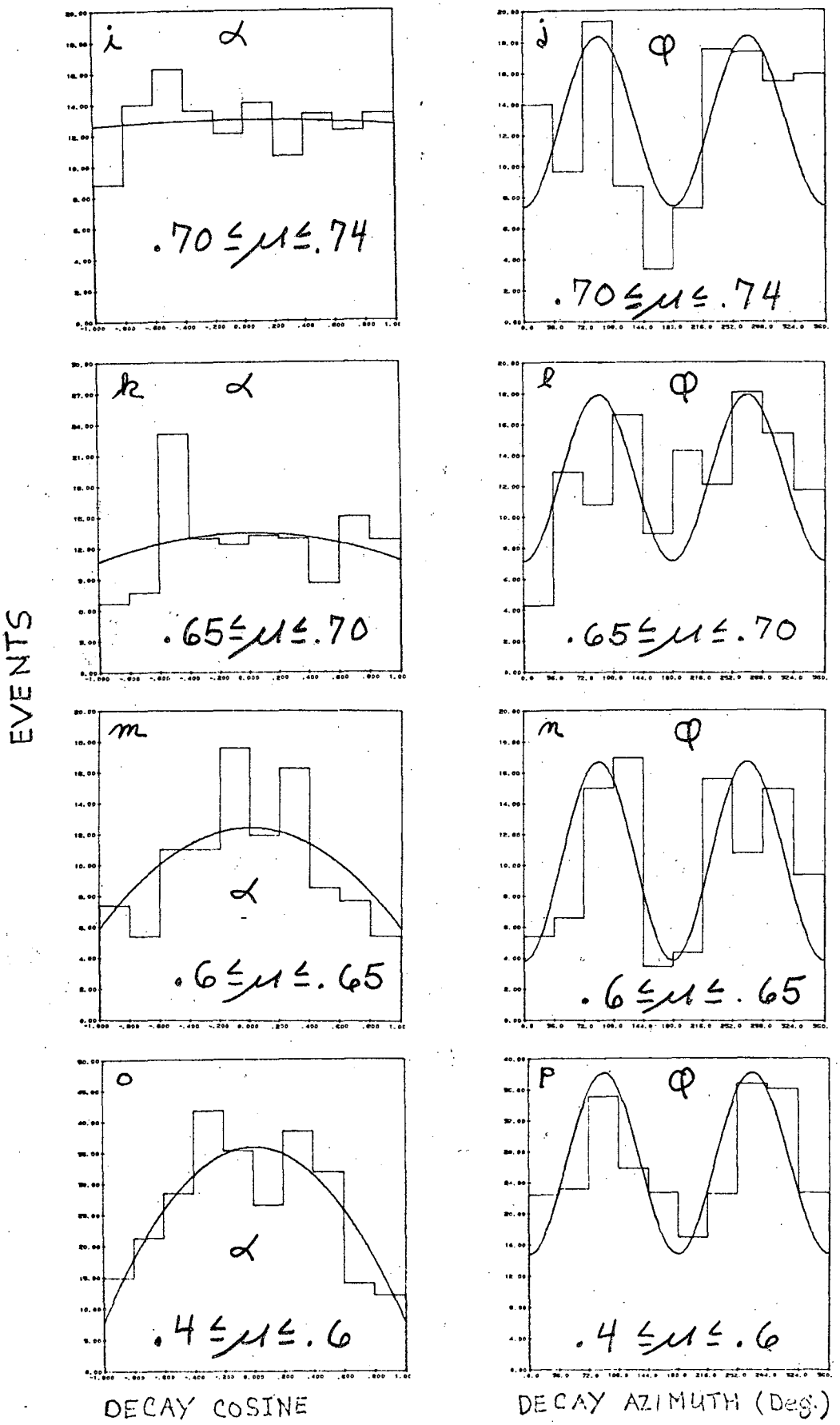
i
α
.70 ≤ μ ≤ .74
j
φ
.70 ≤ μ ≤ .74
k
α
.65 ≤ μ ≤ .70
l
φ
.65 ≤ μ ≤ .70
m
α
.6 ≤ μ ≤ .65
n
φ
.6 ≤ μ ≤ .65
o
α
.4 ≤ μ ≤ .6
p
φ
.4 ≤ μ ≤ .6
EVENTS
DECAY COSINE
DECAY AZIMUTH (Deg.)

Figure 28

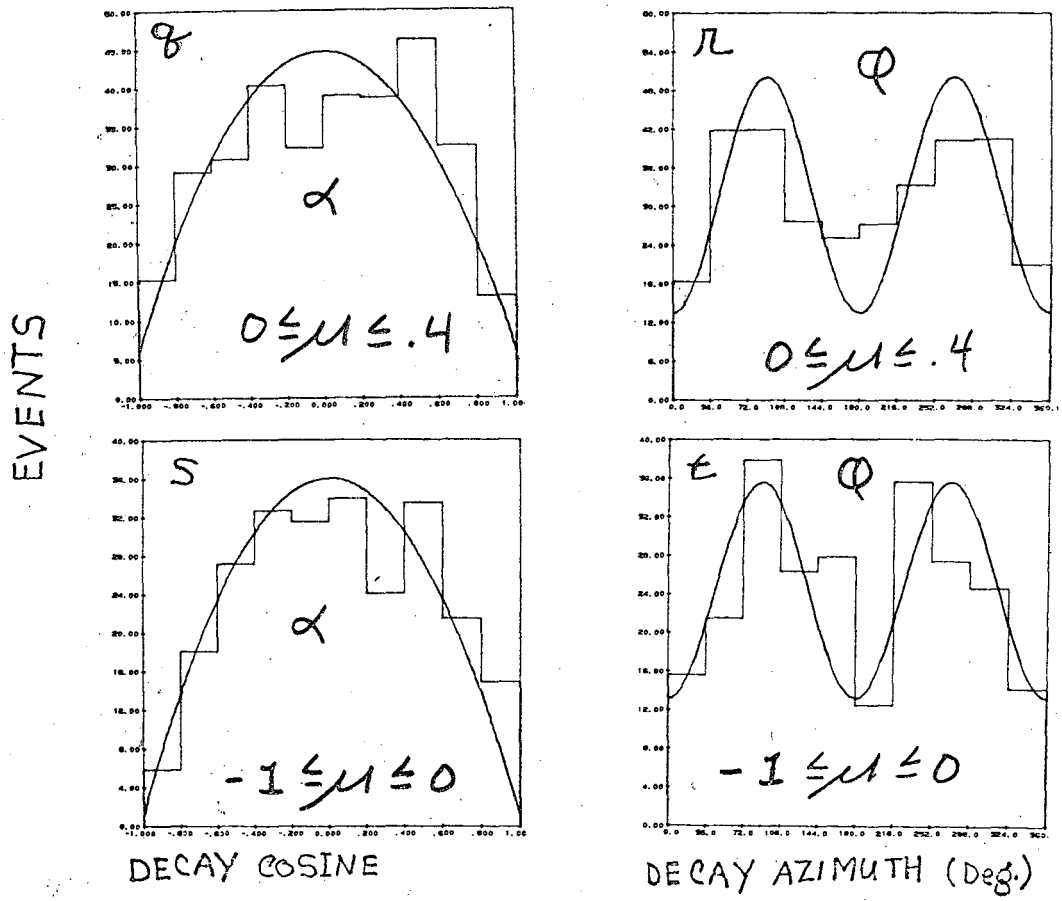
EVENTS
γ
α
$0 \leq \mu \leq .4$
π
φ
$0 \leq \mu \leq .4$
S
α
$-1 \leq \mu \leq 0$
ϵ
φ
$-1 \leq \mu \leq 0$
DECAY COSINE
DECAY AZIMUTH (Deg.)

Figure 29

Differential cross section as a function of center of mass scattering angle for the reaction $K^- p \rightarrow K^{*-} p$ at 2.1 GeV/c.

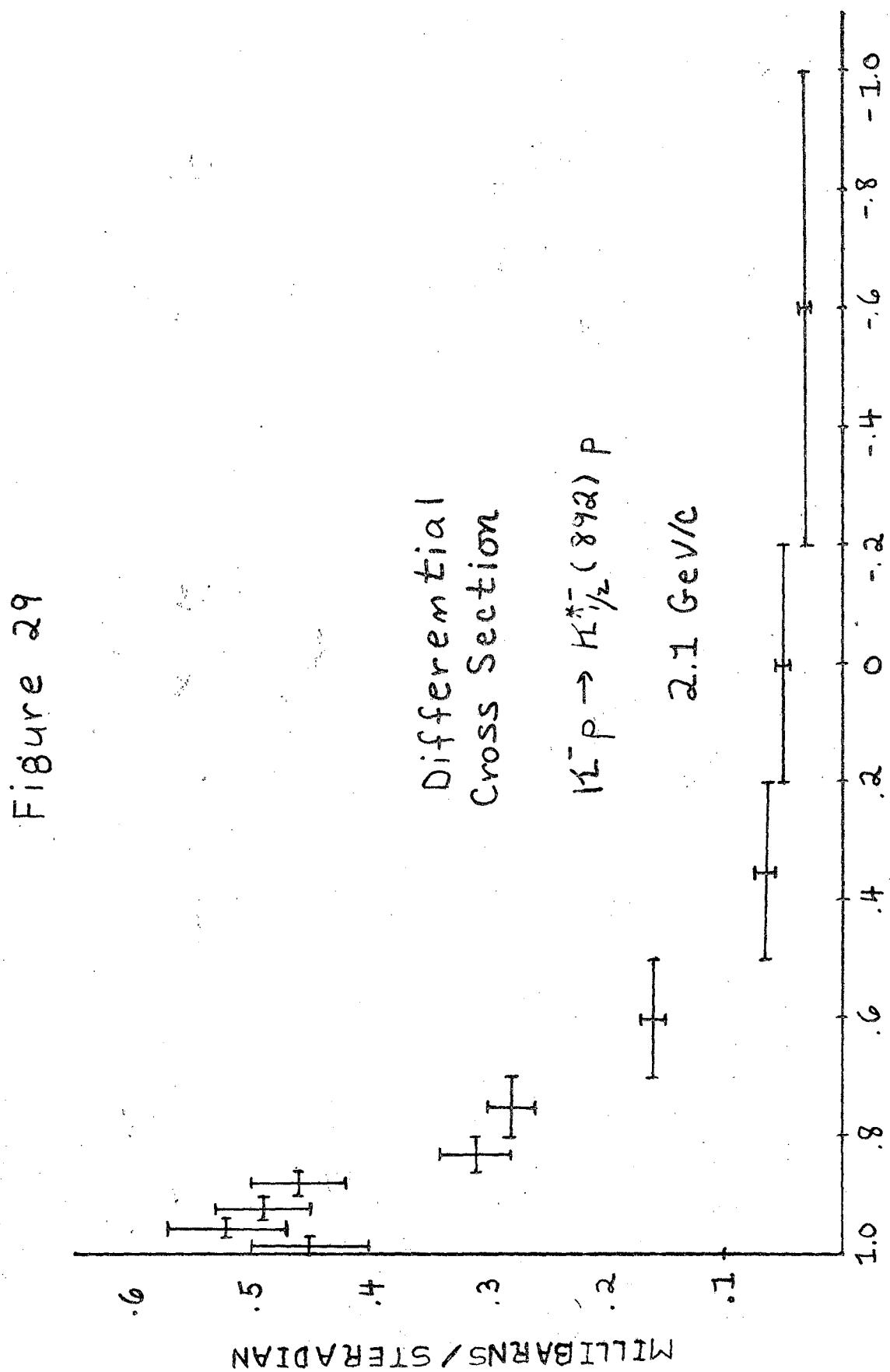
Differential
Cross Section
$K^- p \to K^{*-}_{1/2}(892)\, p$
2.1 GeV/c
MILLIBARNS / STERADIAN
.6
.5
.4
.3
.2
.1
1.0
.8
.6
.4
.2
0
-.2
-.4
-.6
-.8
-1.0
PRODUCTION COSINE

Fiǥure 29

Figure 30

Differential cross section as a function of center of mass scattering angle for the reaction $K^- p \rightarrow K^{*-}_{\frac{1}{2}}(892)\, p$ at the upper beam momenta.

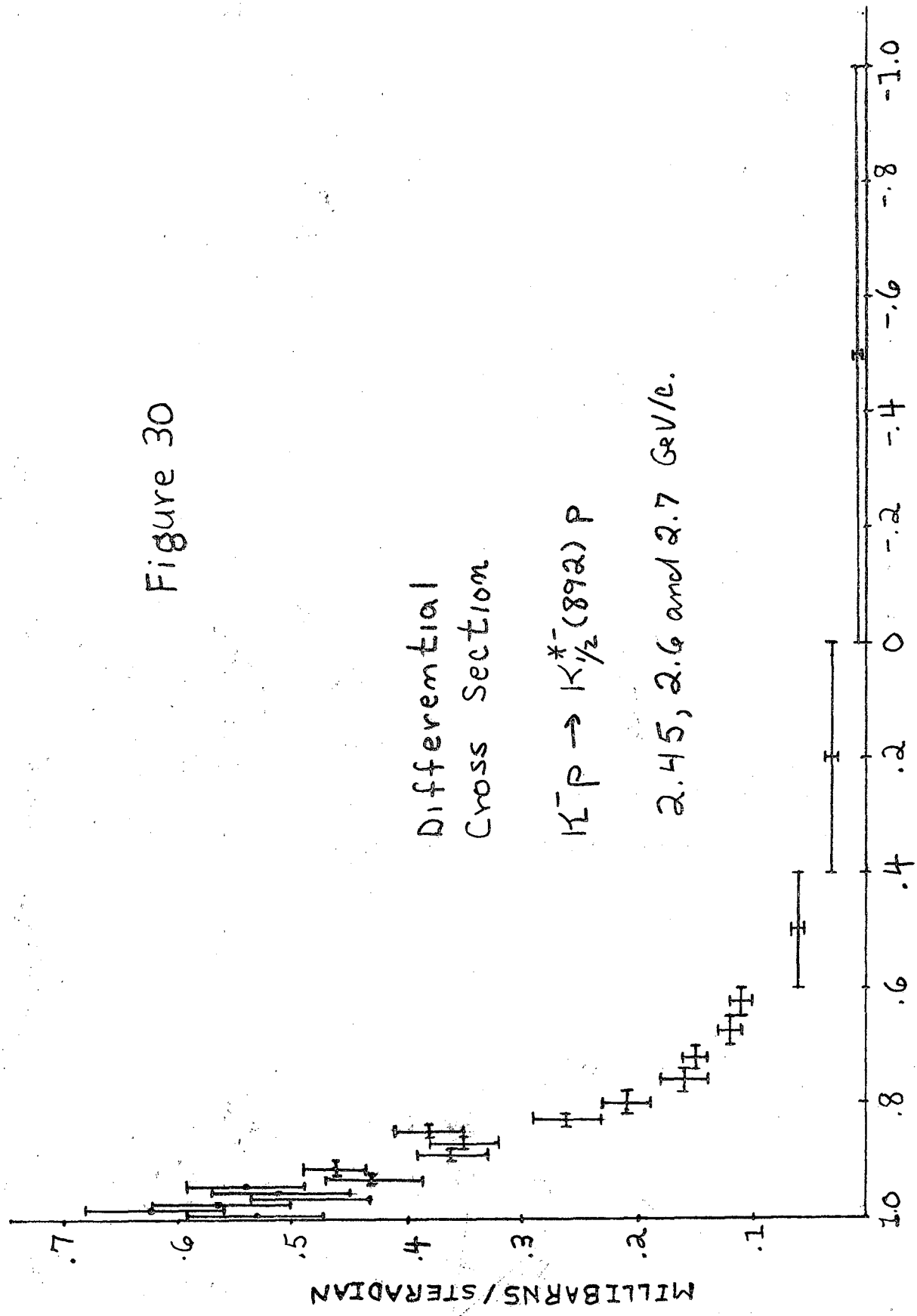
Figure 30
Differential
Cross Section
$K^- p \to K^{*-}_{1/2}(892)\, p$
2.45, 2.6 and 2.7 GeV/c.
MILLIBARNS/STERADIAN
PRODUCTION COSINE
.7
.6
.5
.4
.3
.2
.1
1.0
.8
.6
.4
.2
0
-.2
-.4
-.6
-.8
-1.0

Figure 31

$K^{*-}_{\frac{1}{2}}$ (892) decay angular correlation coefficients as a function of center of mass scattering angle for the reaction $K^- p \rightarrow K^{*-}_{\frac{1}{2}}$ (892) p at 2.1 GeV/c.

a) C_1

b) C_2

c) C_3

Figure 31a

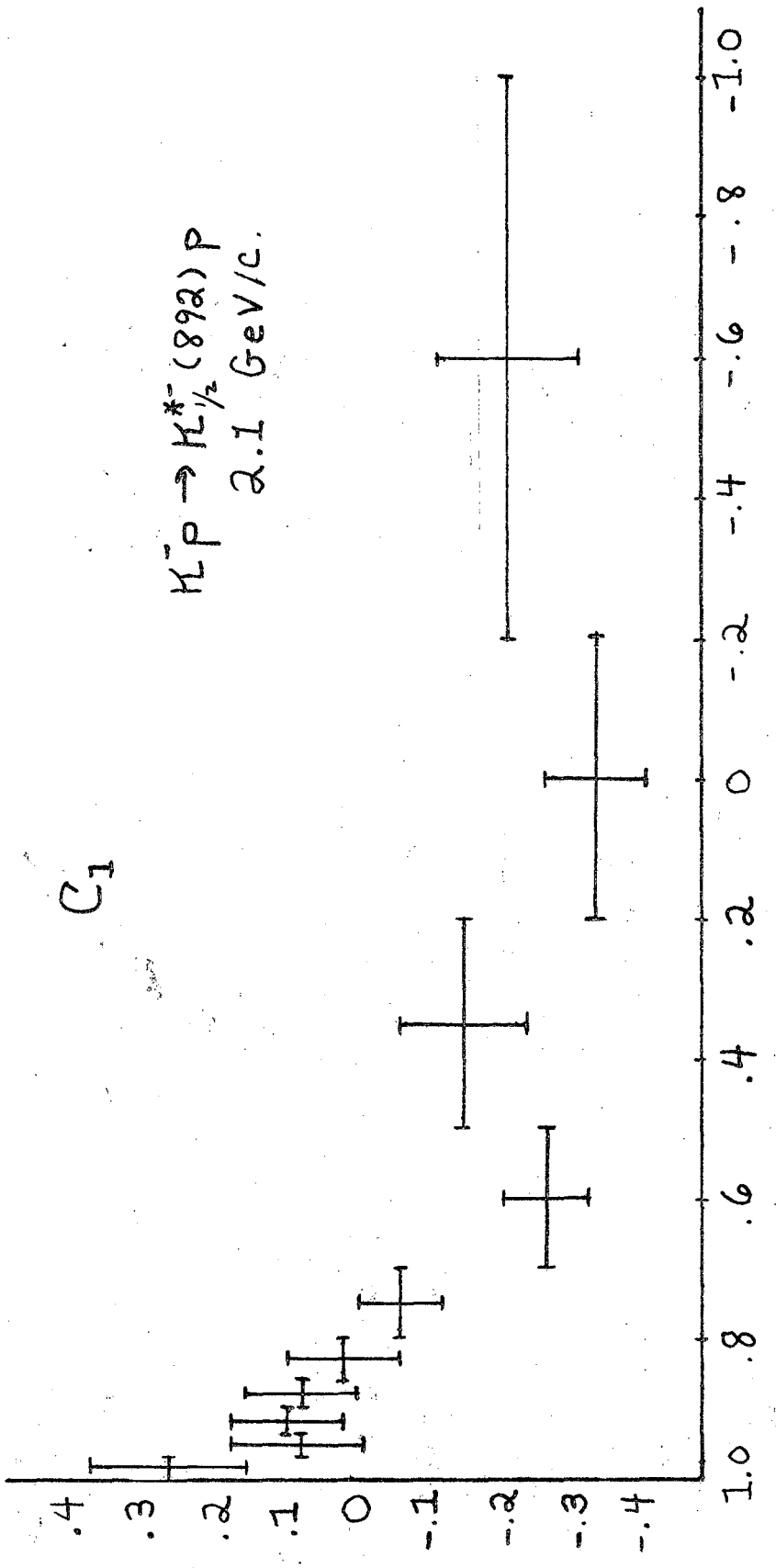
C_1
$K^- p \to K^{*-}_{1/2}(892)\, p$
2.1 GeV/c.
.4
.3
.2
.1
0
-.1
-.2
-.3
-.4
1.0
.8
.6
.4
.2
0
-.2
-.4
-.6
-.8
-1.0
PRODUCTION COSINE

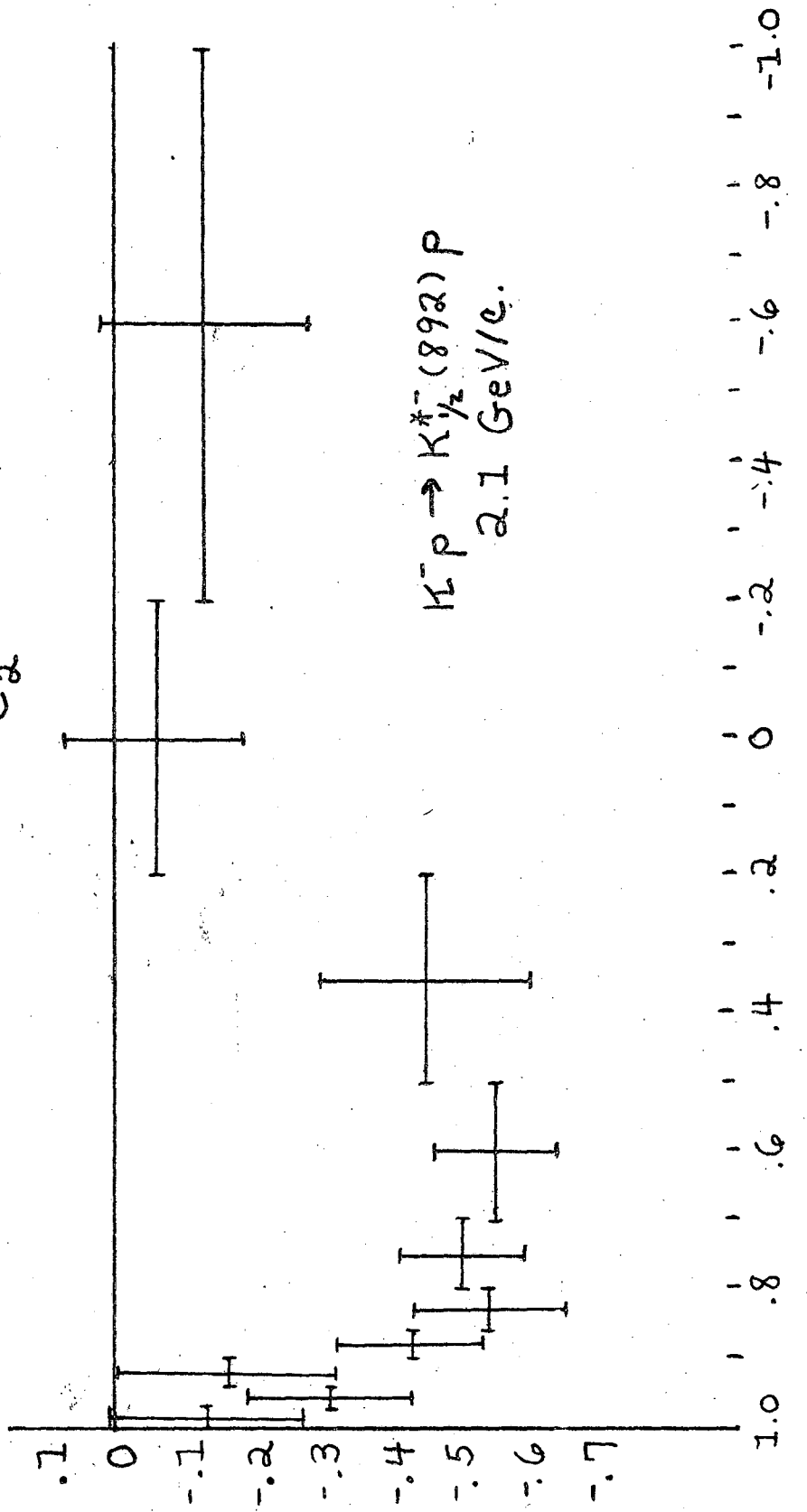

Figure 31 b
C_2

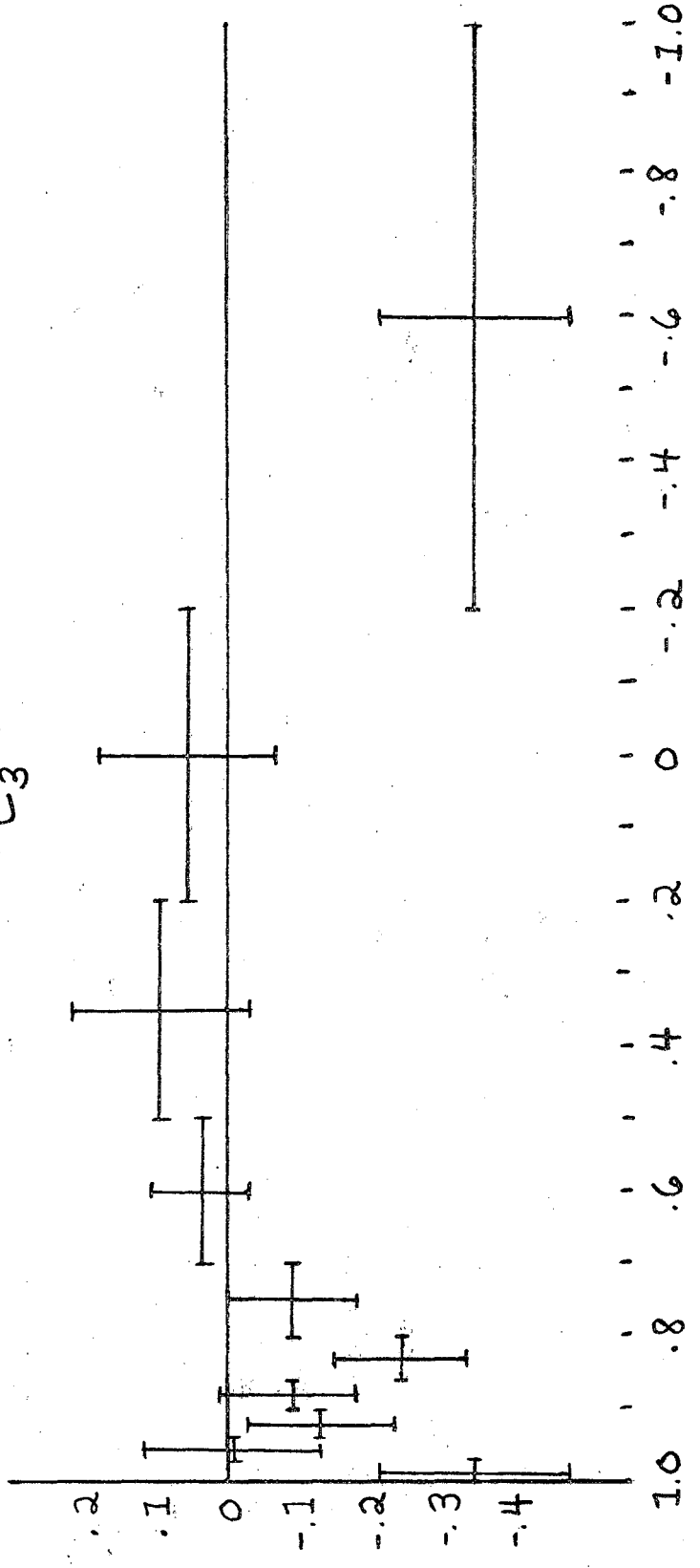

Figure 31c

C_3

$K^- P \to K^{*-}_{1/2}(892) P$

2.1 GeV/c.

Figure 32

$K^{*-}_{\frac{1}{2}}$ (892) decay angular correlation coefficients as a function of center of mass scattering angle for the reaction $K^- p \rightarrow K^{*-}_{\frac{1}{2}}$ (892) p at the upper beam momenta.

a) C_1

b) C_2

c) C_3

Figure 32a

C_1

$K^- p \rightarrow K^{*-}(892)\, p$
2.45, 2.6 and 2.7 GeV/c.

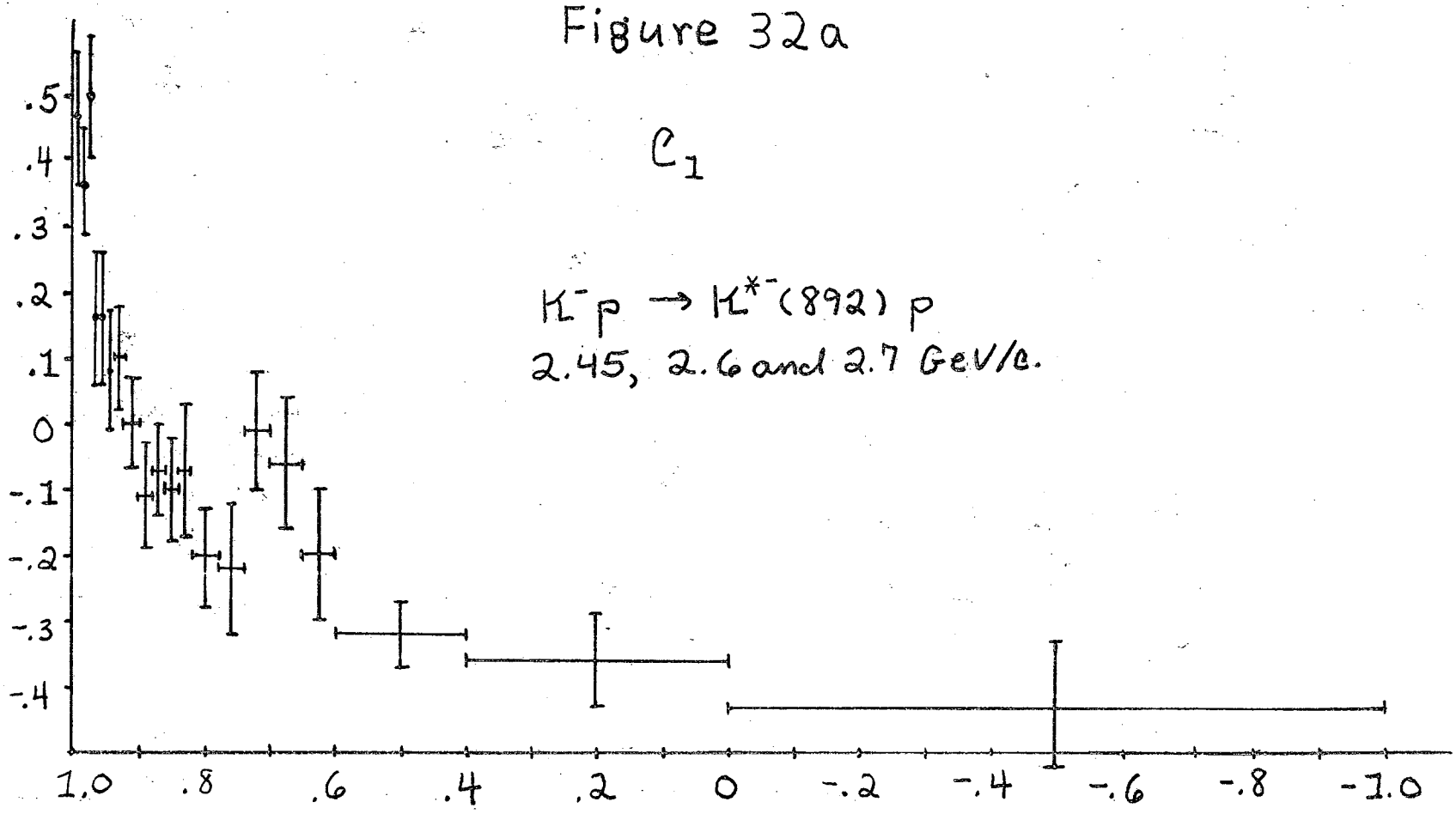

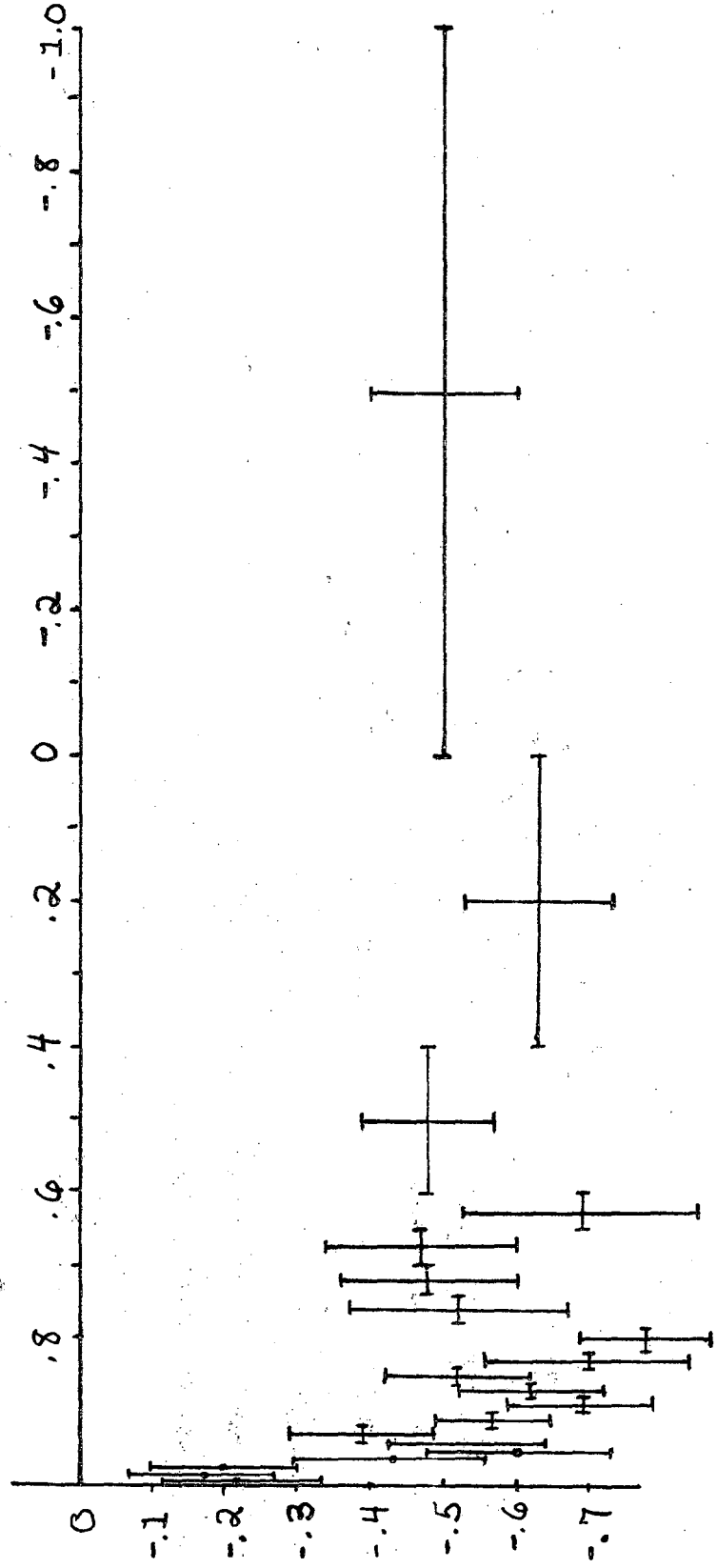

Figure 32b

C_2

PRODUCTION COSINE

$K^-P \rightarrow K^{*-}_{1/2}(892)\,P$

2.45, 2.6 and 2.7 GeV/c

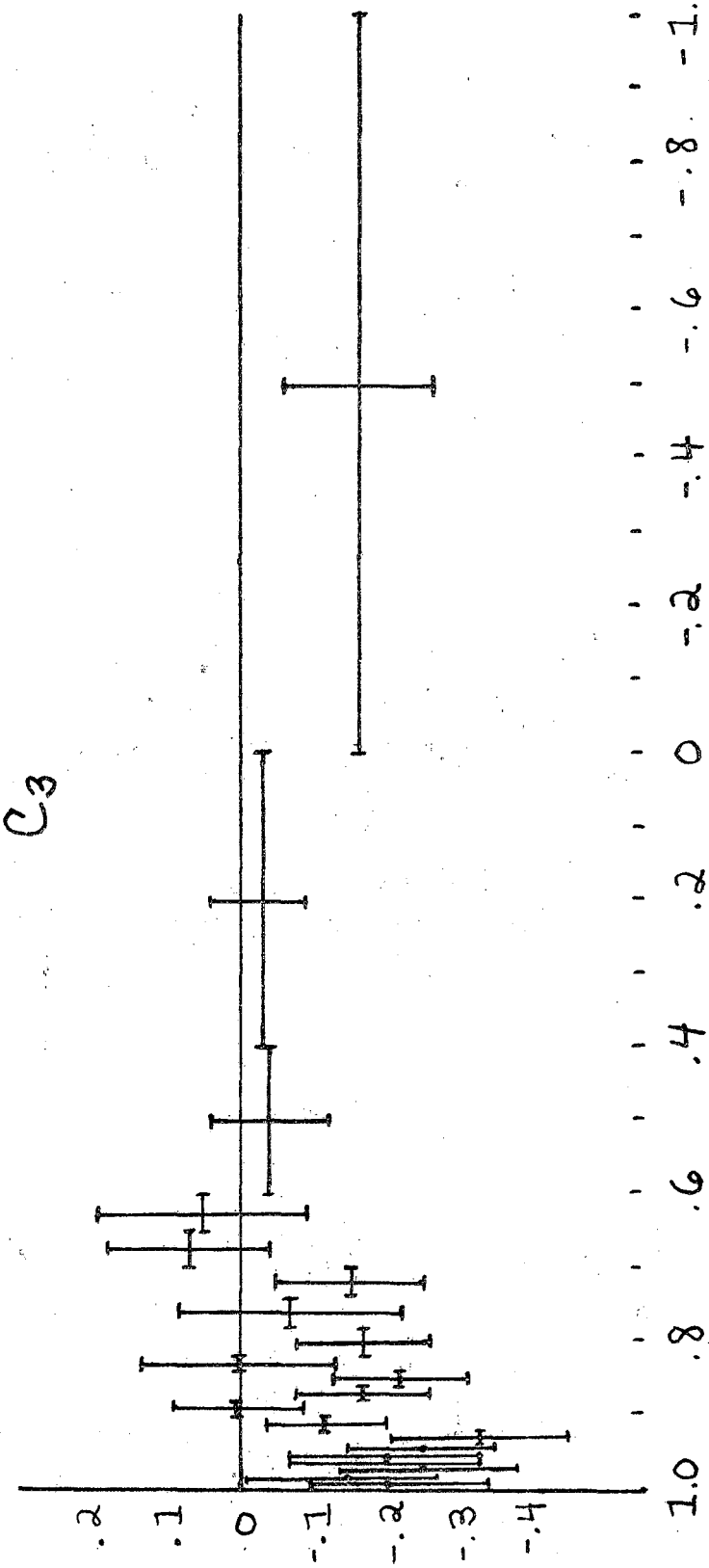

Figure 32c

C_3

$\bar{K}^- p \to K^{*-}_{1/2}(892)\, p$

2.45, 2.6 and 2.7 Gev/c.

Figure 33

Total cross section for the reaction $K^- p \rightarrow \overline{K}^0 \pi^0 \pi^- p$ in the beam momentum range 1 to 3.5 GeV/c as measured by several experiments.

Δ Wojcicki et al (Ref. 48)

O Smith (Ref. 38)

▽ (Ref. 40)

O This experiment

Figure 33

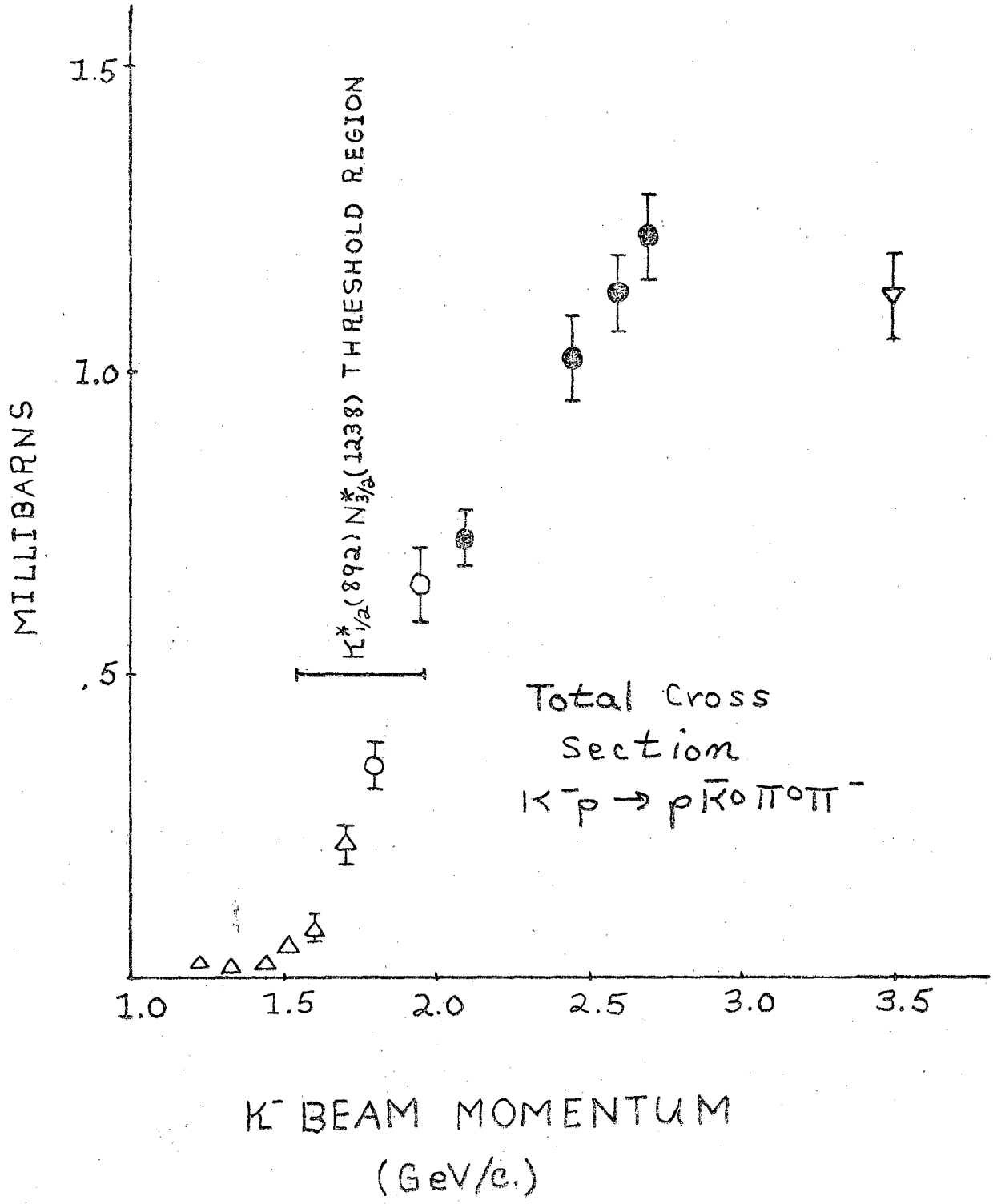
1.5
1.0
.5
MILLIBARNS
$K^*_{1/2}(892)\,N^*_{3/2}(1238)$ THRESHOLD REGION
Total Cross Section
$K^-p \to p\bar{K}^0\pi^0\pi^-$
1.0
1.5
2.0
2.5
3.0
3.5
K^- BEAM MOMENTUM
(GeV/c.)

Figure 34

Histograms of invariant mass squared for the ten particle pairs and triplets in the reaction $K^-p \rightarrow p\bar{K}^0\pi^0\pi^-$ at 2.1 GeV/c. The solid curves are the predictions of the maximum likelihood solution. (See text)

a) $p\bar{K}^0$ b) $p\pi^0$ c) $p\pi^-$ d) $\bar{K}^0\pi^0$

e) $\bar{K}^0\pi^-$ f) $\pi^0\pi^-$ g) $p\bar{K}^0\pi^0$ h) $p\bar{K}^0\pi^-$

i) $p\pi^0\pi^-$ j) $\bar{K}^0\pi^0\pi^-$

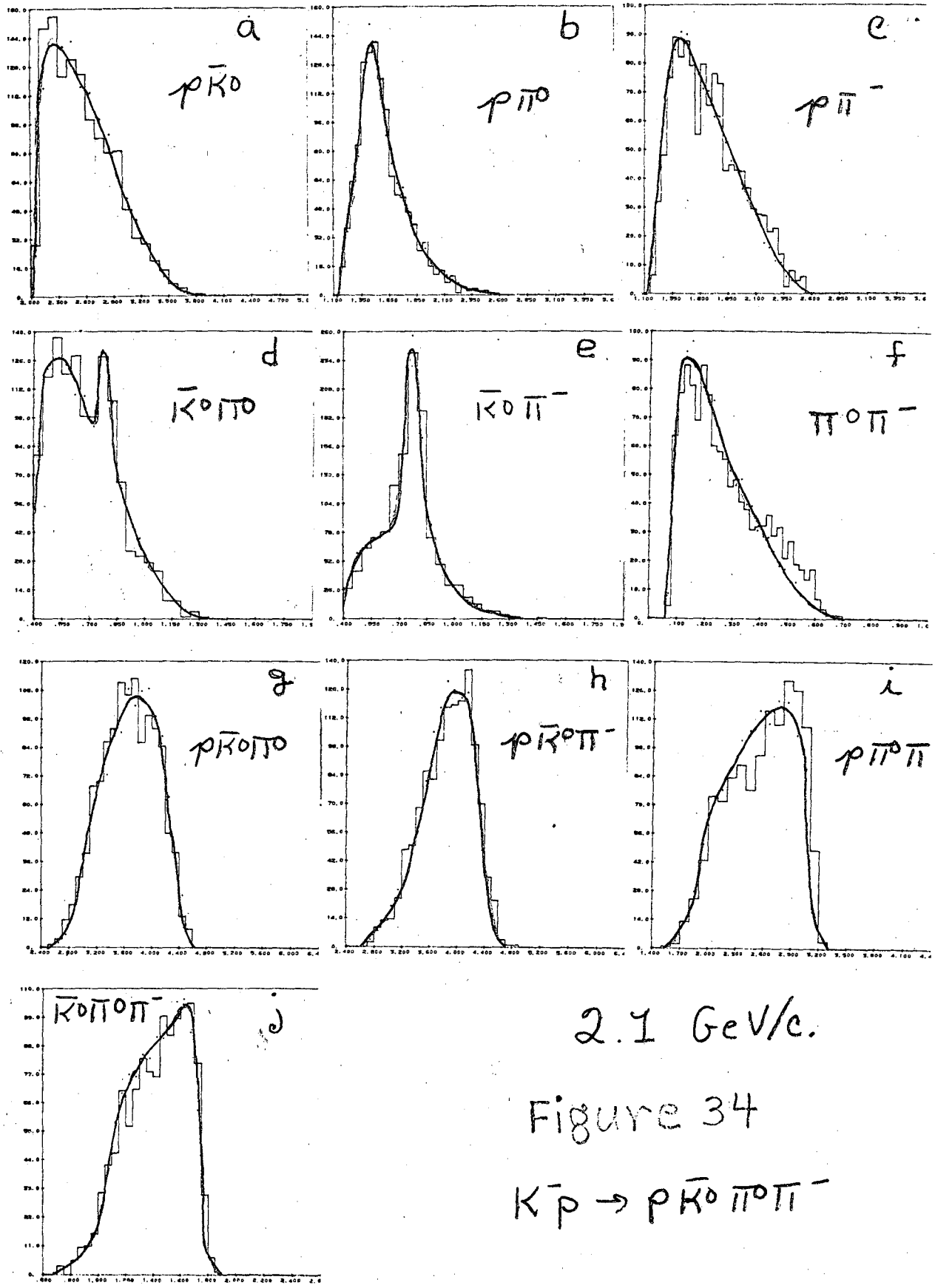

2.1 GeV/c.

Figure 34

$K^-p \rightarrow p\bar{K}^0\pi^0\pi^-$

INVARIANT MASS SQ. $(GeV.)^2$

Figure 35

Histograms of invariant mass squared for the ten particle pairs and triplets in the reaction $K^- p \rightarrow p\bar{K}^0\pi^0\pi^-$ at 2.45 GeV/c. The solid curves are the predictions of the maximum likelihood solution. (See text).

a) $p\bar{K}^0$ b) $p\pi^0$ c) $p\pi^-$ d) $\bar{K}^0\pi^0$

e) $\bar{K}^0\pi^-$ f) $\pi^0\pi^-$ g) $p\bar{K}^0\pi^0$ h) $p\bar{K}^0\pi^-$

i) $p\pi^0\pi^-$ j) $\bar{K}^0\pi^0\pi^-$

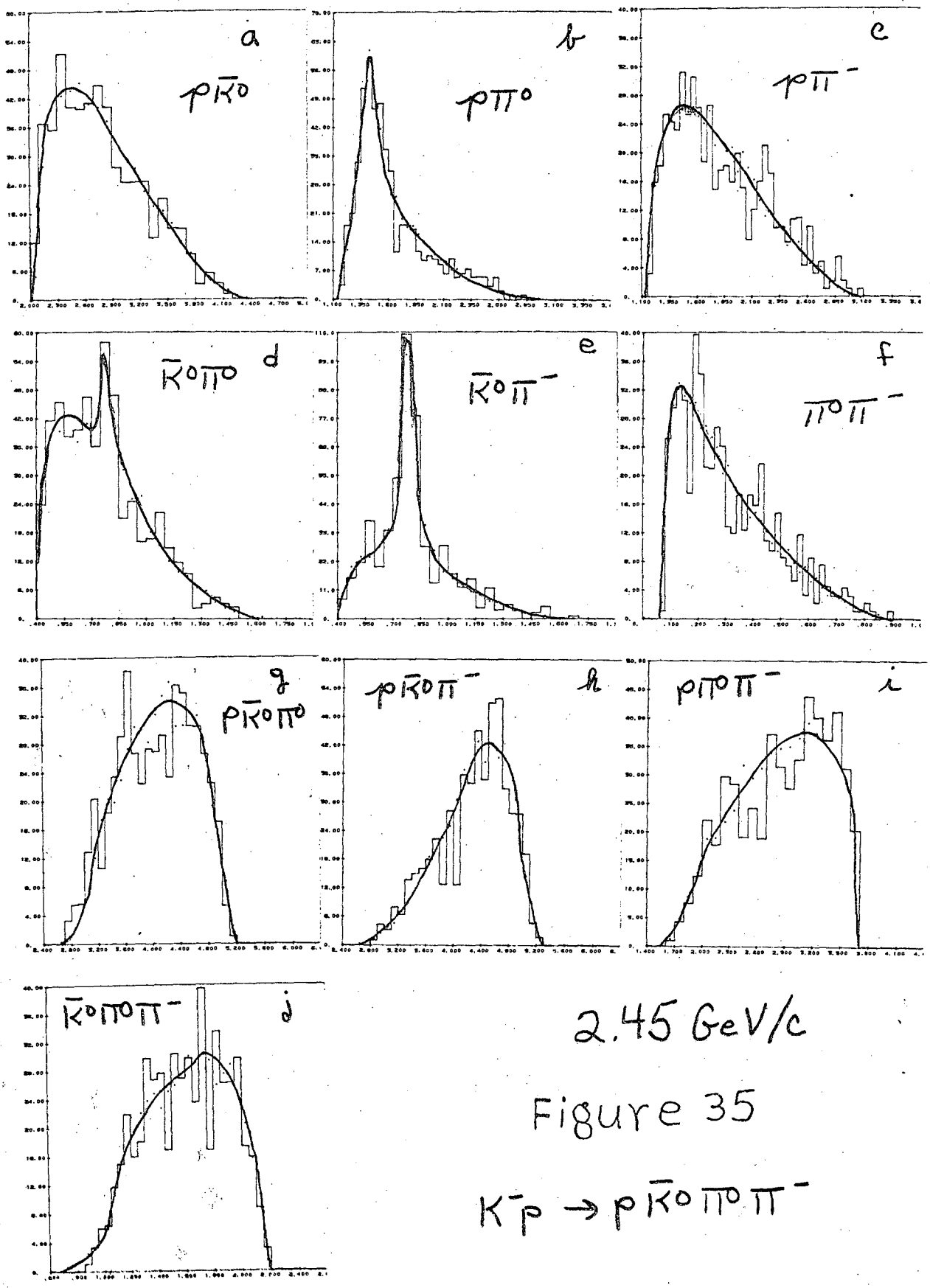

2.45 GeV/c

Figure 35

$K^-p \rightarrow p\bar{K}^0\pi^0\pi^-$

INVARIANT MASS SQ. $(GeV.)^2$

Figure 36

Histograms of invariant mass squared for the ten particle pairs and triplets in the reaction $K^- p \rightarrow p\bar{K}^0\pi^0\pi^-$ at 2.60 GeV/c. The solid curves are the predictions of the maximum likelihood solution. (See text)

a) $p\bar{K}^0$ b) $p\pi^0$ c) $p\pi^-$ d) $\bar{K}^0\pi^0$

e) $\bar{K}^0\pi^-$ f) $\pi^0\pi^-$ g) $p\bar{K}^0\pi^0$ h) $p\bar{K}^0\pi^-$

i) $p\pi^0\pi^-$ j) $\bar{K}^0\pi^0\pi^-$

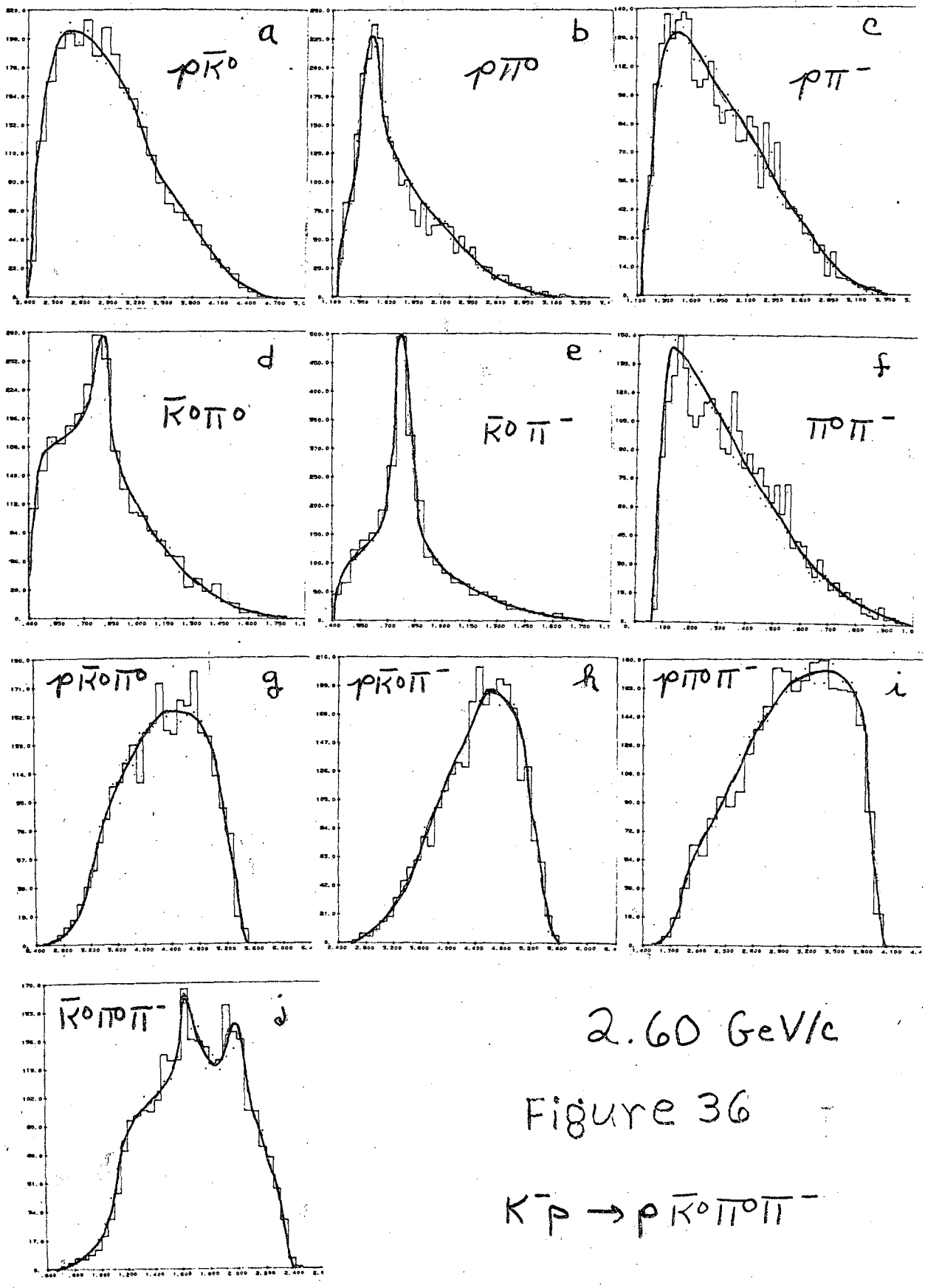

2.60 GeV/c

Figure 36

$K^-p \rightarrow p\bar{K}^0\pi^0\pi^-$

INVARIANT MASS SQ. $(GeV.)^2$

Figure 37

Histograms of invariant mass squared for the ten particle pairs and triplets in the reaction $K^-p \rightarrow p\overline{K}^0\pi^0\pi^-$ at 2.70 GeV/c. The solid curves are the predictions of the maximum likelihood solution. (See text)

a) $p\overline{K}^0$ b) $p\pi^0$ c) $p\pi^-$ d) $\overline{K}^0\pi^0$

e) $\overline{K}^0\pi^-$ f) $\pi^0\pi^-$ g) $p\overline{K}^0\pi^0$ h) $p\overline{K}^0\pi^-$

i) $p\pi^0\pi^-$ j) $\overline{K}^0\pi^0\pi^-$

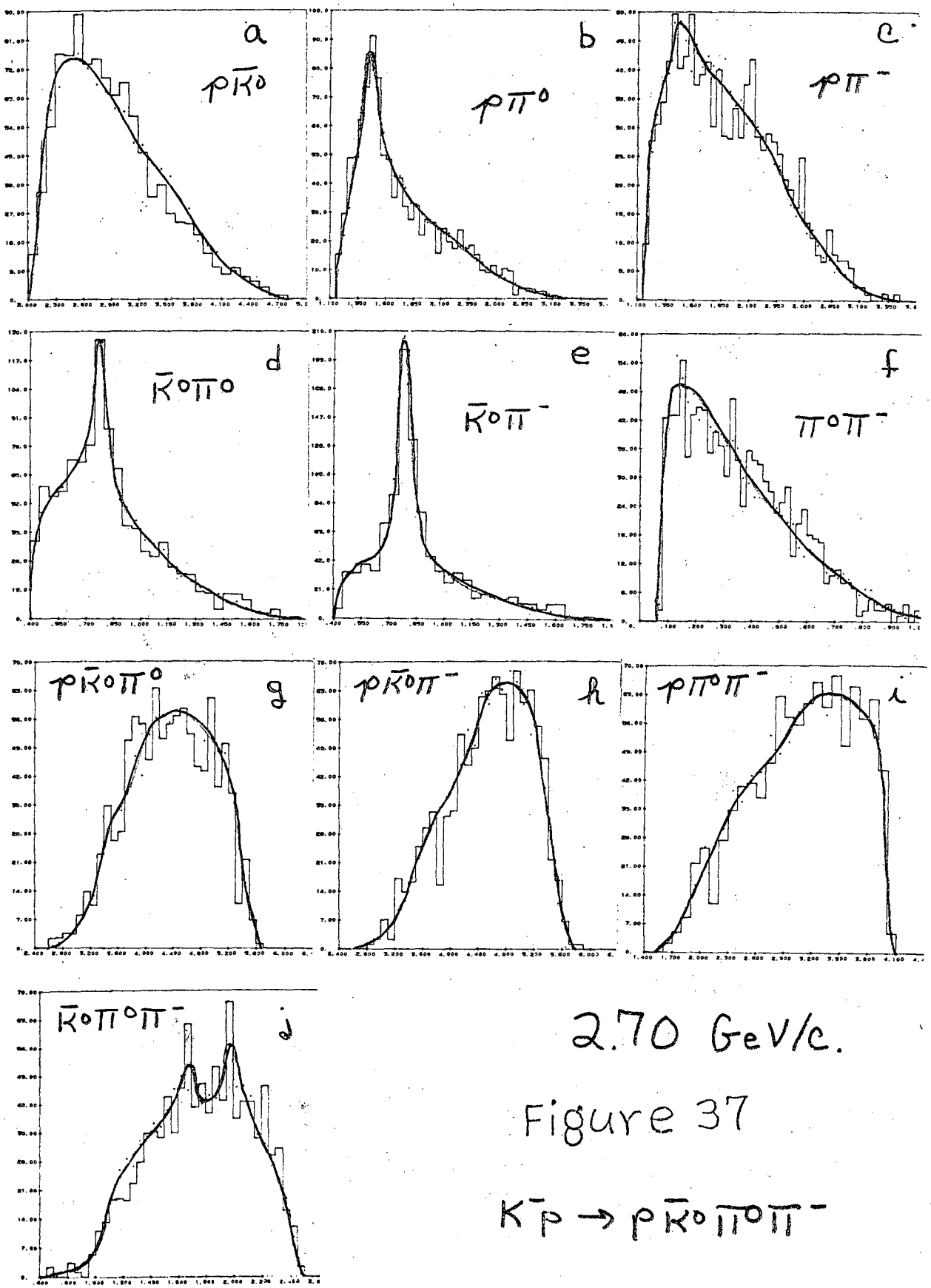

2.70 GeV/c.

Figure 37

$K^-p \rightarrow p\bar{K}^0\pi^0\pi^-$

INVARIANT MASS SQ. $(GeV.)^2$

Figure 38

Total cross section for the reaction $K^- p \to n\bar{K}^0 \pi^+ \pi^-$ in the beam momentum range 1 to 3.5 GeV/c as measured by several experiments.

△ Wojcicki et al. (Ref. 48)

○ Smith (Ref. 38)

▽ (Ref. 40)

● This experiment

Figure 38

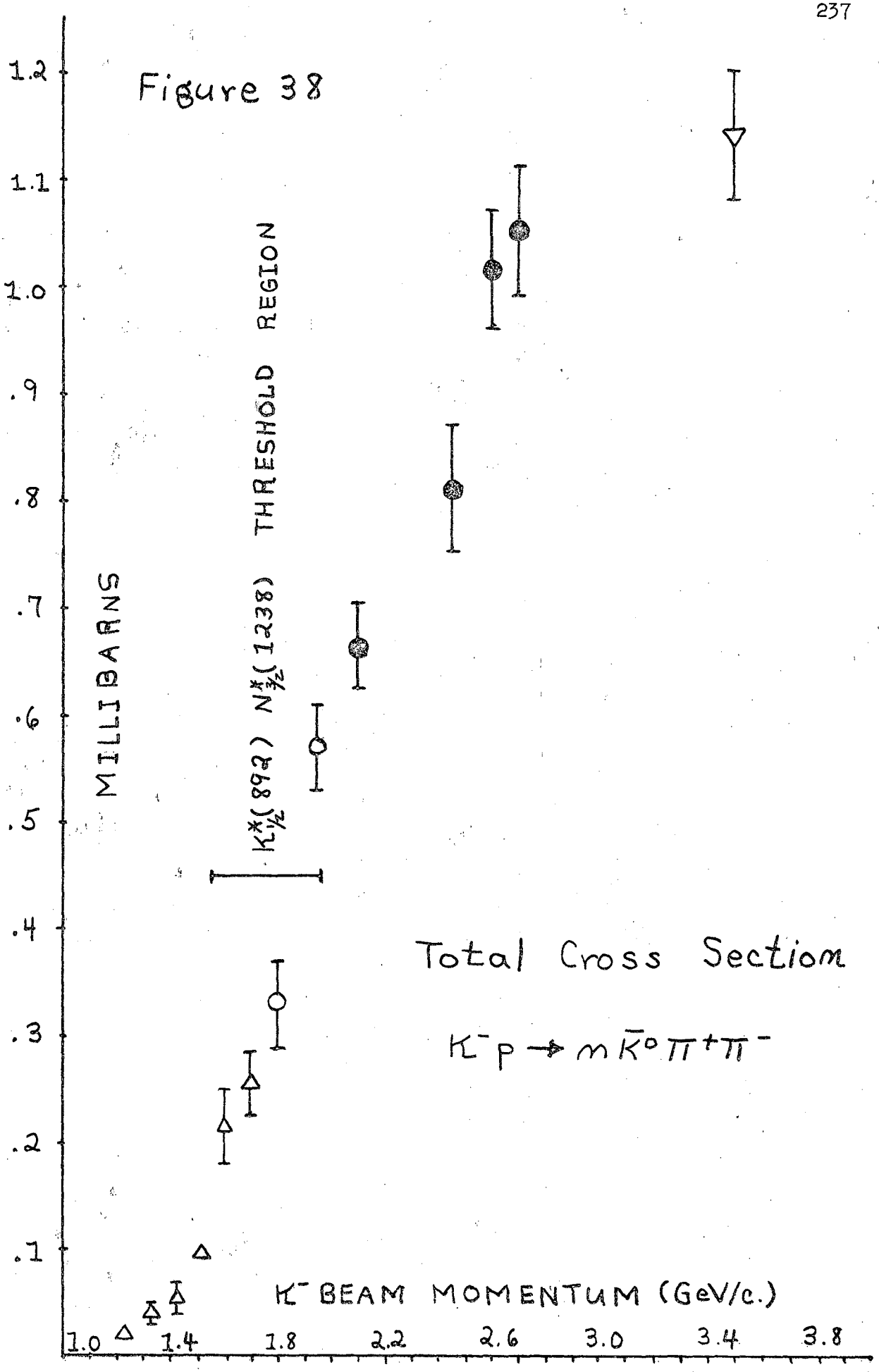
MILLIBARNS
1.2
1.1
1.0
.9
.8
.7
.6
.5
.4
.3
.2
.1
$K^*_{1/2}(892)$ $N^*_{3/2}(1238)$ THRESHOLD REGION
Total Cross Section
$K^- p \to n \bar{K}^0 \pi^+ \pi^-$
K^- BEAM MOMENTUM (GeV/c.)
1.0
1.4
1.8
2.2
2.6
3.0
3.4
3.8

Figure 39

Histograms of invariant mass squared for the ten particle pairs and triples in the reaction $K^- p \rightarrow n\overline{K}^0\pi^+\pi^-$ at 2.1 GeV/c. The solid curves are the predictions of the maximum likelihood solution. (See text)

a) $n\overline{K}^0$ b) $n\pi^+$ c) $n\pi^-$ d) $\overline{K}^0\pi^+$

e) $\overline{K}^0\pi^-$ f) $\pi^+\pi^-$ g) $n\overline{K}^0\pi^+$ h) $n\overline{K}^0\pi^-$

i) $n\pi^+\pi^-$ j) $\overline{K}^0\pi^+\pi^-$

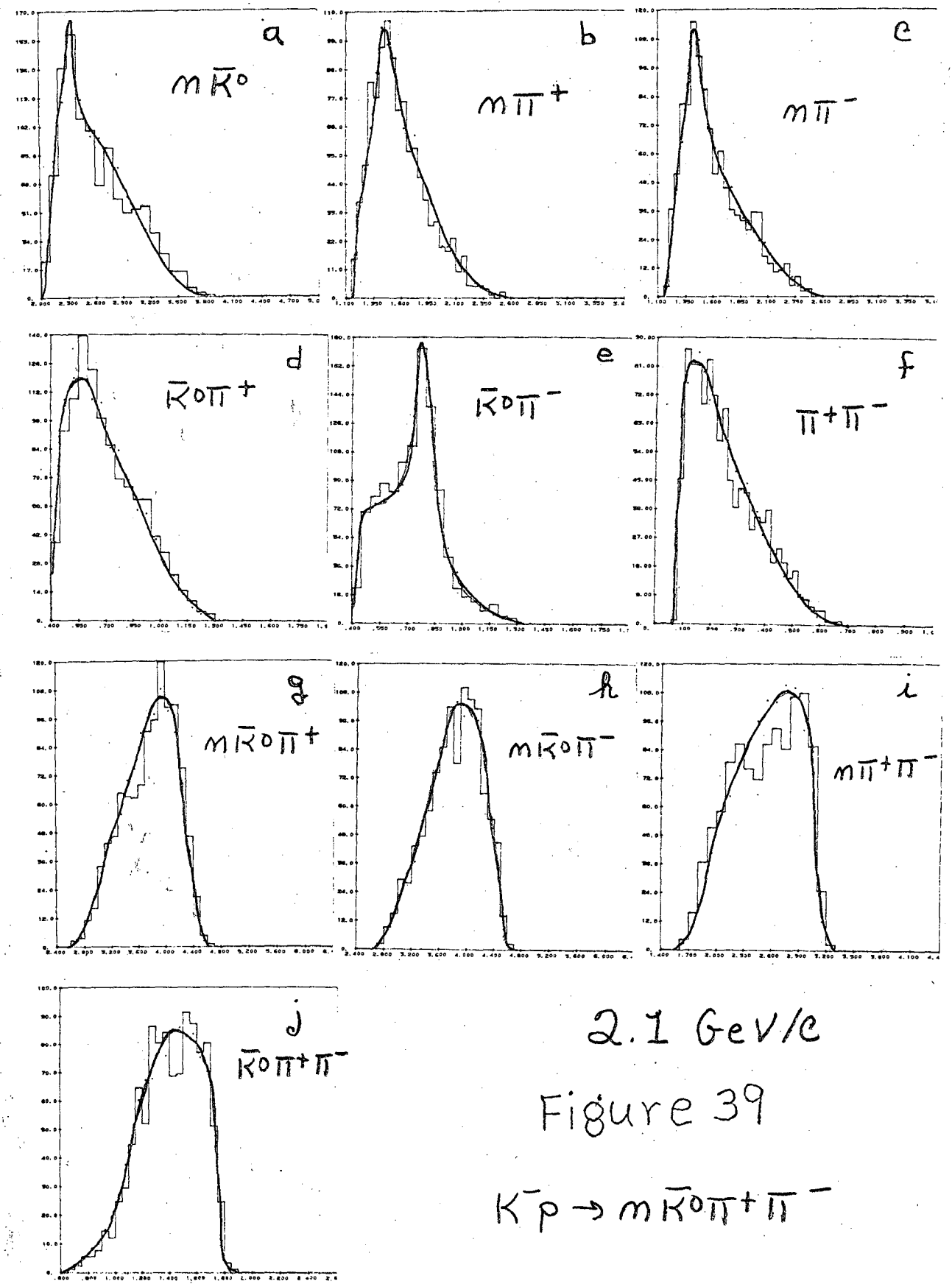

2.1 GeV/c

Figure 39

$K^-p \rightarrow m\bar{K}^0\pi^+\pi^-$

INVARIANT MASS SQ. $(GeV.)^2$

Figure 40

Histograms of invariant mass squared for the ten particle pairs and triples in the reaction $K^-p \rightarrow n\overline{K}^0\pi^+\pi^-$ at 2.45 GeV/c. The solid curves are the predictions of the maximum likelihood solution. (See text)

a) $n\overline{K}^0$ b) $n\pi^+$ c) $n\pi^-$ d) $\overline{K}^0\pi^+$

e) $\overline{K}^0\pi^-$ f) $\pi^+\pi^-$ g) $n\overline{K}^0\pi^+$ h) $nK^\oplus\pi^=$

i) $n\pi^+\pi-$ j) $\overline{K}^0\pi^+\pi^-$

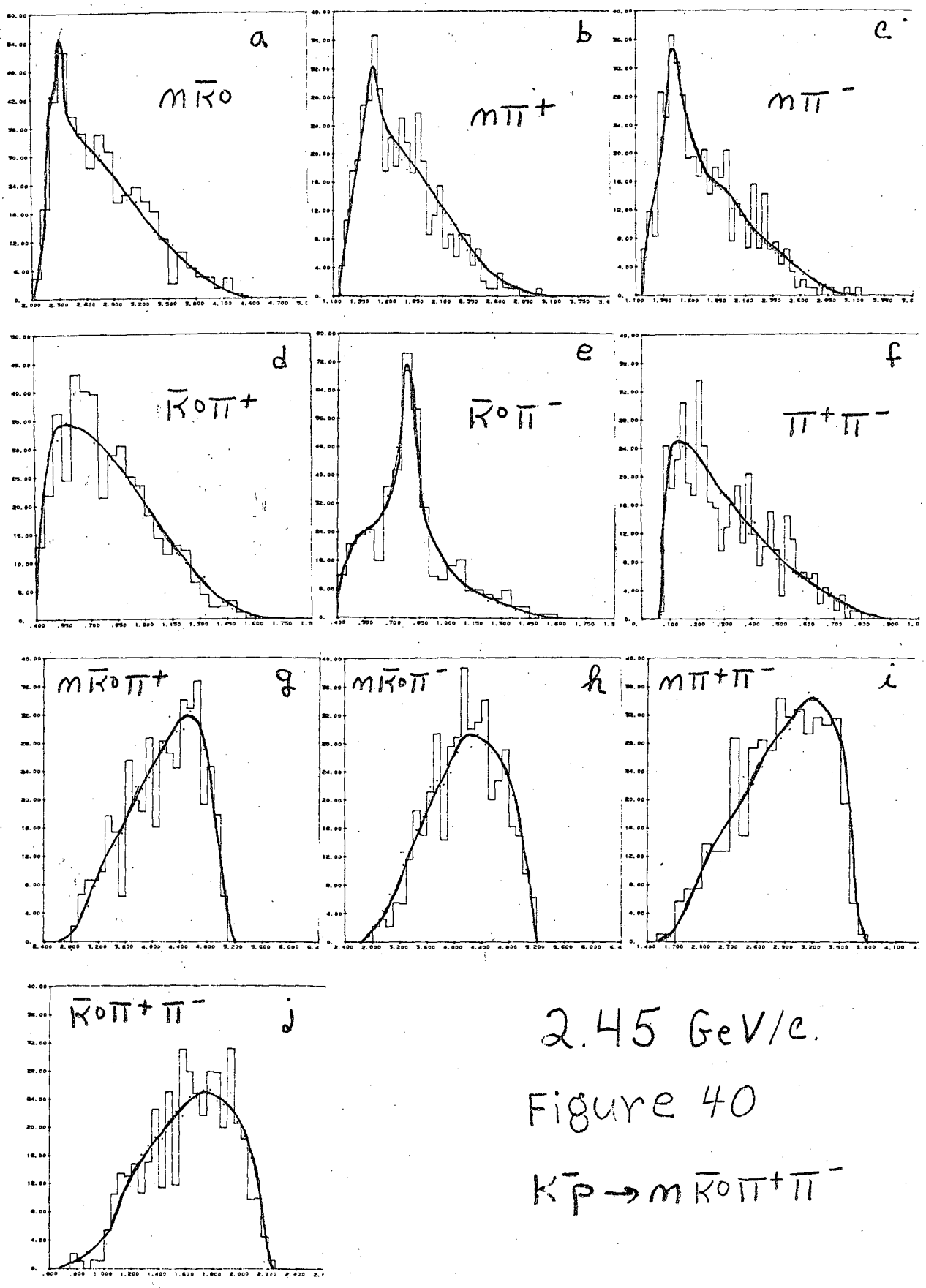

2.45 GeV/c.

Figure 40

$K^-p \rightarrow n\bar{K}^0\pi^+\pi^-$

INVARIANT MASS SQ. $(GeV.)^2$

Figure 41

Histograms of invariant mass squared for the ten particle pairs and triples in the reaction $K^- p \rightarrow n\bar{K}^0\pi^+\pi^-$ at 2.60 GeV/c. The solid curves are the predictions of the maximum likelihood solutions. (See text)

a) $n\bar{K}^0$ b) $n\pi^+$ c) $n\pi^-$ d) $\bar{K}^0\pi^+$

e) $\bar{K}^0\pi^-$ f) $\pi^+\pi^-$ g) $n\bar{K}^0\pi^+$ h) $n\bar{K}^0\pi^-$

i) $n\pi^+\pi^-$ j) $\bar{K}^0\pi^+\pi^-$

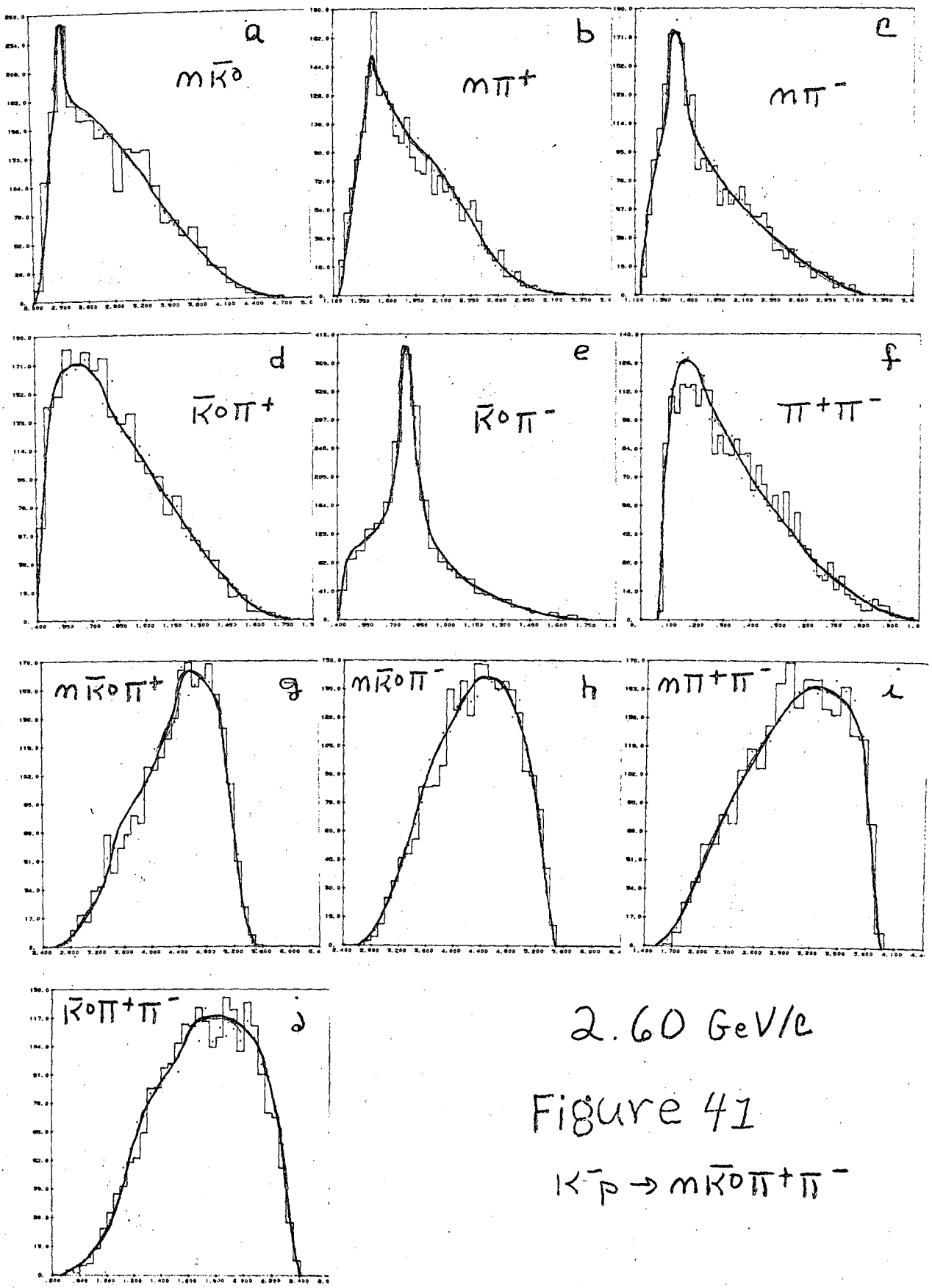

2.60 GeV/c

Figure 41

$K^-p \to m\bar{K}^0\pi^+\pi^-$

INVARIANT MASS SQ. $(GeV.)^2$

Figure 42

Histograms of invariant mass squared for the ten particle pairs and triples in the reaction $K^- p \rightarrow n\bar{K}^0\pi^+\pi^-$ at 2.70 GeV/c. The solid curves are the projections of the maximum likelihood solution. (See text)

a) $n\bar{K}^0$ b) $n\pi^+$ c) $n\pi^-$ d) $\bar{K}^0\pi^+$

e) $\bar{K}^0\pi^-$ f) $\pi^+\pi^-$ g) $n\bar{K}^0\pi^+$ h) $n\bar{K}^0\pi^-$

i) $n\pi^+\pi^-$ j) $\bar{K}^0\pi^+\pi^-$

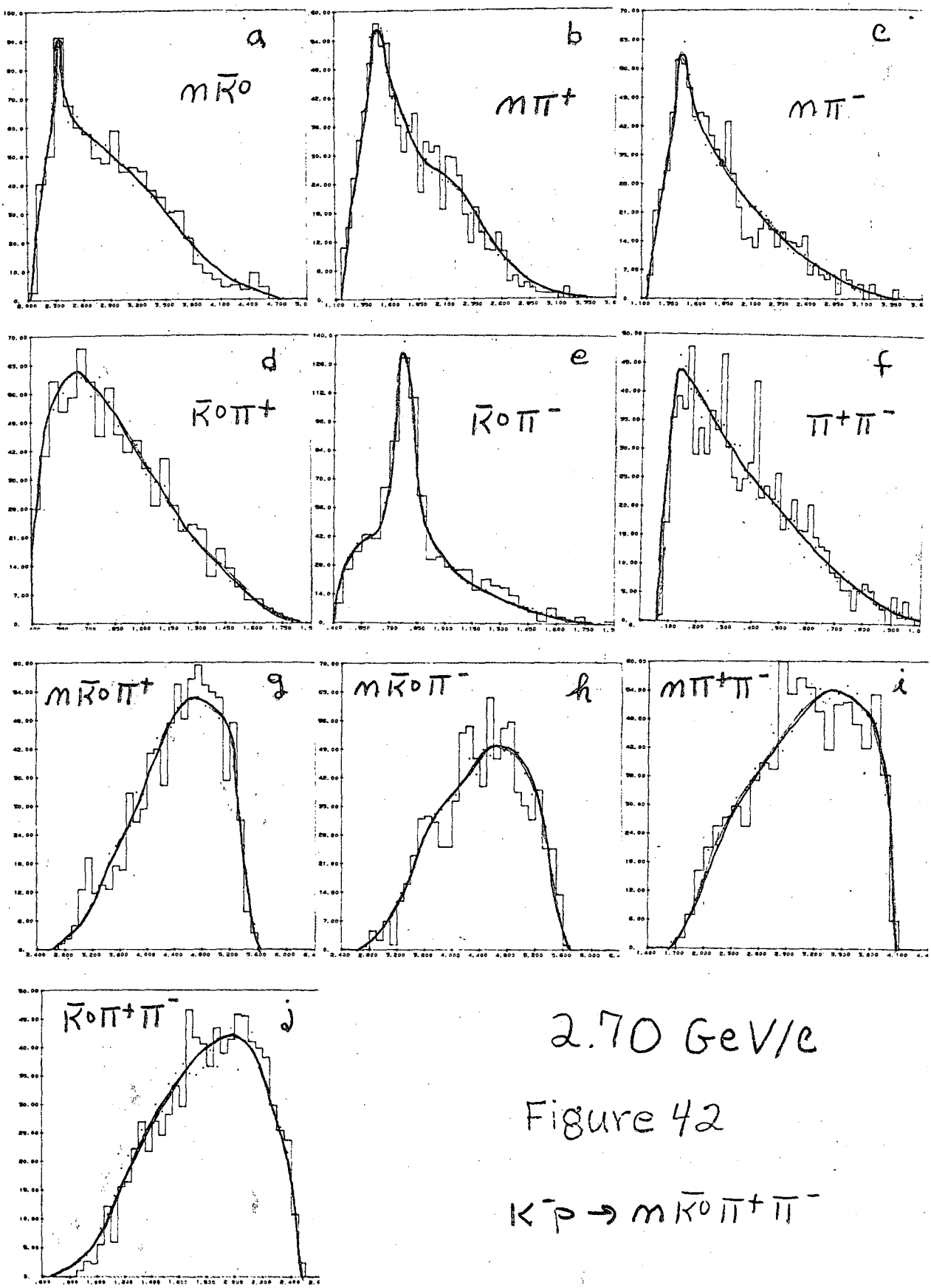

2.70 GeV/c

Figure 42

$K^-p \rightarrow n\bar{K}^0\pi^+\pi^-$

INVARIANT MASS SQ. $(GeV.)^2$

Figure 43

Total cross section for the reaction $K^- p \rightarrow N^*_{3/2}(1238)\ \bar{K}^*_{1/2}(892)$ from 1.8 to 2.7 GeV/c. K^- beam momentum.

○ Smith (Ref. 38)

□ Dauber (Ref. 50)

◎ This experiment

Figure 43

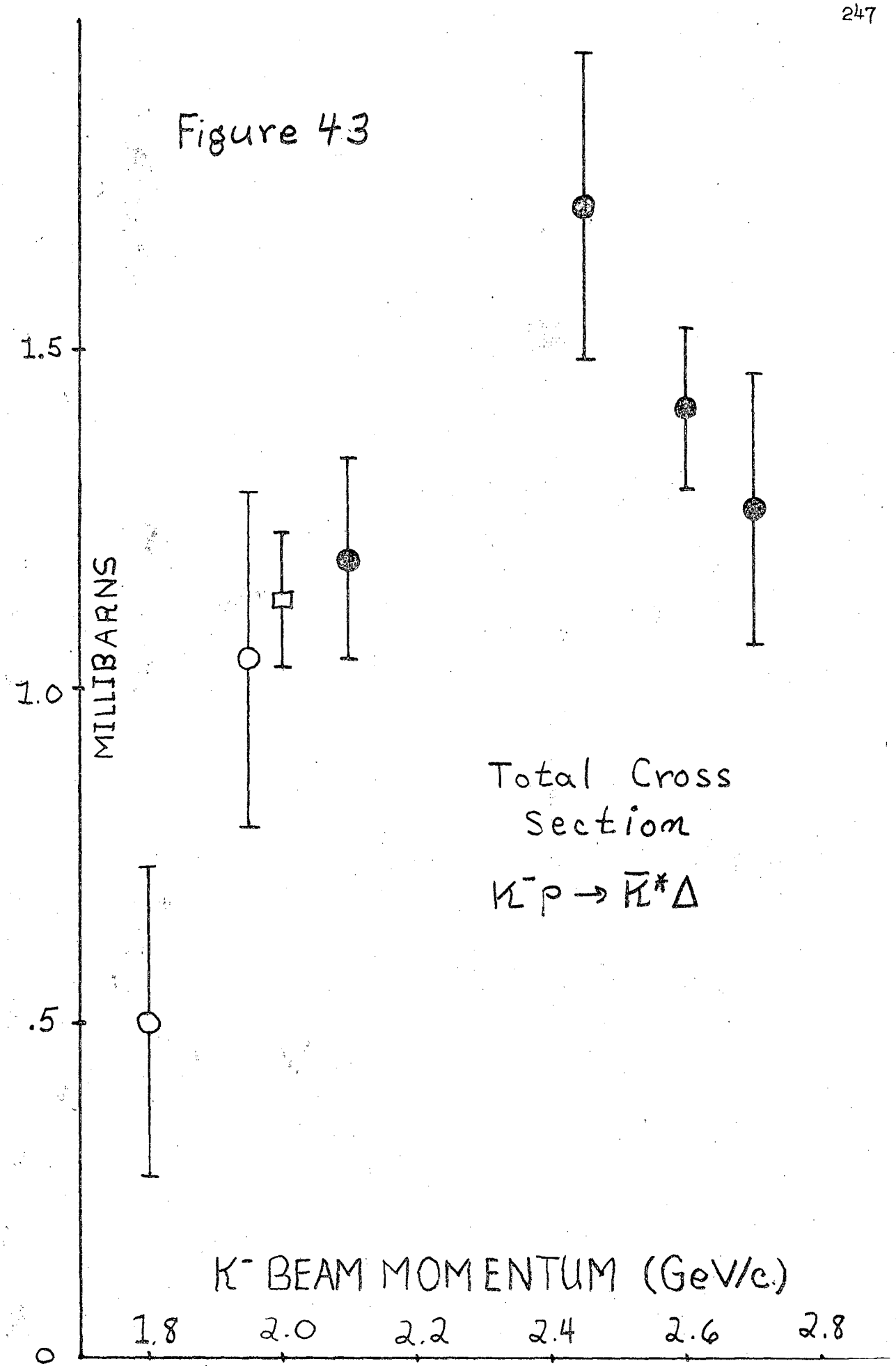
1.5
1.0
.5
0
MILLIBARNS
Total Cross Section
$K^- p \to \bar{K}^* \Delta$
K^- BEAM MOMENTUM (GeV/c.)
1.8
2.0
2.2
2.4
2.6
2.8

Figure 44

Production cosine distribution for the reaction $K^- p \rightarrow K^{*-}_{1/2}$ (892) $N^{*+}_{3/2}$ (1238) at each beam momentum.

a) 2.1 GeV/c

b) 2.45 GeV/c

c) 2.61 GeV/c

d) 2.70 GeV/c

Figure 44

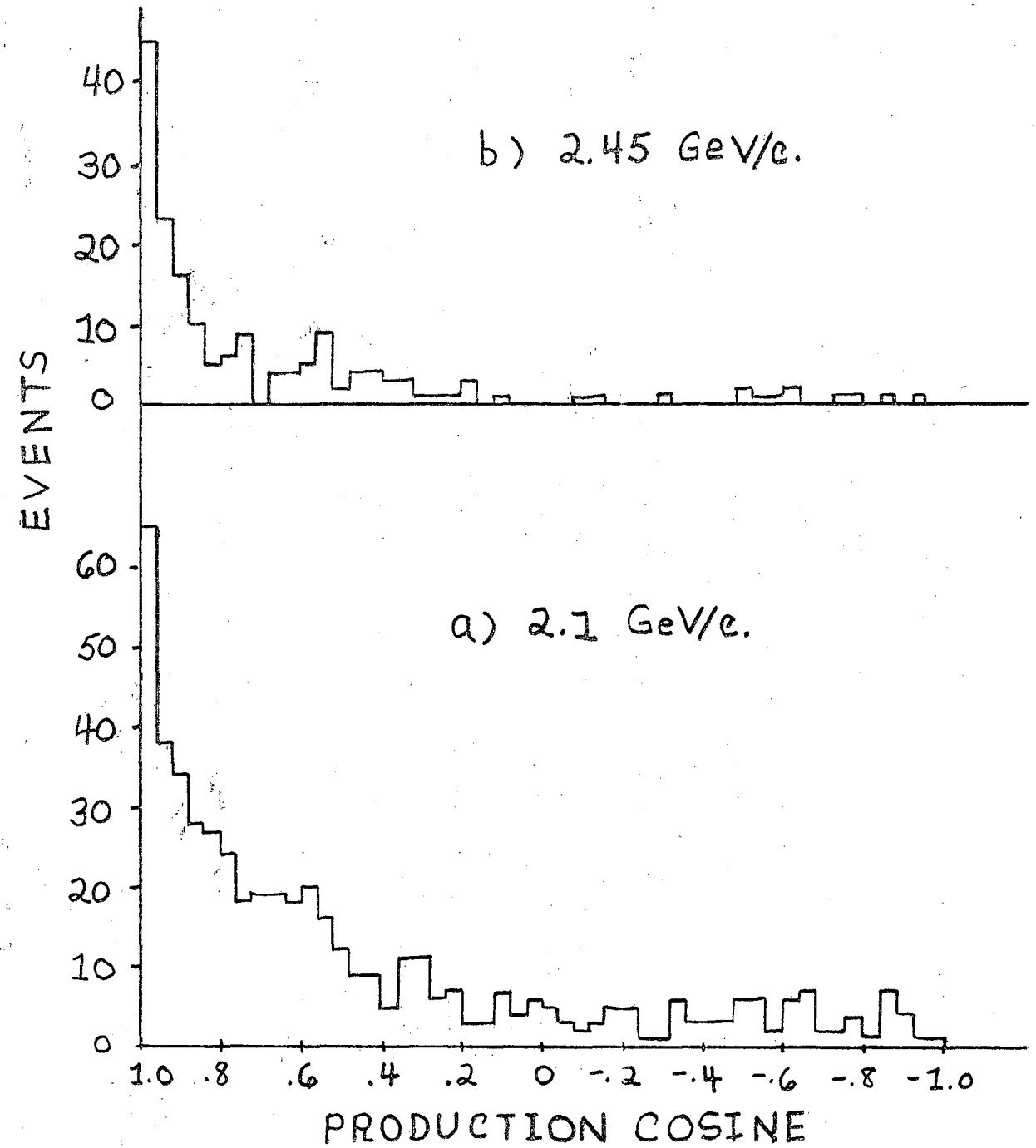
b) 2.45 GeV/c.
a) 2.1 GeV/c.
EVENTS
40
30
20
10
0
60
50
40
30
20
10
0
1.0 .8 .6 .4 .2 0 -.2 -.4 -.6 -.8 -1.0
PRODUCTION COSINE

Figure 44

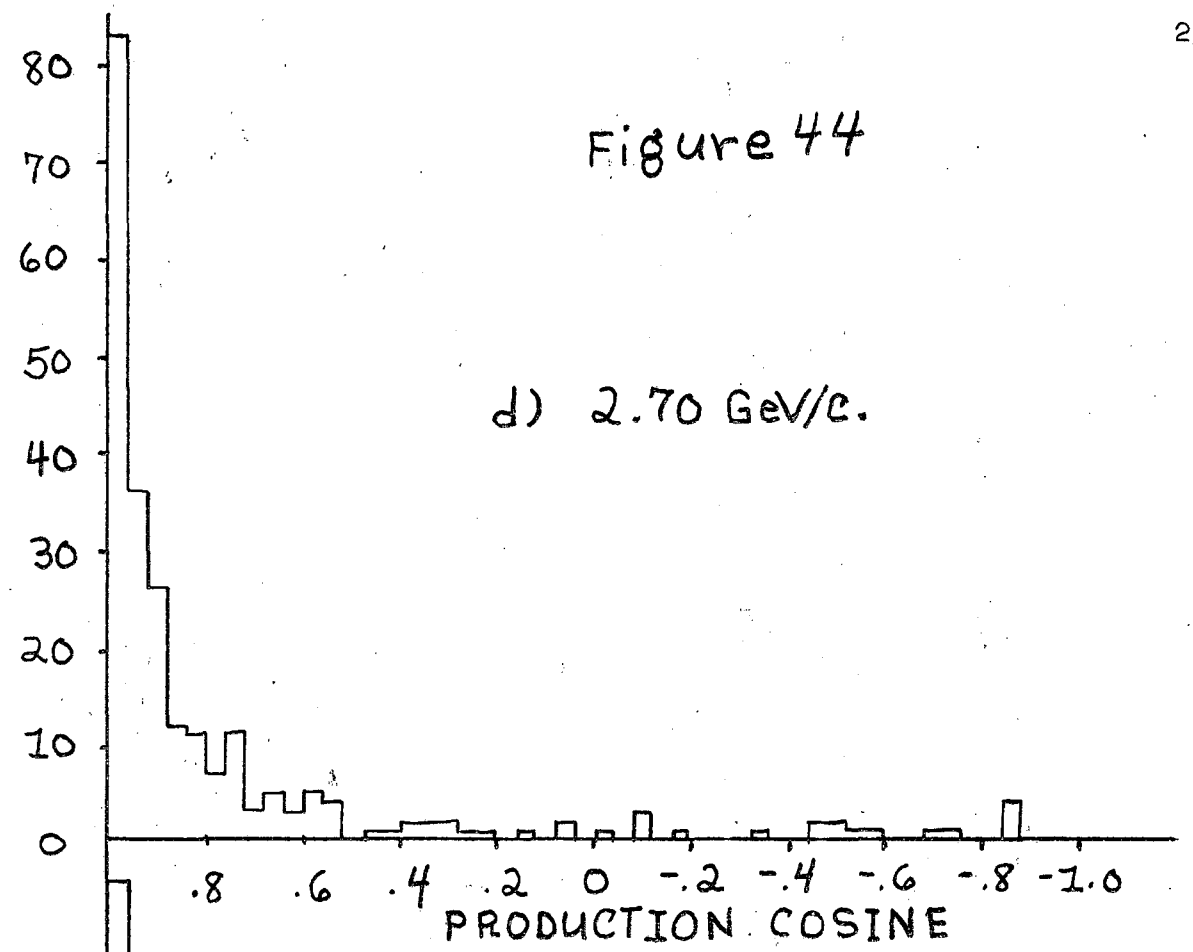
80
70
60
50
40
30
20
10
0
d) 2.70 GeV/c.
.8 .6 .4 .2 0 -.2 -.4 -.6 -.8 -1.0
PRODUCTION COSINE

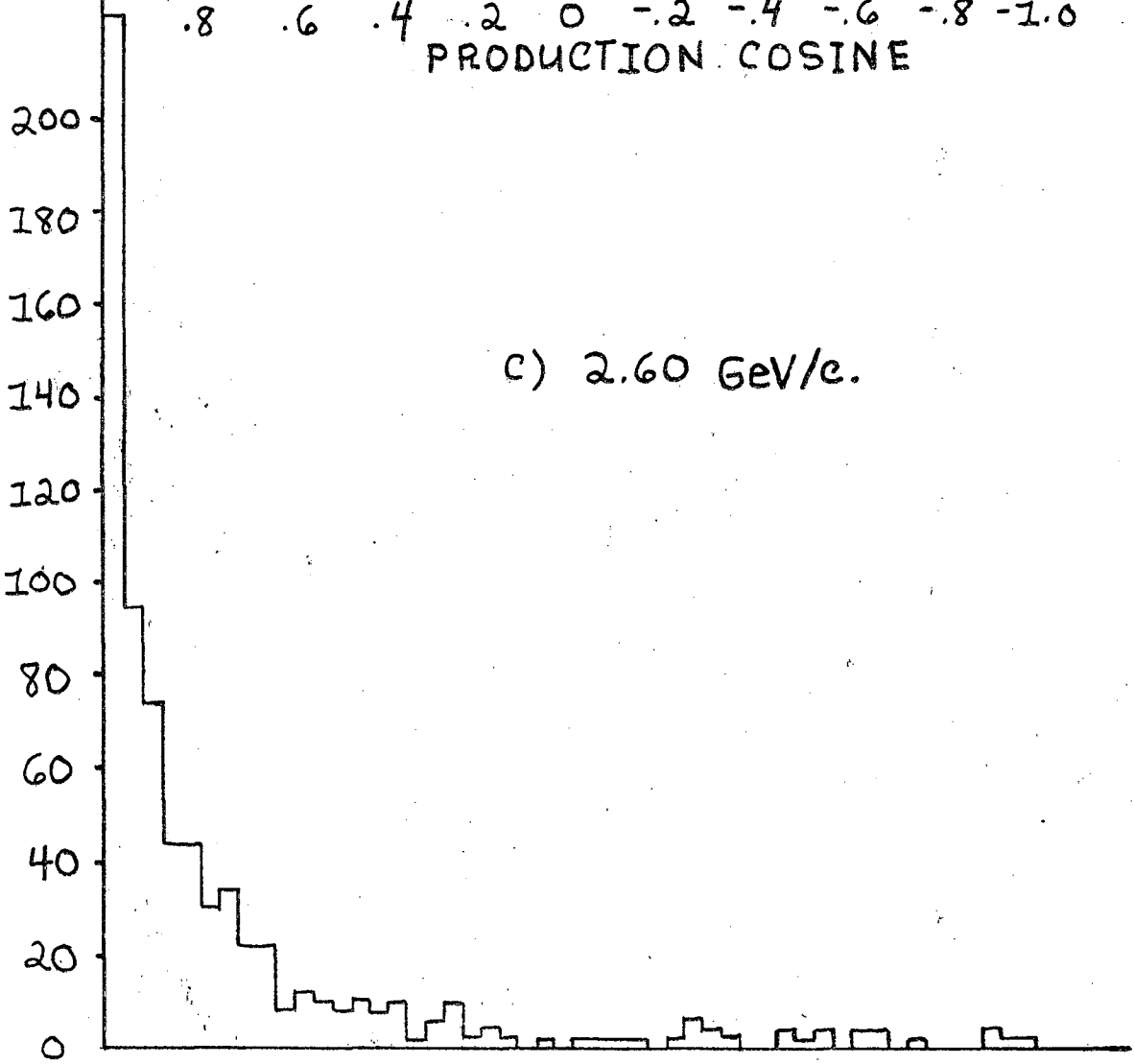
200
180
160
140
120
100
80
60
40
20
0
c) 2.60 GeV/c.

Figure 45

Decay angular distribution parameters for the reaction $K^- p \rightarrow K^{*-}_{\frac{1}{2}}(892)\, N^{*+}_{3/2}(1238)$ averaged over all production angles as a function of K^- beam momentum.

Figure 45

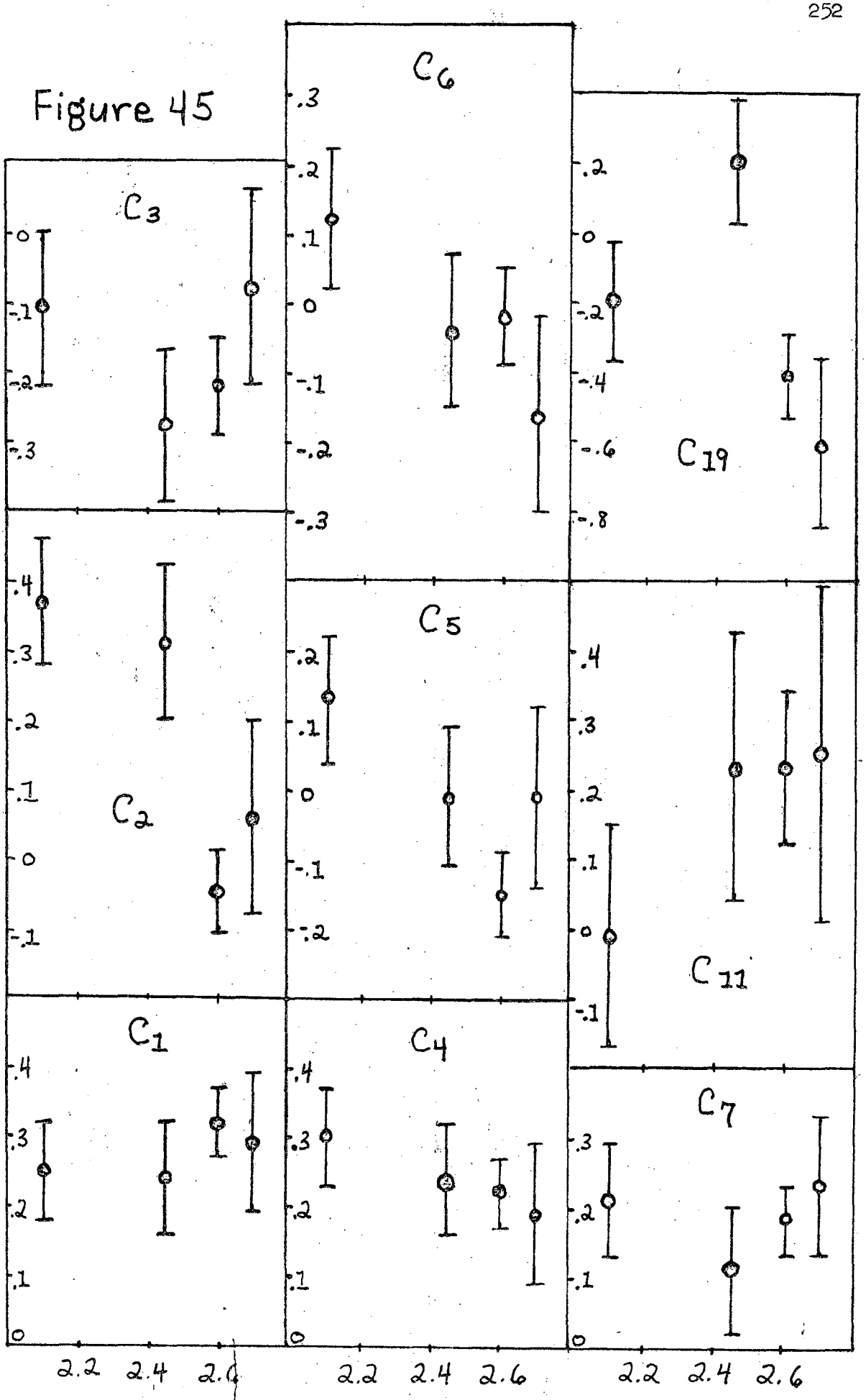

Figure 46

Comparisons of the maximum likelihood solutions for the $\bar{K}^*_{\frac{1}{2}}$ (892) $N^*_{3/2}$ (1238) joint decay angular distributions with projections of the data at 2.1 GeV/c.

a) $K^*_{\frac{1}{2}}$ (892) polar cosine "e_3".

b) $N^*_{3/2}$ (892) polar cosine "p_3".

c) $K^*_{\frac{1}{2}}$ (892) azimuthal angle "Φ_e".

d) $N^*_{3/2}$ (1238) azimuthal angle "Φ_p".

e) $(e_1+e_3)/\sqrt{2}$

f) $(e_1-e_3)/\sqrt{2}$

g) $(p_1+p_3)/\sqrt{2}$

h) $(p_1-p_3)/\sqrt{2}$

i) $\varphi_e + \varphi_p$

j) $\varphi_e - \varphi_p$

k) e_3 for $|p_3| \geq .5$

l) e_3 for $|p_3| < .5$

m) p_3 for $|e_3| > .5$

n) p_3 for $|e_3| < .5$

$K^- p \to \bar{K}^* \Delta$ 2.1 GeV/c.

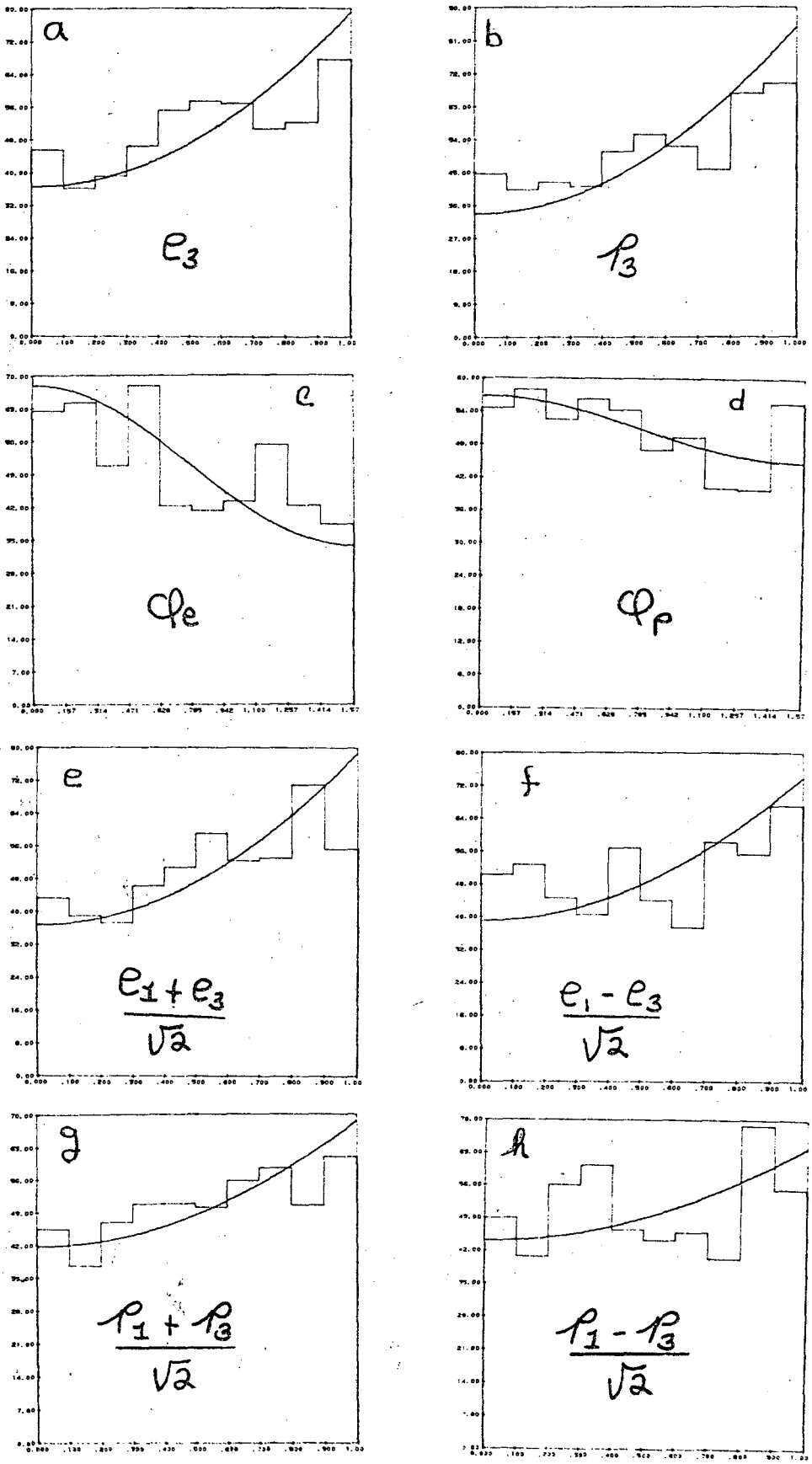

Figure 46

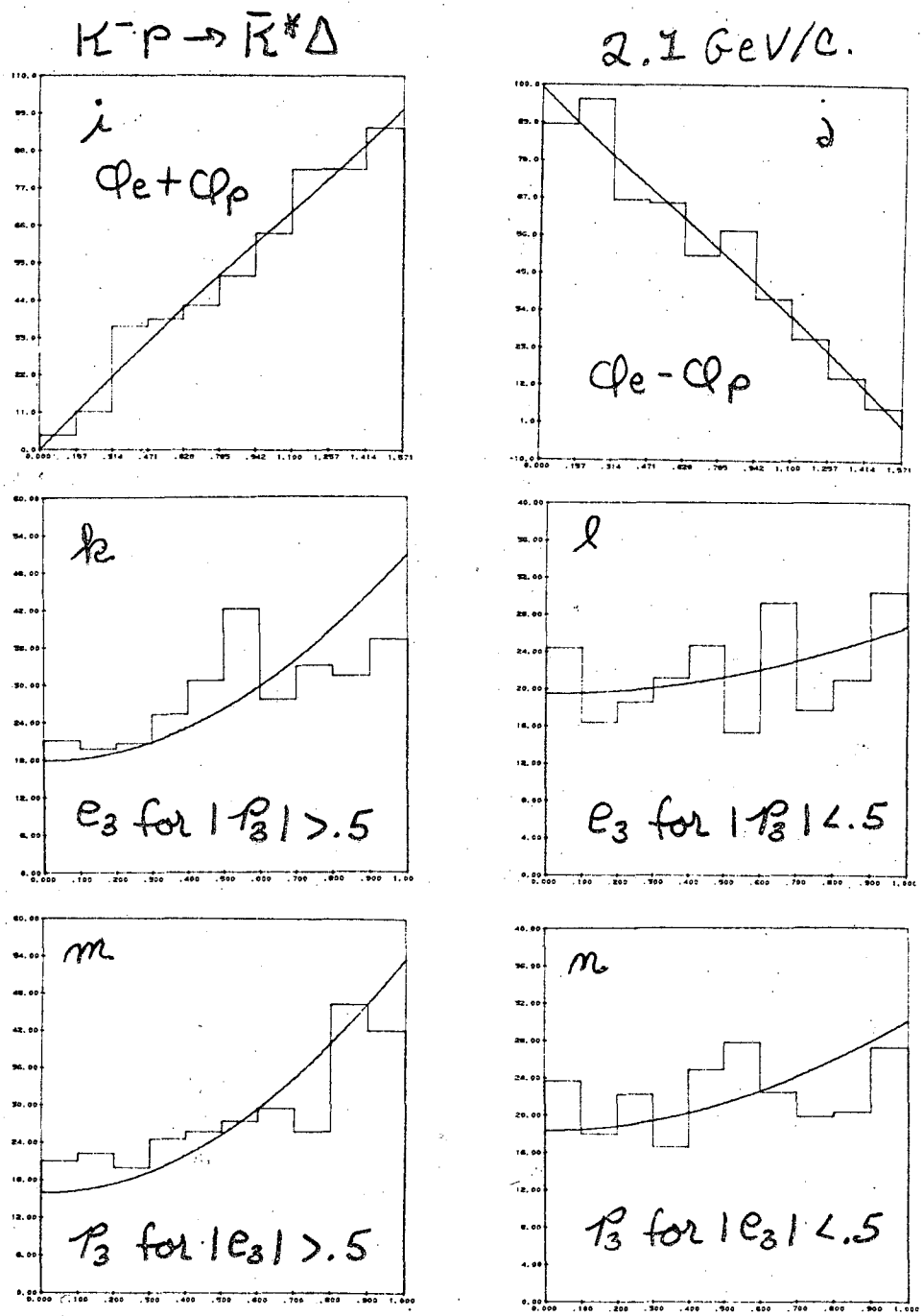
$K^- p \to \bar{K}^* \Delta$
2.1 GeV/c.
i
$Q_e + Q_p$
j
$Q_e - Q_p$
k
e_3 for $|P_3| > .5$
l
e_3 for $|P_3| < .5$
m
P_3 for $|e_3| > .5$
n
P_3 for $|e_3| < .5$

Figure 46

Figure 47

Comparisons of the maximum likelihood solutions for the $\bar{K}^*_{\frac{1}{2}}$ (892) $N^*_{3/2}$ (1238) joint decay angular distributions with projections of the data at 2.45 GeV/c.

a) $K^*_{\frac{1}{2}}$ (892) polar cosine "e_3".

b) $N^*_{3/2}$ (1238) polar cosine "p_3".

c) $K^*_{\frac{1}{2}}$ (892) azimuthal angle "φ_e".

d) $N^*_{3/2}$ (1238) azimuthal angle "φ_p".

e) $(e_1 + e_3)/\sqrt{2}$

f) $(e_1 - e_3)/\sqrt{2}$

g) $(p_1 + p_3)/\sqrt{2}$

h) $(p_1 - p_3)/\sqrt{2}$

i) $\varphi_e + \varphi_p$

j) $\varphi_e - \varphi_p$

k) e_3 for $|p_3| > .5$

l) e_3 for $|p_3| < .5$

m) p_3 for $|e_3| > .5$

n) p_3 for $|e_3| < .5$

$K^- p \to \bar{K}^* \Delta$ 2.45 GeV/c.

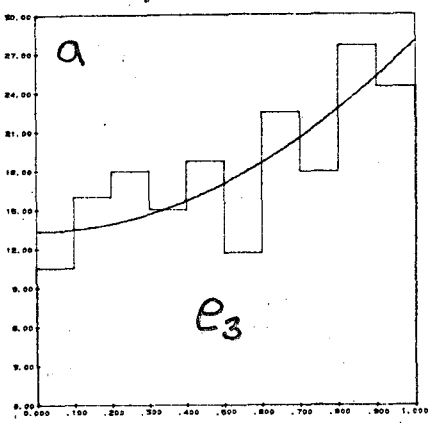

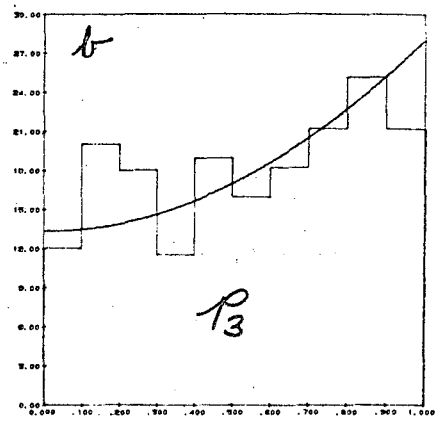

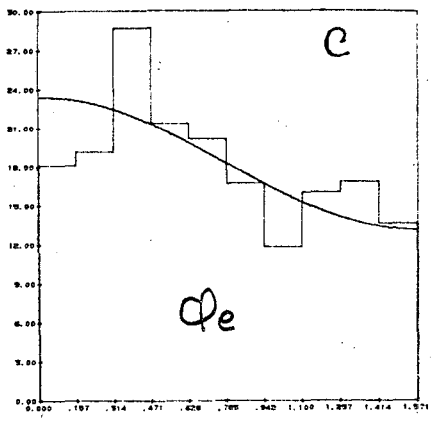

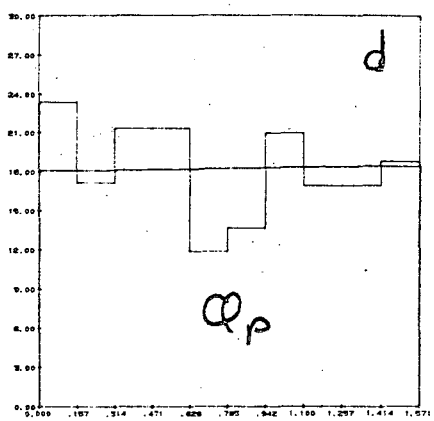

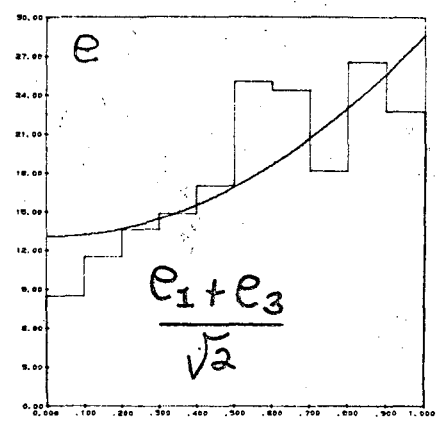

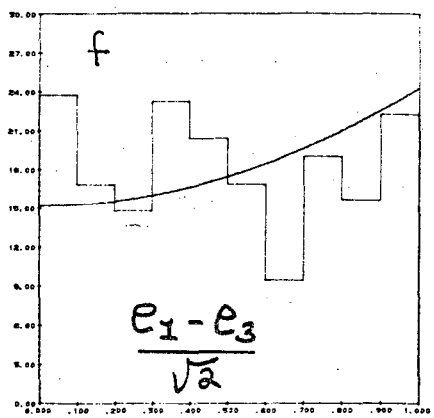

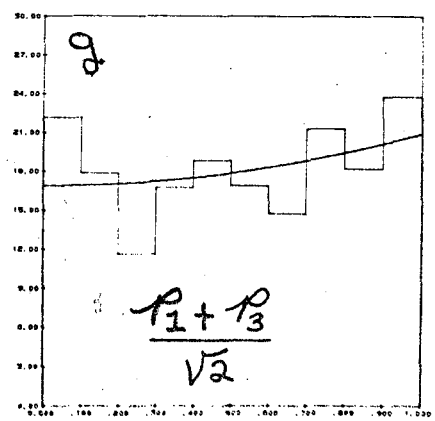

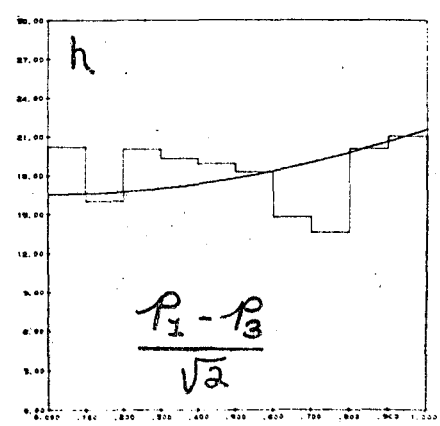

Figure 47

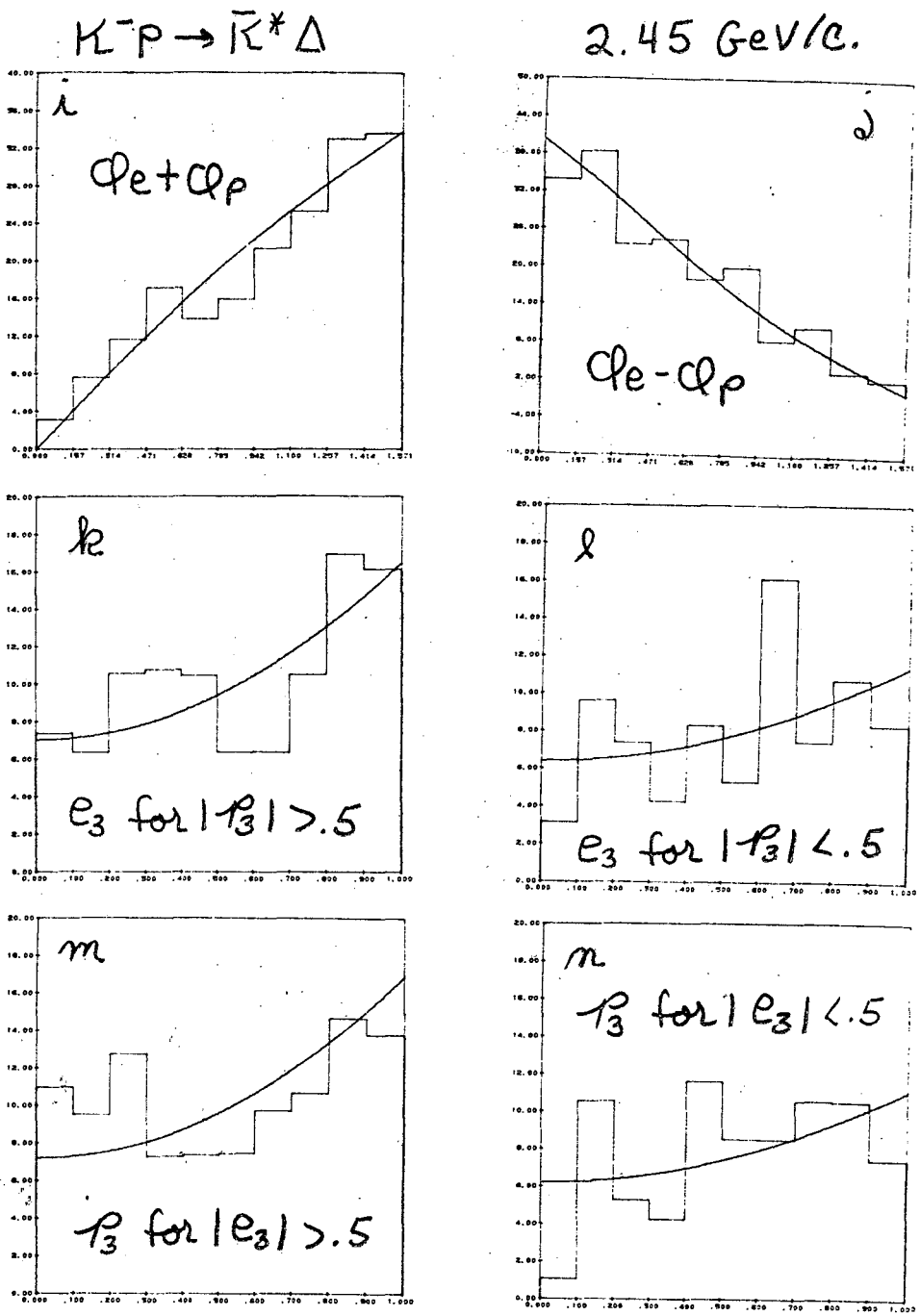
$K^-p \to \bar{K}^*\Delta$
2.45 GeV/c.
i
$Q_e + Q_p$
j
$Q_e - Q_p$
k
e_3 for $|P_3| > .5$
l
e_3 for $|P_3| < .5$
m
P_3 for $|e_3| > .5$
n
P_3 for $|e_3| < .5$

Figure 47

Figure 48

Comparisons of the maximum likelihood solutions for the $K^*_{\frac{1}{2}}(892)$ $N^*_{3/2}(1238)$ joint decay angular distributions with projections of the data at 2.60 GeV/c.

a) $K^*_{\frac{1}{2}}(892)$ polar cosine "e_3".

b) $N^*_{3/2}(1238)$ polar cosine "p_3".

c) $K^*_{\frac{1}{2}}(892)$ azimuthal angle "φ_e".

d) $N^*_{3/2}(1238)$ azimuthal angle "φ_p".

e) $(e_1 + e_3) / \sqrt{2}$

f) $(e_1 - e_3) / \sqrt{2}$

g) $(p_1 + p_3) / \sqrt{2}$

h) $(p_1 - p_3) / \sqrt{2}$

i) $\varphi_e + \varphi_p$

j) $\varphi_e - \varphi_p$

k) e_3 for $|p_3| > .5$

l) e_3 for $|p_3| < .5$

m) p_3 for $|e_3| > .5$

n) p_3 for $|e_3| < .5$

$K^- p \to \bar{K}^* \Delta$ 2.60 GeV/c.

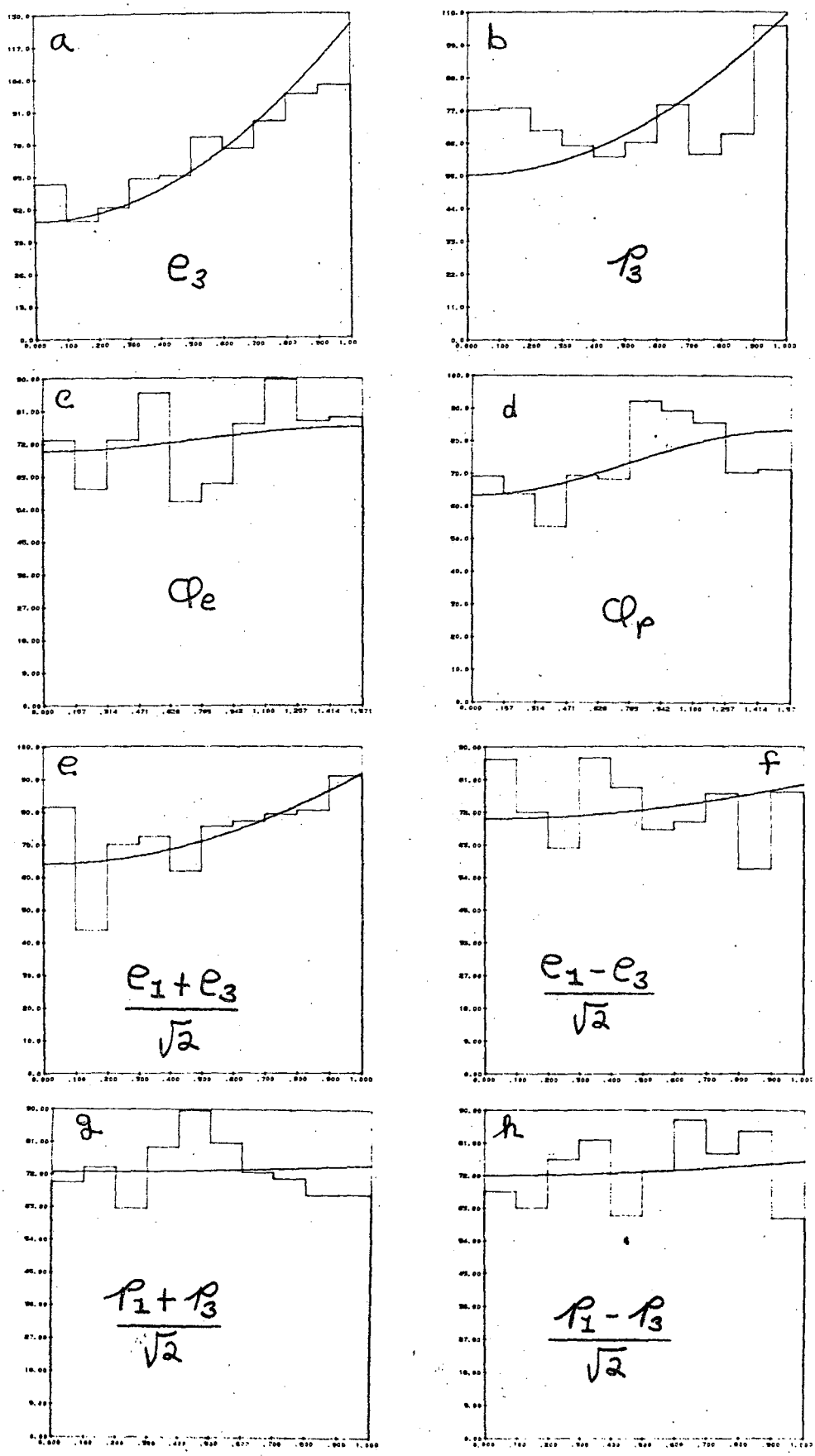

Figure 48

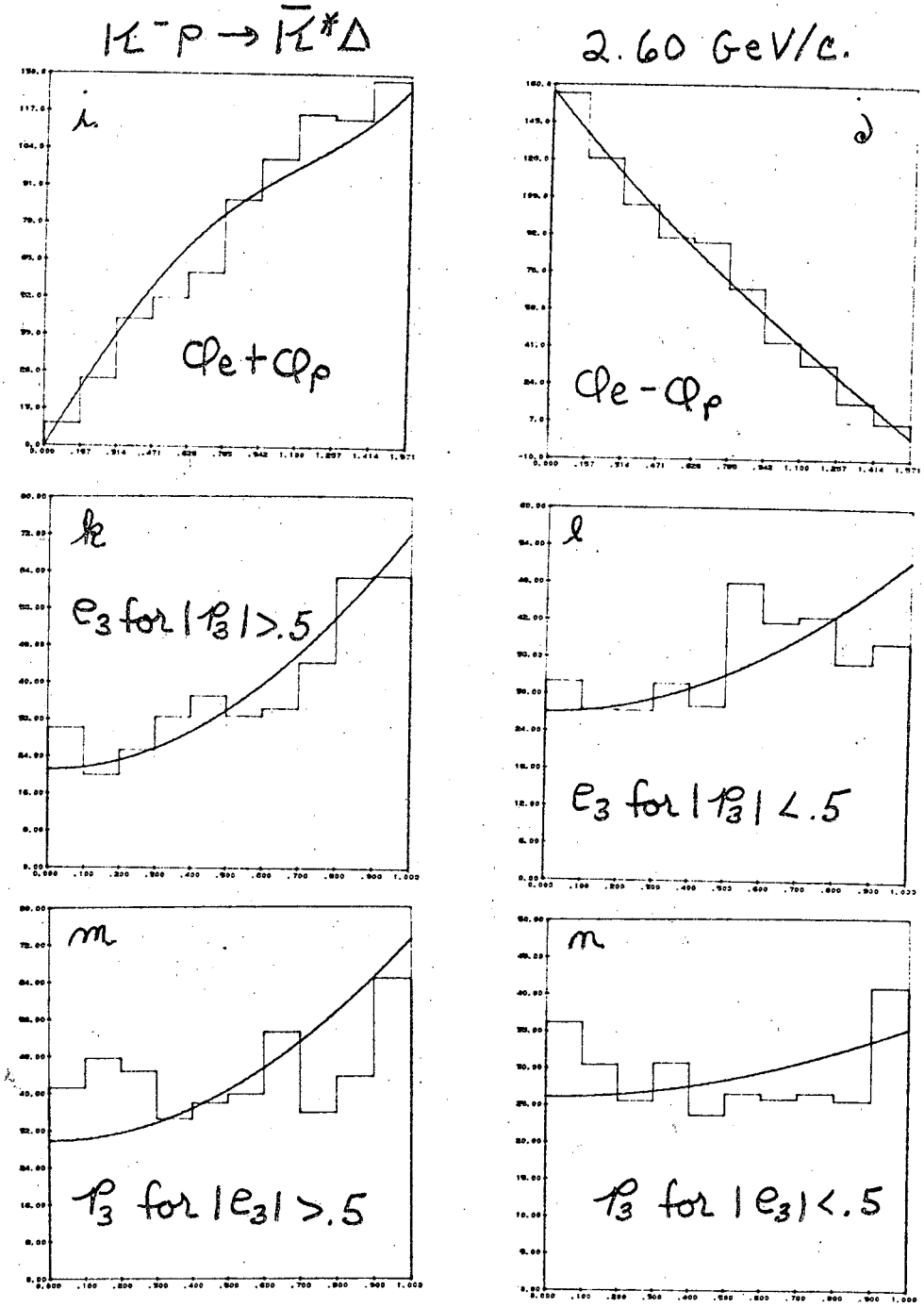
$K^- p \to \bar{K}^* \Delta$
2.60 GeV/c.
i
$\Phi_e + \Phi_p$
j
$\Phi_e - \Phi_p$
k
e_3 for $|P_3| > .5$
l
e_3 for $|P_3| < .5$
m
P_3 for $|e_3| > .5$
n
P_3 for $|e_3| < .5$

Figure 48

Figure 49

Comparisons of the maximum likelihood solutions for the $\bar{K}^*_{\frac{1}{2}}$ (892) $N^*_{3/2}$ (1238) joint decay angular distributions with projections of the data at 2.70 GeV/c.

a) $K^*_{\frac{1}{2}}$ (892) polar cosine "e_3".

b) $N^*_{3/2}$ (1238) polar cosine "p_3".

c) $K^*_{1/2}$ (892) azimuthal angle "φ_e".

d) $N^*_{3/2}$ (1238) azimuthal angle "φ_p".

e) $(e_1 + e_3)/\sqrt{2}$

f) $(e_1 - e_3)/\sqrt{2}$

g) $(p_1 + p_3)/\sqrt{2}$

h) $(p_1 - p_3)/\sqrt{2}$

i) $\varphi_e + \varphi_p$

j) $\varphi_e - \varphi_p$

k) e_3 for $p_3 > .5$

l) e_3 for $p_3 < .5$

m) p_3 for $e_3 > .5$

n) p_3 for $e_3 < .5$

$K^- p \to \bar{K}^* \Delta$ 2.70 GeV/c

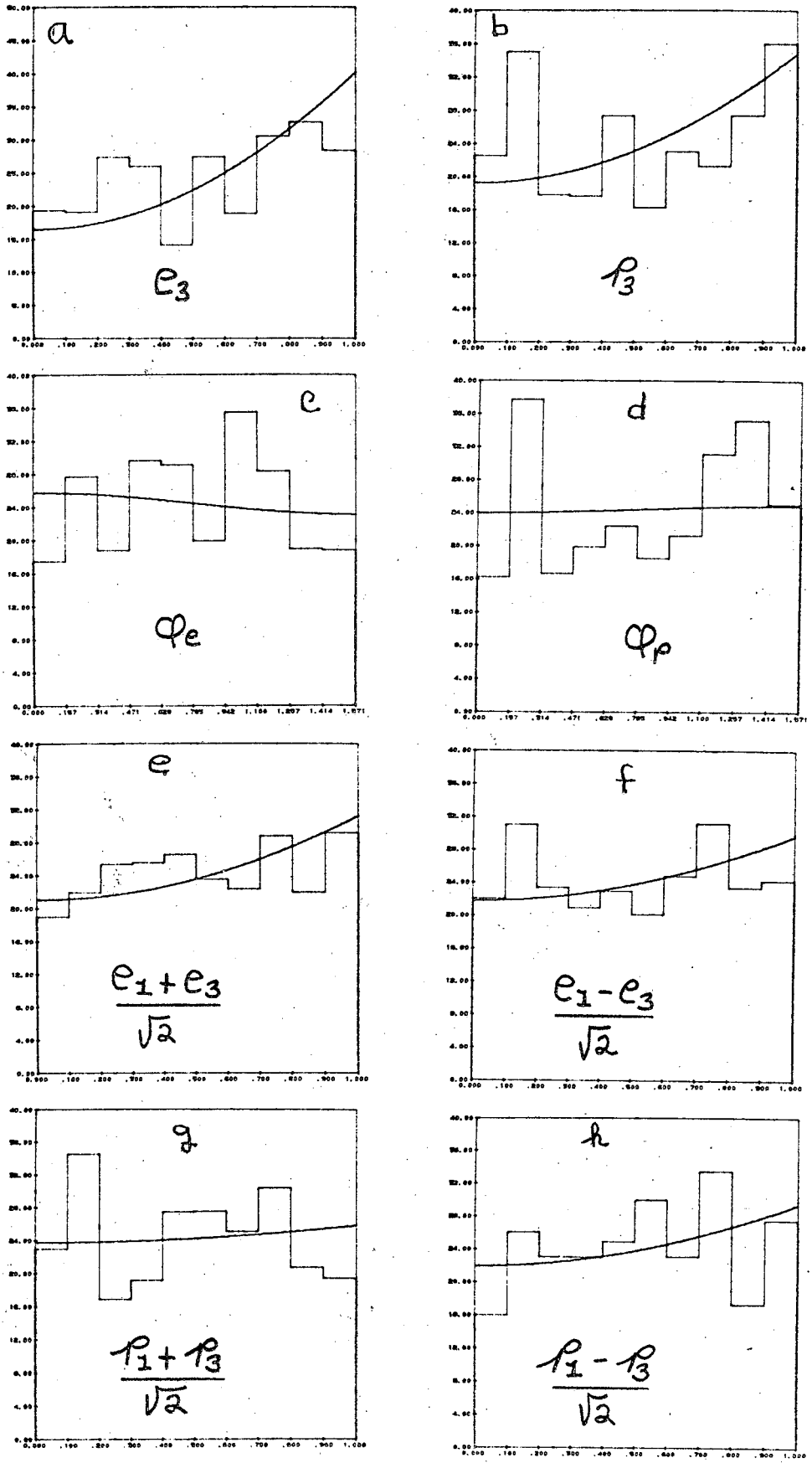

Figure 49

$K^- p \to \bar{K}^* \Delta$ 2.70 GeV/c.

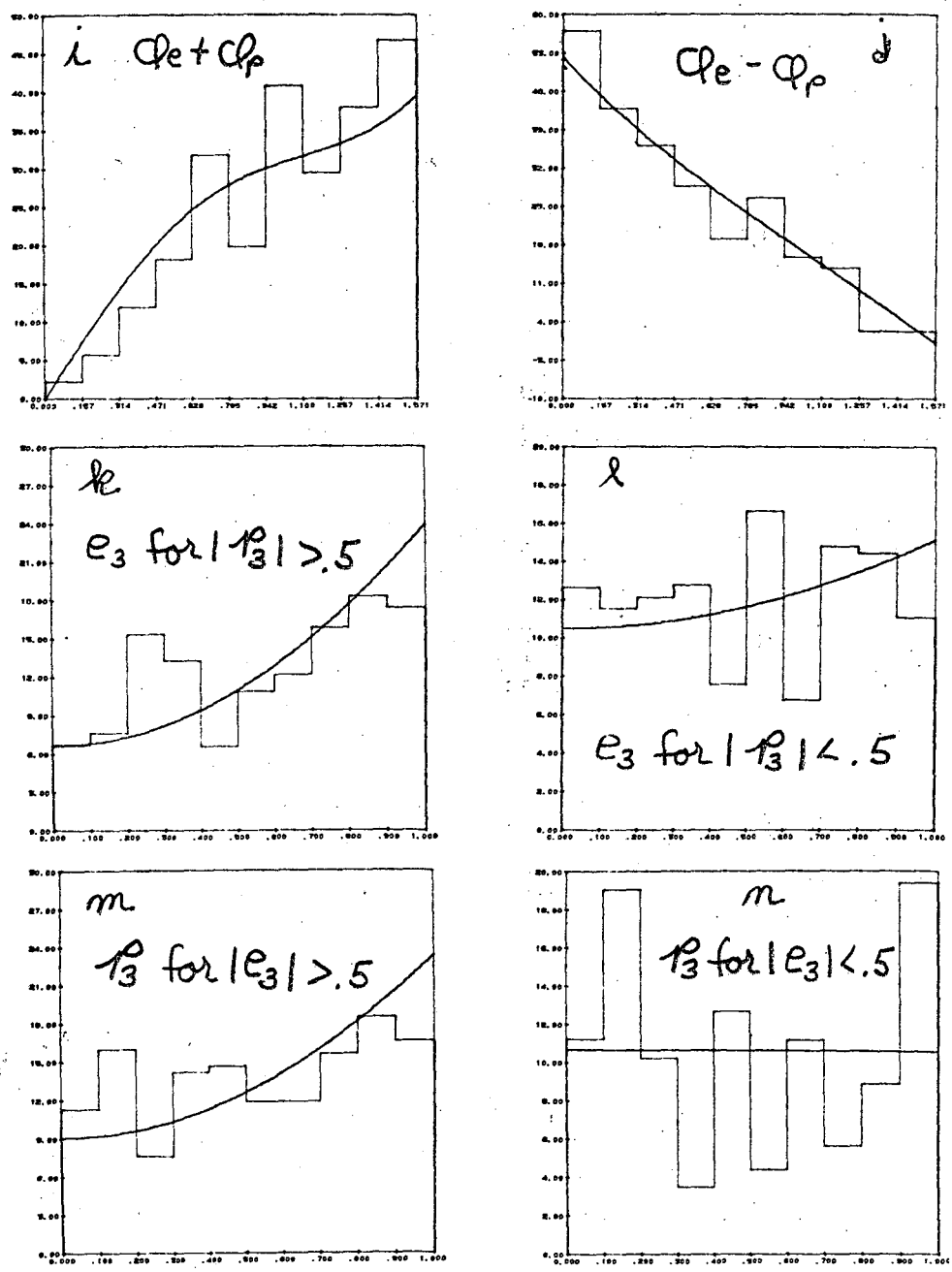

Figure 49

Figure 50

Differential cross section for the reaction $K^- p \to \overline{K}^*_{\frac{1}{2}}$ (892) $N^*_{3/2}$ (1238).

a) 2.1 GeV/c

b) 2.60 and 2.70 GeV/c

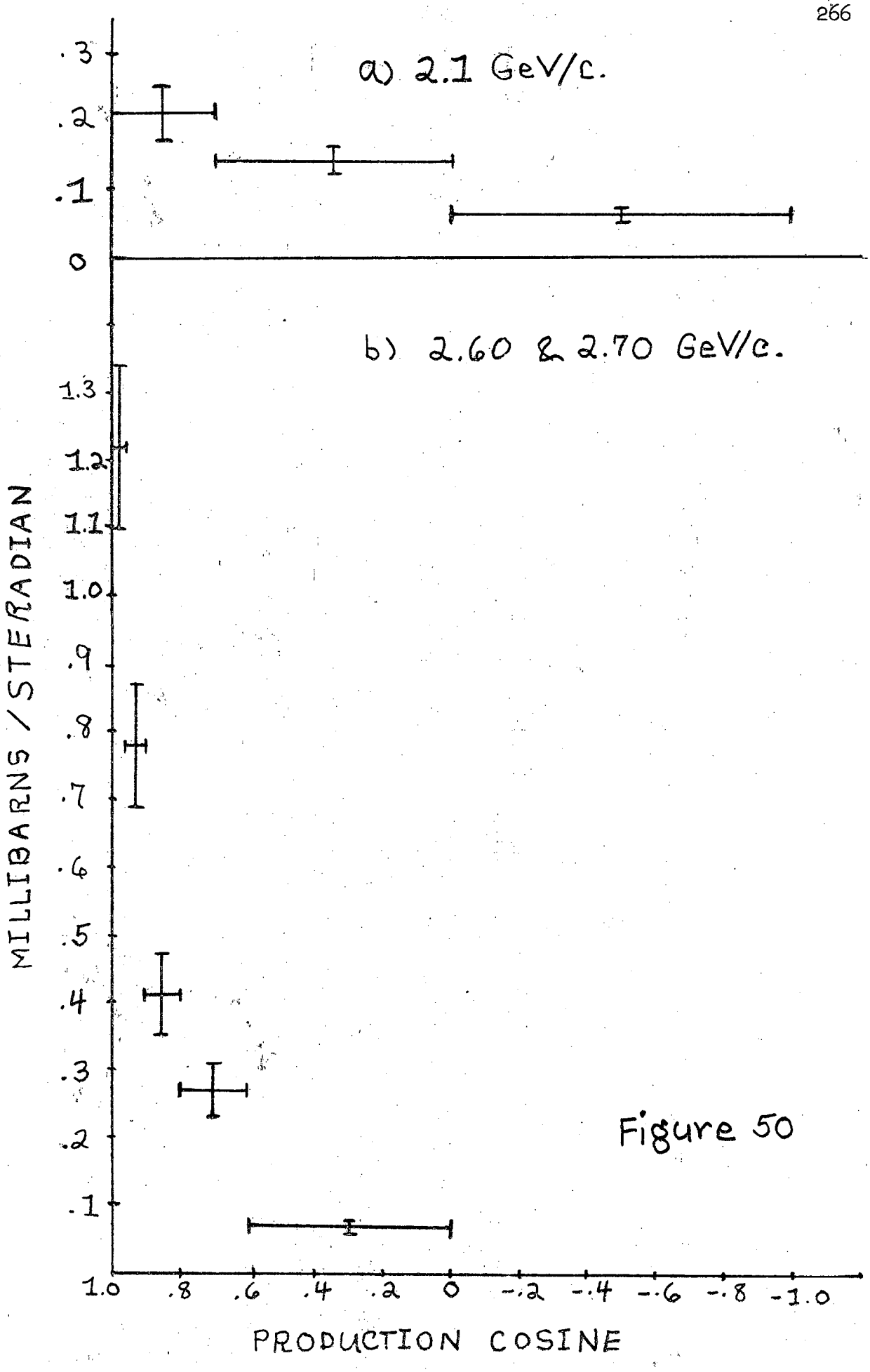
a) 2.1 GeV/c.
b) 2.60 & 2.70 GeV/c.
MILLIBARNS / STERADIAN
PRODUCTION COSINE
.3
.2
.1
0
1.3
1.2
1.1
1.0
.9
.8
.7
.6
.5
.4
.3
.2
.1
1.0
.8
.6
.4
.2
0
-.2
-.4
-.6
-.8
-1.0

Figure 50

Figure 51.

Decay angular distribution parameters for the reaction $K^- p \rightarrow K^*_{\frac{1}{2}}(892)\, N^*_{3/2}(1238)$ for 2.1 GeV/c as a function of production cosine.

a) C_1

b) C_4

c) C_7

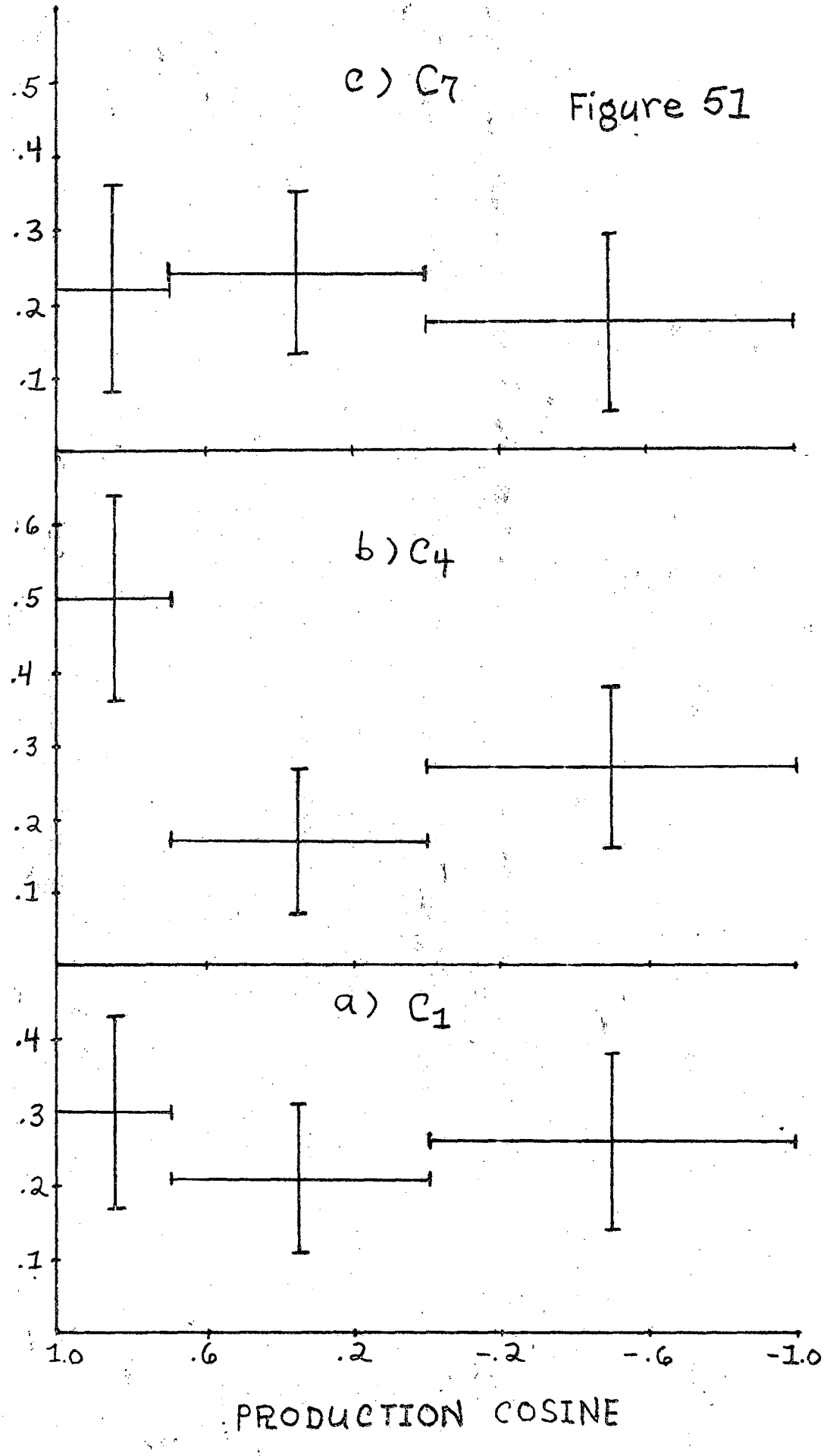

Figure 51

Figure 52

Decay angular distribution parameters for the reaction $K^- p \rightarrow \bar{K}^*_{\frac{1}{2}}(892)\, N^*_{3/2}(1238)$ for 2.60 and 2.70 GeV/c combined as a function of production cosine.

a) C_1

b) C_4

c) C_7

d) C_{19}

e) C_{11}

f) C_2

g) C_5

h) C_3

i) C_6

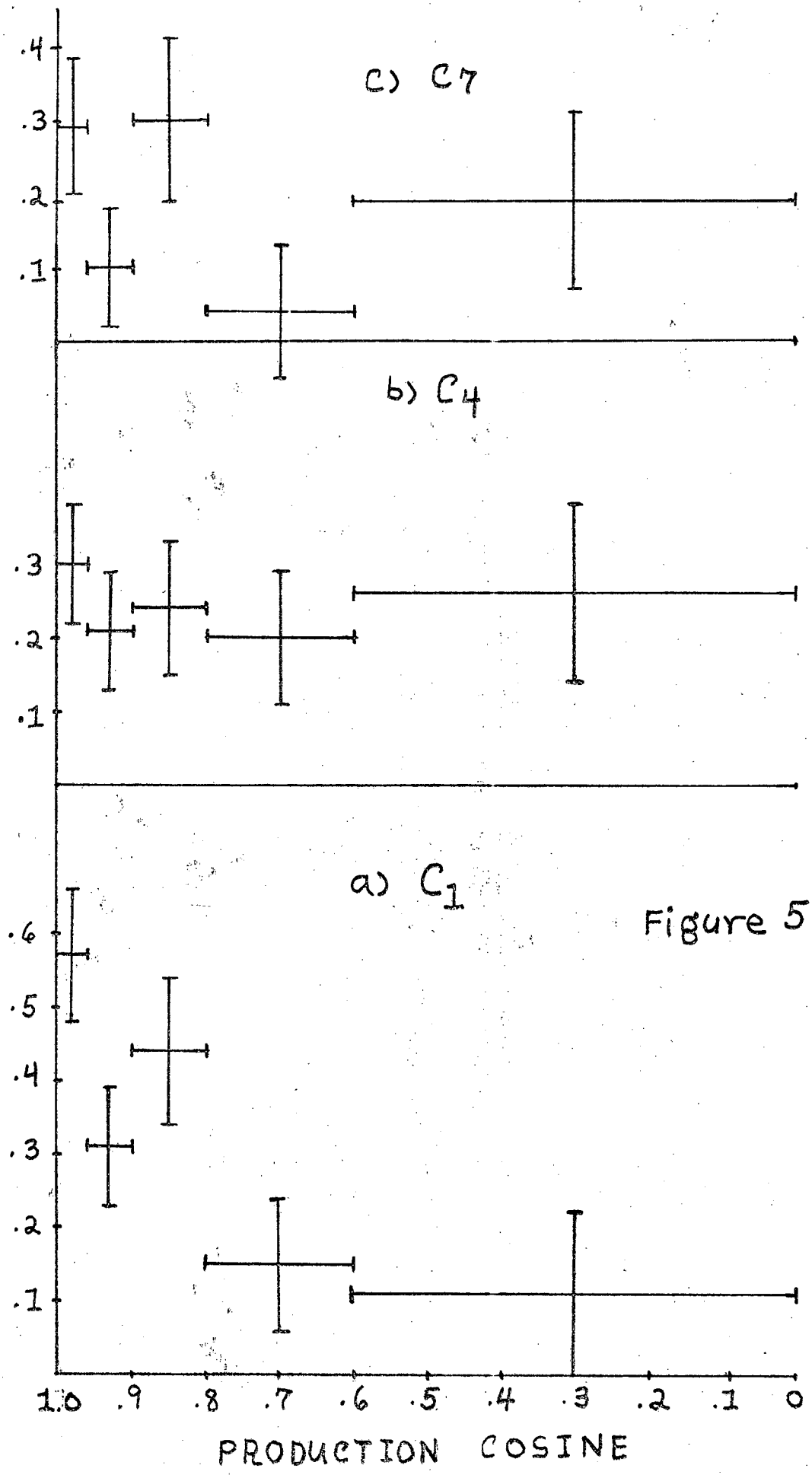
c) C_7
.4
.3
.2
.1
b) C_4
.3
.2
.1
a) C_1
.6
.5
.4
.3
.2
.1
1.0
.9
.8
.7
.6
.5
.4
.3
.2
.1
0
PRODUCTION COSINE

Figure 52

Figure 52

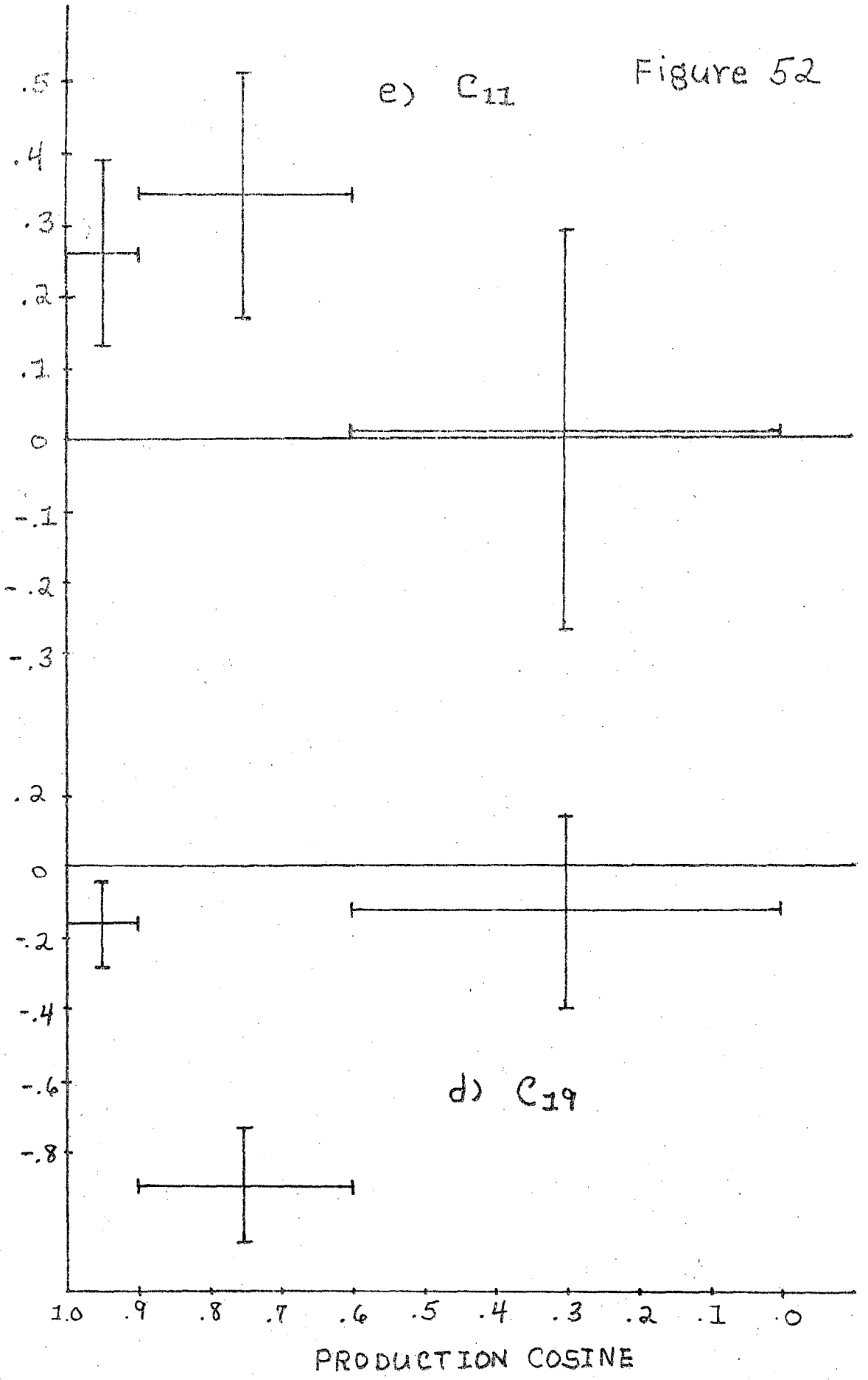
e) C_{11}
.5
.4
.3
.2
.1
0
-.1
-.2
-.3
.2
0
-.2
-.4
-.6
-.8
d) C_{19}
1.0
.9
.8
.7
.6
.5
.4
.3
.2
.1
.0
PRODUCTION COSINE

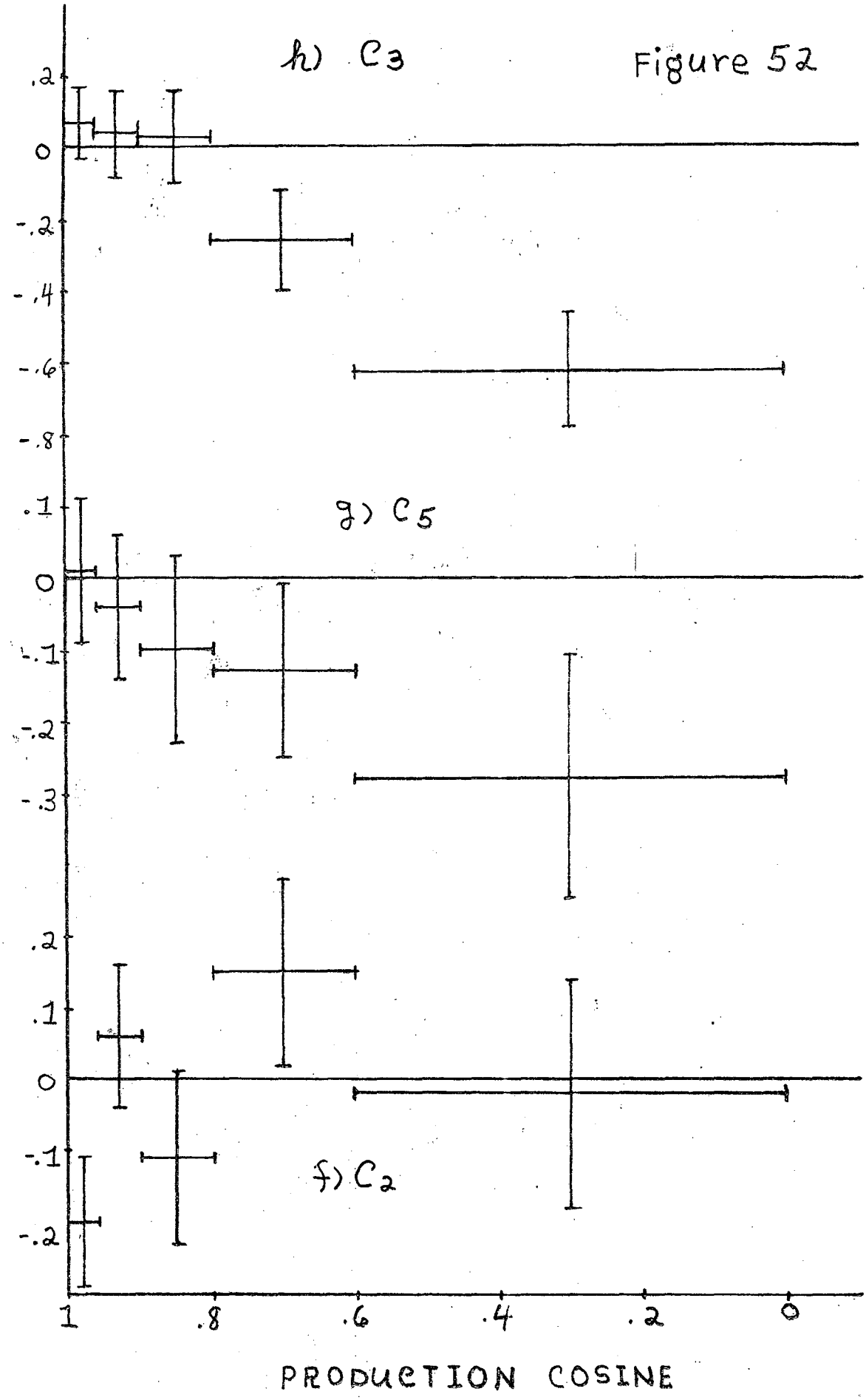
h) C3
Figure 52
.2
0
-.2
-.4
-.6
-.8
g) C5
.1
0
-.1
-.2
-.3
.2
.1
0
-.1
-.2
f) C2
1
.8
.6
.4
.2
0
PRODUCTION COSINE

Figure 52

i) C_6

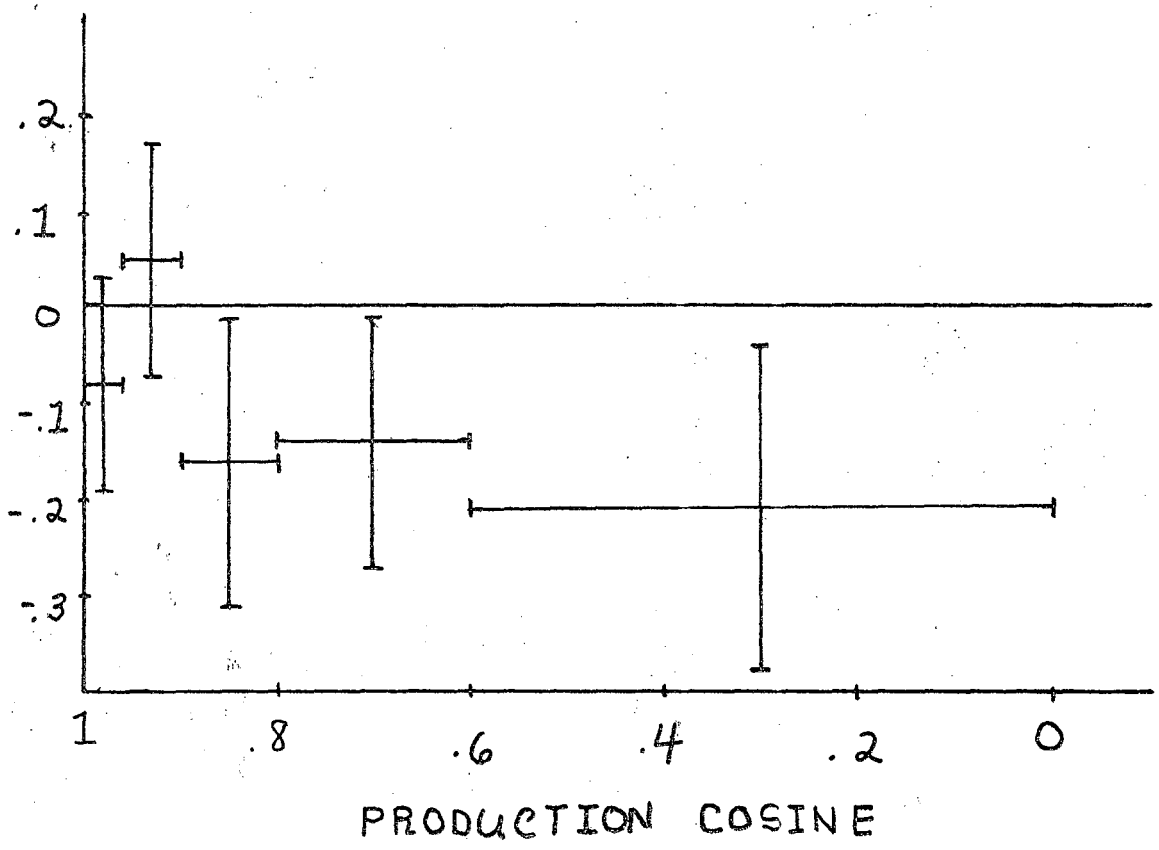

Figure 53

Comparisons of the maximum likelihood solutions for the $\bar{K}^*_{\frac{1}{2}}$ (892) $N^*_{3/2}$ (1238) joint decay angular distributions with projections of the data for various production cosine (μ) intervals at 2.1 GeV/c.

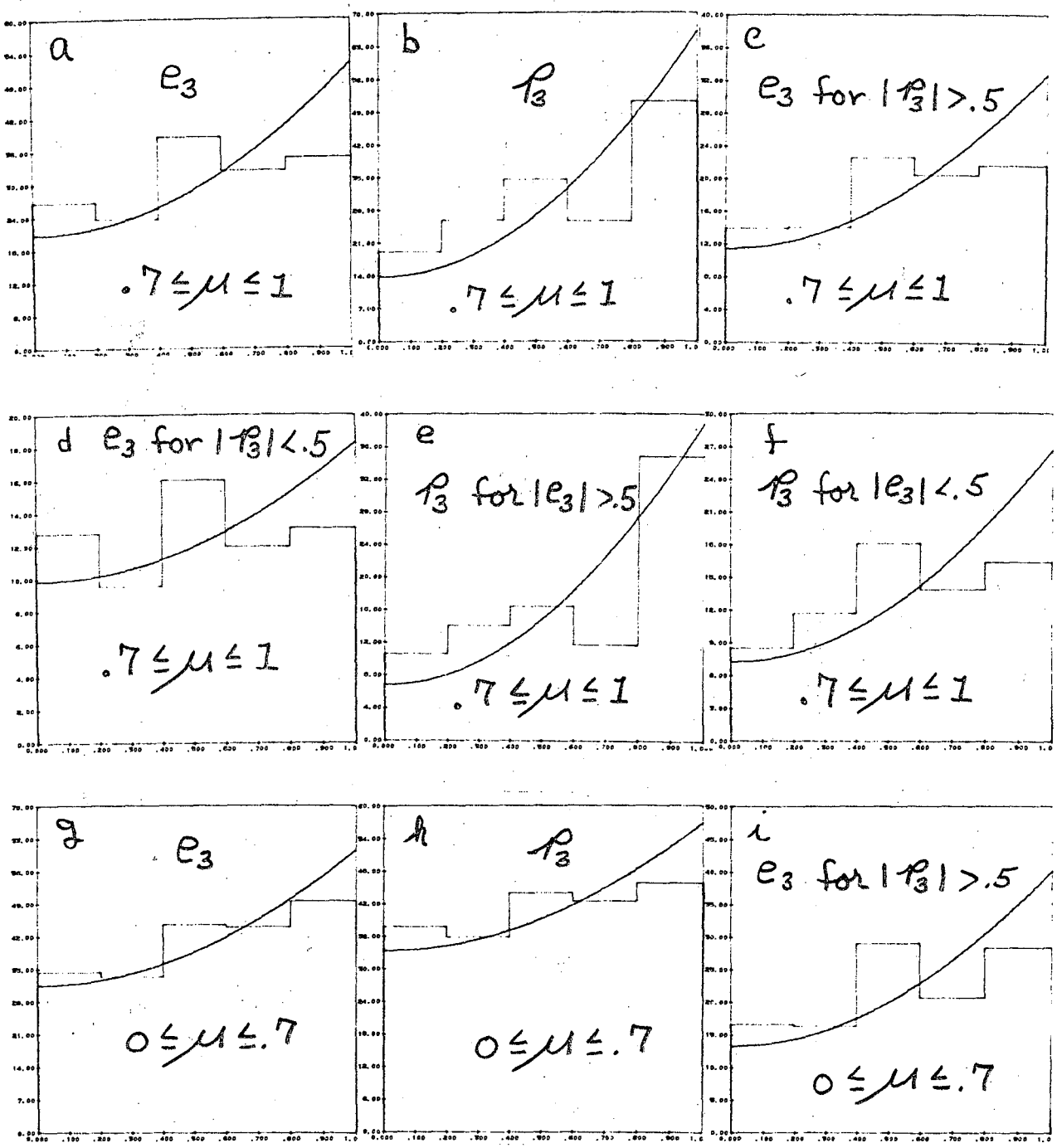
a
e_3
$.7 \leq \mu \leq 1$
b
ρ_3
$.7 \leq \mu \leq 1$
c
e_3 for $|\rho_3| > .5$
$.7 \leq \mu \leq 1$
d e_3 for $|\rho_3| < .5$
$.7 \leq \mu \leq 1$
e
ρ_3 for $|e_3| > .5$
$.7 \leq \mu \leq 1$
f
ρ_3 for $|e_3| < .5$
$.7 \leq \mu \leq 1$
g
e_3
$0 \leq \mu \leq .7$
h
ρ_3
$0 \leq \mu \leq .7$
i
e_3 for $|\rho_3| > .5$
$0 \leq \mu \leq .7$

Figure 53

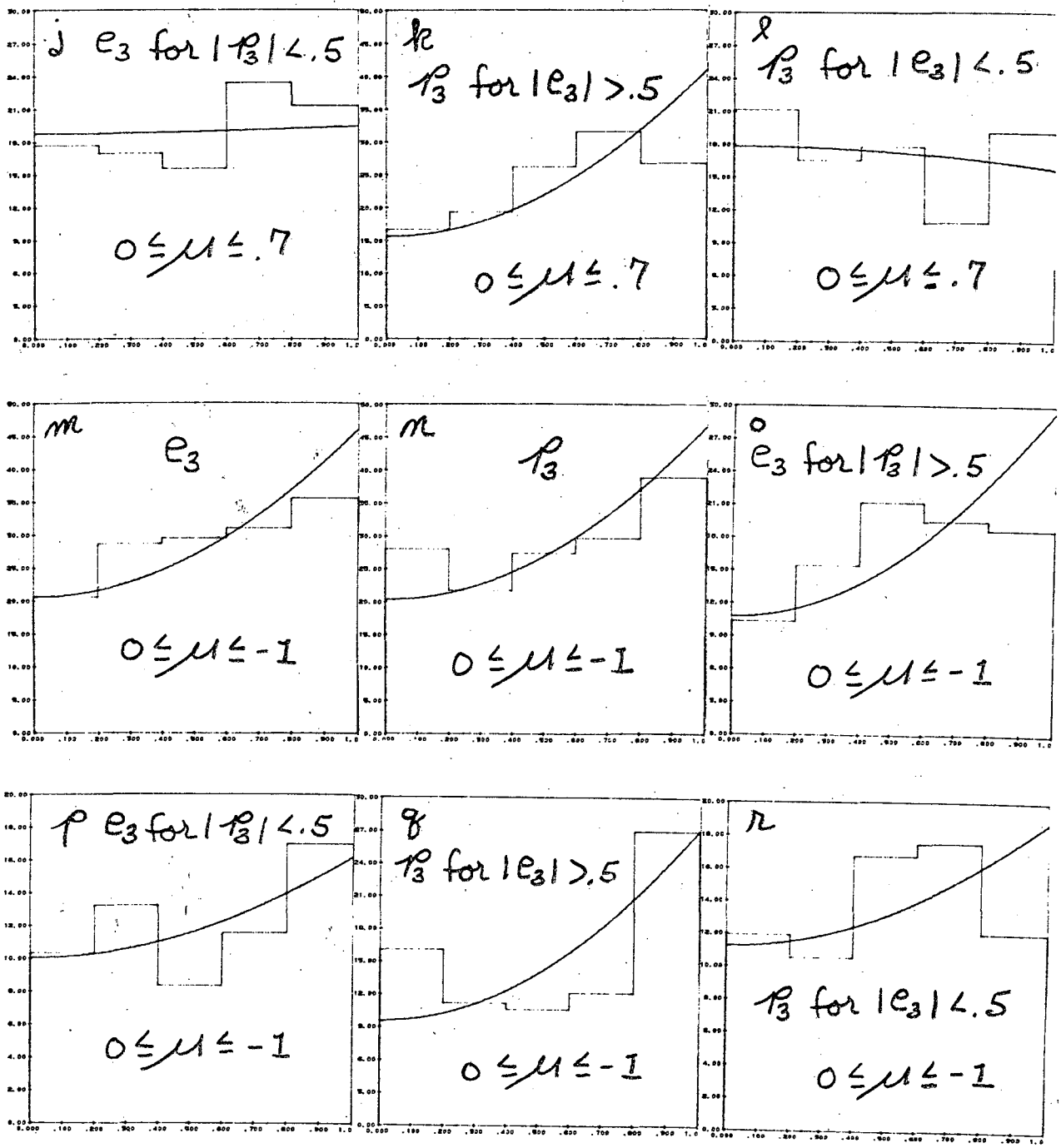
j e_3 for $|\rho_3| < .5$
$0 \leq \mu \leq .7$
k
ρ_3 for $|e_3| > .5$
$0 \leq \mu \leq .7$
l
ρ_3 for $|e_3| < .5$
$0 \leq \mu \leq .7$
m
e_3
$0 \leq \mu \leq -1$
n
ρ_3
$0 \leq \mu \leq -1$
o
e_3 for $|\rho_3| > .5$
$0 \leq \mu \leq -1$
p e_3 for $|\rho_3| < .5$
$0 \leq \mu \leq -1$
q
ρ_3 for $|e_3| > .5$
$0 \leq \mu \leq -1$
r
ρ_3 for $|e_3| < .5$
$0 \leq \mu \leq -1$

Figure 53

Figure 54

Comparisons of the maximum likelihood solutions for the $\bar{K}^*_{\frac{1}{2}}(892)$ $N^*_{3/2}(1238)$ joint azimuthal decay angular distributions with projections of the data for various production cosine (μ) intervals.

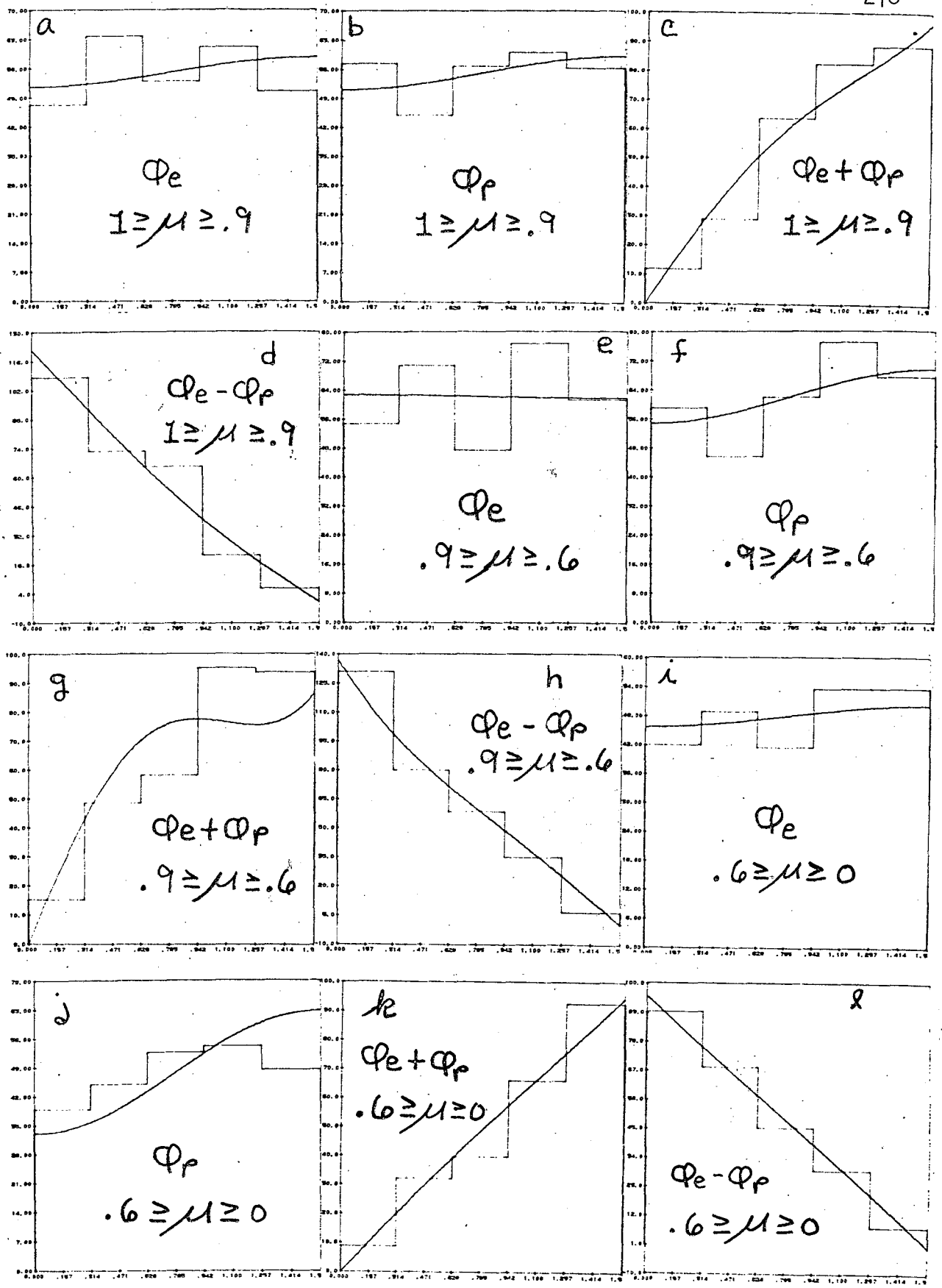
a
Φ_e
$1 \geq \mu \geq .9$
b
Φ_p
$1 \geq \mu \geq .9$
c
$\Phi_e + \Phi_p$
$1 \geq \mu \geq .9$
d
$\Phi_e - \Phi_p$
$1 \geq \mu \geq .9$
e
Φ_e
$.9 \geq \mu \geq .6$
f
Φ_p
$.9 \geq \mu \geq .6$
g
$\Phi_e + \Phi_p$
$.9 \geq \mu \geq .6$
h
$\Phi_e - \Phi_p$
$.9 \geq \mu \geq .6$
i
Φ_e
$.6 \geq \mu \geq 0$
j
Φ_p
$.6 \geq \mu \geq 0$
k
$\Phi_e + \Phi_p$
$.6 \geq \mu \geq 0$
l
$\Phi_e - \Phi_p$
$.6 \geq \mu \geq 0$

Figure 54

Figure 55

Comparisons of the maximum likelihood solutions for the $K^*_{\frac{1}{2}}$ (892) $N^*_{3/2}$ (1238) joint decay angular distributions with projections of the data at 2.60 and .70 GeV/c. for $K^{*-}_{\frac{1}{2}}$ (892) production cosine $1 \leq \mu \leq .96$.

a) e_3

b) p_3

c) φ_e

d) φ_p

e) $(e_1 + e_3)/\sqrt{2}$

f) $(e_1 - e_3)/\sqrt{2}$

g) $(p_1 + p_3)/\sqrt{2}$

h) $(p_1 - p_3)/\sqrt{2}$

i) e_3 for $|p_3| > .5$

j) e_3 for $|p_3| < .5$

k) p_3 for $|e_3| > .5$

l) p_3 for $|e_3| < .5$

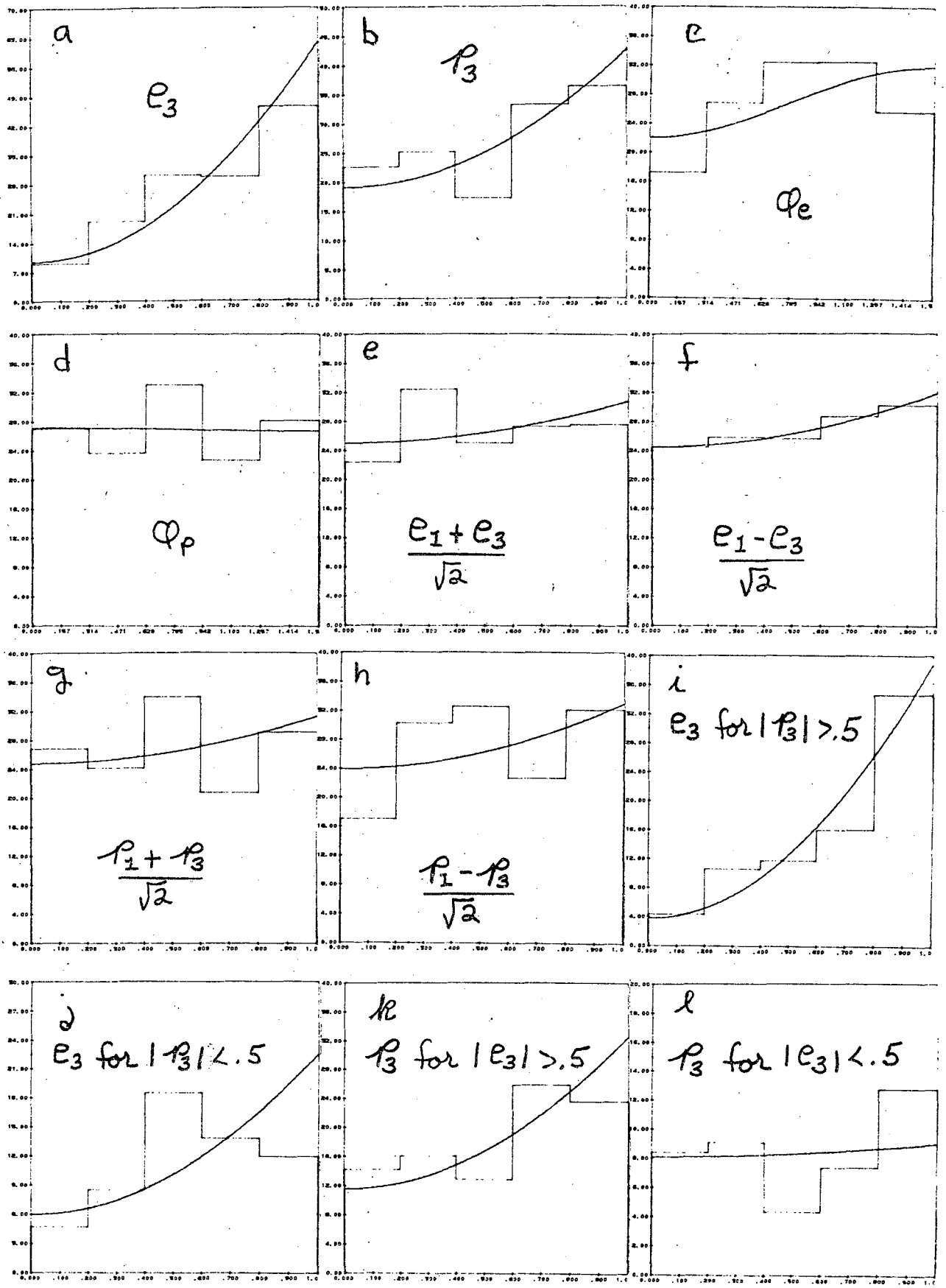

$.96 \leq \mu \leq 1$

Figure 55

Figure 56

Comparisons of the maximum likelihood solutions for the $\bar{K}^*_{\frac{1}{2}}$ (892) $N^*_{3/2}$ (1238) joint decay angular distributions with projections of the data at 2.60 and 2.70 GeV/c for $\bar{K}^*_{\frac{1}{2}}$ (892) production cosine . 96 $\leq \mu \leq$. 9.

a) e_3

b) p_3

c) φ_e

d) φ_e

e) $(e_1 + e_3)/\sqrt{2}$

f) $(e_1 - e_3)/\sqrt{2}$

g) $(p_1 + p_3)/\sqrt{2}$

h) $(p_1 - p_3)/\sqrt{2}$

i) e_3 for $|p_3| > .5$

j) e_3 for $|p_3| < .5$

k) p_3 for $|e_3| > .5$

l) p_3 for $|e_3| < .5$

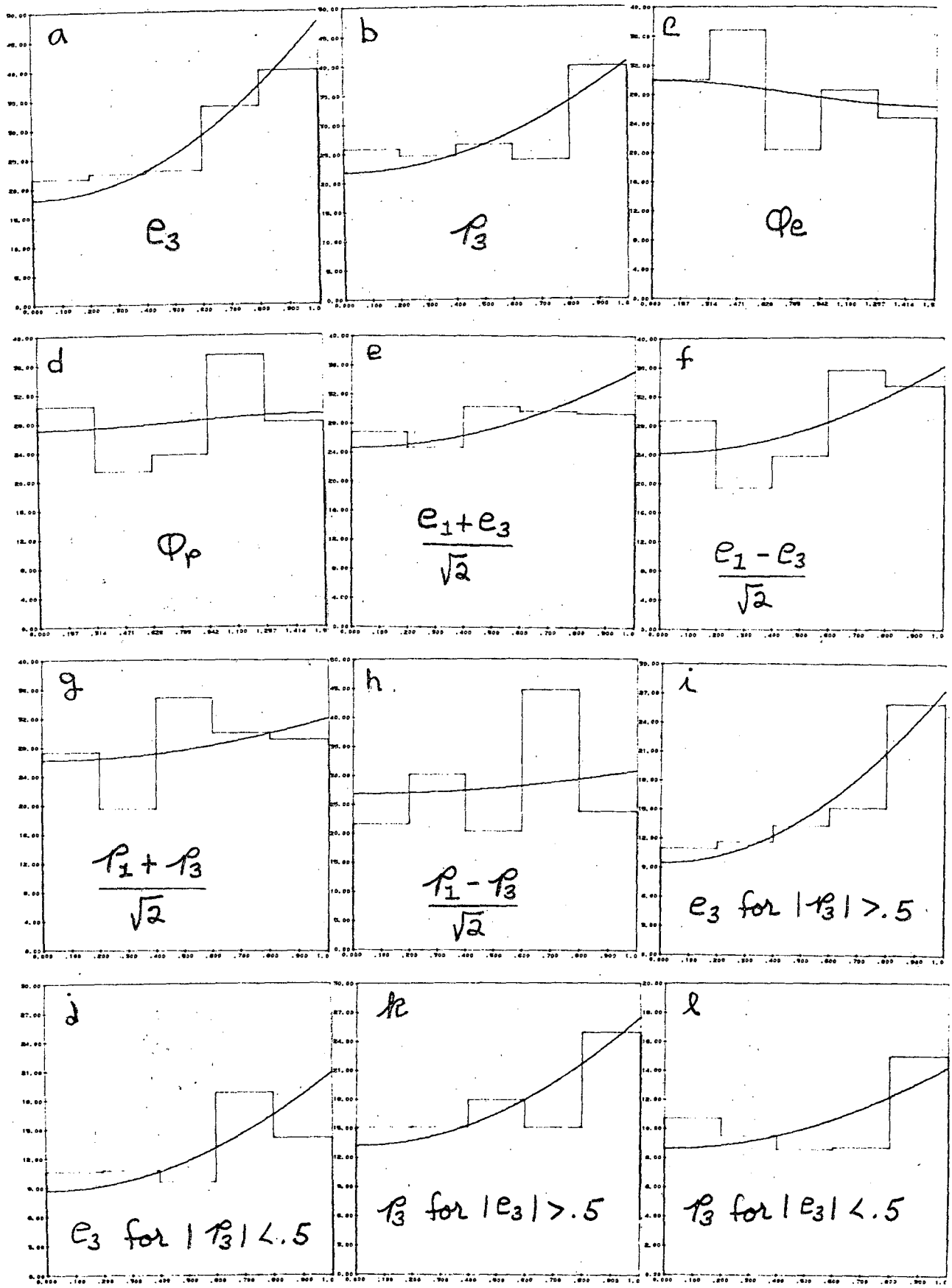

$.9 \leq \mu \leq .96$

Figure 56

Figure 57

Comparisons of the maximum likelihood solutions for the $\bar{K}^*_{\frac{1}{2}}$ (892) $N^*_{3/2}$ (1238) joint decay angular distributions with projections of the data at 2.60 and 2.70 GeV/c for $\bar{K}^*_{\frac{1}{2}}$ (892) production cosine . $9 \leq \mu \leq .8$.

a) e_3

b) p_3

c) φ_e

d) φ_p

e) $(e_1 + e_3)/\sqrt{2}$

f) $(e_1 - e_3)/\sqrt{2}$

g) $(p_1 + p_3)/\sqrt{2}$

h) $(p_1 - p_3)/\sqrt{2}$

i) e_3 for $|p_{31}| > .5$

j) e_3 for $|p_{31}| < .5$

k) p_3 for $|e_{31}| > .5$

l) p_3 for $|e_{31}| < .5$

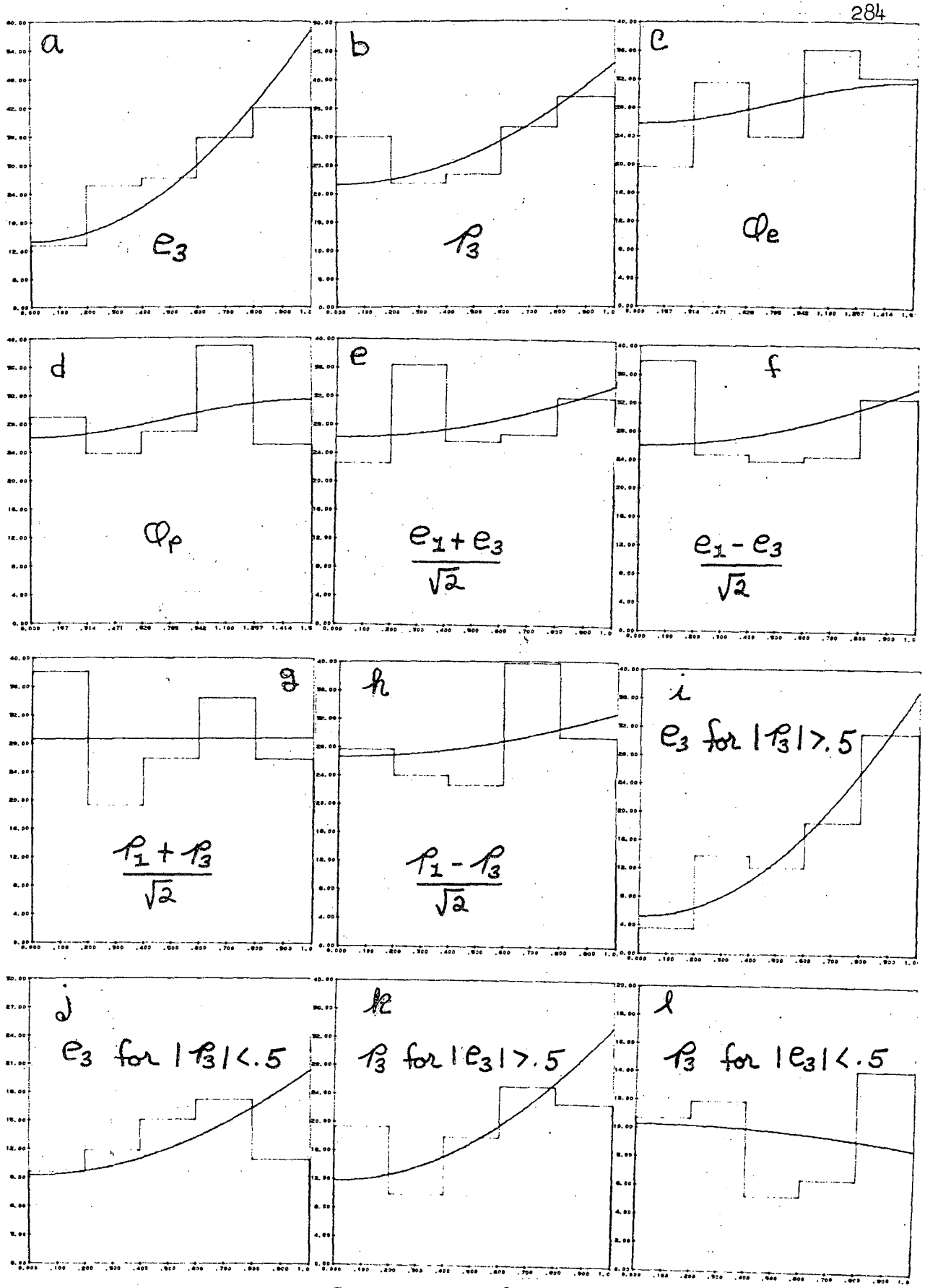

$.8 \leq \mu \leq .9$

Figure 57

Figure 58

Comparisons of the maximum likelihood solutions for the $\bar{K}^*_{\frac{1}{2}}$ (892) $N^*_{3/2}$ (1238) joint decay angular distributions with projections of the data at 2.60 and 2.70 GeV/c for $\bar{K}^*_{\frac{1}{2}}$ (892) production cosine . 8 $\leq \mu \leq$. 6.

a) e_3

b) ρ_3

c) φ_e

d) φ_p

e) $(e_1 + e_3)/\sqrt{2}$

f) $(e_1 - e_3)/\sqrt{2}$

g) $(\rho_1 + \rho_3)/\sqrt{2}$

h) $(\rho_1 - \rho_3)/\sqrt{2}$

i) e_3 for $|\rho_{31}| > .5$

j) e_3 for $|\rho_{31}| < .5$

k) ρ_3 for $|e_{31}| > .5$

l) ρ_3 for $|e_{31}| < .5$

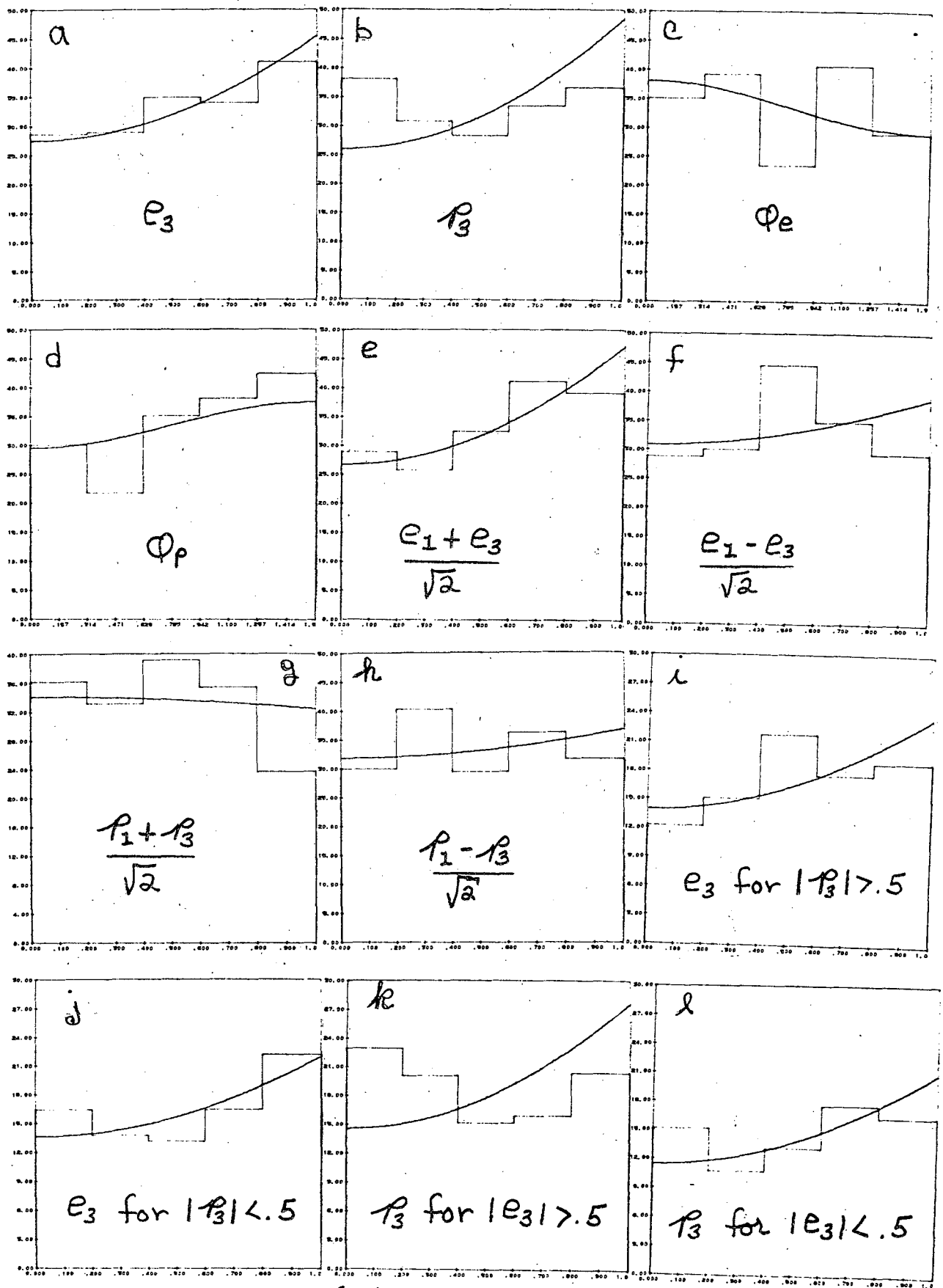

$.6 \leq \mu \leq .8$

Figure 58

Figure 59

Comparisons of the maximum likelihhod solutions for the $\bar{K}^*_{\frac{1}{2}}$ (892) $N^*_{3/2}$ (1238) joint decay angular distributions with projections of the data at 2.60 and 2.70 GeV/c for $\bar{K}^*_{\frac{1}{2}}$ (892) production cosine $.6 \leq \mu \leq 0$.

a) e_3

b) p_3

c) φ_e

d) φ_p

e) $(e_1 + e_3)/\sqrt{2}$

f) $(e_1 - e_3)/\sqrt{2}$

g) $(p_1 + p_3)/\sqrt{2}$

h) $(p_1 - p_3)/\sqrt{2}$

i) e_3 for $|p_3| > .5$

j) e_3 for $|p_3| < .5$

k) p_3 for $|e_3| > .5$

l) p_3 for $|e_3| < .5$

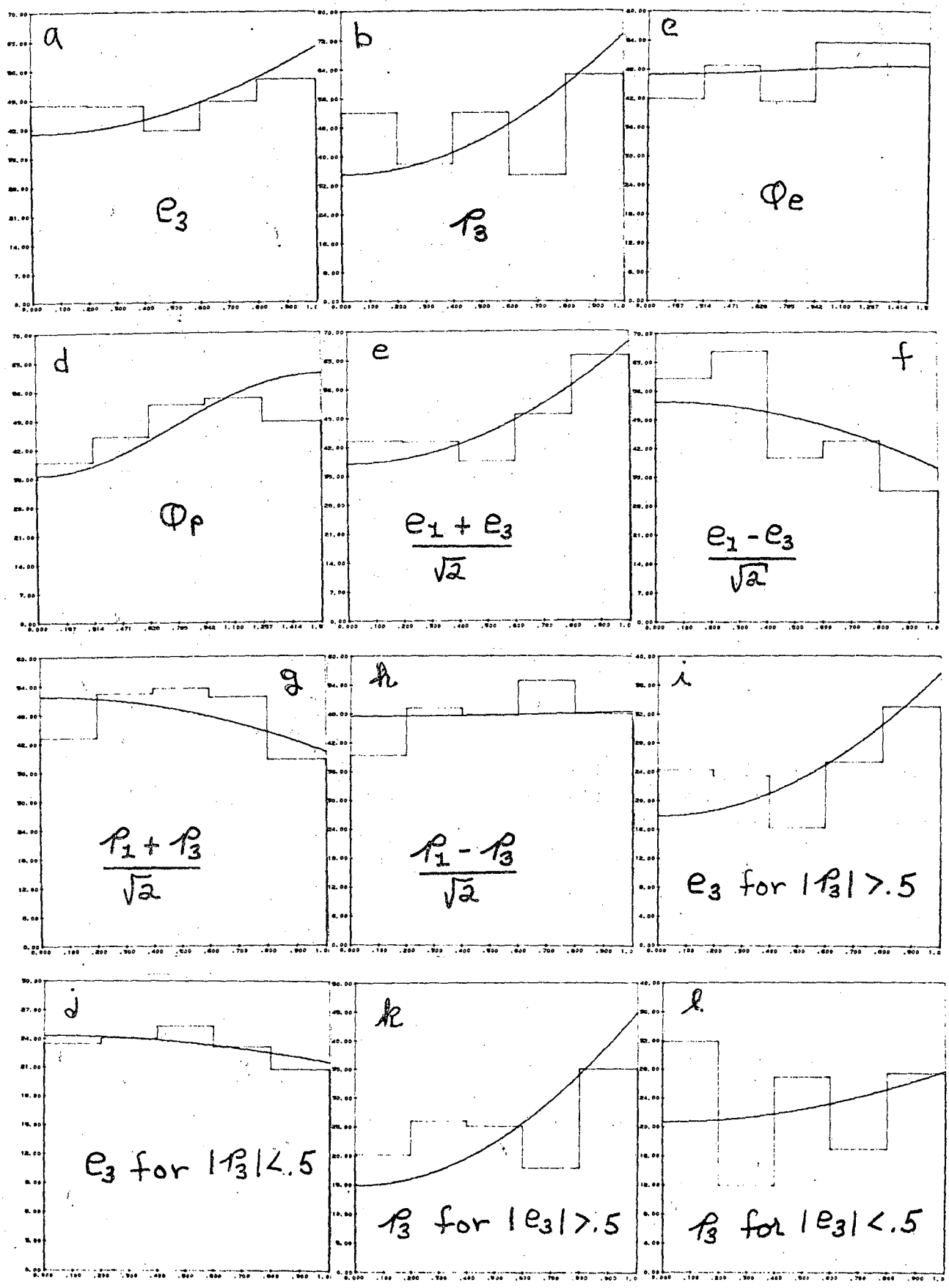

$0 \leq \mu \leq .6$

Figure 59

Figure 60

Contour map of χ^2 in the (x, y) plane for the fit of Jackson and Donohue[45], [46] to the differential cross section of the reaction $\bar{K}p \rightarrow K^{*-}_{\frac{1}{2}}(892)\,p$ at 2.64 GeV/c., using the absorptive peripheral model with pseudoscalar and vector exchange, (See text for definition of x and y).

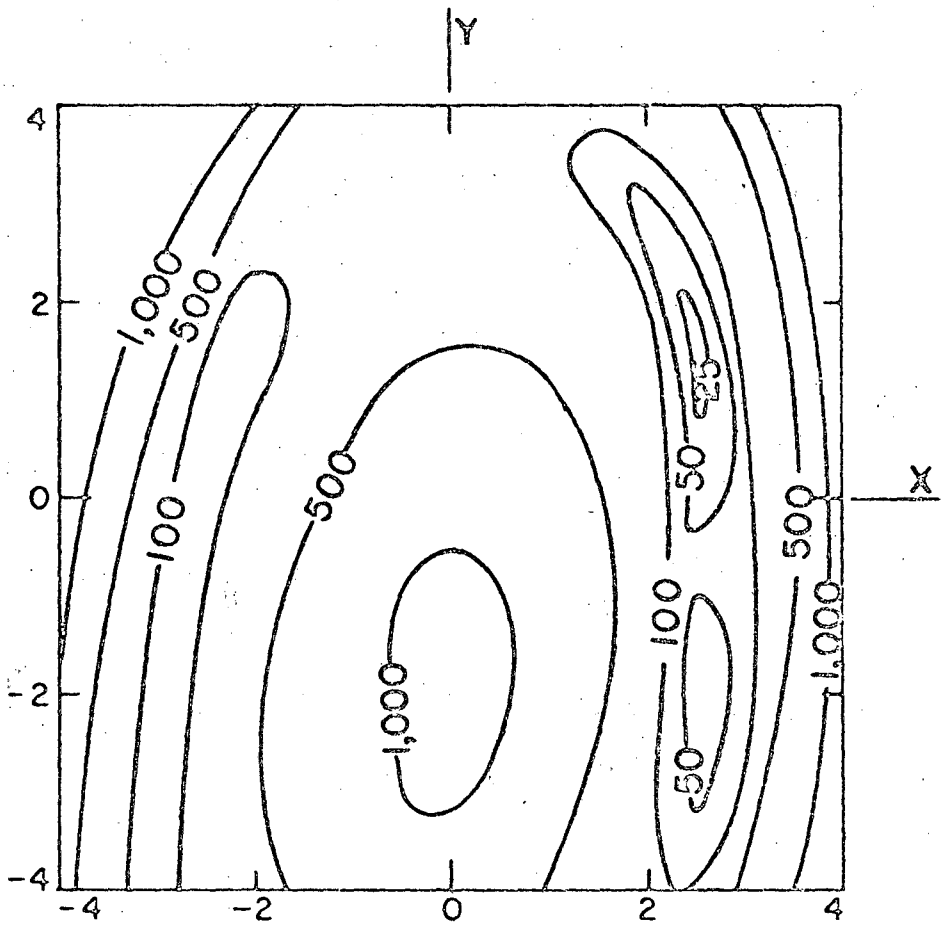

Figure 60

Figure 61

Comparison of the predictions of the absorptive peripheral model of Jackson and Donohue [45], [46] to the measurements of this experiment, for the differential cross section and $K^{*-}_{\frac{1}{2}}(892)$ spin density matrix elements in the reaction $K^- p \to K^{*-}_{\frac{1}{2}}(892)\, p$ at 2.1 and 2.64 GeV/c. The values used for the vector exchange coupling constants are (in the notation of Donohue[45]) (x, y) = (2.5, 1.1).

Figure 61

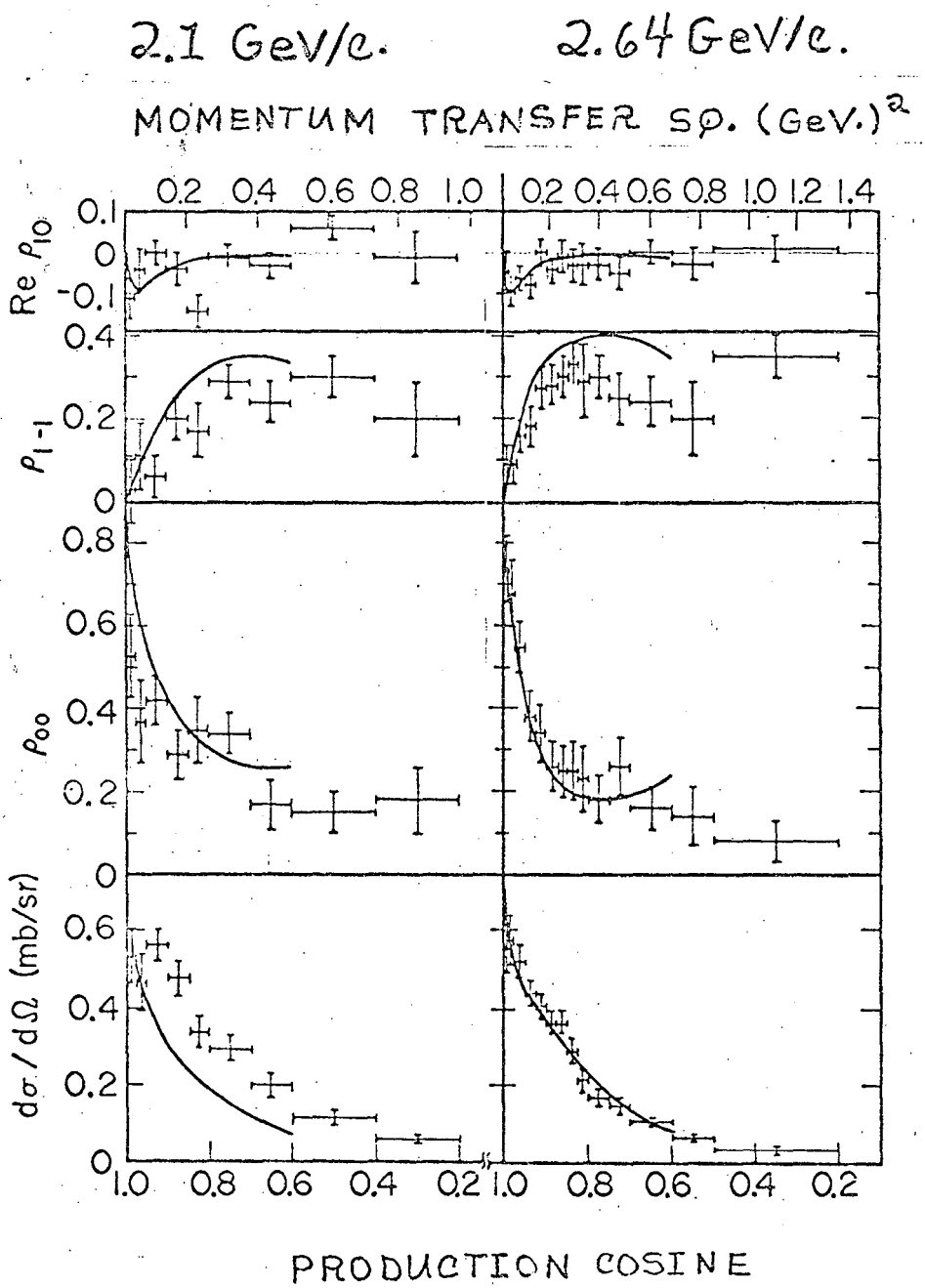
2.1 GeV/c.
2.64 GeV/c.
MOMENTUM TRANSFER SQ. (GeV.)²
0.2 0.4 0.6 0.8 1.0
0.2 0.4 0.6 0.8 1.0 1.2 1.4
Re ρ10
ρ1-1
ρ00
dσ/dΩ (mb/sr)
1.0 0.8 0.6 0.4 0.2
PRODUCTION COSINE

Figure 62

Comparison of the prediction of the absorptive peripheral model of Jackson and Donohue [61] to the measurements of this experiment for the differential cross section of the reaction $K^- p \rightarrow \bar{K}^*_{\frac{1}{2}}(892)\, N^*_{3/2}(1238)$ at 2.64 GeV/c.

Figure 62

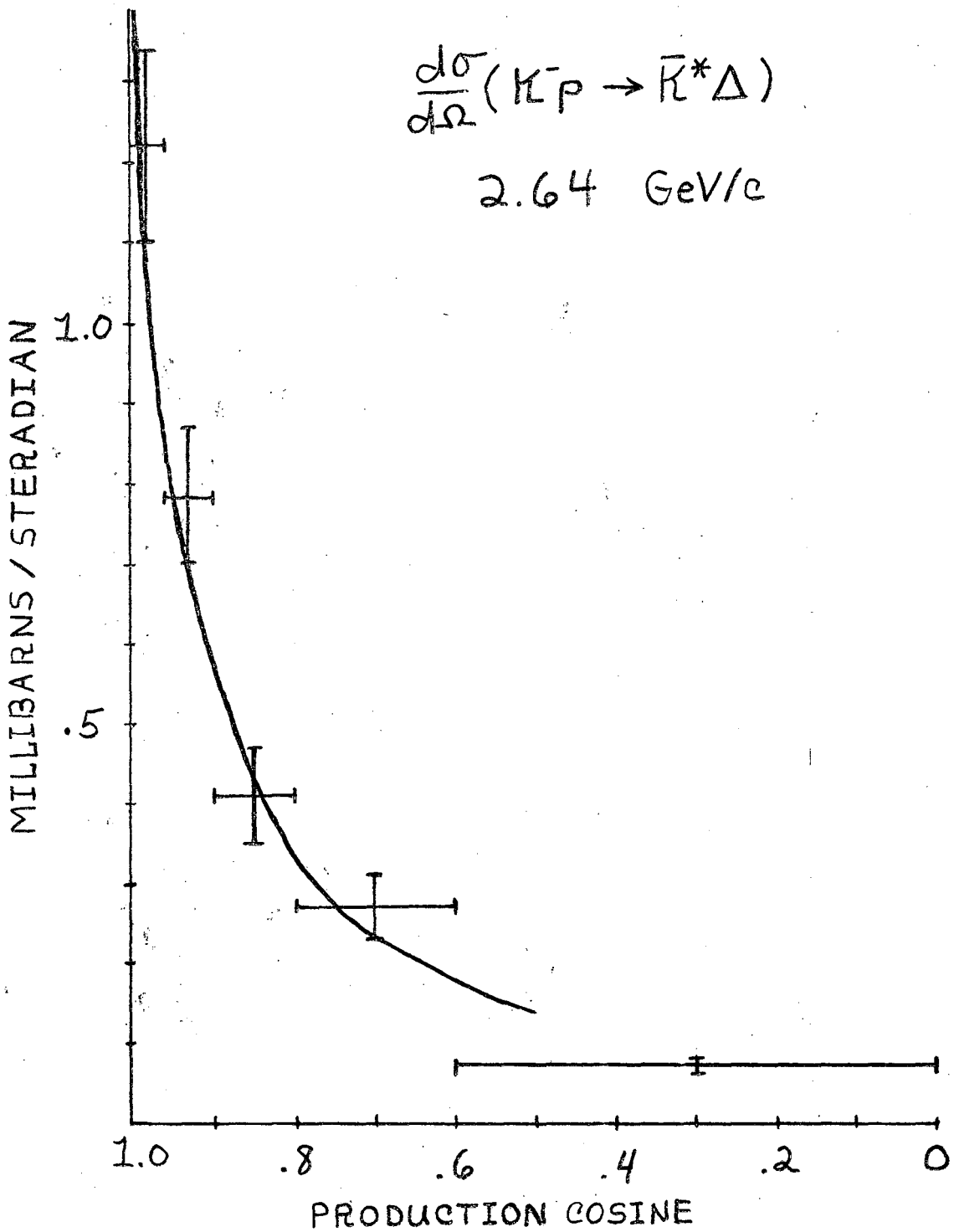
$\frac{d\sigma}{d\Omega}(K^- p \to \bar{K}^* \Delta)$
2.64 GeV/c
MILLIBARNS / STERADIAN
1.0
.5
1.0
.8
.6
.4
.2
0
PRODUCTION COSINE

Figure 63

Comparison of the predictions of the absorptive peripheral model of Jackson and Donohue[61] to the measurements of this experiment for the joint decay angular distribution coefficients in the reaction $K^- p \to \bar{K}^*_{\frac{1}{2}}(892)\, N^*_{3/2}(1238)$ at 2.64 GeV/c.

a) C_1

b) C_4

c) C_7

d) C_{19}

e) C_{11}

f) C_2

g) C_5

h) C_3

i) C_6

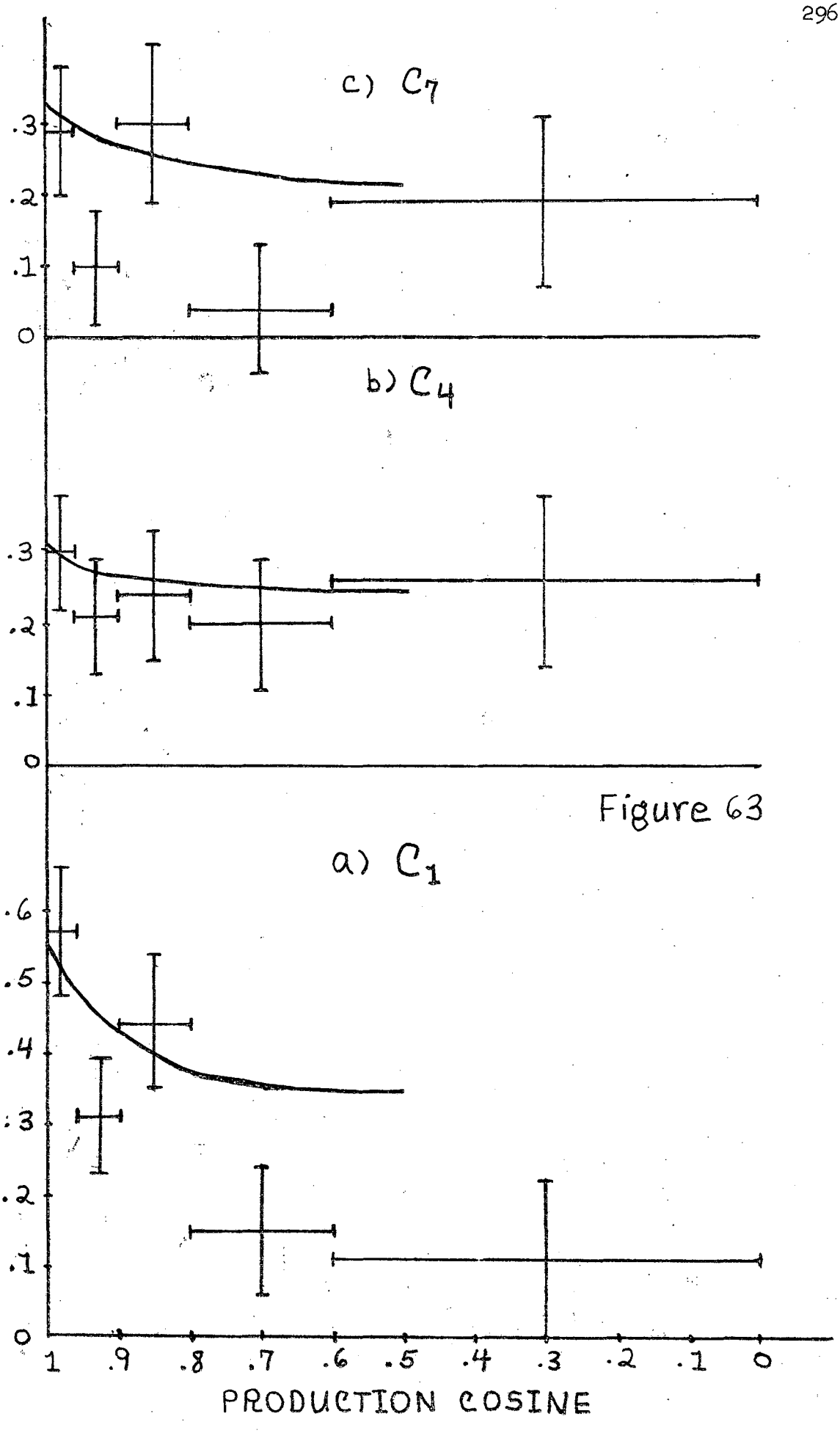
c) C_7
.3
.2
.1
0
b) C_4
.3
.2
.1
0
a) C_1
.6
.5
.4
.3
.2
.1
0
1
.9
.8
.7
.6
.5
.4
.3
.2
.1
0
PRODUCTION COSINE

Figure 63

Figure 63

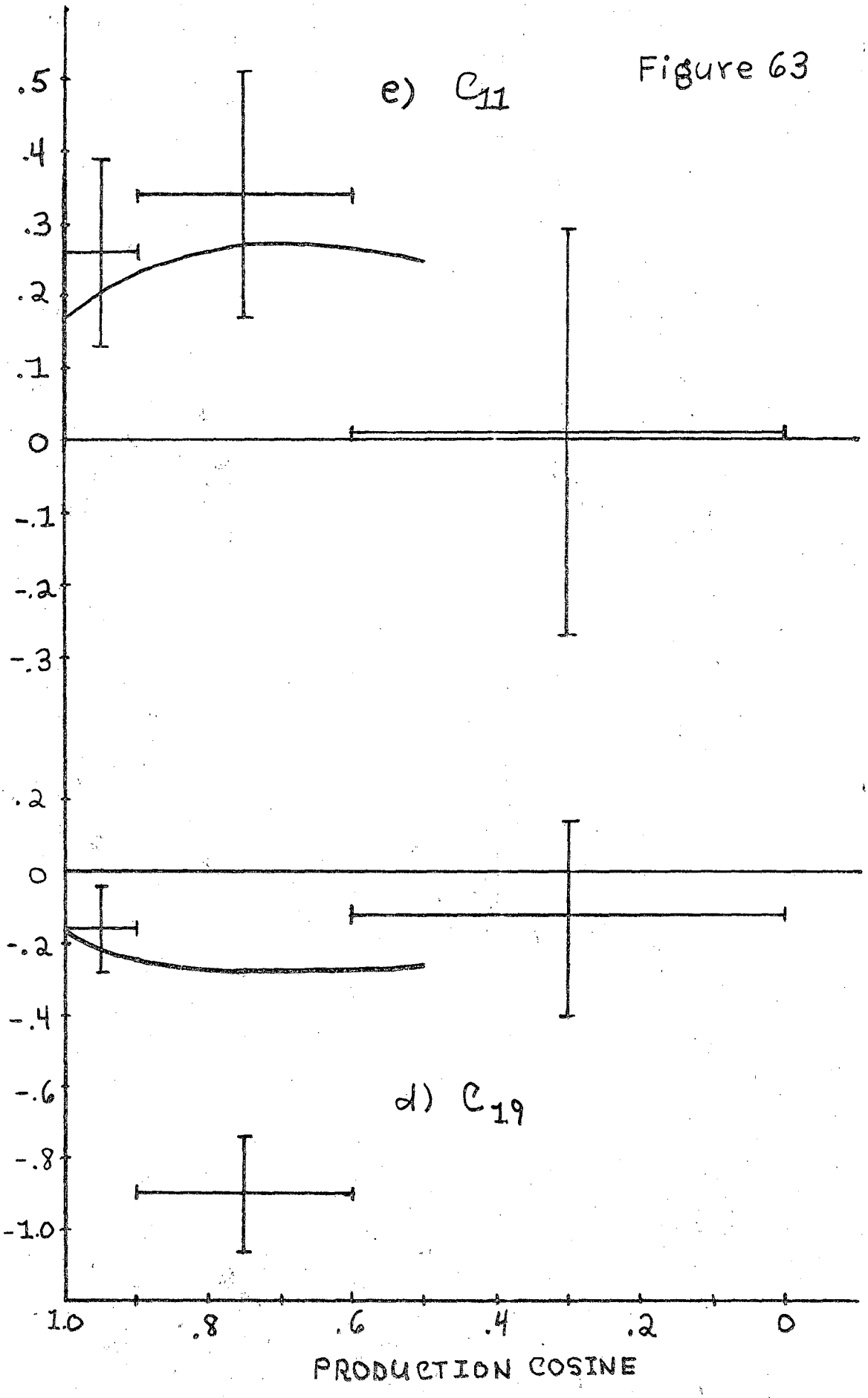

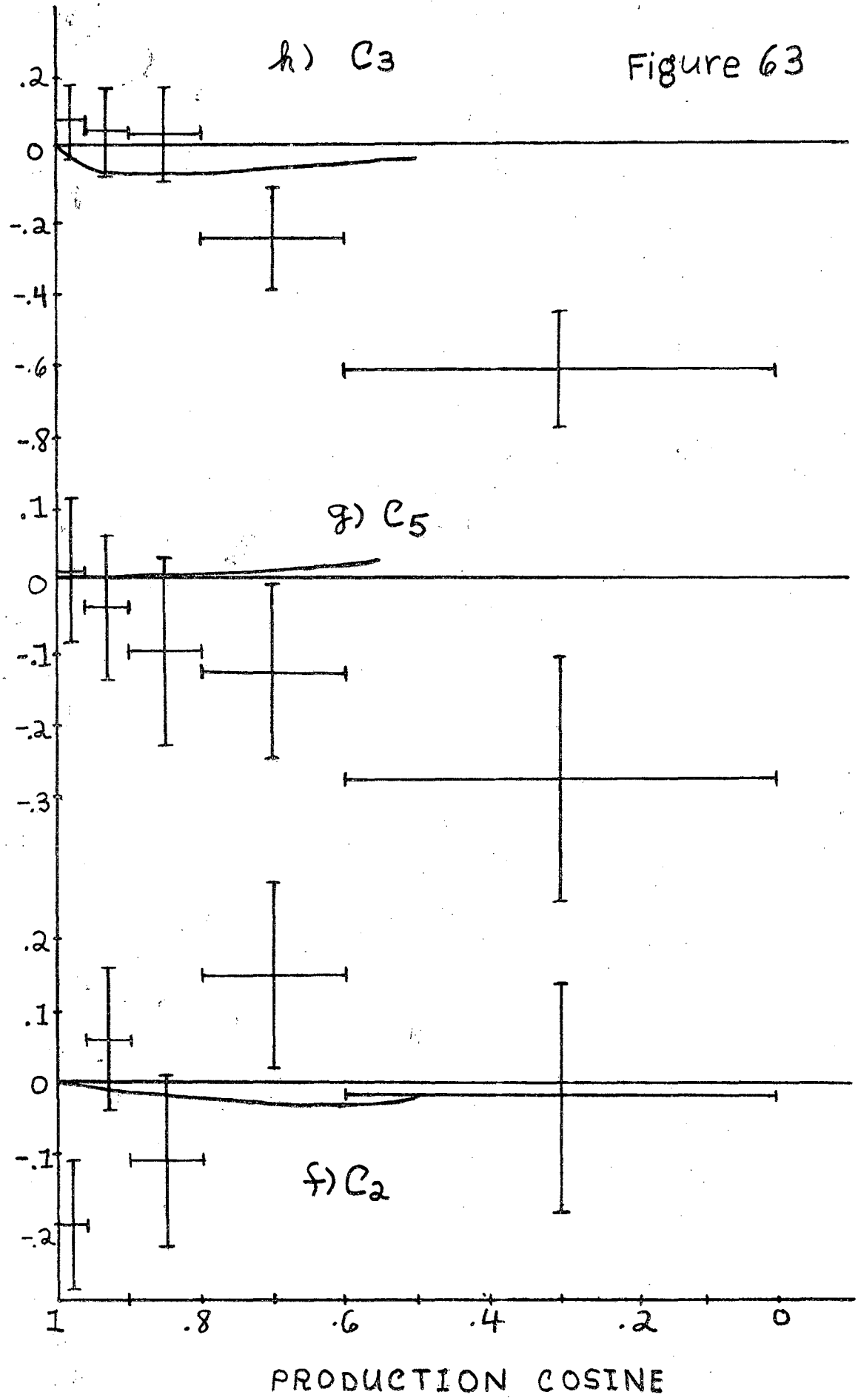

Figure 63

Figure 63

i) C_6

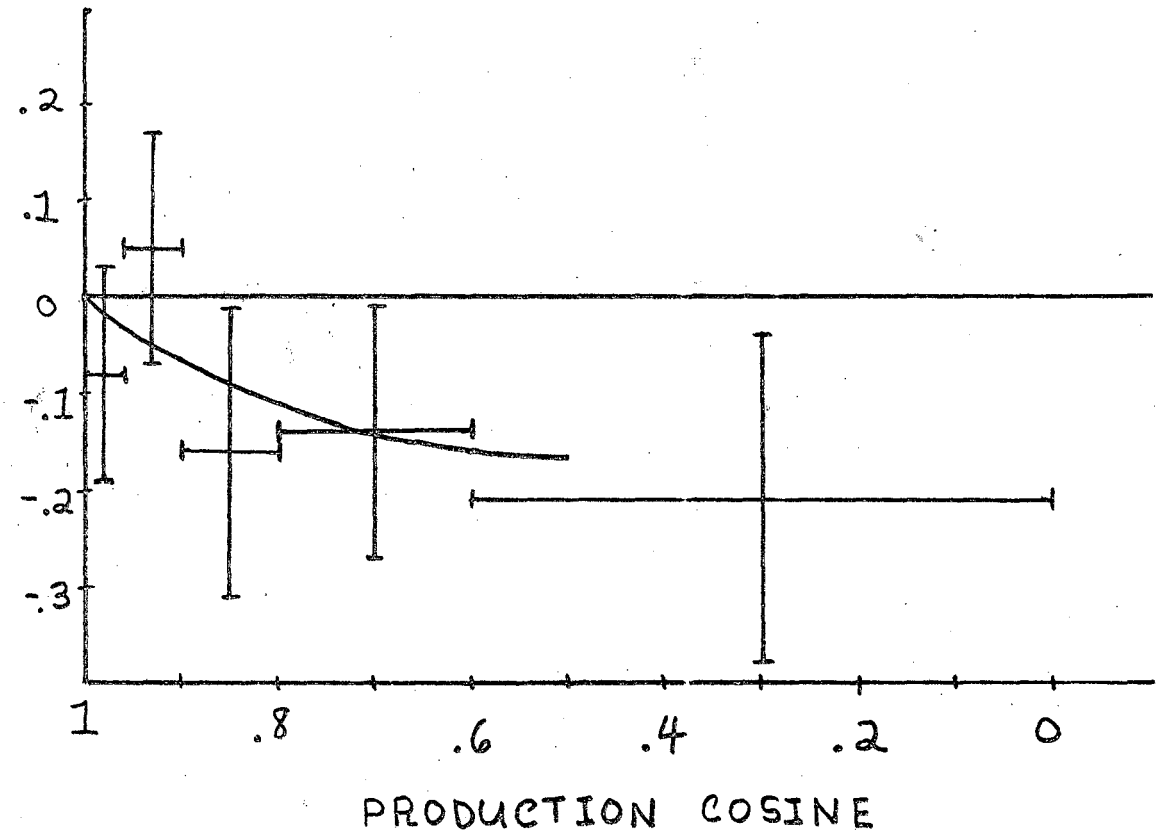

Figure 64

Comparison of the predictions of the Regge pole model of Kaydalov and Karnakov [47] to the measurements of this experiment for the $K^-_{\frac{1}{2}}(892)$ spin density matrix elements in the reaction $K^- p \to K^{*-}_{\frac{1}{2}}(892) p$ at 2.64 GeV/c.

a) $d\sigma/d\Omega$

b) ρ_{00}

c) $\mathrm{Re}\,\rho_{10}$

d) ρ_{1-1}

Figure 64

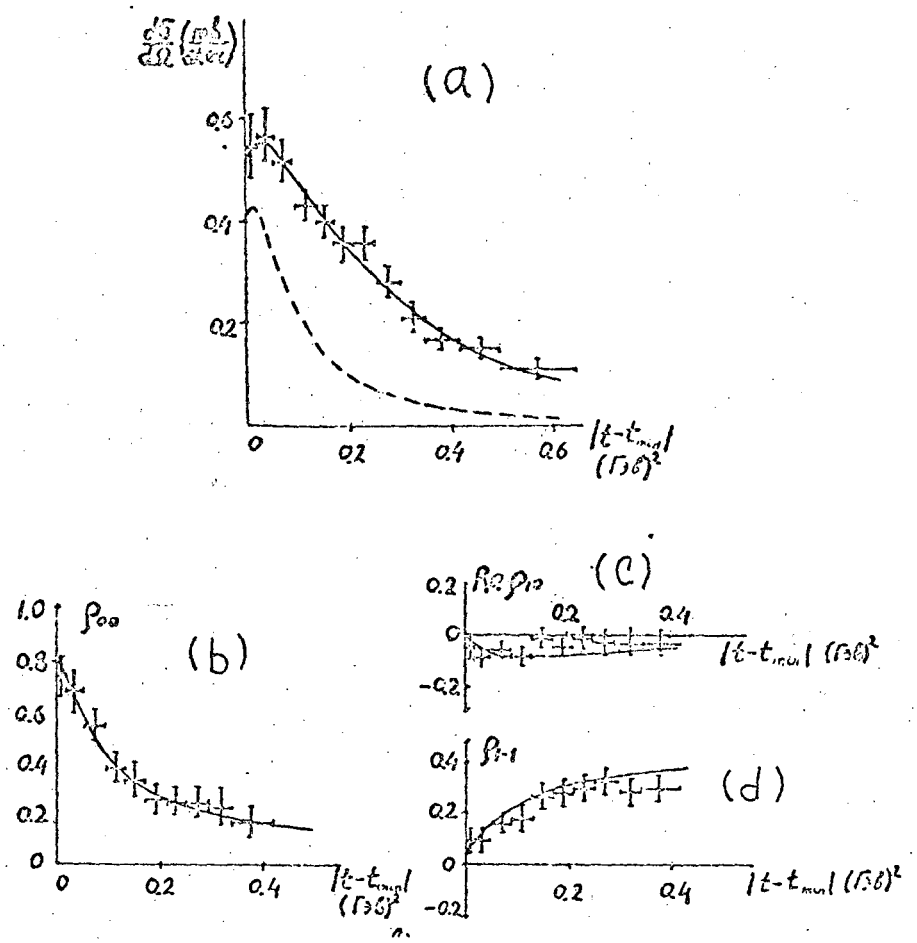
(a)
0.6
0.4
0.2
0
0.2
0.4
0.6
$|t-t_{min}|$ (GeV)^2
(b)
1.0
0.8
0.6
0.4
0.2
0
ρ_{00}
(c)
$Re\,\rho_{10}$
0.2
0
-0.2
(d)
ρ_{1-1}
MOMENTUM TRANSFER Sp. (GeV.)^2

Figure 65

Histograms of $\overline{K}^{o}\pi^{o}\pi^{-}$ invariant mass squared.

a) All momenta

b) All momenta, maximum likelihood solution superimposed assuming no $K\pi\pi$ resonance structure.

c) 2.60 and 2.70 GeV/c combined.

d) 2.60 and 2.70 GeV/c combined, maximum likelihood solution superimposed assuming no $K\pi\pi$ resonance structure.

e) All momenta, maximum likelihood solution assuming 1280 and 1400 MeV enhancements, superimposed.

f) 2.60 and 2.70 GeV/c, maximum likelihood solution assuming 1280 and 1400 MeV enhancements, superimposed.

Figure 65 (continued)

g) 2.1 GeV/c, maximum likelihood solution assuming no 1280 MeV enhancement, superimposed.

h) 2.1 GeV/c, maximum likelihood solution with 1280 MeV enhancement superimposed.

Figure 65

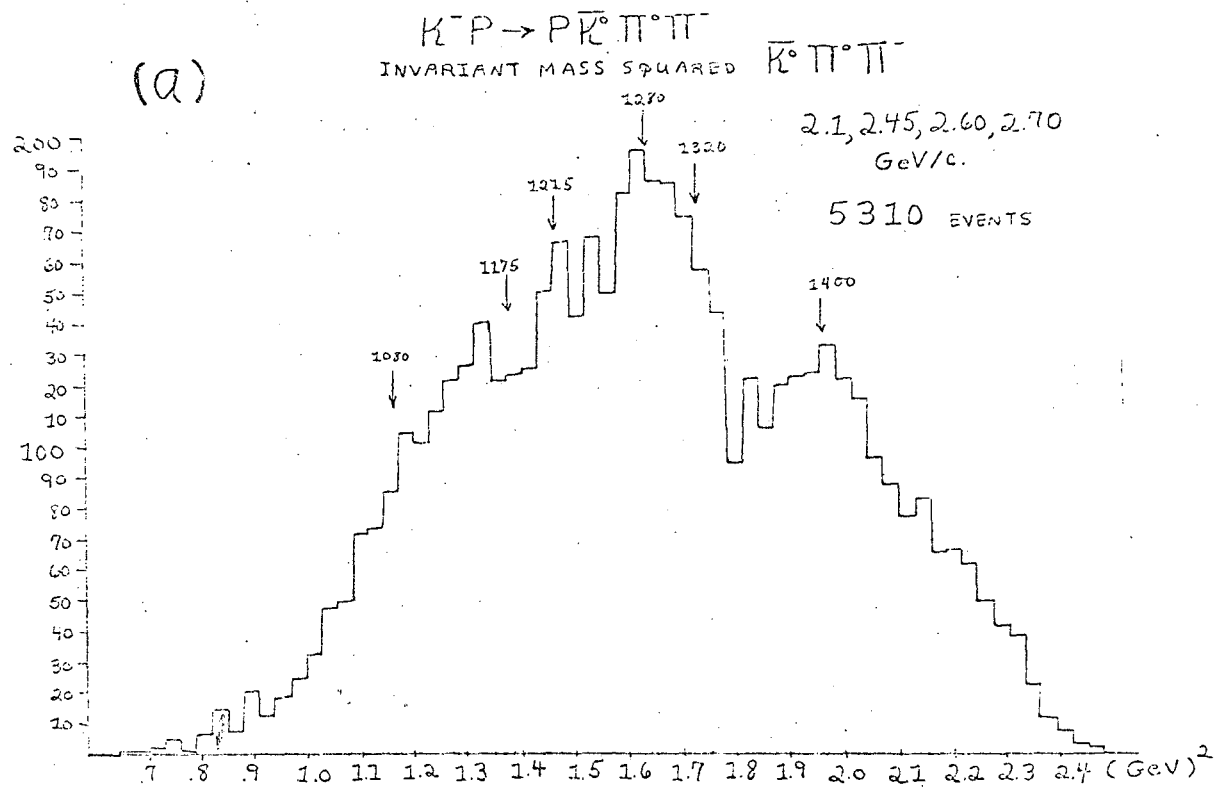
(a)
$K^-P \to P\bar{K}^0\pi^0\pi^-$
INVARIANT MASS SQUARED $\bar{K}^0\pi^0\pi^-$
2.1, 2.45, 2.60, 2.70 GeV/c.
5310 EVENTS
1030
1175
1215
1270
1320
1400
200
100
.7 .8 .9 1.0 1.1 1.2 1.3 1.4 1.5 1.6 1.7 1.8 1.9 2.0 2.1 2.2 2.3 2.4 (GeV)^2

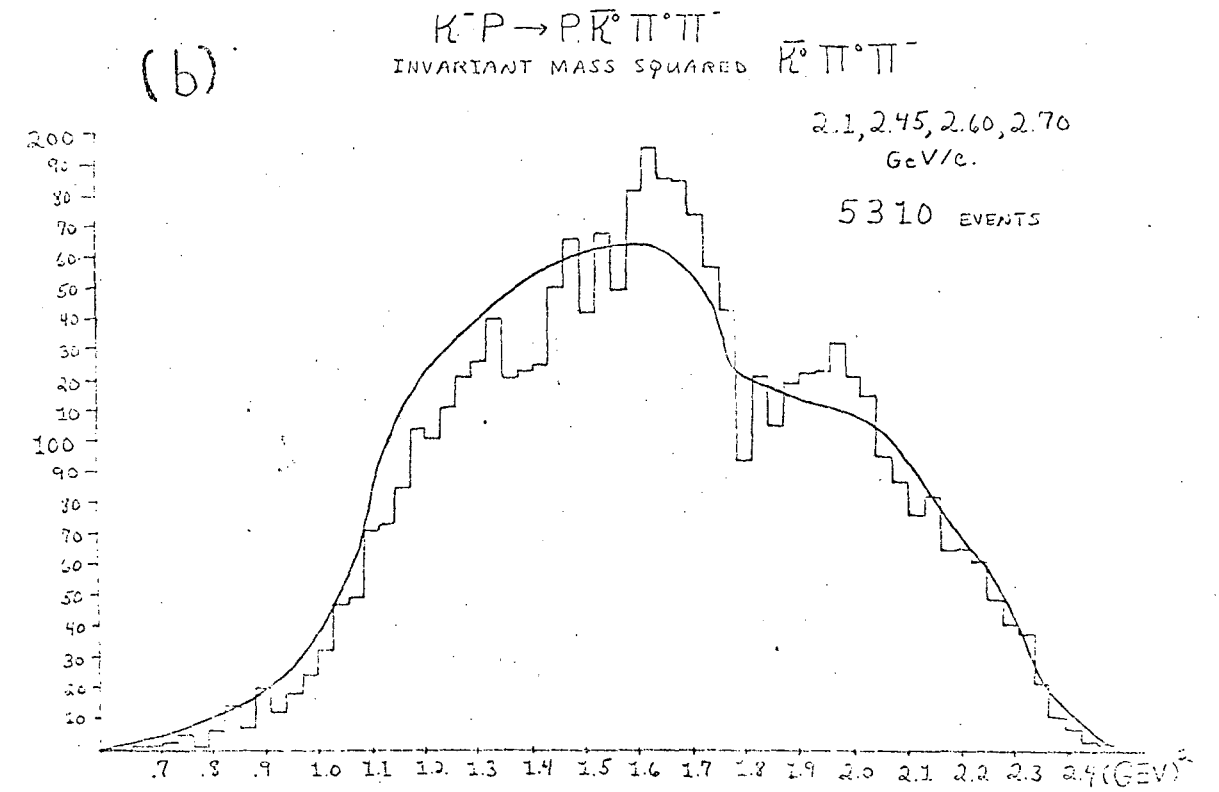
(b)
$K^-P \to P\bar{K}^0\pi^0\pi^-$
INVARIANT MASS SQUARED $\bar{K}^0\pi^0\pi^-$
2.1, 2.45, 2.60, 2.70 GeV/c.
5310 EVENTS
200
100
.7 .8 .9 1.0 1.1 1.2 1.3 1.4 1.5 1.6 1.7 1.8 1.9 2.0 2.1 2.2 2.3 2.4 (GeV)^2

Figure 65 c

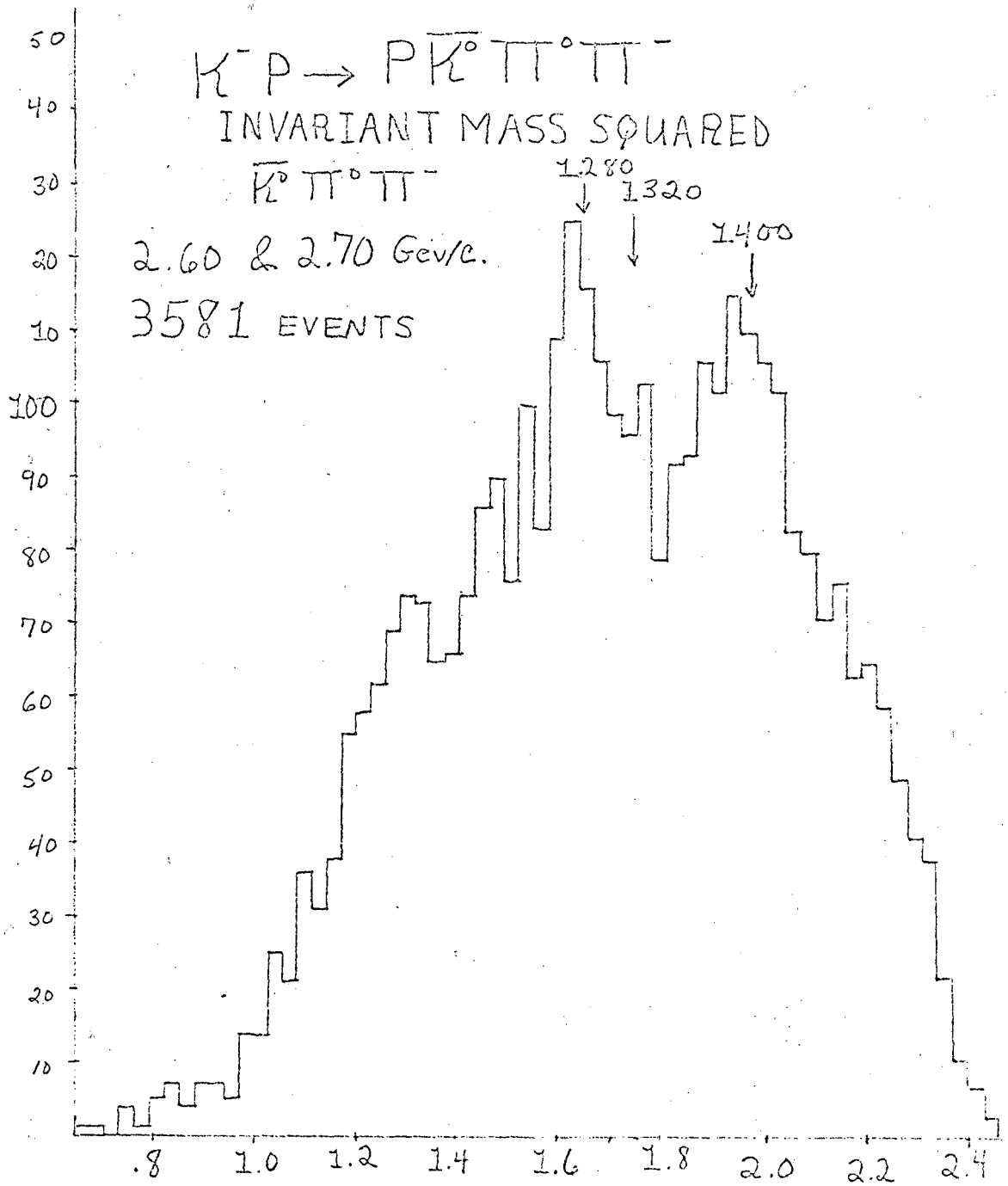
$K^- P \rightarrow P \bar{K}^0 \pi^0 \pi^-$
INVARIANT MASS SQUARED
$\bar{K}^0 \pi^0 \pi^-$
2.60 & 2.70 Gev/c.
3581 EVENTS
1.280
1.320
1.400
50
40
30
20
10
100
90
80
70
60
50
40
30
20
10
.8
1.0
1.2
1.4
1.6
1.8
2.0
2.2
2.4

Figure 65 d

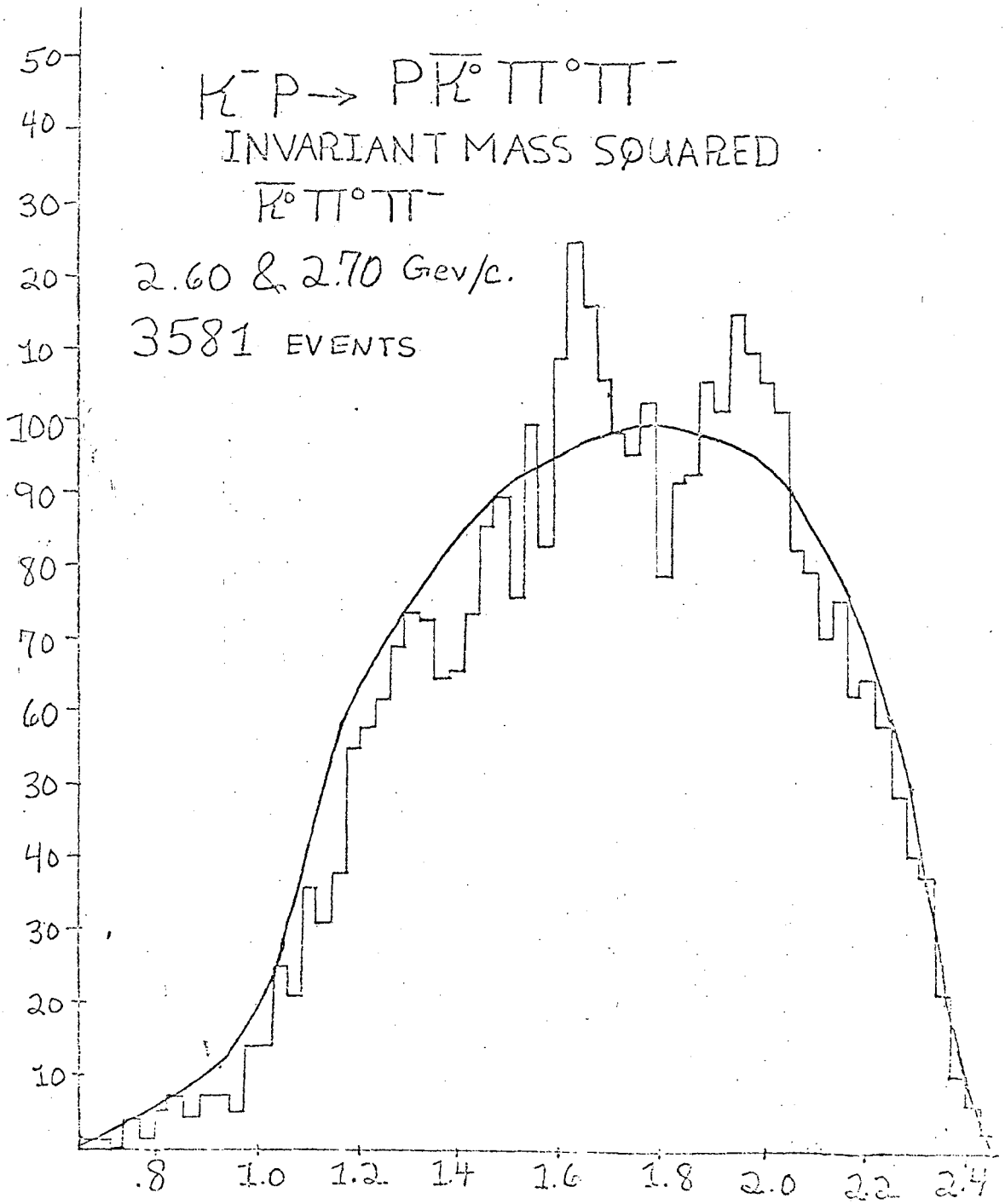
$K^- P \rightarrow P\bar{K}^0 \pi^0 \pi^-$
INVARIANT MASS SQUARED
$\bar{K}^0 \pi^0 \pi^-$
2.60 & 2.70 Gev/c.
3581 EVENTS
50
40
30
20
10
100
90
80
70
60
30
40
30
20
10
.8
1.0
1.2
1.4
1.6
1.8
2.0
2.2
2.4

Figure 65 e

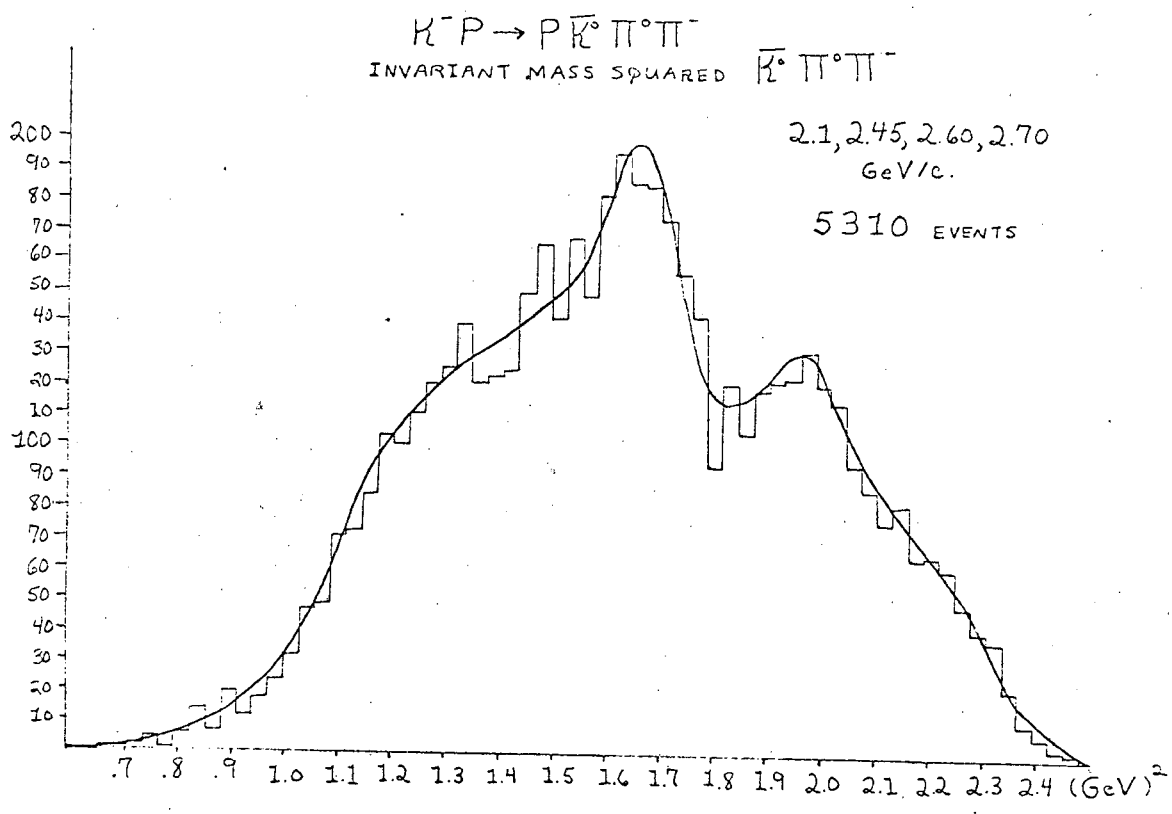
$K^- P \rightarrow P \bar{K}^0 \pi^0 \pi^-$
INVARIANT MASS SQUARED $\bar{K}^0 \pi^0 \pi^-$
2.1, 2.45, 2.60, 2.70 GeV/c.
5310 EVENTS
200
90
80
70
60
50
40
30
20
10
100
90
80
70
60
50
40
30
20
10
.7 .8 .9 1.0 1.1 1.2 1.3 1.4 1.5 1.6 1.7 1.8 1.9 2.0 2.1 2.2 2.3 2.4 (GeV)^2

Figure 65 f

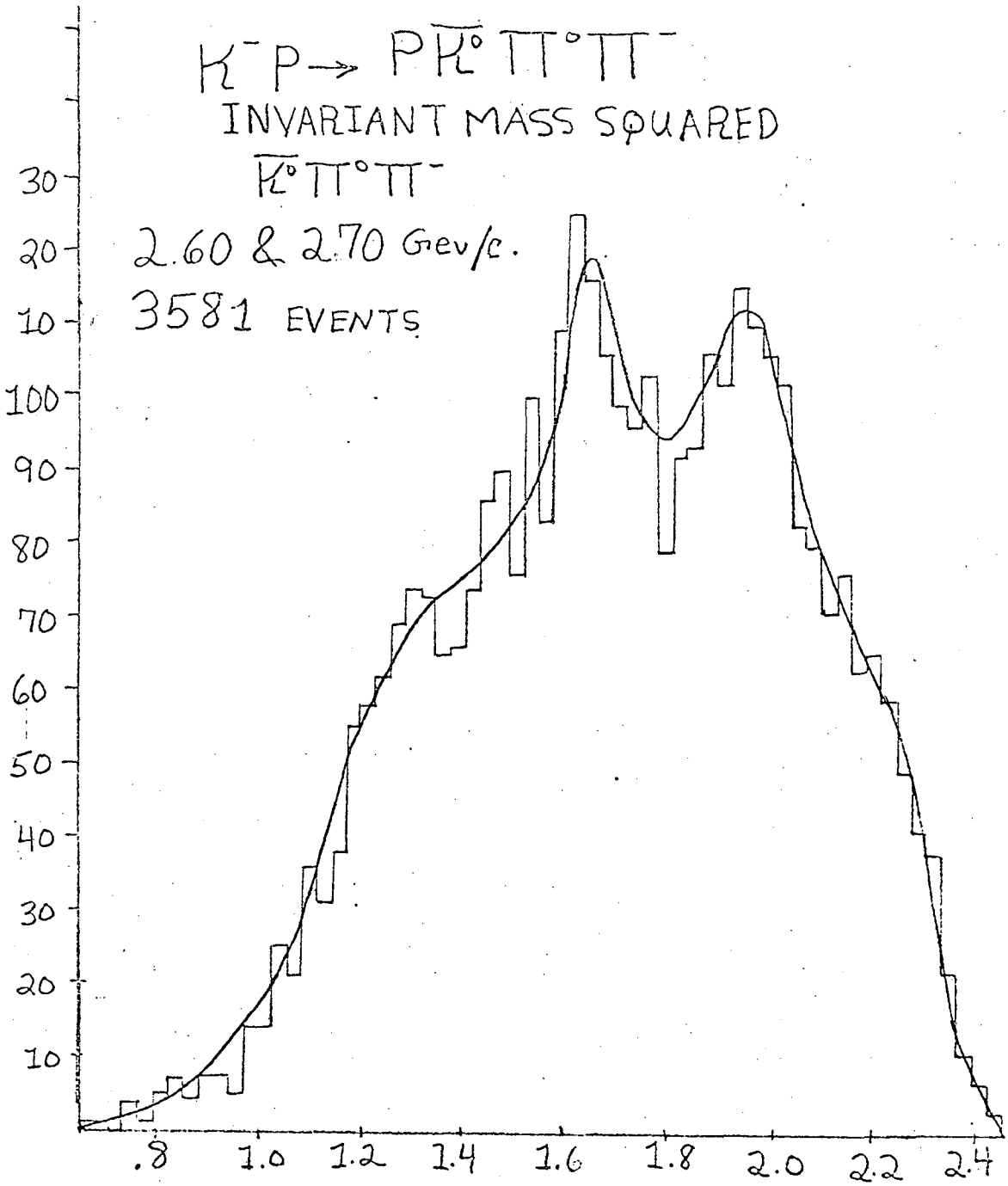
$K^- P \rightarrow P \bar{K}^0 \pi^0 \pi^-$
INVARIANT MASS SQUARED
$\bar{K}^0 \pi^0 \pi^-$
2.60 & 2.70 Gev/c.
3581 EVENTS
30
20
10
100
90
80
70
60
50
40
30
20
10
.8
1.0
1.2
1.4
1.6
1.8
2.0
2.2
2.4

Figure 65

$K^- P \rightarrow P \bar{K}^0 \pi^0 \pi^-$

INVARIANT MASS SQUARED $\bar{K}^0 \pi^0 \pi^-$

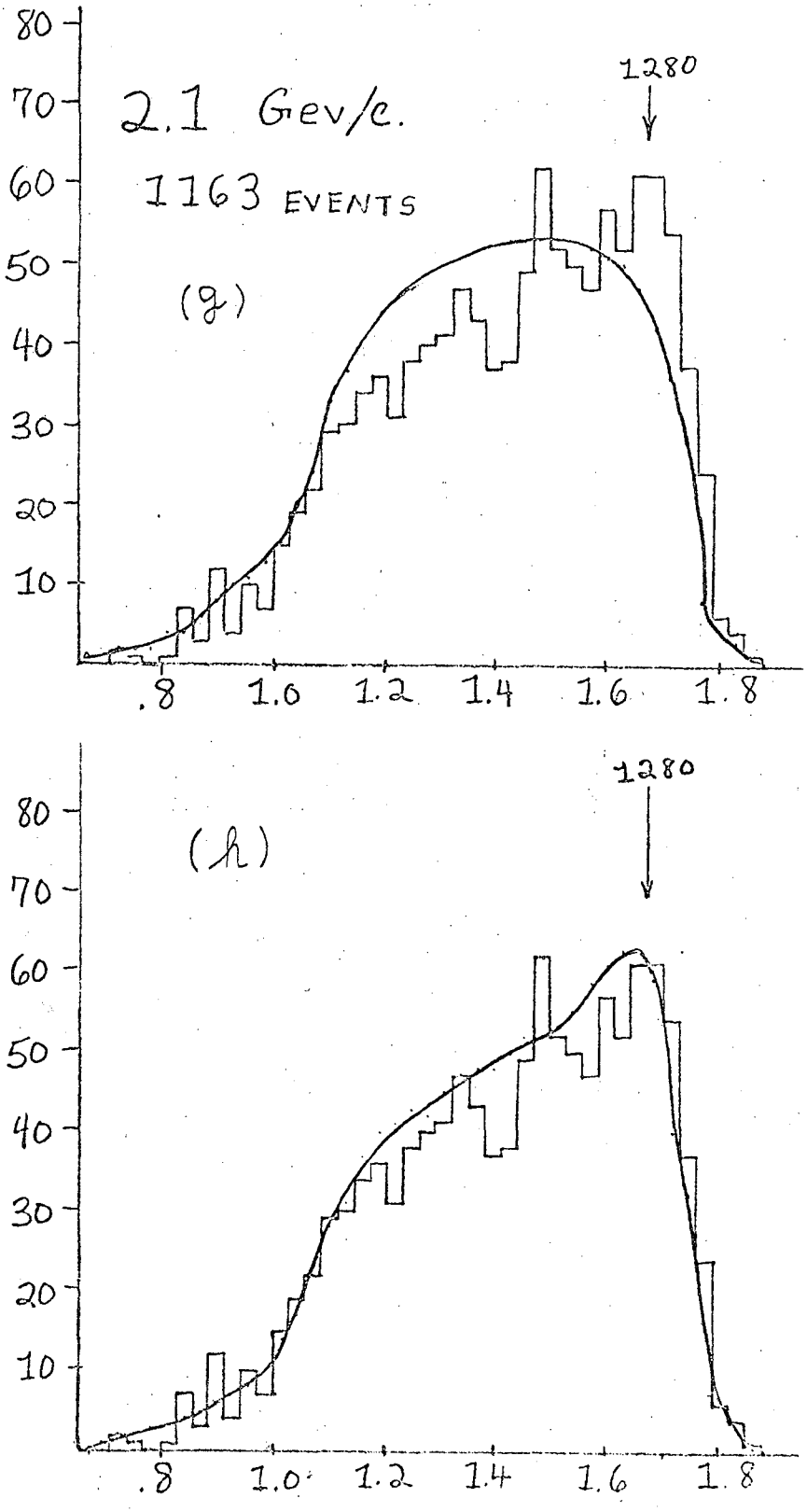

Figure 66

Histograms of $K^{o}\pi^{o}\pi^{-}$ invariant mass.

a) invariant mass $\overline{K}^{o}\pi^{o}$ between .83 and .95 GeV.

b) invariant mass $\overline{K}^{o}\pi^{-}$ between .83 and .95 GeV

Figure 66a

$K^- P \rightarrow P \bar{K}^0 \pi^0 \pi^-$

INVARIANT MASS

$\bar{K}^0 \pi^0 \pi^-$

$.83 \leq M(\bar{K}^0 \pi^0) \leq .95$

2.60 & 2.70 GeV/c.

1198 EVENTS

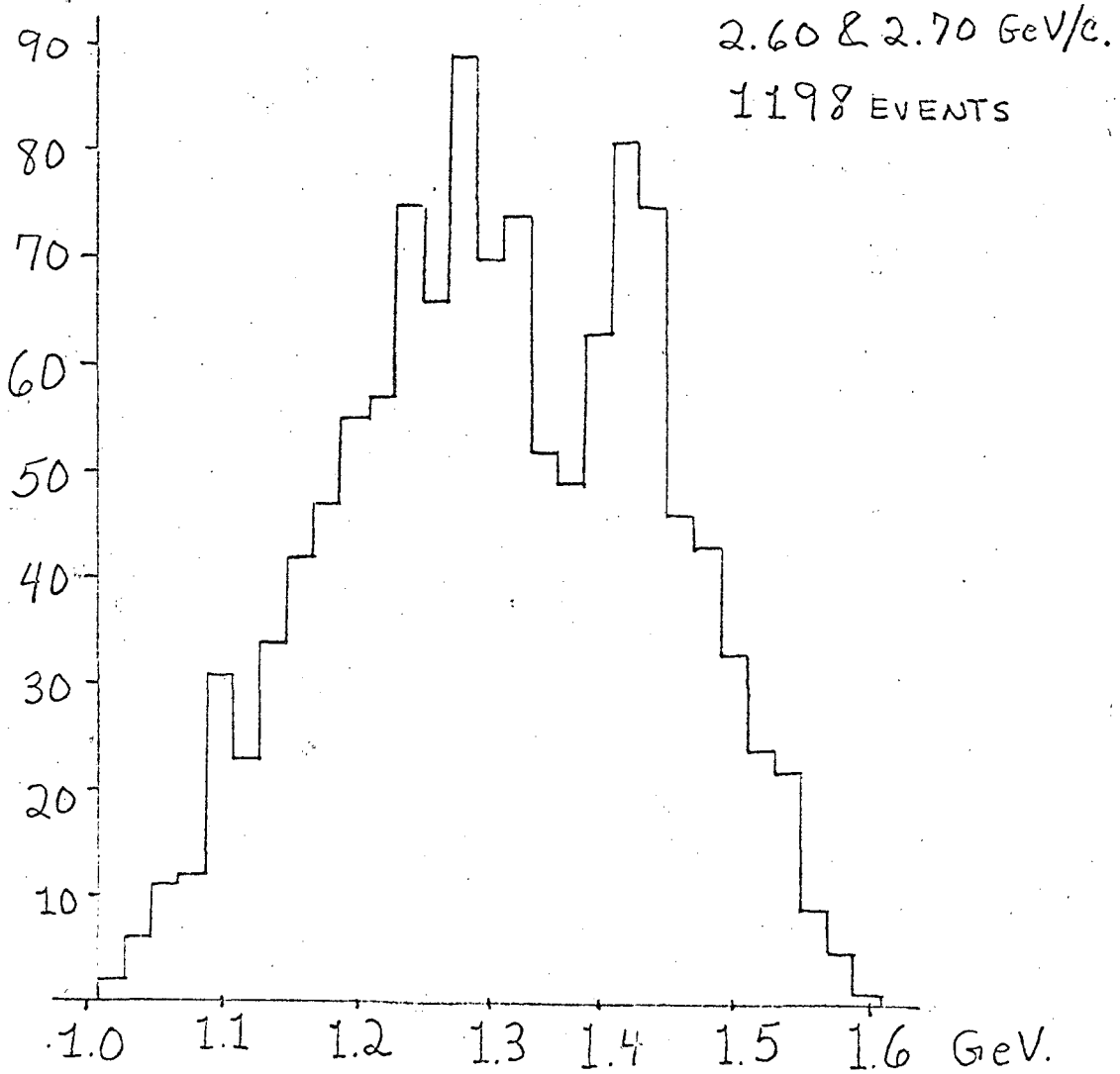

Figure 66b

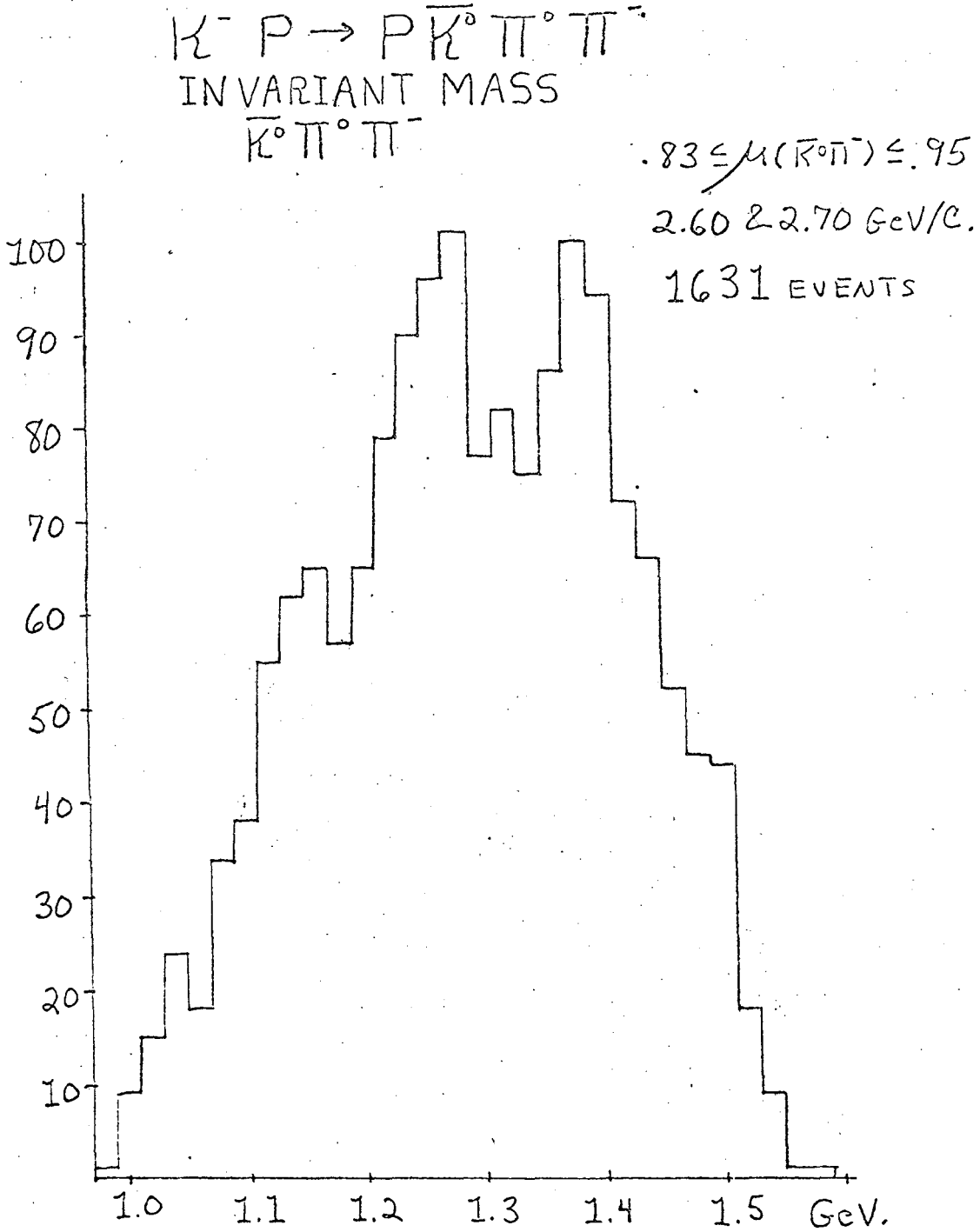
$K^- P \rightarrow P \bar{K}^0 \pi^0 \pi^-$
INVARIANT MASS
$\bar{K}^0 \pi^0 \pi^-$
$.83 \leq \mu(\bar{K}^0\pi^-) \leq .95$
2.60 & 2.70 GeV/C.
1631 EVENTS
100
90
80
70
60
50
40
30
20
10
1.0
1.1
1.2
1.3
1.4
1.5
GeV.

TECHNICAL INFORMATION DIVISION
LAWRENCE RADIATION LABORATORY
UNIVERSITY OF CALIFORNIA
BERKELEY, CALIFORNIA 94720